THE UNIVERSITY OF
WAIKATO
Te Whare Wānanga o Waikato
Research Commons

https://researchcommons.waikato.ac.nz/

Research Commons at the University of Waikato

Copyright Statement:

The digital copy of this thesis is protected by the Copyright Act 1994 (New Zealand).

The thesis may be consulted by you, provided you comply with the provisions of the Act and the following conditions of use:

- Any use you make of these documents or images must be for research or private study purposes only, and you may not make them available to any other person.
- Authors control the copyright of their thesis. You will recognise the author's right to be identified as the author of the thesis, and due acknowledgement will be made to the author where appropriate.
- You will obtain the author's permission before publishing any material from the thesis.

Valorisation of Waste Mussel Shells and Harakeke Fibres for Enhanced Performance in Polypropylene Composites

A thesis submitted in fulfilment of the requirements for the degree
of
Doctor of Philosophy in Engineering
at
The University of Waikato
by
Jing Xu

KO TE TANGATA

THE UNIVERSITY OF
WAIKATO
Te Whare Wānanga o Waikato

2026

Trust in the LORD with all your heart and lean not on your own understanding; in all your ways submit to Him, and He will make your paths straight.

Proverbs 3:5-6

Acknowledgements

I give all glory to God—the Giver of Life, the Way Maker—whose grace and strength sustained me throughout this research journey.

My deepest gratitude goes to my academic supervisors, Associate Professor Michael Mucalo (chief supervisor) and Professor Kim Pickering (co-supervisor), for their invaluable guidance, patience, and unwavering support during this study. Their expertise and encouragement were instrumental in shaping this work.

I am also grateful to every member of the Polymer and Composites Research Group for fostering such a collaborative and inspiring work environment. In particular, I wish to thank Christian Gauss for the many thought-provoking discussions that enriched this work.

I wish to express my sincere gratitude to the technical staff at the Large-Scale Laboratory (LSL), especially Sophia Rodrigues and Jonathan Van Harselaar, whose expertise and support were indispensable to this research. I also thank Professor Hun Xue from Fujian Normal University, China, for her assistance with XPS characterisation, and Helen Turner from the University of Waikato for her contributions to SEM analysis.

I am deeply grateful to my family and friends for their unwavering support. I particularly thank my husband for his encouragement and my daughter for the joy of sharing this journey. I am also thankful to the friends I made along the way, whose support enriched my experience.

Finally, I acknowledge the financial support provided by the New Zealand MBIE Endeavour Fund through the Amimia Aotearoa research programme (UOWX2004) at the University of Waikato, the University of Waikato Doctoral Scholarship (108023). I am also honoured to have received the Merit Award for Doctoral Study from the Waikato Graduate Women Educational Trust.

To all who contributed, directly or indirectly—thank you.

Abstract

This doctoral research develops high-performance, environmentally sustainable polypropylene (PP) composites by valorising low-value biogenic waste. Within a Circular Economy framework, it addresses challenges in plastic sustainability and the need for bio-based alternatives by utilising mussel shells (MS), an aquaculture by-product, and harakeke fibres (HF, Phormium tenax), derived from agricultural waste, as reinforcing materials. Through systematic characterisation, surface modification, filler hybridisation, and multi-scale evaluation, this study demonstrates the successful transformation of these biogenic low-value resources into functional reinforcements for PP.

The structural and surface properties of MS-derived fillers were first investigated, focusing on functionalization with a mussel-inspired polydopamine (PDA) coating. Solid-state nuclear magnetic resonance (SS-NMR) and Fourier-transform infrared spectroscopy (FTIR) confirmed PDA formation, revealing its indole/indoline units and quinonoid groups. X-ray diffraction (XRD), SS-NMR, and FTIR showed that MS contains calcite and aragonite phases, which remain intact after coating. Thermogravimetric analysis (TGA) confirmed the thermal stability of MS, slightly improved by PDA, while X-ray photoelectron spectroscopy (XPS) verified successful coating deposition on MS fillers via nitrogen-containing groups. Surface energy analysis revealed that PDA coating increased MS filler hydrophilicity, whereas maleic anhydride-grafted polypropylene (MAPP) treatment—particularly when combined with PDA—enhanced filler hydrophobicity, establishing PDA/MAPP co-modification as an effective strategy to improve filler interaction with the hydrophobic PP matrix.

Polypropylene (PP) composites reinforced with pristine, maleic anhydride-grafted polypropylene (MAPP)-modified, and PDA/MAPP co-modified mussel shell (MS) fillers were systematically compared with neat PP to assess thermal and mechanical performance. Thermogravimetric analysis (TGA) revealed improved thermal stability across all composites, most notably with PDA/MAPP-MS. X-ray diffraction (XRD) and differential scanning calorimetry (DSC) confirmed that MAPP and PDA/MAPP surface treatments enhanced nucleation and crystallinity, promoting β-crystal formation in the PP matrix. Mechanical testing showed that unmodified MS reduced tensile and flexural strength, an effect mitigated by MAPP modification. PDA/MAPP co-modification yielded the greatest improvements, with tensile strength, flexural strength, and modulus all significantly enhanced at 40 wt.% loading. Dynamic mechanical analysis (DMA), creep–recovery, and melt rheology further supported the advantages of PDA/MAPP co-modification, consistent with scanning electron microscopy (SEM) observations of improved interfacial bonding.

The study further explored hybrid reinforcements combining MS with HF. Crystalline structure analysis showed both fillers acted as nucleating agents, with hybrid systems producing higher crystallinity than neat PP. XRD confirmed the co-existence of α- and β-crystals. Composites with 10% MAPP-MS/30% HF and 10% PDA/MAPP-MS/30% HF showed the highest β-phase content (17.32% and 16.71%, respectively), enhancing toughness and elongation while retaining strength and stiffness. SEM–backscattered electron (BSE) analysis confirmed improved fibre–matrix adhesion and polymer bridging, while energy-dispersive X-ray spectroscopy (EDS) mapping showed uniform filler distribution. These hybrid systems outperformed single-filler composites, with 10% MAPP-MS/30% HF achieving a 48% increase in tensile strength over neat PP. DMA confirmed a higher storage modulus, improved energy dissipation, and better adhesion. Creep-recovery tests demonstrated greater dimensional stability, particularly for the 10% PDA/MAPP-MS/30% HF system. Melt rheology behaviour suggested the formation of a hybrid filler network that further restricts chain mobility.

Finally, composites with 5% PDA/MAPP-MS fillers demonstrated superior UV stability. After 1,000 hours of accelerated weathering, neat PP exhibited cracking, roughening, and discolouration, while PDA/MAPP-MS composites retained smooth, intact surfaces. FTIR confirmed their lowest carbonyl index increase, reflecting suppressed photo-oxidative degradation. XRD and DSC showed a stable crystalline structure, and mechanical testing revealed only a 15.6% tensile strength loss, compared to 62% for neat PP. DMA further confirmed superior viscoelastic stability. These results indicate dual protection: MS act as UV shield, while PDA scavenges free radicals to delay degradation.

Overall, this research establishes mussel shell and harakeke fibre as sustainable, high-performance reinforcements for PP. PDA/MAPP co-modification and hybridisation strategies optimise filler–matrix interactions, yielding composites with enhanced thermal, mechanical, rheological, and weathering properties. These findings highlight the potential of low-value biogenic fillers for sustainable, durable, and environmentally resilient composites.

Table of Contents

List of Figures

List of Tables

List of Abbreviations

BE	Binding energy
BSE	Backscattered Electron
CC	Calcium carbonate
CI	Crystallinity index
DMA	Dynamic mechanical analysis
DSC	Differential scanning calorimetry analysis
DTG	Derivative Thermogravimetry
EDS	Electron dispersive spectra
FE-SEM	Field Emission Scanning Electron Microscope
FTIR	Fourier transform infrared spectroscopy
FWHM	Full Width at Half Maximum
HF	Harakeke fibre
MAPP	Maleic anhydride-grafted polypropylene
MAPP-MS	MAPP-modified mussel shell
MS	Mussel shell
MW	Molecular weight
PDA	Polydopamine
PDA/MAPP-MS	PDA and MAPP co-modified mussel shell
PP	Polypropylene
SEM	Scanning electron microscopy
SMC	Super-mass-collider
SS-NMR	Solid-state Nuclear Magnetic Resonance spectroscopy
TGA	Thermogravimetric analysis
THR	Total heat released
TRIS	Tris(hydroxymethyl)-aminomethane
UV-vis	Ultraviolet - visible (UV-vis) spectroscopy
XPS	X-ray photoelectron spectroscopy
XRD	Powder X-ray diffraction

List of Symbols

ΔHc	Cooling enthalpy
ΔHm	Melting enthalpy
X%	Degrees of crystallinity
Tc	Crystallisation temperatures
E'	Storage modulus
E''	Loss modulus
$\tan \delta$	Damping factor
G'	Storage modulus (melt rheology)
G''	Loss modulus (melt rheology)
D_{50}	Median particle size
γ	Surface energy
γ_s	Total solid surface energy
γ_l	Total liquid surface energy
γ_s^p	Polar surface energy components of a solid
γ_s^d	Dispersive surface energy components of a solid
W	work of adhesion
ΔWa	Potential energy difference
W_{FF}	Filler-filler interface energy
W_{PP}	Polymer-polymer interface energy
$T_{5\%}$	Temperature at 5% weight loss
E'_g	Storage modulus in the glassy region
E'_r	Storage modulus in the rubbery region
Tg	Glass transition temperatures
ε_{max}	Maximum creep strain
ε_p	Permanent deformation

Chapter 1 Introduction

1.1 Background

New Zealand faces significant challenges to sustainable economic development arising from resource scarcity, environmental degradation, and climate change. In response, the country pursues a transition toward a low-carbon, resource-efficient economy to ensure long-term environmental and economic stability [1]. As a signatory to the Paris Agreement and under its Climate Change Response Act (Zero Carbon) Amendment 2019, New Zealand has established a legally binding target of net-zero greenhouse gas (GHG) emissions by 2050 [2].

Legislative and strategic actions have underpinned these commitments. The Resource Management Act 1991 marked a pivotal step, prioritising sustainability in planning and resource management [3]. The government's first sustainable development strategy, "Sustainable Development for New Zealand: Programme of Action"[4], further established this trajectory. More recently, New Zealand has adopted the Circular Economy (CE) as a strategic framework to reduce resource and energy consumption, minimise waste, and stimulate economic growth [3].

The Circular Economy, valued for its restorative and regenerative principles, has attracted widespread attention across policy, industry, and academic circles.[5]. According to the Ellen MacArthur Foundation, a Circular Economy aims to keep products, components, and materials at their highest utility and value, distinguishing between technical and biological cycles [6]. This approach moves beyond the traditional linear "extract-produce-consume-dispose" model, instead promoting cyclical material flows, renewable energy use, and the cascading of resources to maximise value and minimise waste [7; 8].

The building sector, recognised as resource- and energy-intensive, is a major contributor to global GHG emissions, accounting for approximately 32% of total global final energy use in 2010 [9]. As urbanisation accelerates, the sector's energy consumption, carbon emissions, and waste generation have become increasingly problematic [10]. Policymakers are consequently urging a transition from a linear to a circular model, as reflected in initiatives such as the European Construction Products Directive [11].

Integrating Circular Economy principles into the building sector encourages the use of renewable resources, efficient material utilisation, and the reintegration of waste into closed-loop systems. This paradigm shift requires redefining "resource" and "waste," and prioritising environmental considerations alongside functional, technical, and financial requirements in building material selection [12; 13].

Polymers, due to their versatility, corrosion resistance, chemical inertness, and moisture resistance, are increasingly used in non-structural building applications such as cladding, insulation, and decking [14]. Compared to traditional materials like timber, steel, and concrete, polymers offer advantages in long-term durability and reduced maintenance requirements. However, significant challenges remain. The production of polymers remains heavily dependent on non-renewable fossil fuel feedstocks, a dependency that accelerates resource depletion and impedes progress toward a more sustainable built environment.. Additionally, their non-biodegradable nature and susceptibility to UV exposureraise concerns about long-term durability and environmental impact [15; 16]. Beyond environmental concerns, fire safety presents an equally pressing challenge — polymers are often flammable and can release toxic fumes during combustion [17], which limits their broader application in the building sector.

Polymer composites offer a promising pathway for designing high-performance, sustainable building materials. Typically composed of a continuous polymer matrix and fillers, composites enable the reduction of fossil fuel-derived feedstock and the incorporation of reinforcement or functional additives [18]. The selection and combination of matrix and fillers, as well as their dispersion and interfacial compatibility, are critical for optimising composite properties [19].

Among thermoplastics, polypropylene (PP) stands out due to its low density, versatility, and recyclability. Since its commercial introduction in the 1950s, PP has found widespread use in packaging, automotive, building, and other sectors [20; 21]. In the building industry, PP offers excellent wind and hail resistance, moisture barrier properties, and waterproofing, making it an attractive material for various applications [22]. From a Circular Economy perspective, PP is particularly advantageous. As a thermoplastic, polypropylene exhibits excellent recyclability, retaining its mechanical properties through multiple reprocessing cycles. This characteristic significantly enhances its sustainability credentials by enabling closed-loop material recovery and reducing demand for virgin polymer production [23; 24]. In New Zealand, significant quantities of PP are collected from recycling streams, presenting an opportunity to divert this material from landfill and recirculate it as valuable feedstock [25]. By leveraging PP-based composites, the building sector can advance toward a more circular and sustainable material economy, addressing both environmental and economic objectives.

1.2 Research rationale

The building industry is one of the most material-intensive sectors. Growing concerns over resource scarcity and the need for sustainable development are driving efforts to adopt alternative building materials, particularly those derived from bio-renewable sources. Bio-genic fillers, such as natural fibres and mollusc shells, have attracted increasing interest as substitutes for mineral fillers and synthetic fibres in polymer composites. These materials help reduce environmental impacts, lower production costs, and promote resource circularity.

Natural fibre-reinforced polymer composites have been widely investigated owing to their high specific strength and stiffness [26; 27]. However, the use of mollusc shells as fillers in polymers remains relatively underexplored. Mollusc shells are composed primarily of calcium carbonate (>95%), making them a viable bio-based alternative to mineral-derived calcium carbonate in composite formulations. Recent studies have investigated the incorporation of shell waste into various polymer matrices [28-32]. Incorporating shell fillers into polymers not only helps reduce product costs and improve processing aspects, such as mould release, but also enhances mechanical properties [33-35]. These findings highlight the potential to valorise shell waste into high-value, bio-renewable materials.

Despite these advantages, incorporating mollusc shell fillers into polypropylene (PP) presents challenges. The hydrophilic nature of mollusc shell particles makes them incompatible with the non-polar, hydrophobic PP matrix. This incompatibility weakens interfacial adhesion, leading to reduced mechanical performance. Although several interfacial modifiers- such as surfactants, silane or titanate coupling agents, and maleic anhydride-grafted polypropylene (MAPP) -have been employed to address this issue, the limited surface functionality of the shells results in low modification efficiency. Consequently, interfacial bonding remains insufficient to enable effective stress transfer, compromising the structural performance of PP composites. Poor filler–matrix compatibility also promotes particle agglomeration during processing, particularly at higher filler loadings. A key research challenge is therefore to determine how to incorporate sufficient shell fillers to reduce non-renewable polymer content without compromising the material's functional properties.

In addition, PP is known to degrade under ultraviolet (UV) radiation, leading to discolouration, embrittlement, and loss of mechanical properties. This degradation is of particular concern in New Zealand, where UV radiation levels are higher than in many parts of Europe and North America [36]. UV degradation can, however, be mitigated through the incorporation of stabilisers, pigments, and other functional additives. Careful selection and formulation of these additives are essential to ensure that polymeric materials are suitable for their intended building applications.

This study aims to address the challenges associated with using mollusc shell fillers in PP composites. Three surface modification strategies were applied: polydopamine (PDA) coating, MAPP treatment, and a combined PDA/MAPP co-modification. Specifically, the PDA coating, inspired by the adhesive properties of mussel foot proteins, introduces abundant functional groups onto the shell surface [37; 38], thereby facilitating further MAPP modification. The chemical composition, crystalline structure, thermal stability, and surface characteristics of unmodified and modified shell powders were thoroughly characterised to assess their potential as composite fillers.

Subsequently, the effects of these untreated and modified fillers on PP composite properties were evaluated. This study focused on how filler type and content influence thermal behaviour, crystallinity, mechanical properties, creep resistance, and rheological performance. The extent of improvement achieved through each surface treatment was examined, and the underlying mechanisms related to enhanced interfacial bonding were discussed.

Hybrid composites provide an opportunity to combine the individual advantages of different reinforcement materials, potentially leading to improved properties and cost reductions [39-43]. This study also investigated hybrid composites incorporating both shell fillers and harakeke fibre (Phormium tenax), a native New Zealand flax valued for its cultural significance and mechanical strength [44]. Following the investigation of single-filler composites, the synergistic effects of combining modified mussel shell powders with alkali-treated harakeke fibres were assessed. By preparing composites with a total filler content of 40 wt.% and analysing their thermal, structural, and mechanical properties, this research aims to provide comprehensive insights into the potential benefits of hybridisation.

To evaluate UV resistance and weathering behaviour, neat polypropylene (PP) and selected PP composites- namely those containing 5% MAPP-modified mussel shell

(MAPP-MS) and 5% PDA/MAPP-modified mussel shell (PDA/MAPP-MS)- were subjected to accelerated weathering for up to 1000 hours under controlled exposure to heat, moisture, and ultraviolet (UV) radiation. Characterisation was carried out at 250-hour intervals to assess changes in surface morphology, crystallinity, thermal behaviour, chemical composition (with emphasis on the carbonyl index as a degradation indicator), and mechanical properties. This analysis aimed to elucidate the degradation mechanisms of mussel shell-reinforced composites, particularly the role of polydopamine modification, and to support predictions of their long-term performance under natural weathering conditions.

1.3 Research objectives

The current research aims to improve the performance of polypropylene composites with bio-generic fillers, specifically from mussel shells and harakeke leaves. Evaluate the potential of these fillers, single or in combination, with surface modification or without, in the application of PP composites and their influence on the thermal, mechanical, UV resistance properties. The specific objectives of the current work are summarised as follows:

1. To characterise the physicochemical properties of mussel shell waste and assess its suitability as a bio-based filler for polypropylene (PP) composites, focusing on its composition, crystallinity, thermal stability, and surface reactivity.
2. To synthesise and apply polydopamine (PDA) coatings on mussel shell particles and investigate their potential to enhance interfacial compatibility with the PP matrix through subsequent surface modification using maleic anhydride polypropylene (MAPP).
3. To evaluate the effects of mussel shell fillers- both unmodified and surface-modified- on the thermal, mechanical, crystalline, and rheological properties of PP composites at various filler loadings.
4. To investigate the synergistic effects of hybrid reinforcement by combining alkali-treated harakeke fibres with modified mussel shell fillers, and to assess their combined impact on the structural, thermal, and mechanical performance of PP composites.
5. To examine the effects of accelerated weathering on the thermal and mechanical degradation of neat PP and mussel shell-filled PP composites, and to determine the

role of PDA/MAPP surface modification in improving UV resistance and long-term durability.

6. To establish structure-property relationships within the developed composites and to identify the most effective modification strategy for enhancing performance, with a focus on achieving sustainable, high-performance materials from food and agricultural waste.
7. To demonstrate the feasibility of using waste-derived fillers and natural fibres to produce PP composites with properties suitable for non-structural building applications, contributing to the development of environmentally friendly and circular-material solutions.

1.4 Thesis outline

This thesis is divided into eight chapters:

Chapter 1 introduces the study by outlining the research background, rationale, aims, and structure of the thesis.

Chapter 2 presents a comprehensive literature review covering the fundamentals and recent developments relevant to this research. It begins with an overview of polymer composites and their components- matrix and fillers- followed by a detailed discussion of thermoplastic matrices, with emphasis on polypropylene (PP). The chapter then explores the microstructure and physical properties of PP and reviews the potential of biogenic fillers such as mollusc shells and natural plant fibres (e.g., hemp and harakeke). Particular attention is given to the use of mollusc shell-derived calcium carbonate in PP composites, surface modification strategies, fibre pretreatment, and hybrid filler systems for enhanced composite performance.

Chapter 3 outlines the materials and methods used in this study, including the surface functionalisation of mussel shell fillers using polydopamine and maleic anhydride polypropylene (MAPP), the fabrication of PP composites, and the characterisation techniques used to assess their structural, thermal, and mechanical properties.

Chapter 4 presented a comprehensive characterisation of mussel shell-derived fillers and their surface modifications, aimed at improving compatibility with the non-polar PP matrix. The self-polymerisation of dopamine into polydopamine (PDA) was confirmed, revealing structural transformations that impart chemical versatility and highlight its potential as a UV stabiliser for PP. The surface properties of both untreated and surface-modified mussel shell fillers were evaluated using two empirical models, enabling the assessment of hydrophobicity levels and the prediction of their tendencies for agglomeration and re-agglomeration upon incorporation into PP.

Chapter 5 investigates the incorporation of mussel shell fillers- either unmodified or surface-modified with MAPP or PDA/MAPP- into polypropylene (PP) composites. The study first examines how these fillers influence the microstructure of the composites, followed by an evaluation of their effects on key material properties. These include thermal stability, crystallinity, mechanical performance, and rheological behaviour, assessed across a range of filler loading levels.

Chapter 6 explores hybrid composites made by combining alkali-treated harakeke fibres with modified mussel shell fillers. The synergistic effects on microstructural, thermal, and mechanical properties are evaluated to determine their suitability for sustainable composite applications.

Chapter 7 evaluates the effect of low filler loadings (5% MAPP-MS or PDA/MAPP-MS) on the weathering resistance of PP composites. Neat PP and PP composites were subjected to varying durations of accelerated weathering and assessed for changes in surface morphology, microstructure, and mechanical performance. The influence of fillers on enhancing UV durability was examined, and underlying mechanisms were proposed to guide the future outdoor application of these PP composite materials.

Chapter 8 concludes the thesis by summarising the main findings, linking the structure–property relationships established throughout the study, and evaluating the feasibility of using food and agricultural waste to produce environmentally sustainable composites for non-structural building applications. Future research directions are also proposed.

1.5 References

1. Ministry for the Environment. (2021). *Ōhanga āmiomio - Circular Economy*. https:// environment.govt.nz/ what- government- is- doing/ areas- of- work/ waste/ ohanga- amiomio- circular- economy/

2. Ministry for the Environment. (2019). *Climate change response (Zero carbon) amendment act*. https://www.mfe.govt.nz/ climate- change/ zero- carbon- amendment- act

3. Resource Management Act reform, (2023). https://environment.govt.nz/what-government-is-doing/areas-of-work/rma/

4. NZ Government. (2003). *Sustainable Development for New Zealand Programme of Action*.

5. Mayer, A., Haas, W., Wiedenhofer, D., *et al.* (2019). Measuring progress towards a circular economy: a monitoring framework for economy-wide material loop closing in the EU28. *Journal of Industrial Ecology*, *23*(1), 62-76.

6. Foundation, E. M. (2013). *Towards the circular economy Vol. 1: an economic and business rationale for an accelerated transition*.

7. Korhonen, J., Honkasalo, A., & Seppälä, J. (2018). Circular Economy: The Concept and its Limitations. *Ecological Economics*, *143*, 37-46.

8. Kirchherr, J., Reike, D., & Hekkert, M. (2017). Conceptualizing the Circular Economy: An analysis of 114 definitions. *Resources, Conservation and Recycling*, *127*, 221-232.

9. Cabeza, L. F., Boquera, L., Chàfer, M., *et al.* (2021). Embodied energy and embodied carbon of structural building materials: Worldwide progress and barriers through literature map analysis. *Energy and buildings*, *231*, 110612.

10. Verhagen, T. J., Sauer, M. L., van der Voet, E., *et al.* (2021). Matching Demolition and Construction Material Flows, an Urban Mining Case Study. *Sustainability*, *13*(2), 653.

11. Regulation EU. (2011). *Regulation (EU) No. 305/2011 of the European Parliament and of the Council of 9 March 2011 laying down harmonized conditions for the marketing of construction products and repealing Council Directive 89/106/EEC*.

12. Zuo, J., Read, B., Pullen, S., *et al.* (2012). Achieving carbon neutrality in commercial building developments – Perceptions of the construction industry. *Habitat International*, *36*(2), 278-286.

13. Jain, R., & Lee, L. E. (2012). Fiber Reinforced Polymer (FRP) Composites for Infrastructure Applications-Focusing on Innovation, Technology Implementation and Sustainability. *Strategies for Sustainability*. (R. Jain & L. Lee, Eds.). Springer Science & Business Media.

14. Arıoğlu Akan, M. Ö., Dhavale, D. G., & Sarkis, J. (2017). Greenhouse gas emissions in the construction industry: An analysis and evaluation of a concrete supply chain. *Journal of Cleaner Production*, *167*, 1195-1207.

15. Ali, S. S., Elsamahy, T., Koutra, E.*, et al.* (2021). Degradation of conventional plastic wastes in the environment: A review on current status of knowledge and future perspectives of disposal. *Science of The Total Environment*, *771*, 144719.

16. Riahinezhad, M., Hallman, M., & Masson, J. (2021). Critical Review of Polymeric Building Envelope Materials: Degradation, Durability and Service Life Prediction. *Buildings*, *11*(7), 299.

17. Zhao, W., Kundu, C. K., Li, Z.*, et al.* (2021). Flame retardant treatments for polypropylene: Strategies and recent advances. *Composites Part A: Applied Science and Manufacturing*, 106382.

18. Clyne, T. W., & Hull, D. (2019). An introduction to composite materials. Cambridge university press.

19. Samal, S., & Blanco, I. (2021). Investigation of Dispersion, Interfacial Adhesion of Isotropic and Anisotropic Filler in Polymer Composite. *Applied Sciences*, *11*(18), 8561.

20. Jubinville, D., Esmizadeh, E., Saikrishnan, S.*, et al.* (2020). A comprehensive review of global production and recycling methods of polyolefin (PO) based products and their post-recycling applications. *Sustainable Materials and Technologies*, *25*, e00188.

21. Maddah, H. A. (2016). Polypropylene as a promising plastic: A review. *Am. J. Polym. Sci*, *6*(1), 1-11.

22. Shirvanimoghaddam, K., Balaji, K. V., Yadav, R.*, et al.* (2021). Balancing the toughness and strength in polypropylene composites. *Composites. Part B, Engineering*, *223*, 109121.

23. Grigore, M. E. (2017). Methods of recycling, properties and applications of recycled thermoplastic polymers. *Recycling*, *2*(4), 24.

24. Sanvezzo, P. B., & Branciforti, M. C. (2021). Recycling of industrial waste based on jute fiber-polypropylene: Manufacture of sustainable fiber-reinforced polymer

composites and their characterization before and after accelerated aging. *Industrial Crops and Products*, *168*, 113568.

25. WasteMINZ. (2020). *The Truth about Plastic Recycling in Aotearoa New Zealand in 2020*. https://www.wasteminz.org.nz/ files/ Behaviour%20Change/ The%20Truth%20about%20Plastic%20Recycling%20report.pdf

26. Akindoyo, J. O., Pickering, K., Beg, M. D.*, et al.* (2023). Combined digestion and bleaching of New Zealand flax /harakeke fibre and its effects on the mechanical, thermal, and dynamic mechanical properties of poly(lactic) acid matrix composites. *Composites. Part A, Applied science and manufacturing*, *164*, 107326.

27. Bhingare, N. H., Prakash, S., & Jatti, V. S. (2019). A review on natural and waste material composite as acoustic material. *Polymer Testing*, *80*, 106142.

28. Cangiotti, J., Scatto, M., Araya-Hermosilla, E.*, et al.* (2022). Valorization of seashell waste in polypropylene composites: An accessible solution to overcome marine landfilling. *European Polymer Journal*, *162*, 110877.

29. Kochan, C., Selli, F., & Erdogan, U. H. (2020). Using mussel shell wastes as an additive for the production of thermally improved polypropylene composite monofilaments. *J. Text. Eng.*, *112*(5), 683-690.

30. Gigante, V., Cinelli, P., Righetti, M. C.*, et al.* (2020). Evaluation of Mussel Shells Powder as Reinforcement for PLA-Based Biocomposites. *International Journal of Molecular Sciences*, *21*(15).

31. Lap, M. O., Kanbur, Y., & Tayfun, Ü. (2021). The use of mussel shell as a bio-additive for poly (lactic acid) based green composites. *Chemistry and Chemical Technology*, *15*(4), 621-626.

32. Şişmanoğlu, S., Kanbur, Y., Popescu, C.-M.*, et al.* (2024). Beneficial use of mussel shell as a bioadditive for TPU green composites by the valorization of an aqueous waste. *Waste Disposal & Sustainable Energy*, *6*(1), 123-137.

33. Karthick, R., Sirisha, P., & Sankar, M. R. (2014). Mechanical and Tribological Properties of PMMA-Sea Shell based Biocomposite for Dental application. *Procedia Materials Science*, *6*, 1989-2000.

34. Peceño, B., Alonso-Fariñas, B., Arenas, C., & Leiva, C. (2021). Influence of particle size of mussel shells in physical, mechanical and insulating properties of fireproof materials Procedia Environmental Science, Engineering and Management,

35. Chong, M. H., Chun, B. C., Chung, Y.-C., *et al.* (2006). Fire-retardant plastic material from oyster-shell powder and recycled polyethylene. *Journal of Applied Polymer Science*, *99*(4), 1583-1589.

36. Marston, N., & Jones, M. (2007). *Weathering of Polymeric Materials in New Zealand*. J. BRANZ Ltd, New Zealand. https:// d39d3mj7qio96p.cloudfront.net/ media/ documents/ SR182_ Weathering_ of_ polymeric_ materials_ in_New_ Zealand.pdf

37. Hemmatpour, H., De Luca, O., Crestani, D., *et al.* (2023). New insights in polydopamine formation via surface adsorption. *Nat. Commun.*, *14*(1), 664.

38. Hu, J., Yang, L., Yang, P., *et al.* (2020). Polydopamine free radical scavengers. *Biomaterials Science*, *8*(18), 4940-4950.

39. Szeluga, U., Kumanek, B., & Trzebicka, B. (2015). Synergy in hybrid polymer/nanocarbon composites. A review. *Composites Part A: Applied Science and Manufacturing*, *73*, 204-231.

40. Xu, H., Li, Y., Han, X., *et al.* (2021). Carbon black enhanced wood-plastic composites for high-performance electromagnetic interference shielding. *Materials Letters*, *285*, 129077.

41. Hemath, M., Mavinkere Rangappa, S., Kushvaha, V., *et al.* (2020). A comprehensive review on mechanical, electromagnetic radiation shielding, and thermal conductivity of fibers/inorganic fillers reinforced hybrid polymer composites. *Polymer Composites*, *41*(10), 3940-3965.

42. Oladele, I. O., Ibrahim, I. O., Akinwekomi, A. D., *et al.* (2019). Effect of mercerization on the mechanical and thermal response of hybrid bagasse fiber/CaCO3 reinforced polypropylene composites. *Polymer Testing*, *76*, 192-198.

43. Gwon, J. G., Lee, S. Y., Chun, S. J., *et al.* (2011). Physical and mechanical properties of wood–plastic composites hybridized with inorganic fillers. *Journal of Composite Materials*, *46*(3), 301-309.

44. Lowe, B. J., Carr, D. J., McCallum, R. E., *et al.* (2010). Understanding the variability of vegetable fibres: a case study of harakeke (Phormium tenax). *Textile Research Journal*, *80*(20), 2158-2166.

Chapter 2

Literature review

2.1 Polymer composite

2.1.1 Composite components- Matrix and fillers

In recent decades, composite materials have emerged as one of the most significant innovations in material science, owing to their exceptional performance characteristics. These versatile engineered materials combine two or more distinct constituents with differing physical or chemical properties, resulting in new materials that exhibit synergistic characteristics unattainable by the individual components alone. Composites feature a complex morphology comprising distinct phases: a continuous phase (the matrix) and one or more discontinuous phases (fillers or reinforcements) [1]. This engineered structure underpins their widespread application across various sectors, including furniture, packaging, decking, construction, automotive, and marine industries, and military and aerospace manufacturing.

Composites are broadly classified according to the type of continuous matrix phase, encompassing categories such as ceramic matrix composites (CMCs), metal matrix composites (MMCs), intermetallic matrix composites, carbon-carbon composites (CCCs), and polymer matrix composites (PMCs) [1]. Among these, PMCs have garnered substantial research interest. This focus is driven by escalating demand for advanced materials that offer optimal combinations of high specific stiffness (stiffness-to-weight ratio), toughness, corrosion resistance, and design flexibility, particularly within sustainability-conscious applications [2].

Within PMCs, the polymeric matrix binds the constituents and transfers mechanical load to the embedded fillers. Fillers exhibit diverse geometries, including fibres, flakes, spheres, or particles, and may be classified as inorganic (e.g., calcium carbonate, talc, glass, silica, clay), organosynthetic (e.g., carbon fibre, polymer fibres), or bioderived. Bioderived fillers, sourced from renewable materials such as plant fibres (e.g., flax, hemp, jute), wood flour, chitin, or agricultural waste residues, have emerged as sustainable alternatives [3-6]. They offer compelling advantages, including reduced environmental impact, enhanced biodegradability, and potential cost-effectiveness. However, their inherent hydrophilicity and variable morphological characteristics often hinder effective interfacial compatibility with typically hydrophobic polymer matrices, necessitating specific surface treatments [7].

A critical region determining composite performance exists at the boundary between filler and matrix: a nanoscale layer of constrained or immobilised polymer adjacent to the filler surface, termed the interphase [8]. This interphase, often considered a distinct third phase, governs the fundamental adhesion mechanisms, such as mechanical interlocking, chemical bonding, and van der Waals interactions, between the constituents. Consequently, it exerts a dominant influence on the composite's bulk mechanical, thermal, and physical properties. For bioderived fillers, deliberate engineering of this interphase through surface modifications (e.g., mercerisation, silanisation, acetylation) becomes particularly crucial to improve interfacial bonding between matrix and filler and to facilitate efficient stress transfer [1].

Therefore, the overall performance of PMCs is critically influenced by several factors: the selection of the polymer matrix and filler type—particularly bioderived options for sustainability—the fabrication methods employed, and the pretreatment protocols used to optimise interfacial compatibility. Most importantly, the characteristics of the interphase region play a decisive role in determining adhesion efficiency and stress transfer within the composite.

2.1.2 Polymer Matrix

The matrix plays a crucial role in polymer composites by binding the fillers, protecting them from mechanical wear and chemical attack, and transferring stress to ensure structural stability. It determines the composite’s shape, surface quality, and key performance characteristics such as environmental resistance, shear strength, compressive strength, and thermal stability [9]. The matrix also significantly influences failure mechanisms, with the composite’s load-bearing capacity largely dependent on the chemical structure of the matrix—whether thermosetting (brittle) or thermoplastic (ductile). Both types are commonly used, and matrix selection depends on the composite’s intended function and processing requirements.

Thermosets are typically chosen for superior creep resistance and are well suited to moulding large parts with various fibre forms. In contrast, thermoplastics offer greater damage tolerance and recyclability, making them favourable for sustainable composite development [2].

2.1.2.1 Thermosetting matrices

In the early development of polymer matrix composites (PMCs), thermosetting polymers were widely used. This preference stemmed from their excellent mechanical properties, as well as their chemical and dimensional stability. Thermosets cure via chemical crosslinking, forming a rigid, three-dimensional network structure that resists solvents and exhibits high creep resistance [10]. Common thermosetting resins such as polyester, vinyl ester, and epoxy have attracted considerable industrial and commercial interest.

Despite their advantages, thermoset-based composites exhibit certain drawbacks. For instance, phenolic resin matrices are often brittle and prone to shrinkage. Moreover, due to the permanent crosslinked structure, thermoset polymers cannot be remelted or reshaped once cured. As a result, recycling is technically difficult and economically unviable, requiring energy-intensive processes such as chemical degradation and repolymerisation. These limitations have led to growing interest in thermoplastic matrices, particularly for applications focused on recyclability and sustainability.

2.1.2.2 Thermoplastic matrices

Compared to thermosets, thermoplastics have become the dominant choice as matrix materials in composite applications, particularly in bio-composites. Thermoplastics soften upon heating and harden when cooled; this process is reversible and repeatable because they do not undergo cross-linking during processing [11]. Their molecular structure is held together by relatively weak intermolecular forces, such as van der Waals interactions and hydrogen bonding [12].

Thermoplastics have attracted substantial scholarly attention owing to their capacity for large-scale manufacturing, reduced environmental footprint and lower chemical hazards. Presently, they account for approximately 85% of the global polymer manufacturing output. Given that recycling is integral to promoting a Circular Economy, thermoplastics are particularly appealing as they can be readily reprocessed via thermal and mechanical means, facilitating their transformation into novel products without marked degradation of performance [13].

In contrast to thermosets, thermoplastics exhibit plastic deformation and flow characteristics when subjected to heating, permitting repeated cycles of melting and reshaping. This recyclability is attributed to their linear or branched-chain molecular configurations. Among the diverse range of thermoplastics, polyethylene (PE), isotactic polypropylene (iPP), polystyrene (PS), polyethylene terephthalate (PET), and polyvinyl chloride (PVC) are extensively employed due to their advantageous properties and economic viability [2]. It is noteworthy that polypropylene and its composites possess considerable versatility, rendering them suitable for a multitude of applications across the packaging, automotive, textiles, construction, and aerospace sectors [14].

2.1.3 Fillers

The development of multifunctional composites can be achieved through the incorporation of functional fillers into the polymeric matrix. These fillers are generally characterised by their rigidity, immiscibility with polymers, and the formation of distinct dispersed phases within the matrix. Most fillers, especially those derived from biological sources, are relatively low-cost, and their incorporation contributes to the mitigation of dependence on petroleum-based polymers, consequently leading to a reduction in the overall expenses associated with composite production. As the demand for polymer composites continues to escalate, fillers assume an increasingly pivotal role in augmenting both the performance and sustainability of these composites. Fillers encompass a diverse range of chemical families and compositions. This diversity includes inorganic substances such as calcium carbonate, talc, kaolin, mica, wollastonite, silica, and montmorillonite, in addition to organic and synthetic variants such as wood flour, glass fibres, PET or PVA fibres, carbon fibres, and plant fibres [8].

The selection of fillers is often determined by the functional specifications required of the ultimate composite material. For example, aluminium hydroxide (ATH) and magnesium hydroxide (MH) are extensively utilised as halogen-free flame retardants within both thermoset and thermoplastic matrices, serving as substitutes for hazardous halogenated substances [15]. Similarly, carbon-based fillers (e.g., carbon black, carbon nanotubes) can enhance electrical conductivity when integrated into polymers such as polypropylene or polyethylene [16].

Based on their geometric characteristics, fillers can be classified into spherical, flake, platelet, fibrous, and irregular particles. Fibrous fillers are characterised by a high aspect ratio, which enhances load transfer efficiency, interfacial bonding, and crack resistance, while simultaneously facilitating tailored directional strength and lightweight performance. Common examples of synthetic fibres include glass fibres, carbon fibres, nylon, and acrylic; however, the processing of synthetic fibres necessitates energy-intensive procedures (≥800 °C) for either melting or pyrolysis. Consequently, these materials are regarded as highly embedded energy substances. Considering the environmental emphasis of this study, these synthetic fibres are excluded from the scope of investigation. Particulate fillers, particularly mineral fillers, possess a longstanding application history in polymer composites, attributable to their abundance and cost-effective accessibility. Due to the rigid nature of mineral fillers, the incorporation of such fillers contributes to enhanced stiffness of polymer composites, along with improvements in thermal properties, creep resistance, and shrinkage. Nevertheless, the inclusion of mineral particles within the polymer matrix can lead to a decline in the toughness and strength of the composites. Various factors, including the nature of the polymer matrix, particle size, aggregate size, surface morphology, and interfacial interactions between the filler and matrix, govern the properties of the resulting polymer composite.

Beyond mere functionality, considerations of sustainability and the reduction of weight have emerged as pivotal factors in the selection of fillers. In light of escalating energy expenses and heightened environmental apprehensions, biogenic fillers, particularly those derived from agricultural by-products such as plant fibres, as well as food wastes like seashell and eggshell residues, have attracted considerable attention as viable sustainable alternatives for fillers [17-19]. Derived from renewable resources, these biogenic fillers offer advantages, including diminished reliance on fossil fuels, reduced raw material and energy consumption, and enhanced biodegradability [18].

2.2 Polypropylene

The integration of plastics within a Circular Economy frameworkis essential to reducing environmental impact, preserving natural resources, and mitigating the emissions of greenhouse gases (GHG) [20]. Plastics inherently possess significant durability; however, they often remain insufficiently utilized subsequent to a singular application.. In the year 2020, the global production of plastic approximated 370 million tonnes, with a mere 14% undergoing recycling [21]. This scenario presents both a dilemma and an opportunity: the dilemma of enduring plastic pollution, contrasted with the opportunity to reintroduce valuable plastic waste as a secondary raw material. Thermoplastics, exemplified by polypropylene (PP), are exceptionally well-suited toa circular economic framework. Their capacity for repeated melting and remoulding facilitates effective recycling and reprocessing [22]. Furthermore, thermoplastics necessitate substantially lower energy expenditures for recycling compared to the production of new materials, thereby contributing to diminished GHG emissions and a reduced dependency on fossil resources [23].

Among thermoplastics, polypropylene (PP) has emerged as one of the most widely used polymers worldwide, owing to its low density (~0.90 g/cm^3), cost-effectiveness, and broad applicability. Since its commercial introduction in the 1950s, PP has been extensively employed in sectors such as packaging, automotive, construction, consumer goods, and textiles [14]. In New Zealand, for instance, over 10,000 tonnes of PP were retrieved in 2020 from both recycling initiatives and general waste streams [24], highlighting its potential for reintegration into production cycles under a Circular Economy framework.

From a technical standpoint, PP presents a favourable combination of properties that make it a strong candidate for composite applications. As a semi-crystalline thermoplastic, it offers high stiffness, good impact resistance, and dimensional stability. Its hydrophobic nature limits moisture uptake, which is an essential factor in preserving the mechanical integrity of natural fibre-reinforced composites. In addition, PP demonstrates excellent chemical resistance, processability, and durability over multiple reprocessing cycles [25; 26].

Importantly, the relatively low processing temperature of PP (160-175 °C) renders it particularly amenable to thermally sensitive bio-based fillers such as natural fibres, which are prone to degradation at elevated temperatures. This compatibility, in conjunction with its recyclability and performance attributes, positions PP as an optimal matrix for the formulation of sustainable composite materials [27].

Understanding the intrinsic properties of polypropylene is crucial for establishing structure–property–performance relationships in its application as a sustainable composite matrix. The characteristics of polypropylene are predominantly governed by its microstructural attributes—specifically, its molecular configuration and tacticity, degree of crystallinity, and hierarchical arrangement of crystalline and amorphous regions. This microstructural framework significantly influences the mechanical, thermal, and viscoelastic properties of PP. A comprehensive understanding of these structural characteristics is, therefore, crucial for forecasting and enhancing the macroscopic performance of PP-based composites.

2.2.1 Microstructure of polypropylene

Polypropylene (PP) is synthesised from the propylene monomer ($CH_3–CH=CH_2$), typically using Ziegler-Natta catalysts. Since the 1980s, metallocene catalysts have also been adopted in industrial production [14]. A representative molecular structure of PP is shown in Figure 2-1.

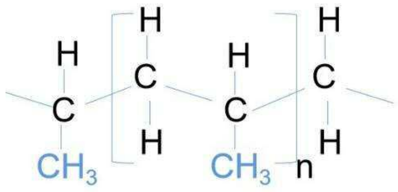

Figure 2- 1:The structure of polypropylene

The microstructure of PP can be characterised at four hierarchical levels, as shown in the schematic image in Figure 2-2: the primary level involves chain architecture; the secondary level relates to the crystal structure; the tertiary level constitutes the lamellae structure; and the quaternary level involves larger crystal aggregates or super-molecular structures [28].

At the primary level, chain characteristics include molecular weight and molecular weight distribution. Particular attention should be paid to the spatial arrangement of methyl groups ($–CH_3$) along the polymer backbone.This sequence, known as tacticity or stereoregularity, critically influences the polymer's crystallisation behaviour, melting characteristics, and mechanical properties [29; 30]. Depending on methyl group positioning, PP exhibits three basic chain configurations: isotactic (*iPP*), with methyl groups uniformly aligned on one side of the chain; syndiotactic (*sPP*), with methyl groups alternating sides; and atactic (*aPP*), with methyl groups arranged randomly [31].

Despite its relatively simple hydrocarbon composition, PP exhibits significant complexity in its crystalline phases at the secondary level. High chain regularity enables PP to crystallise readily under standard processing conditions. Both *iPP* and *sPP* are semi-crystalline polymers, whereas *aPP* is entirely amorphous. Regarding crystallinity, most commercial *iPP* exhibits levels ranging from 40% to 60%, while *sPP* typically has a crystallinity of approximately 30% [32]. Semi-crystalline polymers, such as PP, are best described by a three-phase model comprising crystalline, amorphous, and rigid amorphous regions. The amorphous phase, composed of disordered polymer chains between lamellae and spherulites, plays a critical role in mechanical performance. Evidence indicates that thermal treatment enhances the mobility of the amorphous phase at elevated temperatures, leading to increased crystallinity as the crystalline phase grows at the expense of the amorphous phase. Furthermore, within polypropylene, the rigid amorphous phase can crystallise, contributing to its characteristic cross-hatched structure [28].

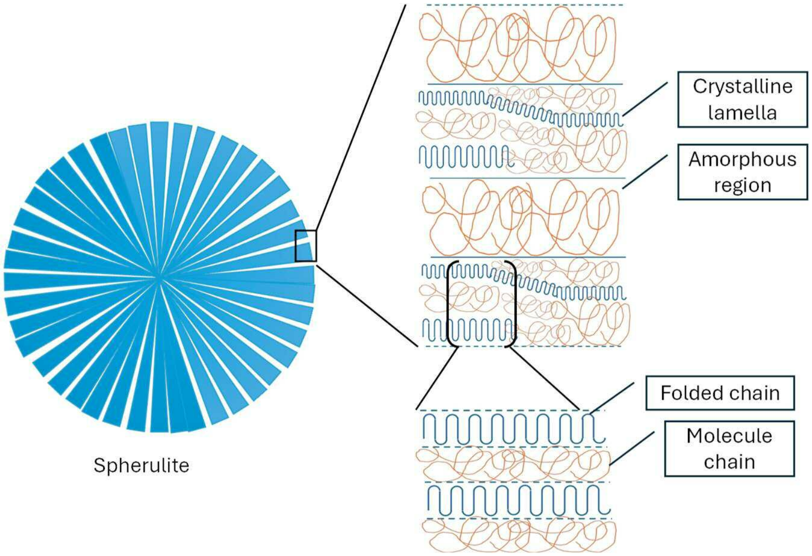

Figure 2- 2: Schematic presentation of polymer microstructure [121].

PP exhibits polymorphism, manifesting three primary crystalline forms: α-monoclinic, β-trigonal, and γ-orthorhombic [31]. The crystal structure formed depends critically on crystallisation conditions. Key factors include melting and cooling rates, pressure, the presence of nucleating agents or fillers, and processing conditions such as shear treatment [33; 34]. Among these crystalline forms, α-PP is the most thermodynamically stable and predominant form found in extruded or injection-moulded PP. The β-form is favoured by a temperature gradient [35; 36], within a flow field [37], or prompted by nucleating agent during crystallisation [38-40]. The γ-form, the least common, is generally found in low molecular weight PP.

The tertiary level of microstructure involves the lamellae structure. Lamellae are thin (typically 10-20 nm thick), plate-like crystalline fundamental units where polymer chains fold back and forth. The quaternary level involves spherulites, which are spherical aggregates of lamellae growing radially from a central nucleus, consisting of individual lamellae or bundles of lamellae. Melt crystallisation under slow cooling typically yields the common spherulitic morphology. Conversely, rapid quenching often results in a non-spherulitic morphology [41]. Spherulite formation can be observed using polarised light microscopy, where the radial growth pattern of lamellae from the nucleus becomes evident as spherical, polycrystalline aggregates.

2.2.2 Physical properties of polypropylene

The desirable physical properties of polypropylene (PP) are intrinsically linked to its microstructure. As a semi-crystalline polymer, PP comprises both crystalline lamellae and amorphous regions. The relative proportions of these phases, along with molecular arrangement and chain mobility, govern its overall mechanical, thermal, and viscoelastic performance.

Tacticity, or the stereoregularity of methyl groups along the polymer backbone, plays a critical role in determining crystallinity and, consequently, physical behaviour. Isotactic polypropylene (*iPP*) is the most commercially significant form due to its high crystallinity, low density, high stiffness, and excellent chemical resistance. However, its relatively poor impact resistance limits its broader application [30]. Syndiotactic PP (*sPP*), known for its elasticity and optical clarity, is constrained in practice by low mechanical strength, slow crystallisation rates, and complex polymorphism [29]. Atactic PP (*aPP*), which is entirely amorphous and behaves like a viscous liquid or gum depending on its molecular weight, is generally considered a low-value by-product. However, due to its compatibility with *iPP*, *aPP* can serve as a low-cost modifier to improve toughness. Additionally, blending *iPP* and *sPP* in equal parts (50/50) has been shown to improve fibre drawability compared to *sPP* alone [42]. Zhang *et al.,* [43] blended different proportions of *aPP* (Exxon Mobil 399) with *iPP* (S1003). At low *aPP* contents (10- 20 wt.%), the tensile strength decreased slightly (from 45.9 MPa to 40.5 MPa), but toughness, as indicated by breaking energy, improved from 31.8 MJ/m^3 (neat iPP) to 33.9 and 42.6 MJ/m^3, respectively. However, at

50 wt.% *aPP*, tensile strength dropped by 50%, attributed to the disruption of the *iPP* crystalline network by excessive *aPP*, which compromises stress transfer.

Crystallinity is a key determinant of mechanical performance. In general, higher crystallinity results in increased stiffness, tensile strength, and hardness, though often at the cost of ductility and impact resistance. The Young's modulus, a fundamental measure of tensile behaviour, is strongly correlated with crystallinity. Li *et al.,* found that increasing the crystallinity of isotactic polypropylene (iPP) from 38.97% to 50.67% resulted in a corresponding rise in both the Young's modulus, as measured by tensile testing, and the storage modulus, as determined by dynamic mechanical analysis [44].

The polymorphism of PP also influences its mechanical properties. The two main crystalline forms, α and β, exhibit distinct mechanical characteristics. α-PP, the most common and thermodynamically stable form, provides high tensile strength and rigidity. In contrast, β-PP is known for its superior toughness, greater elongation at break, lower density, improved transparency, and enhanced impact and tear strength [33].

The amorphous phase complements the crystalline phase by providing flexibility and acting as the main conduit for gas and moisture permeability, as well as chemical diffusion and environmental degradation. The mobility and volume fraction of amorphous chains significantly affect the material's viscoelastic response and toughness [45].

Lastly, spherulitic morphology, representing the highest level of crystalline aggregation, plays an essential role in defining bulk properties. Larger spherulites are typically associated with increased brittleness and optical haze. In contrast, smaller spherulites, often induced by rapid cooling or nucleating agent, can enhance stiffness, yield strength, transparency, and sometimes toughness [46].

2.3 Biogenic fillers for polymer composite

2.3.1 Biogenic calcium carbonate - Mollusc shells

Conventional commercial production of calcium-containing minerals, such as calcium carbonate and calcium oxide, primarily relies on geogenic sources like limestone. These processes are labour- and energy-intensive, involving mining operations that not only alter natural landscapes but also contribute to resource depletion and other environmental burdens [47]. In contrast, the recovery of calcium-rich by-products from aquacultural and food processing industries presents a sustainable alternative that well-suited toCircular

Economy principles. Transforming such waste into value-added products contributes to waste reduction and resource efficiency. These biogenic calcium sources are generally considered non-toxic, biocompatible, and suitable for a wide range of applications, including food supplements, plastics, paper production, and biomedical materials [48; 49].

Calcium carbonate is among the most widely used calcium-containing mineral fillers globally, with an estimated annual production of approximately 150 million tonnes [50]. Due to its low cost and ready availability, it is frequently employed as a filler in polymer composites to improve mechanical performance and thermal stability, while also providing enhanced surface finish [8]. Additionally, calcium carbonate has been shown to increase the onset crystallisation temperature of polymer matrices and to reduce moulding cycle times during injection processing, thus influencing the overall crystallinity of the composite system [51].

One promising biogenic source of calcium carbonate is mollusc shells, which are composed of over 95 wt.% calcium carbonate. Molluscs form the second largest animal phylum after arthropods, occupying diverse habitats ranging from marine and freshwater to terrestrial ecosystems. Representative species include snails, clams, oysters, scallops, cockles, and mussels. The global production of bivalve molluscs—accounting for inland, coastal, and marine aquaculture—was estimated at 17.7 million tonnes [52]. In New Zealand, aquaculture is a rapidly growing industry, largely centred around Greenshell™ mussels, Pacific oysters, and Chinook salmon. In 2020 alone, approximately 101,657 tonnes of mussels and 1,364 tonnes of oysters were harvested, with a combined commercial value of around NZD $400 million [53]. Given that shells make up approximately 70–80% of the total organism weight for mussels and oysters [54; 55], it is estimated that over 70,000 tonnes of mollusc shell waste were generated in New Zealand that year alone.

Despite their considerable quantity, waste mollusc shells presently possess limited opportunities for repurposing. In the absence of developed markets, they are generally relegated to landfills. In certain instances, they are also discarded into marine environments. Nevertheless, this practice has recently been curtailed under New Zealand legislation owing to its associated ecological hazards. This scenario poses a significant environmental dilemma. The organic matrix contained within mollusc shells—which encompasses glycoproteins, chitin, and polysaccharides—undergoes microbial decomposition, yielding malodorous and deleterious gases such as ammonia (NH_3), hydrogen sulphide (H_2S), and volatile amines. These emissions not only produce offensive odours but also exacerbate localised pollution. As a result, the disposal of waste mollusc shells is increasingly perceived as a pressing environmental concern, both within New Zealand and on a global scale.

Considering their mineralogical composition and physical attributes, mollusc shells constitute a promising source of biogenic calcium carbonate for functional applications. Comprising approximately 95–99 wt.% calcium carbonate and 0.1–5 wt.% organic matter, the compositional characteristics of the shells remain relatively uniform across various species. Among molluscs, oyster and cockle shells have been documented to possess the highest concentrations of calcium carbonate, reaching levels of up to 98% [54; 56]. Hence, the valorisation of waste mollusc shells as fillers in polymer composites provides a dual advantage: mitigating the environmental impact associated with shell disposal while fostering the advancement of sustainable, bio-renewable composite materials derived from locally sourced feedstocks.

2.3.1.1 Mollusc shell-derived filler in polypropylene composites

The potential of mollusc shells as bio-fillers in polymer composites has been widely explored. Studies have examined various mollusc species, including clam [57; 58], snail [59; 60], blue mussel and oyster [61; 62], scallop [63], cockle [56], and periwinkle [64]. Owing to the shared chemical composition of mollusc shells- primarily calcium carbonate (over 95%)- some research has utilised mixed-species shells, such as combinations of oyster, scallop, and clam [50], or generalised mollusc shell waste [65; 66].

As a form of food or aquaculture waste, mollusc shells require pre-treatment before being used as fillers. The pre-treatment process typically aims to control particle size and remove impurities and bacterial contaminants. Most studies have employed simple cleaning procedures, such as washing and drying at approximately 100 °C, occasionally followed by mild chemical treatment with 4% w/v sodium hydroxide to strip organic layers and expose the nacreous region [67]. Martínez-García *et al.,* [68] proposed thermal disinfection at 135 °C for 32 minutes to meet EU standards for pathogen control, while more elaborate pre-treatments such as multi-stage ball milling and calcination at up to 500 °C were demonstrated by Hamester *et al.,* [61] to facilitate shell brittleness and particle refinement.

Mollusc shell fillers have consistently demonstrated the ability to improve the thermal stability of polypropylene (PP) composites. Xia *et al.,* [58] observed a steady increase in the initial decomposition temperature of PP with shell loadings from 5 wt.% to 30 wt.%, attributing this to the barrier effect of the inorganic phase. Similar thermal advantages were observed by Essabir *et al.,* [69], who demonstrated improved degradation resistance for snail shell-filled PP, comparable to commercial $CaCO_3$ composites.

Mechanical reinforcement from shell fillers is generally evident in stiffness-related properties such as Young's modulus and flexural modulus. Li *et al.,* [62] compared mussel shells with commercial $CaCO_3$ as fillers in PP. At 10 wt.% loading, mussel shell-filled PP showed an 85% increase in Young's modulus, outperforming the 79% increase achieved with 5 wt.% $CaCO_3$. The authors attributed this to better interfacial compatibility provided by organic residues in the shells. This finding supports the general understanding that filler crystallinity and stiffness strongly affect the tensile modulus, with Young's modulus serving as a key indicator of mechanical performance [70].

In a separate comparative study, Essabir *et al.,* [69] found that snail shell particles (~10 μm) provided mechanical and thermal performance similar to commercial $CaCO_3$ at up to 30 wt.% loading. Young's modulus improved by 91% with snail shell and 97% with $CaCO_3$, though tensile strength declined by around 10% in both cases, indicating improved stiffness at the cost of ductility. Likewise, incorporating 10–30 wt.% oyster shell into recycled PP increased thermal stability, stiffness (by 10.4%), and microhardness (by 21.1%), while raising the storage modulus to 1.45 GPa. However, this also led to minor reductions in ductility, tensile strength, and impact resistance [71].

Impact properties are also influenced by shell filler type, loading, and treatment. For instance, Yang Naide [72] observed that untreated oyster shell fillers increased notched Izod impact strength of PP composites up to 41% at 8.5 wt.%, while titanate-treated shells further boosted impact strength to 65% at 8 wt.%. Similarly, Yao *et al.,* [57] found that furfural-modified clam shell fillers led to progressively increasing impact strength up to 9.35 kJ/m² at 30 wt.%, whereas unmodified fillers peaked at 6.83 kJ/m² at 10 wt.% before declining. These differences were attributed to improved dispersion and stronger matrix-filler bonding from surface modification.

Mollusc shell fillers were also reported to influence the crystal structures of PP. Scallop shells were also reported to act as β-nucleating agents in PP, promoting the formation of β-crystalline phase and improving mechanical performance, especially when combined with pimelic acid treatment [63].

Further insights into filler-matrix interactions were gained via surface energy analysis using inverse gas chromatography (IGC). Yao *et al.,* [70] compared commercial calcium carbonate(CC) with clam shell (CS) using inverse gas chromatography (IGC) to understand their surface properties and potential as polymer fillers. Both CS and CC exhibited similar ranges for their dispersive surface free energy (γ_d). CS values ranged from 35.24–47.93 mJ/m², while CC values ranged from 41.35–53.92 mJ/m². However, CS demonstrated markedly higher surface heterogeneity and a greater capacity to enhance the toughness of PP composites, making it a promising bio-filler for polymer applications. The differences in their surface properties and mechanical performance were attributed to variations in origin and microstructure. Specifically, the presence of organic matter, diverse surface functionalities, and internal heterogeneity in CS particles reduced filler–filler interactions and promoted improved dispersion within the PP matrix. These observations are consistent with previous studies reporting that surface-modified $CaCO_3$ (e.g., treated with stearic acid or silane) exhibits reduced dispersive surface energy (γds) and enhanced compatibility with polymer matrices [73].

2.3.1.2 Surface modification - from geogenic calcium carbonate to mollusc shell fillers

2.3.1.2.1 Surface modification on geogenic calcium carbonate

The performance of particulate-filled polymer composites is determined not only by the intrinsic properties of the filler and polymer matrix, but also by the interfacial adhesion between them. In particular, calcium carbonate ($CaCO_3$) particles pose several challenges due to their high surface energy, which leads to agglomeration and poor dispersion within the polymer matrix. This aggregation can significantly reduce the impact resistance of composites [74]. Furthermore, the inherently hydrophilic nature of $CaCO_3$ limits its adhesion to hydrophobic polymer matrices [75].

To address these limitations, various surface modification strategies have been investigated. A common approach involves coating the $CaCO_3$ particles with low-molecular-weight hydrophobic surfactants such as stearic, oleic, or palmitic acid. These agents reduce interparticle friction and suppress agglomeration by introducing long hydrocarbon chains, thus enhancing compatibility with non-polar polymers. Alternatively, silane and titanate coupling agents, which possess reactive functional groups, have been used to chemically bridge the inorganic filler and the organic polymer matrix [76; 77].

However, the van der Waals forces between these small molecules and the polymer chains are often insufficient to produce strong and thermodynamically stable interfacial adhesion.

To overcome this, researchers have employed polymer-based coupling agents, particularly grafted polymers, which can provide more effective dispersion and durable interfacial bonding. For example, Bao et al., [78] investigated polymer-grafted $CaCO_3$ for enhanced mechanical performance.

Wang *et al.*, [79] studied the effects of three such coupling agents on PP/nano-$CaCO_3$ composites, namely maleic anhydride-grafted polypropylene (MAPP), ethylene-octene copolymer grafted with MA (POE-g-MA), and ethylene-vinyl acetate grafted with MA (EVA-g-MA). Despite their shared polar functionalities, the different polymer backbones led to varied interfacial compatibilities. MAPP demonstrated the best compatibility with PP, evidenced by indistinct interfacial regions in SEM images, indicating strong adhesion. This led to improved tensile strength and Young's modulus, although a decrease in impact strength was observed. This reduction is attributed to inhibited debonding at the filler-matrix interface, which restricts energy dissipation under impact.

Similar trends were reported by Fuad *et al.*, [80]. The use of MAPP encapsulated $CaCO_3$ particles within the PP matrix, leading to increases in both tensile strength and Young's modulus. At low filler contents (5 wt.% nano-precipitated $CaCO_3$), impact strength also improved. However, higher filler loading led to a decline in impact strength even with MAPP, likely due to agglomeration and the formation of stress concentration sites.

Azizi and Faghihi [81] further confirmed that PP composites filled with 30 wt.% $CaCO_3$ experienced reduced tensile strength (16 MPa) but improved impact strength (33 J/m). When 3 wt.% MAPP was added, both tensile strength (to 23 MPa) and impact strength (to 37 J/m) increased. These enhancements were attributed to improved filler dispersion and a reduction in stress concentration regions.

2.3.1.2.2 Surface modification on mollusc shell fillers- surfactants

Given the comparable chemical composition and the presence of calcium carbonate in mollusc shells, these surface modification strategies provide a valuable reference for enhancing the compatibility of shell-based fillers in polymer matrices. Mollusc shells, like $CaCO_3$, are hydrophilic and prone to agglomeration in non-polar matrices such as polypropylene (PP). Thus, surface treatments are essential for improving their dispersion and interfacial bonding. Fatty acid coatings (surfactants), silane coupling, and polymer grafting have been widely used to enhance shell filler compatibility in polymer matrices.

Low molecular weight surfactants such as stearic acid, furfural, and pimelic acid have proven effective in modifying shell surfaces. These surfactants reduce surface energy and interparticle friction, facilitating better dispersion and matrix bonding. For instance, a mixture of oyster, clam, and scallop shells was treated with an aqueous sodium stearate dispersion. This treatment formed a chemisorbed monolayer of stearate, followed by the deposition of multiple physiosorbed calcium stearate layers. During drying, the aliphatic tails oriented outward, creating a hydrophobic surface with reduced surface energy. The unique polymorphic textures of the shells promoted multilayer stacking, enhancing the surfactant's adsorption. The modified particles demonstrated improved compatibility and processability within PP composites [50].

Lin *et al.,* [63] used pimelic acid (PA) in acetone to modify scallop shell powders. The PA reacted with shell $CaCO_3$ to form calcium pimelate, a β-nucleating agent. This induced β-phase crystallisation (Kβ = 0.56) in the PP matrix, increasing impact strength by 240 % at a 5 wt.% shell loading. The improvements were attributed to the formation of β-crystals, improved filler dispersion, and reduced interface debonding. However, tensile and flexural strengths slightly declined, likely due to the lower stiffness of the β-phase.

Similarly, Xia *et al.,* [58] applied furfural treatment to clam shells via mechanochemical ball milling (shell: furfural =1:5 ratio), creating amphiphilic particles. These modified clam shells (MCS) enabled up to 30 wt.% loading in PP (compared to 10 wt.% for commercial $CaCO_3$). Impact strength increased by 61% (9.35 kJ/m^2), with the best stiffness-toughness balance at 15 wt.%. Compatibility was improved due to interactions between furfural's hydrophobic character and the shell's organic matrix (e.g., proteins and chitin), which operated on a "like dissolves like" principle, reducing agglomeration and improving stress transfer.

2.3.1.2.3 Surface modification on mollusc shell fillers- coupling agents

Coupling agents such as silanes and titanates are widely used to enhance the interfacial bonding between inorganic fillers and polymer matrices. These agents help to mitigate interfacial incompatibilities, particularly in composites with high filler content.

Silane coupling agents function by forming covalent Si–O–Ca bonds with surface hydroxyl groups on calcium carbonate-based fillers. This typically occurs through a silanol–siloxane condensation reaction in the presence of water. Silanes are particularly effective in polar polymers like epoxy or polyester. However, since mollusc shell-derived

$CaCO_3$ has a relatively low number of surface hydroxyl groups, the effectiveness of silane treatment may be limited unless the surface is pre-treated to introduce additional reactive sites [8].

Shen *et al.,* [82] successfully applied a silane coupling agent (KH560) to oyster shell powder (OSP) using ethanol-based solution treatment (3 wt.% KH560, pH = 9, stirred at 600 rpm for 6 hours). The treated OSP (termed OSP@KH560) enabled high filler loading (30 wt.%) in polybutylene succinate (PBS) composites. Compared with untreated shell-filled PBS, the modified composite exhibited a 366.7% increase in tensile strength (from 6 MPa to 28 MPa), a 48.1% increase in modulus, and maintained impact strength equivalent to neat PBS at 5 wt.% loading. Thermal stability also improved, with a 15 °C increase in $T_{5\%}$. These improvements were attributed to dual interfacial reactions: the Si–OH groups formed covalent Si–O–Ca bonds with the OSP surface, while epoxy groups reacted with PBS chain terminals, promoting better stress transfer and acting as thermal barriers. However, nucleation induced by OSP@KH560 restricted chain mobility, reducing crystallinity by 35.65%.

Titanate coupling agents, in contrast, are particularly suited for non-polar polymer systems such as polypropylene. Unlike silanes, titanates can form coordination bonds with surface protons on $CaCO_3$ without requiring hydroxylation or water condensation. This results in the formation of an organophilic monomolecular layer that improves compatibility and stress transfer while reducing filler agglomeration [8].

Yang Naide [72] employed a titanate coupling agent to modify oyster shell fillers for PP composites. The modified fillers improved compatibility with the hydrophobic PP matrix and enhanced impact strength by 65% at 8 wt.%, compared to a 41% increase achieved with untreated fillers at 8.5 wt.%. The improvements were attributed to reduced agglomeration, enhanced stress transfer, and stronger interfacial bonding, which facilitated more efficient energy dissipation.

Similarly, Melo *et al.,* [83] utilised isopropyl tri(dioctylpyrophosphate) titanate to treat mollusc shell waste (MSW) prior to blending with high-density polyethylene (HDPE). Fine shell particles (44 μm) exhibited superior dispersion, resulting in a 36% improvement in flexural modulus and enhanced impact strength at 2 wt.% loading. FTIR analysis confirmed the formation of Ti–O–Ca linkages (observed at 1030 cm^{-1}), while SEM images showed reduced voids and improved interface morphology. Thermal stability also increased, with the temperature at 20% mass loss rising by 26 °C at 5 wt.%

loading. However, tensile properties showed limited improvement at higher filler contents, likely due to weak interfacial adhesion and filler agglomeration. At low loading levels (2 wt.%), crystallinity and yield strength increased by approximately 10% and 7%, respectively, but agglomeration became dominant at ≥8 wt.%, negatively affecting reinforcement efficiency.

In summary, titanate coupling agents are particularly advantageous for non-polar systems and offer strong interfacial adhesion even when hydroxyl groups are scarce. Silanes are more effective for polar systems but may be less suitable for mollusc shells unless additional hydroxylation steps are employed.

2.3.1.2.4 Surface modification on mollusc shell fillers- polymer coating

In addition to low-molecular-weight surfactants and coupling agents, macromolecular surface modifiers have been explored to improve the compatibility of mollusc shell fillers with polymer matrices. These polymer coatings offer stronger interfacial adhesion through physical entanglement, encapsulation, and improved matrix interaction.

Melo *et al.*, [84] used polyethylene glycol (PEG) to modify calcined mollusc shells (CS) before incorporating them into recycled polypropylene (rPP) at a 20 wt.% loading. The PEG-modified shell (CS/PEG) increased melt viscosity but led to significant drawbacks. Severe void formation and particle agglomeration were observed, reducing tensile strength by 23.7%, yield strength by 30.6%, and impact strength by 23%. These negative effects were attributed to the hydrophilic nature of PEG, which caused interfacial incompatibility with the hydrophobic rPP matrix. Although slight β-crystal formation was detected (DSC peak at 147 °C), PEG's plasticising effect did not enhance toughness. In contrast, untreated CS composites exhibited a 41% increase in impact strength due to debonding-driven toughening.

Shah *et al.,* [85] demonstrated that combining particle size reduction with polyvinyl alcohol (PVA) surface treatment significantly improved the mechanical and thermal performance of oyster shell powder (OSP)-reinforced PP composites. Reducing the particle size from 148 μm to 63 μm enhanced tensile strength by 4.7% and flexural strength by 74%, while reducing agglomeration and debonding. When combined with PVA treatment, tensile strength increased by 10%, thermal stability improved (onset degradation temperature reached 290 °C), and fire retardancy was enhanced. These improvements were confirmed by FTIR and FESEM analyses, which showed better filler dispersion and improved interfacial bonding.

Inspired by the adhesive proteins in marine mussels, polydopamine (PDA) has emerged as a promising bio-based coating for surface modification. PDA can be deposited under mild conditions (room temperature, pH = 8.5) and adheres strongly to various substrates through catechol-based interactions such as hydrogen bonding, π–π stacking, coordination, and hydrophobic effects [86]. Additionally, PDA provides multifunctional benefits such as UV shielding, radical scavenging, electrical conductivity, and biocompatibility, due to its amine, catechol, and imine groups [87; 88].

Li *et al.,* [89] reported an in situ PDA coating on waste oyster shell powder (WOSP), producing hydroxyl-functionalised and roughened surfaces. During PP melt processing, the β-nucleating agent TMB-5 self-assembled into mycelium-like structures on the PDA-coated WOSP, forming interlocking structures at the interface. At 5 wt.% loading, the resulting composite achieved a 69% increase in impact strength without compromising tensile strength. This improvement was attributed to the synergistic effects of mechanical interlocking, interfacial bonding, and β-crystal nucleation.

Polydopamine improves adhesion more effectively when combined with other surface treatments than when used alone. Tran et al. (2018) found that polydopamine (PDA) alone is unsuitable for structural adhesive bonding of aluminium plates with an epoxy resin. Specifically, PDA forms a weak boundary layer at the interface during curing, attributed to its aggregate structure which lacks covalent bonding. Consequently, increased PDA film thickness correlated with reduced lap shear strength. Furthermore, PDA offered no significant benefit over tris buffer alone; indeed, at longer deposition times, tris buffer-treated surfaces outperformed PDA-treated ones. Conversely, polydopamine-3-aminopropyltriethoxysilane (APTES) hybrid treatments effectively mitigated these limitations. Hybrid systems, particularly those rich in APTES, achieved lap shear data statistically comparable to conventional APTES-treated controls under both dry and hot/wet conditions. The authors attribute this improvement to the individual contributions of tris buffer and APTES, collectively enhancing bond durability [87].

2.3.2 Natural plant fibre

Fibre Reinforced Polymer Composites (FRCs), characterised by a polymer matrix reinforced with load-bearing fibres, represent the most prevalent class of composite materials. In response to escalating environmental concerns, plant-derived natural fibres, namely hemp, flax, jute, sisal, and coir, are gaining significant attention as alternatives to synthetic reinforcements like glass and carbon fibres [5; 90]. These advantages include low density (typically 0.9-1.6 g/cm³) coupled with promising specific strength and stiffness, renewability, low cost, and minimal energy requirements during production. Furthermore, the manufacturing processes of polymer composites with natural plant fibres involve lower hazards, exhibiting less abrasive damage to processing equipment compared to glass or carbon fibres [90], and the type of composites generates lower emissions of toxic fumes when exposed to heat or during end-of-life incineration.

Life cycle assessment studies strongly support the environmental superiority of natural fibres. Pervaiz and Sain [91] showed that a polypropylene composite reinforced with 65% hemp fibre requires only 37% of the energy needed to produce a similar composite containing 30% glass fibre, underlining the potential for energy savings across the material lifecycle.

However, the adoption of natural fibre reinforced polymer composites (NFRCs) also faces challenges stemming from the inherent properties of the fibres. The high moisture absorption capacity of plant fibres often leads to dimensional instability and swelling. Their limited thermal stability restricts processing options, while their relatively lower strength and impact resistance can constrain structural applications [27]. Additionally, the variability in fibre quality, stemming from differences in plant species, cultivation conditions, and extraction methods, also affects composite consistency and performance. Pre-treatment or surface modification of fibres is often required to improve fibre-matrix adhesion and mitigate these drawbacks.

In the context of New Zealand, locally abundant plant fibres such as hemp and harakeke (New Zealand flax) present a sustainable and regionally viable reinforcement option for polymer composites. Their utilisation supports Circular Economy principles and reduces the carbon footprint associated with transportation and raw material sourcing [5].

2.3.2.1 Hemp and harakeke fibre-Properties

Hemp fibre is a bast fibre extracted from the outer cell layers of the plant stalk. Industrial hemp, defined by its low tetrahydrocannabinol (THC) content (<0.35%), is among the most accessible natural bast fibres. It is fast-growing and can reach up to 4 m in height within 12 weeks under warm climatic conditions. The stem diameter ranges between 4 and 20 mm. Owing to its versatility, hemp is used across a wide range of industries, including textiles, construction composites, cosmetics, nutraceuticals, and functional foods [92].

Harakeke, the Māori name for New Zealand flax (Phormium tenax), is a native fibre plant unique to New Zealand. In contrast to hemp, harakeke fibres are extracted from its long, sword-like leaves, which can grow up to 3 m in length and 125 mm in width. These leaves are characteristically stiff and tough, making harakeke well-suited for fibre extraction [93].

Natural plant fibres generally consist of three organic components: cellulose, hemicellulose, and lignin. These are typically found in a ratio of approximately 4:3:3, though the exact composition varies depending on the fibre species [94]. Cellulose is a linear, unbranched polymer composed of β-(1,4)-D-glucose units. It forms tightly packed, highly crystalline microfibrils through hydrogen bonding and Van der Waals interactions, and it plays a critical role in defining fibre strength. Hemicellulose, in contrast, is a branched polysaccharide of lower molecular weight. It is closely associated with cellulose and lignin in the plant cell wall and significantly influences moisture uptake, thermal degradation, and flammability. Lignin, a complex aromatic polymer, is not a carbohydrate but contributes to UV resistance and promotes char formation during combustion, enhancing fire resistance [94].

The chemical composition of harakeke fibre has been reported as 61% cellulose, 27.4% hemicellulose, and 7.8% lignin [4]. In comparison, hemp fibre typically contains 70–74% cellulose, 20% hemicellulose, and up to 5.7% lignin [27], indicating higher crystallinity and, therefore, higher mechanical performance in hemp.

The thermal stability of hemp fibre has been investigated by different researchers. Shahzad [95] reported that thermal degradation of hemp begins at approximately 150–200 °C, with the main decomposition peak occurring around 360 °C, attributed to cellulose breakdown. Beckermann and Pickering [96] demonstrated that alkali treatment improved the thermal stability of hemp fibres, increasing the degradation onset temperature from 205 °C to 240 °C. This improvement was due to the removal of thermally unstable components such as hemicellulose and pectin.

The relatively low densities of natural plant fibres highlight their potential as reinforcement materials in polymer composites, particularly when specific mechanical properties are considered. Harakeke fibre has a density of approximately 1.27 g/cm^3, which is lower than that of hemp at 1.5 g/cm^3 [97]. When normalised by density, both fibres exhibit promising mechanical properties. Hemp demonstrates specific tensile strengths between 370–740 MPa·g^{-1}·cm^3 and specific Young's moduli ranging from 21–

50 $GPa \cdot g^{-1} \cdot cm^3$. Harakeke shows comparable values, with specific tensile strengths of 338–761 $MPa \cdot g^{-1} \cdot cm^3$ and specific moduli between 11–25 $GPa \cdot g^{-1} \cdot cm^3$. These results suggest that harakeke is competitive with hemp in terms of reinforcement capability [27].

When compared to conventional synthetic E-glass fibre, which is characterised by a specific tensile strength of 800- 1400 $MPa \cdot g^{-1} \cdot cm^3$ and a specific modulus of 29 $GPa \cdot g^{-1} \cdot cm^3$, both hemp and harakeke fibres exhibit lower absolute mechanical properties [27]. However, they still provide sufficient strength and stiffness for many composite applications, especially where low weight and sustainability are prioritised.

Polypropylene (PP) has a tensile strength of 26- 41.4 MPa and a Young's modulus of 0.95- 1.77 GPa [98]. With a density of approximately 0.9 g/cm^3, the specific mechanical properties of PP remain significantly lower than those of hemp and harakeke fibres. This reinforces the suitability of both fibres as effective reinforcements in PP-based composite systems.

2.3.2.2 Fibre pretreatment and applications in polymer composites

The performance of natural fibre-reinforced polymer composites is heavily influenced by the interfacial bonding between the fibre and the matrix [5]. When stress is applied, it is transferred from the polymer matrix to the fibre through shear forces at the fibre–matrix interface. Therefore, fibre dispersion, surface roughness, wettability, and compatibility with the polymer matrix are critical factors affecting stress transfer and overall composite performance [2]. As such, most applications of hemp and harakeke fibres in composites incorporate pretreatment processes designed to enhance fibre characteristics and interfacial bonding. Fibre pretreatment methods can be broadly categorised into chemical, physical, and biological approaches [27]. To maximise performance gains, these are often used in combination.

Some studies have demonstrated the use of untreated harakeke fibres in composites. Jayaraman *et al.*, [99] integrated mechanically stripped harakeke fibres (300–350 µm wide, 900–2100 mm long, cut to 10 mm) into waste plastic blends using screwless extrusion, followed by injection moulding. Despite some voids and unmelted PET particles, the resulting composites showed substantial mechanical improvements: tensile strength increased by ~15% (18.0 MPa vs. 15.6 MPa), tensile modulus by 55% (2.65 GPa vs. 1.71 GPa), and impact strength by 35% (77.60 J/m vs. 53.80 J/m). The fibre reinforcement also enabled thermoforming into complex shapes with high dimensional precision and surface quality. Although granulation reduced fibre length to ~2 mm, the process effectively integrated harakeke fibres into recycled matrices for sustainable applications.

Orientated harakeke fibre-reinforced epoxy composites, fabricated via hot compression moulding, demonstrated substantial mechanical enhancements proportional to fibre content [97]. At 55 wt.% fibre loading, the composites achieved peak tensile strength and Young's modulus values of 223 MPa and 17 GPa, respectively, representing 4.6- and 4.3-fold increases compared to neat epoxy. Flexural properties reached their optimum at 49 wt.% fibre, with a flexural strength of 223 MPa and modulus of 14 GPa, beyond which performance plateaued. In tensile tests, harakeke composites outperformed sisal-based systems in strength, while exhibiting competitive modulus values, although sisal fibres provided slightly higher stiffness. The low density of harakeke fibre (1.27 g/cm^3), combined with its high intrinsic tensile strength (778 MPa) and modulus (32.09 GPa), highlights its excellent specific properties. Predictive modelling of the relationship between fibre content and composite strength further validated harakeke's potential for high-performance fibre composite applications.

Alkali treatment, or mercerisation, is one of the most common chemical pretreatments. It removes non-cellulosic components such as hemicellulose, lignin, pectin, waxes, and fats, which hinder good fibre–matrix adhesion. This removal exposes more hydroxyl groups on cellulose, increasing the potential for chemical bonding and enhancing surface roughness, which promotes mechanical interlocking with the matrix. Additionally, the elimination of amorphous components improves cellulose crystallinity and facilitates better stress relaxation [100].

The effectiveness of alkali treatment depends on the concentration and type of alkali, treatment duration, and temperature. Sodium hydroxide (NaOH), either alone or combined with sodium sulphite (Na_2SO_3), is commonly used. For instance, hemp bundles treated with 5 wt.% NaOH and 2 wt.% Na_2SO_3 exhibited effective fibre separation, promoting better dispersion and fewer voids in the polymer matrix [101]. Kim *et al.*, [102] found that 10 wt.% NaOH at 160°C for 45 minutes produced well-separated fibres. However, a further increase to 15 wt.% NaOH led to a decline in tensile strength, likely due to cellulose degradation.

Sullins *et al.*, [103] reported rougher and cleaner hemp fibre surfaces after 5 wt.% NaOH treatment. Untreated fibres showed uneven deposits, whereas treated fibres revealed increased hydroxyl group exposure. Compared to untreated fibre-reinforced polypropylene (PP), 5% and 10% NaOH-treated hemp (15 wt.%) composites displayed significantly enhanced flexural and tensile properties due to better interfacial bonding.

Dayo and co-workers [104] compared three surface treatments on hemp: washing with cyclohexane/ethanol, 10 wt.% NaOH, and silane treatment. Alkali-treated fibres showed improved thermal stability, with initial degradation temperatures increasing to 285°C, indicating the removal of thermally unstable hemicellulose. Among the treatments, silane-modified fibres yielded the greatest mechanical improvements when incorporated into polybenzoxazine composites, attributed to enhanced fibre–matrix adhesion and more uniform dispersion.

The addition of maleic anhydride-grafted polypropylene (MAPP) is another widely used strategy to improve compatibility between hydrophilic fibres and hydrophobic polymer matrices. MAPP forms covalent and hydrogen bonds with hydroxyl groups on the fibre surface, while also physically entangling with the polymer matrix. Sullins *et al.* [103] reported that PP composites reinforced with 30 wt.% hemp and 5 wt.% MAPP showed increases of 91%, 132%, 122%, and 297% in flexural strength, flexural modulus, tensile strength, and Young's modulus, respectively, compared to neat PP. SEM analysis confirmed strong fibre–matrix adhesion, with minimal interfacial gaps observed after fibre fracture.

Physical pretreatments, such as boiling and mechanical shear, increase fibre surface area and improve fibre-matrix interaction [105].However, these methods may not alter fibre surface chemistry sufficiently and are often combined with chemical treatments. Ultrasonication paired with surfactants can effectively remove non-cellulosic materials, yielding cleaner fibre surfaces and better composite performance [106]. These methods are often less chemically intensive and can be environmentally friendlier alternatives.

Steam explosion is one of the physical pretreatment methods. Vignon *et al.*, [107] applied alkaline impregnation (2 wt.% NaOH) followed by steam explosion at 200°C for 90 seconds to semi-retted hemp bast fibres. This process degraded the pectin-rich middle lamellae, enabling the release of elementary fibres. Subsequent surface treatment with MAPP significantly improved compatibility with PP, facilitating the production of high-performance bio-composites.

Sun *et al.*,[105] investigated the effects of boiling and blending (debundling) and alkaline treatment on hemp-epoxy composites. Debundling increased the fibre surface area by 3.5 times, while alkaline treatment improved surface chemistry. The combination significantly enhanced interfacial bonding, resulting in better tensile and flexural properties.

Biological pretreatments have also been explored. Akindoyo *et al.*, [108] developed a mechanenzyme process for harakeke, combining mechanical refining with enzymatic treatments using pectinase and laccase. The process reduced fibre diameter to 13 µm and length to 2.3 mm, removed non-cellulosic components (e.g., lignin), and improved thermal stability and surface functionality. These changes are expected to enhance fibre–matrix bonding, though direct composite testing was not conducted.

Beg *et al*. [109] employed a sequential treatment of harakeke fibre involving alkaline digestion, H_2O_2 bleaching, and ultrasonication. The process improved interfacial bonding in polylactic acid (PLA) composites for FDM 3D printing. Bleaching increased cellulose content to 92 wt.%, and ultrasonication produced microfibrils that promoted mechanical interlocking. Optimised composites achieved a tensile strength of 79.3 MPa and modulus of 8.7 GPa, the highest reported for short-fibre PLA composites. The storage modulus at 60°C increased six-fold compared to neat PLA, confirming the mechanical and thermal benefits of the treatment sequence.

In summary, fibre pretreatment plays a critical role in enhancing interfacial adhesion and mechanical performance of natural fibre composites. A combination of physical, chemical, and biological methods can be tailored to unlock the full reinforcing potential of hemp and harakeke fibres, thereby supporting their use in sustainable, high-performance composite applications.

2.3.3 Hybridisation fillers

While single-filler reinforced polymer composites have been widely studied, hybridisation strategies are increasingly adopted to overcome the limitations of individual fillers. A single filler may improve one property—such as stiffness or thermal stability—but compromise others, including toughness or dimensional stability. For instance, natural fibres can effectively reinforce polymers without adding significant weight due to their low density. However, they often introduce dimensional instability because of their moisture absorption tendency [110]. Conversely, mollusc shell fillers, primarily composed of calcium carbonate, improve stiffness and thermal stability but reduce toughness and elongation [111]. When combined, these two types of fillers can offset each other's weaknesses, resulting in optimised composite performance.

Hybridisation refers to the incorporation of two or more types of fillers with differing shapes and characteristics into a polymer matrix [112]. This approach allows for balancing mechanical, thermal, and physical properties by leveraging the complementary advantages of each component. It enables the tuning of composite performance through synergistic effects, thereby broadening the range of potential applications.

The benefits of hybridisation often arise from variation in the shape and size of the fillers. Natural fibres are typically fibrous with high aspect ratios and elongated forms, whereas inorganic fillers such as shell-derived calcium carbonate appear as cubical or platy particles on the micrometre scale. This contrast in morphology enables smaller mineral particles to occupy voids between larger fibres and polymer chains, thus reducing porosity, limiting moisture uptake, and improving interfacial adhesion [113]. Huuhilo *et al.* [114] reported that the addition of calcium carbonate to wood-plastic composites (WPCs) substantially decreases both water absorption and thickness swelling. For example, following 28 days' immersion, WPCs without mineral additives absorbed 33% water and exhibited 10% thickness swelling, whereas mineral-enriched composites showed water absorption between 11–16% and thickness swelling of 4–6%. These results were attributed to the hybrid filler's ability to densify the structure and block moisture pathways.

Hybrid filling techniques minimise particle agglomeration, which is a common issue in nano-filled composites, thus improving the load-bearing capacity of the matrix. Hongzhen *et al*. [115] reported that incorporating calcium carbonate alongside wood flour in polyethylene (PE) composites improved both tensile strength and elongation at break, particularly at 15 wt.% calcium carbonate. Scanning electron microscopy (SEM) showed that the smaller particles filled the gaps in wood flour, thereby enhancing uniformity. Maleic anhydride polypropylene (MAPP) served as a coupling agent to further improve compatibility.

A major advantage of hybridisation lies in its ability to generate synergistic improvements in mechanical properties. Combining stiff inorganic particles with flexible or renewable natural fibres results in higher tensile strength, modulus, and impact resistance. Sanvezzo *et al*. [112] evaluated a polypropylene (PP) composite containing jute fibres and nano-calcium carbonate. Individually, jute and nano-$CaCO_3$ improved the elastic modulus by 135% and 158%, respectively. When used together, the modulus increased by 186%, reflecting a synergistic enhancement of 33% and 18% over the individual fillers. This demonstrates the potential of hybrid systems to yield superior performance while using sustainable or recycled materials.

Oladele *et al*. [116] reinforced PP with calcium carbonate and mercerised bagasse fibre. The optimal hybrid formulation, containing 15 wt.% $CaCO_3$ and bagasse fibre, delivered a 130% increase in flexural strength and a 150% increase in tensile strength compared to the control. These improvements were linked to robust interfacial bonding and enhanced fibre–matrix compatibility, aided by the mercerisation process. A formulation with 12 wt.% $CaCO_3$ achieved the highest Young's modulus (477.95 MPa), underscoring the importance of both filler types in improving stiffness and strength.

Gbadeyan *et al*., [117] also used banana fibres (20 wt.%) and snail shell powder (1–5 wt.%) to reinforce green epoxy. The optimal blend (2 wt.% shell) achieved a 75% increase in tensile strength (180 MPa), a 66% increase in flexural strength, and higher impact resistance. However, filler agglomeration at higher loadings reduced mechanical performance, emphasising the importance of optimising filler ratios.

Hybrid fillers also improve thermal and flame-retardant properties. Zhao *et al*. [118] showed that calcium carbonate addition in wood flour/polymer composites delayed ignition and reduced combustion heat, improving flame resistance. These outcomes support the use of organic–inorganic filler combinations to meet diverse performance requirements.

Biogenic hybrid fillers, derived from natural or waste materials, offer a low-carbon, high-value route to sustainable composites. Gbadeyan *et al*. [119] investigated the hybrid reinforcement of epoxy resin using eggshell and snail shell fillers. At 10 wt.%, eggshell-filled composites exhibited an 11.54% increase in tensile strength, while snail shell-filled composites showed a 49.40% improvement. Notably, the hybrid system achieved a 49.84% increase, indicating that the snail shell was the primary driver of enhancement, owing to its higher carbon content, which imparted a tougher structure. Furthermore, the uniform particle size and shape of the eggshell filler may have contributed to improved stress distribution. Regarding water resistance, the hybrid system displayed the lowest moisture absorption rates, reducing uptake by 88–99.7% as the filler loading increased from 5% to 20%. This reduction is ascribed to denser particle packing and improved dispersion, leading to lower porosity and restricted water penetration.

Echeverria *et al*. [120] developed polypropylene (PP) composites containing two categories of biogenic, locally sourced fillers: mixed wood sawdust sourced as residue from urban furniture manufacturing was used as the primary filler, while marine litter—specifically kelp (Phaeophyceae) and bivalve mollusc shells—served as secondary bio-fillers. These materials are regarded as multifunctional due to their favourable properties. Composite panels were prepared with a filler-to-matrix ratio of 60/40 wt.%, comprising wood dust (either 40 or 20 wt.%) and secondary bio-fillers (10 or 20 wt.%). Wood particulates provided structural reinforcement, thermal and acoustic insulation, and low toxicity, while the mineral-rich marine fillers were incorporated to enhance mechanical strength, thermal and acoustic behaviour, and moisture resistance. The results indicated that the inclusion of marine bio-fillers, individually at 10 wt.%, increased the modulus of rupture (MOR) and modulus of elasticity (MOE) of the panels. In addition, reducing the particle size of the blended fillers from 850 µm (20 mesh) to 425 µm (40 mesh) further improved the composite's mechanical performance, yielding MOR values comparable to those attained using a coupling agent (maleic anhydride-grafted polypropylene, MAPP).

These studies demonstrate that hybrid fillers provide a versatile method for enhancing the multifunctionality of polymer composites. In particular, biogenic fillers offer substantial environmental and economic benefits. They enable waste valorisation by converting residues (e.g., marine litter and wood by-products) into functional reinforcements, supporting Circular Economy principles. Such fillers reduce dependency on petrochemical inputs while improving mechanical strength, barrier performance, and sustainability. Regulatory trends increasingly favour such innovations, positioning biogenic hybrid composites as viable alternatives for future materials. With appropriate technical adjustments (e.g., particle size control and surface treatments), bio-composites can achieve comparable performance to conventional composites, underlining their industrial relevance.

2.4 Reference

1. Clyne, T. W., & Hull, D. (2019). An introduction to composite materials. Cambridge university press.
2. Hsissou, R., Seghiri, R., Benzekri, Z., *et al.* (2021). Polymer composite materials: A comprehensive review. *Composite Structures*, *262*, 113640.
3. Ao, X., Vázquez-López, A., Mocerino, D., *et al.* (2024). Flame retardancy and fire mechanical properties for natural fiber/polymer composite: A review. *Composites Part B: Engineering*, *268*, 111069.
4. Aruan Efendy, M. G., & Pickering, K. L. (2014). Comparison of harakeke with hemp fibre as a potential reinforcement in composites. *Composites Part A: Applied Science and Manufacturing*, *67*, 259-267.

5. Awais, H., Nawab, Y., Amjad, A., *et al.* (2020). Environmental benign natural fibre reinforced thermoplastic composites: A review. *Composites Part C: Open Access*, 100082.
6. Cangiotti, J., Scatto, M., Araya-Hermosilla, E., *et al.* (2022). Valorization of seashell waste in polypropylene composites: An accessible solution to overcome marine landfilling. *European Polymer Journal*, *162*, 110877.
7. Cheung, H.-y., Ho, M.-p., Lau, K.-t., *et al.* (2009). Natural fibre-reinforced composites for bioengineering and environmental engineering applications. *Composites. Part B, Engineering*, *40*(7), 655-663.
8. Xanthos, M. E. (2010). Functional fillers for plastics. (M. Xanthos, Ed. Second ed.). WILEY-VCH Verlag GmbH & Co. KGaA, Weinheim.
9. Pickering, K. L., Efendy, M. G. A., & Le, T. M. (2016). A review of recent developments in natural fibre composites and their mechanical performance. *Composites Part A: Applied Science and Manufacturing*, *83*, 98-112.
10. Asim, M., Saba, N., Jawaid, M., *et al.* (2018). A review on phenolic resin and its composites. *Current Analytical Chemistry*, *14*(3), 185-197.
11. Chang, I. Y., & Lees, J. K. (1988). Recent Development in Thermoplastic Composites: A Review of Matrix Systems and Processing Methods. *Journal of THERMOPLASTIC COMPOSITE MATERIALS*, *1*, 277-296.
12. Hemath, M., Mavinkere Rangappa, S., Kushvaha, V., *et al.* (2020). A comprehensive review on mechanical, electromagnetic radiation shielding, and thermal conductivity of fibers/inorganic fillers reinforced hybrid polymer composites. *Polymer Composites*, *41*(10), 3940-3965.
13. Turi, E. (2012). Thermal characterization of polymeric materials. (E. Turi, Ed. Second edition ed., Vol. 1&2). Academic Press Limited.
14. Maddah, H. A. (2016). Polypropylene as a promising plastic: A review. *Am. J. Polym. Sci*, *6*(1), 1-11.
15. Xiao, W.-D., & Kibble, K. A. (2008). Comparison of aluminium hydroxide and magnesium hydroxide as flame retardants in SEBS-based composites. *Polymers and Polymer Composites*, *16*(7), 415-422.
16. Gulrez, S. K., Ali Mohsin, M., Shaikh, H., *et al.* (2014). A review on electrically conductive polypropylene and polyethylene. *Polymer Composites*, *35*(5), 900-914.
17. Checa, A. G. (2018). Physical and Biological Determinants of the Fabrication of Molluscan Shell Microstructures [Review]. *Frontiers in Marine Science*, *5*.
18. Bashir, A. S., & Manusamy, Y. (2015). Recent developments in biocomposites reinforced with natural biofillers from food waste. *Polymer-Plastics Technology and Engineering*, *54*(1), 87-99.
19. Bhingare, N. H., Prakash, S., & Jatti, V. S. (2019). A review on natural and waste material composite as acoustic material. *Polymer Testing*, *80*, 106142.
20. MacArthur, E. (2013). Towards the Circular Economy, economic and business rationale for an accelerated transition. *Ellen MacArthur Foundation: Cowes, UK*, 21-34.
21. Ali, S. S., Elsamahy, T., Koutra, E., *et al.* (2021). Degradation of conventional plastic wastes in the environment: A review on current status of knowledge and future perspectives of disposal. *Science of The Total Environment*, *771*, 144719.
22. Sharuddin, S. D. A., Abnisa, F., Daud, W. M. A. W., *et al.* (2016). A review on pyrolysis of plastic wastes. *Energy conversion and management*, *115*, 308-326.
23. Material Economics. (2018). *The Circular Economy - a Powerful Force for Climate Mitigation*. https://materialeconomics.com/publications/the-circular-economy-a-powerful-force-for-climate-mitigation-1

24. WasteMINZ. (2020). *The Truth about Plastic Recycling in Aotearoa New Zealand in 2020*. https://www.wasteminz.org.nz/files/Behaviour%20Change/The%20Truth%20about%20Plastic%20Recycling%20report.pdf
25. Cui, Y.-H., Wang, X.-X., Xu, Q., *et al.* (2011). Research on moisture absorption behavior of recycled polypropylene matrix wood plastic composites. *Journal of THERMOPLASTIC COMPOSITE MATERIALS*, *24*(1), 65-82.
26. Mohammad, D. H. B. (2007). *The Improvement of Interfacial Bonding, Weathering and Recycling of Wood Fibre Reinforced Polypropylene Composites* The University of Waikato].
27. Pickering, K. L., Efendy, M. G. A., & Le, T. M. (2016). A review of recent developments in natural fibre composites and their mechanical performance. *Compos. Part A: Appl. Sci. Manuf.*, *83*(1), 98-112.
28. Busico, V., & Cipullo, R. (2001). Microstructure of polypropylene. *Progress in Polymer Science*, *26*(3), 443-533.
29. Iedema, P. D., Remerie, K., Seegers, D., *et al.* (2021). Tacticity Changes during Controlled Degradation of Polypropylene. *Macromolecules*, *54*(19), 8921-8935.
30. Antoniadis, S. J., Samara, C. T., & Theodorou, D. N. (1999). Effect of Tacticity on the Molecular Dynamics of Polypropylene Melts. *Macromolecules*, *32*(25), 8635-8644.
31. Jones, A. T., Aizlewood, J. M., & Beckett, D. R. (1964). Crystalline forms of isotactic polypropylene. *Die Makromolekulare Chemie*, *75*(1), 134-158.
32. Callister Jr, W. D., & Rethwisch, D. G. (2020). Materials science and engineering: an introduction. John wiley & sons.
33. Gohn, A. M., Rhoades, A. M., Okonski, D., *et al.* (2018). Effect of Melt-Memory on the Crystal Polymorphism in Molded Isotactic Polypropylene. *Macromolecular materials and engineering*, *303*(8), n/a.
34. Pauksztа, D., & Bednarek, W. H. (2018). In situ optical microscope studies at isotactic polypropylene crystallization induced by shear forces – A review. *Polymer Testing*, *72*, 238-243.
35. Ye, L., Li, H., Qiu, Z., *et al.* (2015). The melt–recrystallization behavior of highly oriented α-iPP fibers embedded in a HIPS matrix [10.1039/C4CP05910G]. *Physical Chemistry Chemical Physics*, *17*(11), 7576-7580.
36. Qin, W., Liu, K., Xin, Z., *et al.* (2020). Zinc pimelate as an effective β-nucleating agent for isotactic polypropylene at elevated pressures and under rapid cooling rates. *POLYMER CRYSTALLIZATION*, *3*(3), e10132.
37. Zhang, B., Wang, B., Chen, J., *et al.* (2016). Flow-Induced Dendritic β-Form Isotactic Polypropylene Crystals in Thin Films. *Macromolecules*, *49*(14), 5145-5151.
38. Chen, P., Xu, M., Li, X., *et al.* (2022). The influence of melt status and beta-nucleation agent distribution on the crystallization of isotactic polypropylene [10.1039/D1CE01660A]. *CrystEngComm*, *24*(13), 2429-2445.
39. Li, J., & Cheung, W. (1997). Pimelic acid-based nucleating agents for hexagonal crystalline polypropylene. *Journal of Vinyl and Additive Technology*, *3*(2), 151-156.
40. Liu, S., Yang, J., Liu, Q., *et al.* (2019). Polydopamine particles as a β-nucleating agent and antioxidant for isotactic polypropylene. *Chemical Engineering Journal*, *363*, 1-12.
41. do Nascimento, E. M., Eiras, D., & Pessan, L. A. (2016). Effect of thermal treatment on impact resistance and mechanical properties of

polypropylene/calcium carbonate nanocomposites. *Composites Part B: Engineering*, *91*, 228-234.

42. Zhang, X., Zhao, Y., Wang, Z.*, et al.* (2005). Morphology and mechanical behavior of isotactic polypropylene (iPP)/syndiotactic polypropylene (sPP) blends and fibers. *Polymer*, *46*(16), 5956-5965.
43. Zhang, Z., Lei, J., Chen, Y.*, et al.* (2013). Tailored Structure and Properties of Injection-Molded Atactic Polypropylene/Isotactic Polypropylene Blend. *ACS Sustainable Chemistry & Engineering*, *1*(8), 937-949.
44. Li, J., Zhu, Z., Li, T.*, et al.* (2020). Quantification of the Young's modulus for polypropylene: Influence of initial crystallinity and service temperature. *Journal of Applied Polymer Science*, *137*(16), 48581.
45. Fayolle, B., Richaud, E., Colin, X.*, et al.* (2008). Review: degradation-induced embrittlement in semi-crystalline polymers having their amorphous phase in rubbery state. *JOURNAL OF MATERIALS SCIENCE*, *43*(22), 6999-7012.
46. Awaya, H. (1988). Morphology of different types of isotactic polypropylene spherulites crystallized from melt. *Polymer*, *29*(4), 591-596.
47. Rötzer, N., & Schmidt, M. (2020). Historical, Current, and Future Energy Demand from Global Copper Production and Its Impact on Climate Change. *Resources*, *9*(4), 44.
48. Fiume, E., Magnaterra, G., Rahdar, A.*, et al.* (2021). Hydroxyapatite for biomedical applications: A short overview. *Ceramics*, *4*(4), 542-563.
49. Miller, M. R., Abshirini, M., Wolber, F. M.*, et al.* (2023). Greenshell Mussel Products: A Comprehensive Review of Sustainability, Traditional Use, and Efficacy. *Sustainability*, *15*(5), 3912.
50. Basile, M. L., Triunfo, C., Gartner, S.*, et al.* (2024). Stearate-Coated Biogenic Calcium Carbonate from Waste Seashells: A Sustainable Plastic Filler. *ACS omega*, *9*(10), 11232-11242.
51. Hadal, R. S., Dasari, A., Rohrmann, J.*, et al.* (2004). Effect of wollastonite and talc on the micromechanisms of tensile deformation in polypropylene composites. *Materials science & engineering. A, Structural materials : properties, microstructure and processing*, *372*(1), 296-315.
52. Food and Agriculture Organization of the United Nations. (2020). *FAO Fisheries & Aquaculture—Statistics—Introduction.* http:// www.fao.org/ fishery/ statistics/en
53. Aquaculture New Zealand. (2020). *AQUACULTURE FOR NEW ZEALAND - A sector overview with key facts and statistics for 2020*. https://www.aquaculture.org.nz/resources/general/ 2020 sector overview
54. H Silva, T., Mesquita-Guimarães, J., Henriques, B.*, et al.* (2019). The potential use of oyster shell waste in new value-added by-product. *Resources*, *8*(1), 13.
55. Naik, A. S., & Hayes, M. (2019). Bioprocessing of mussel by-products for value added ingredients. *Trends in Food Science & Technology*, *92*, 111-121.
56. Munusamy, Y., Sethupathi, S., & Choon, C. H. (2019). Potential use of waste cockle shell as filler for thermoplastic composite. *Journal of Material Cycles and Waste Management*, *21*(5), 1063-1074.
57. Yao, Z. T., Chen, T., Li, H. Y.*, et al.* (2013). Mechanical and thermal properties of polypropylene (PP) composites filled with modified shell waste. *J. Hazard Mater.*, *262*(15), 212-217.
58. Xia, M. S., Yao, Z. T., Ge, L. Q.*, et al.* (2015). A potential bio-filler: The substitution effect of furfural modified clam shell for carbonate calcium in polypropylene. *J. Compo. Mater.*, *49*(7), 807-816.

59. Echeverria, C., Pahlevani, F., Gaikwad, V.*, et al.* (2017). The effect of microstructure, filler load and surface adhesion of marine bio-fillers, in the performance of Hybrid Wood-Polypropylene Particulate Bio-composite. *J. Clean. Prod.*, *154*(1), 284-294.
60. Gbadeyan, O. J., Adali, S., Bright, G.*, et al.* (2020). Optimization of milling procedures for synthesizing nano-CaCO3 from Achatina fulica shell through mechanochemical techniques. *J. Nanomater.*, *2020*(4), 1-9.
61. Hamester, M. R. R., Balzer, P. S., & Becker, D. (2012). Characterization of calcium carbonate obtained from oyster and mussel shells and incorporation in polypropylene. *Mater. Res.*, *15*(2), 204-208.
62. Li, H. Y., Tan, Y. Q., Zhang, L.*, et al.* (2012). Bio-filler from waste shellfish shell: preparation, characterization, and its effect on the mechanical properties on polypropylene composites. *J. Hazard. Mater.*, *217-218*(30), 256-262.
63. Lin, Z., Guan, Z., Chen, C.*, et al.* (2013). Preparation, structures and properties of shell/polypropylene biocomposites. *Thermochim. Acta*, *551*(10), 149-154.
64. Nwanonenyi, S., Obidiegwu, M., & Onuegbu, G. (2013). Effects of particle sizes, filler contents and compatibilization on the properties of linear low density polyethylene filled periwinkle shell powder. *Int. J. Eng. Sci.*, *2*(2), 1-8.
65. Kuciel, S., Rusin-Żurek, K., & Kurańska, M. (2024). New Polymer Biocomposites Based on Biopoly(Ethylene Terephthalate) and Waste Mollusc Shells. *Materials*, *17*(19), 4752.
66. Patrícia Maria Alves de Melo, L. B. S., Amélia S. F. Santos,Tibério A. Passos,everino J. G. (2013). Evaluation of thermal and mechanical behavior of HDPE/Mollusk shell composites prepared in single screw extruder 22nd International Congress of Mechanical Engineering Conference,
67. Currey, J., & Taylor, J. (1974). The mechanical behaviour of some molluscan hard tissues. *Journal of Zoology*, *173*(3), 395-406.
68. Martínez-García, C., González-Fonteboa, B., Carro-López, D.*, et al.* (2020). Mussel shells: A canning industry by-product converted into a bio-based insulation material. *Journal of Cleaner Production*, *269*, 122343.
69. Essabir, H., Bensalah, M. O., Rodrigue, D.*, et al.* (2017). A comparison between bio- and mineral calcium carbonate on the properties of polypropylene composites. *Constr. Build. Mater.*, *134*(1), 549-555.
70. Yao, Z., Ge, L., Ji, X.*, et al.* (2015). Surface properties studies of bivalve shell waste by the IGC technique: Probing its significant potential application in the polymer industry. *Journal of Alloys and Compounds*, *621*, 389-395.
71. Bouiadjra, B. A. B., Albedah, A., Mohammed, S. M. A. K.*, et al.* Thermal stability and mechanical characterization of oyster shell reinforced recycled polypropylene biocomposite. *Journal of Reinforced Plastics and Composites*, *0*(0), 07316844241273006.
72. Yang Naide, l. X., Wang Gui, Zhao juan. (2013). Reusing waste oyster shells in polypropylene and its performances. *Advanced Materials Research*, *641-642*, 1001-1004.
73. Ahsan, T., Colenutt, B., & Sing, K. (1991). Application of gas chromatography for the study of precipitated calcium carbonate. *Journal of Chromatography A*, *464*, 416-421.
74. Karger-Kocsis, J. (2012). Polypropylene structure, blends and composites: Volume 3 composites. Springer Science & Business Media.
75. Cao, Z., Daly, M., Clémence, L.*, et al.* (2016). Chemical surface modification of calcium carbonate particles with stearic acid using different treating methods. *Applied Surface Science*, *378*, 320-329.

76. Demjen, Z., Pukanszky, B., Földes, E., *et al.* (1997). Interaction of silane coupling agents with CaCO3. *Journal of colloid and interface science*, *190*(2), 427-436.
77. Kamal, M., Sharma, C., Upadhyaya, P., *et al.* (2012). Calcium carbonate (CaCO3) nanoparticle filled polypropylene: Effect of particle surface treatment on mechanical, thermal, and morphological performance of composites. *Journal of Applied Polymer Science*, *124*(4), 2649-2656.
78. Bao, L., Yang, S., Luo, X., *et al.* (2015). Fabrication and characterization of a novel hydrophobic CaCO3 grafted by hydroxylated poly (vinyl chloride) chains. *Applied Surface Science*, *357*, 564-572.
79. Wang, Y., Shen, H., Li, G., *et al.* (2009). Effect of interfacial interaction on the crystallization and mechanical properties of PP/nano-CaCO3 composites modified by compatibilizers. *Journal of Applied Polymer Science*, *113*(3), 1584-1592.
80. Fuad, M., Hanim, H., Zarina, R., *et al.* (2010). Polypropylene/calcium carbonate nanocomposites--effects of processing techniques and maleated polypropylene compatibiliser. *EXPRESS Polymer Letters*, *4*(10).
81. Azizi, H., & Faghihi, J. (2009). An investigation on the mechanical and dynamic rheological properties of single and hybrid filler/polypropylene composites based on talc and calcium carbonate. *Polymer Composites*, *30*(12), 1743-1748.
82. Shen, Y., Ren, L., Ma, H., *et al.* (2024). Fabrication and properties of biodegradable poly (butylene succinate) composites by regulating the dispersed oyster shell powder with the silane coupling agent. *Journal of Polymer Research*, *31*(7), 216.
83. Melo, P. M. A., Macêdo, O. B., Barbosa, G. P., *et al.* (2019). High-density polyethylene/mollusk shell-waste composites: effects of particle size and coupling agent on morphology, mechanical and thermal properties. *Journal of Materials Research and Technology*, *8*(2), 1915-1925.
84. Melo, P. M. A., Macêdo, O. B., Barbosa, G. P., *et al.* (2020). Reuse of Natural Waste to Improve the Thermal Stability, Stiffness, and Toughness of Postconsumer Polypropylene Composites. *Journal of Polymers and the Environment*, *29*(2), 538-551.
85. Shah, A. U. R., Prabhakar, M., Wang, H., *et al.* (2018). The influence of particle size and surface treatment of filler on the properties of oyster shell powder filled polypropylene composites. *Polymer Composites*, *39*(7), 2420-2430.
86. Zhang, C., Gong, L., Xiang, L., *et al.* (2017). Deposition and Adhesion of Polydopamine on the Surfaces of Varying Wettability. *ACS Appl Mater Interfaces*, *9*(36), 30943-30950.
87. Tang, Z., Miao, Y., Zhao, J., *et al.* (2021). Mussel-inspired biocompatible polydopamine/carboxymethyl cellulose/polyacrylic acid adhesive hydrogels with UV-shielding capacity. *Cellulose (Lond)*, 1-14.
88. Hu, J., Yang, L., Yang, P., *et al.* (2020). Polydopamine free radical scavengers. *Biomaterials Science*, *8*(18), 4940-4950.
89. Li, Y., Huang, P., Guo, S., *et al.* (2020). A promising and green strategy for recycling waste oyster shell powder as bio-filler in polypropylene via mycelium-enlightened interfacial interlocking. *Journal of Cleaner Production*, *272*, 122694.
90. Peças, P., Carvalho, H., Salman, H., *et al.* (2018). Natural fibre composites and their applications: a review. *Journal of Composites Science*, *2*(4), 66.
91. Pervaiz, M., & Sain, M. M. (2003). Carbon storage potential in natural fiber composites. *Resources, Conservation and Recycling*, *39*(4), 325-340.

92. Kumeroa, F., Komahan, S., Sofkova-Bobcheva, S., *et al.* (2022). Characterization of the Volatile Profiles of Six Industrial Hemp (Cannabis sativa L.) Cultivars. *Agronomy*, *12*(11), 2651.
93. Lowe, B. J., Carr, D. J., McCallum, R. E., *et al.* (2010). Understanding the variability of vegetable fibres: a case study of harakeke (Phormium tenax). *Textile Research Journal*, *80*(20), 2158-2166.
94. Chen, H. (2014). Chemical Composition and Structure of Natural Lignocellulose. In H. Chen (Ed.), *Biotechnology of Lignocellulose: Theory and Practice* (pp. 25-71). Springer Netherlands.
95. Shahzad, A. (2013). A study in physical and mechanical properties of hemp fibres. *Advances in Materials Science and Engineering*, *2013*.
96. Beckermann, G. W., & Pickering, K. L. (2008). Engineering and evaluation of hemp fibre reinforced polypropylene composites: Fibre treatment and matrix modification. *Composites Part A: Applied Science and Manufacturing*, *39*(6), 979-988.
97. Le, T. M., & Pickering, K. L. (2015). The potential of harakeke fibre as reinforcement in polymer matrix composites including modelling of long harakeke fibre composite strength. *Composites. Part A, Applied science and manufacturing*, *76*, 44-53.
98. Thakur, V. K., Thakur, M. K., Raghavan, P., *et al.* (2014). Progress in green polymer composites from lignin for multifunctional applications: a review. *ACS Sustainable Chemistry & Engineering*, *2*(5), 1072-1092.
99. Jayaraman, K., & Halliwell, R. (2009). Harakeke (phormium tenax) fibre–waste plastics blend composites processed by screwless extrusion. *Composites Part B: Engineering*, *40*(7), 645-649.
100. Pickering, K. L., Beckermann, G. W., Alam, S. N., *et al.* (2007). Optimising industrial hemp fibre for composites. *Composites Part A: Applied Science and Manufacturing*, *38*(2), 461-468.
101. Oliveira, M. A., Pickering, K. L., Sunny, T., *et al.* (2021). Treatment of hemp fibres for use in rotational moulding. *Journal of Polymer Research*, *28*(2), 1-9.
102. Pickering, K. L., Beckermann, G. W., Alam, S. N., *et al.* (2007). Optimising industrial hemp fibre for composites. *Composites. Part A, Applied science and manufacturing*, *38*(2), 461-468.
103. Sullins, T., Pillay, S., Komus, A., *et al.* (2017). Hemp fiber reinforced polypropylene composites: The effects of material treatments. *Composites Part B: Engineering*, *114*, 15-22.
104. Dayo, A. Q., Zegaoui, A., Nizamani, A. A., *et al.* (2018). The influence of different chemical treatments on the hemp fiber/polybenzoxazine based green composites: Mechanical, thermal and water absorption properties. *Materials Chemistry and Physics*, *217*, 270-277.
105. Sun, S., Yan, Y., Zhou, C., *et al.* (2024). Mechanical performance of epoxy matrix composites reinforced by physically and chemically treated hemp fiber. *Polymer Composites*, *45*(16), 15113-15124.
106. Karaduman, Y., Secinti-Klopf, H., & Sahbaz Karaduman, N. (2024). Ultrasonication-assisted alkali treatment of hemp fibers to improve the fiber/matrix interface of hemp/epoxy composites: The influence of sodium dodecyl sulfate surfactant. *Polymer Composites*, *45*(9), 8187-8201.
107. Vignon, M. R., Dupeyre, D., & Garcia-Jaldon, C. (1996). Morphological characterization of steam-exploded hemp fibers and their utilization in polypropylene-based composites. *Bioresource technology*, *58*(2), 203-215.

108. Akindoyo, J. O., Pickering, K., Mucalo, M.*, et al.* (2024). Mechanenzymatic production of natural fibre from harakeke (New Zealand flax) and its characterization for potential use in composites for building and construction applications. *Industrial Crops and Products*, *214*, 118507.
109. Beg, M. D. H., Pickering, K. L., & Gauss, C. (2023). The effects of alkaline digestion, bleaching and ultrasonication treatment of fibre on 3D printed harakeke fibre reinforced polylactic acid composites. *Composites Part A: Applied Science and Manufacturing*, *166*, 107384.
110. Mochane, M., Mokhena, T. C., Mokhothu, T.*, et al.* (2019). Recent progress on natural fiber hybrid composites for advanced applications: A review.
111. Owuamanam, S., & Cree, D. (2020). Progress of Bio-Calcium Carbonate Waste Eggshell and Seashell Fillers in Polymer Composites: A Review. *Journal of Composites Science*, *4*(2).
112. Sanvezzo, P. B., & Branciforti, M. C. (2021). Recycling of industrial waste based on jute fiber-polypropylene: Manufacture of sustainable fiber-reinforced polymer composites and their characterization before and after accelerated aging. *Industrial Crops and Products*, *168*, 113568.
113. Taib, M. N. A. M., & Julkapli, N. M. (2019). Dimensional stability of natural fiber-based and hybrid composites. In *Mechanical and Physical Testing of Biocomposites, Fibre-Reinforced Composites and Hybrid Composites* (pp. 61-79). Elsevier.
114. Huuhilo, T., Martikka, O., Butylina, S.*, et al.* (2010). Impact of mineral fillers to the moisture resistance of wood-plastic composites. *Baltic forestry*, *16*(1), 126-131.
115. Hongzhen, C., Keyan, Y., & Weiming, Y. (2017). Effects of calcium carbonate on preparation and mechanical properties of wood/plastic composite. *International Journal of Agricultural and Biological Engineering*, *10*(1), 184-190.
116. Oladele, I. O., Ibrahim, I. O., Akinwekomi, A. D.*, et al.* (2019). Effect of mercerization on the mechanical and thermal response of hybrid bagasse fiber/CaCO3 reinforced polypropylene composites. *Polymer Testing*, *76*, 192-198.
117. Gbadeyan, O. J., Adali, S., Bright, G.*, et al.* (2021). Mechanical, microstructure, and dynamic mechanical analysis of nano-shell and plant fiber hybrid biocomposite. *Journal of Composite Materials*.
118. Zhao, Y., Sun, Q., & Wang, K. (2013). Effects of nano-calcium carbonate on properties of wood/PVC composites. *Polymer Materials Science & Engineering*, *29*(2), 66-69.
119. Gbadeyan, O., Adali, S., Bright, G.*, et al.* (2020). Studies on the mechanical and absorption properties of achatina fulica snail and eggshells reinforced composite materials. *Composite Structures*, *239*, 112043.
120. Echeverria, C. A., Ozkan, J., Pahlevani, F.*, et al.* (2020). Multifunctional marine bio-additive with synergistic effect for non-toxic flame-retardancy and anti-microbial performance. *Sustainable Materials and Technologies*, *25*.
121. Wang, A., Chen, C., Liao, L.*, et al.* (2020). Enhanced β-Phase in Direct Ink Writing PVDF Thin Films by Intercalation of Graphene. *Journal of Inorganic and Organometallic Polymers and Materials*, *30*(5), 1497-1502.

Chapter 3

Materials and Methods

3.1 Materials

3.1.1 Mussel shells

Mussel shells were kindly supplied by North Island Mussels Ltd. At the processing facility, the shells were initially broken down into pieces measuring approximately 5–10 cm in length.

3.1.2 Harakeke fibres

Harakeke fibres (Phormium tenax) were kindly provided in bundles by the Templeton Flax Milling Heritage Trust, New Zealand.

3.1.3 Polypropylene

Polypropylene (Moplen EP548S), with a density of 0.9 g/cm^3 and a melt flow index of 44 g/10 min, was procured from LyondellBasell.

3.1.4 Chemicals

All chemicals were used as received. Tris(hydroxymethyl)aminomethane (TRIS, 99 %), dopamine hydrochloride (DOPA-HCl, 98 %), hydrochloric acid (HCl, 37 %), sodium hydroxide (NaOH, >98 %), sodium thiosulfate ($Na_2S_2O_3$, >98 %), diiodomethane (99 %), commercial calcium carbonate (CC, > 98 %), and maleic anhydride-grafted polypropylene (MAPP; Mn = 8000, melting point = 140 °C, acid number = 15) were purchased from Sigma-Aldrich. Potassium bromide (IR spectroscopy grade) was obtained from Merck.

3.2 Methods

3.2.1 Polydopamine (PDA) coating

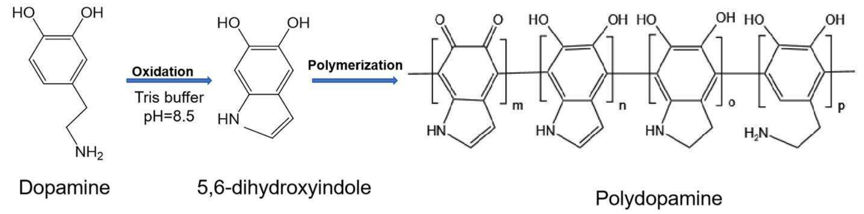

Figure 3- 1:Schematic illustration of the proposed self-polymerisation mechanism of polydopamine (PDA) from dopamine (DA) [1].

Mussel shells underwent a washing process using tap water to remove mud, sand, and other impurities. To ensure the elimination of bacteria and moisture, the cleaned shell pieces were dried in an oven at 135 °C for 0.5 hours, followed by further drying at 100 ± 5 °C for 12 hours. The dried mussel shells (MS) were then subjected to dry milling in a planetary ball mill (Retsch® PM 100, Germany) for 45 minutes, after which they were sieved to obtain particles smaller than 200 µm.

A 2 L solution of Tris-HCl (20 mM) buffer was prepared and adjusted to pH 8.5 using 1 M HCl. The buffer solution was stirred and heated to 45 °C. With vigorous stirring at 600 rpm, 20 g of mussel shell particles (10 g/L) and 4 g of dopamine (2 g/L) were added. The suspension was then continuously stirred at 45 °C for 24 hours to facilitate the self-polymerisation reaction. The potential self-polymerisation mechanism of polydopamine from dopamine is illustrated in Figure 3-1. Due to the structural complexity of polydopamine, the structural model was adapted from the literature [1].

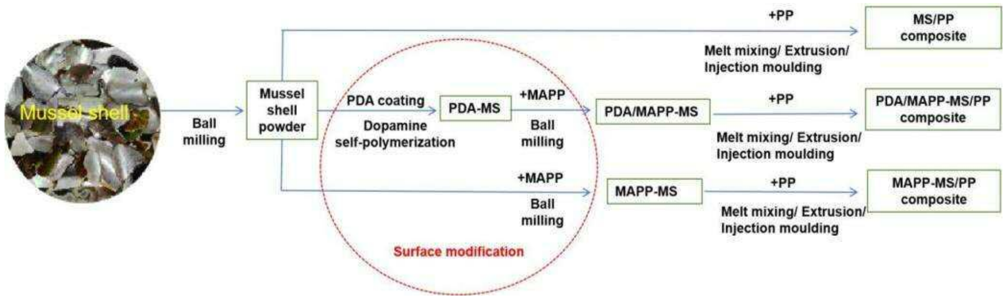

Figure 3- 2:Schematic illustration of the synthesis procedure for PP composites.

The treated mussel shell particles were filtered and washed with deionized water multiple times to remove dopamine residue, until the pH of the filtrate was measured to reach 7 , then were dried in an oven at 100 ±5 °C for 12 h.

3.2.2 MAPP or PDA/MAPP combined surface modification

MAPP-modified mussel shells (MAPP-MS) were prepared by dry-milling MAPP together with mussel shells in a planetary ball mill (Retsch® PM 100, Germany) for 45 minutes, maintaining a weight ratio of MAPP to mussel shells of 3:5. The resulting mixture was then sieved to obtain particles smaller than 200 µm. Similarly, polydopamine and MAPP co-modified mussel shells (PDA/MAPP-MS) were prepared by dry-milling MAPP and polydopamine-modified mussel shells at the same weight ratio of 3:5. Before the milling process, MAPP, mussel shell powders, and PDA-MS powders were dried in an oven at 100 ± 5 °C for 1 hour. A schematic illustration of the surface modification procedure (highlighted with a red circle) is presented in Figure 3-2.

3.2.3 Harakeke fibre digestion and fibrillation

Harakeke fibres were cut into lengths of 2-3 cm using a guillotine slider before being digested in a lab-scale pulp digester (see Figure 3-3), with a schematic image adapted from the literature [2]. This digestion process utilised a solution consisting of 5 wt.% NaOH and 2 wt.% Na2SO3. The fibres were placed in four stainless steel canisters, maintaining a weight ratio of 1:8 with the solution. A programmed controller managed a precise 4-step cycle: initial heating from room temperature to 50 °C over 30 minutes, followed by a gradual increase to 160 °C over 2 hours, a 2-hour hold at 160 °C, and finally, a rapid quenching to approximately 30 °C using tap water. After digestion, the fibres were thoroughly washed with continuous tap water until a pH range of 6.5-7.5 was achieved.

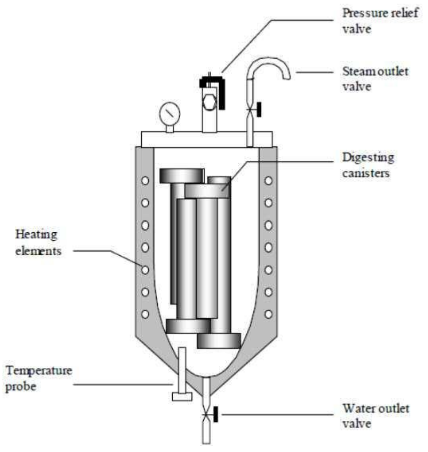

Figure 3- 3: Schematic of laboratory-scale batch digester [3].

Fibrillation of the fibres was performed using an ultra-fine friction grinder (Super-Mass-Colloider, SMC, Masuko Sangyo Version IV, Japan). Following digestion, 100 g of fibres were suspended in 10 L of water for 24 hours, with the motor speed of the SMC set to 1500 rpm. The suspension underwent two passes with the gap between the upper and lower grinding discs set at 200 µm, followed by two additional passes with the gap reduced to 100 µm. After processing in the Super-Mass -Colloider, the fibres were sieved to remove excess water and subsequently stored in a refrigerator at 4 °C until further analysis.

3.2.4 Master batch preparation

Master batches of polypropylene (PP) composites were formulated through melt mixing PP with various types of mussel shell fillers, specifically unmodified mussel shell,

Table3- 1: Sample formulation and code names of materials studied.

Specimen	PP (wt%)	MAPP (wt%)	MS (wt%)	PDA-MS (wt%)
PP	100	-	-	-
5%MS/PP	95	-	5	-
10%MS/PP	90	-	10	-
15%MS/PP	85	-	15	-
20%MS/PP	80	-	20	-
30%MS/PP	70	-	30	-
40%MS/PP	60	-	40	-
5%MAPP-MS/PP	92	3	5	-
10%MAPP-MS/PP	90	3	7	-
15%MAPP-MS/PP	85	3	12	-
20%MAPP-MS/PP	80	3	17	-
30%MAPP-MS/PP	70	3	27	-
40%MAPP-MS/PP	60	3	37	-
5%PDA/MAPP-MS/PP	92	3	-	5
10%PDA/MAPP-MS/PP	90	3	-	7
15%PDA/MAPP-MS/PP	85	3	-	12
20%PDA/MAPP-MS/PP	77	3	-	17
30%PDA/MAPP-MS/PP	70	3	-	27
40%PDA/MAPP-MS/PP	60	3	-	37

MAPP-modified mussel shell, and PDA/MAPP co-modified mussel shell. The weight ratio of PP to filler in each master batch was consistently maintained at 1:1. The compounding process was executed using a custom sigma blade melt compounder, which operated at a temperature of 185 °C and a mixing speed of 30 rpm. Subsequently, the composite material was pelletized utilizing a Moretto GR knife mill plastic granulator.

3.2.5 Extrusion

The composites were produced using a Thermo Scientific Process 16 twin-screw extruder. Before the extrusion process and between successive samples, the extruder was purged with neat polypropylene (PP) to ensure consistency and prevent contamination. The extrusion was conducted at a screw speed of 40 rpm, with barrel temperatures maintained between 175 and 185 °C. During this phase, additional polypropylene was introduced to adjust the filler content in the composite, targeting a range of 5 to 40 wt.%, while maintaining the maleic anhydride grafted polypropylene (MAPP) content at 3 wt.%. After the extrusion process, the resulting materials were granulated using a Moretto GR knife mill plastic granulator. Table 3-1 presents the formulations and corresponding code names of the samples analysed in this research.

3.2.6 Injection moulding

The injection moulding procedures were carried out using a BOY 35A injection moulding machine. For sample preparation, the injection profile consisted of several key temperature settings: the feeding zone was maintained at 120 °C, while the compression zone temperature varied between 165 °C and 185 °C. The metering zone was set to 190 °C, and the nozzle temperature was also kept at 185 °C. The mould temperature was maintained at 35 °C. The injection duration was 0.5 seconds, followed by a cooling period of 30 seconds.

3.2.7 Particle size measurement

The size distribution profiles of various materials, including commercial CaCO3, mussel shell powder, PDA modified mussel shell powder, MAPP modified mussel shell powder, and PDA and MAPP co-modified mussel shell powder, were analysed using laser diffraction with a Malvern Mastersizer 3000. For the analysis, the sample powders were dispersed in distilled water while maintaining a stirring speed of 300 RPM. The refractive index for the samples was set at 1.58. To ensure reliability, three repetitions were conducted for each sample, and the average data was calculated to determine the particle size distribution.

3.2.8 X-ray photoelectron spectroscopy (XPS)

X-ray photoelectron spectroscopy (XPS) measurements were performed using a K Alpha X-ray photoelectron spectrometer (Thermo Fisher Scientific, U.K.). The instrument operated at a power of 200 W with an anode voltage set to 12 kV, while maintaining a constant pressure of 2.0×10^{-7} mbar within the analysis chamber. Pass energies were configured at 150 eV for survey scans and 50 eV for higher resolution scans. The Thermo Scientific Advantage software (Version 5.948) was employed for peak fitting and background subtraction. Binding energies (BEs) were calibrated against the C1s binding energy of adventitious carbon, which was defined as 284.8 eV. The analysis of core peaks utilised a nonlinear Shirley-type background subtraction method. Additionally, high-resolution spectra were analysed using a weighted least-squares fitting approach, optimizing peak positions and areas with a combination of 70 % Gaussian and 30 % Lorentzian line shapes.

3.2.9 Solid-state Nuclear Magnetic Resonance (SS-NMR) spectroscopy

The acquisition of the ^{13}C MAS NMR spectra was performed using a JEOL 600 MHz NMR spectrometer equipped with a broadband solids probe designed for magic angle spinning. Powder samples were carefully packed into 3.2 mm zirconia rotors fitted with PTFE caps and spun at a frequency of 10 kHz. The spectra were recorded at a frequency of 150.9 MHz for ^{13}C, utilizing a single pulse with decoupling, a relaxation delay of 180 seconds, and a temperature maintained between 20-21 °C. The fully decoupled free induction decay (FID) was accumulated over a range of 172 to 640 scans. The resulting data underwent Fourier transformation, accompanied by phase and baseline corrections, to yield the final line spectrum. Spectral integration was conducted using Delta™ Software v5.3.3, with chemical shifts referenced against a separately acquired ^{13}C-^{1}H cross-polarized spectrum of solid adamantane spun at 5 kHz.

3.2.10 Powder X-ray diffraction (XRD)

X-ray diffraction (XRD) analysis was performed using a Panalytical Empyrean diffractometer equipped with CuKα radiation (λ = 1.54 nm). Powder and short fibre samples, including both untreated and surface-modified mussel shells and harakeke fibres, were prepared by compacting the material into steel sample holders. A glass slide was used to level the surface, and excess powder was removed from the edges to ensure uniformity. The sample holder was then inserted into the XRD instrument, and scans were conducted over the 2θ range of 20–60°, with a step size of 0.026° and a scanning speed of 1° per minute.

For polymer and composite samples, the specimens were trimmed to fit bulk sample holders designed for the instrument. These were analysed over a 2θ range of 5–40°, maintaining the same scan step and scanning speed. As α- and β-crystalline phases are the dominant polymorphs in polypropylene (PP) and its composites, the relative content of the β-phase was calculated using the Turner–Jones equation, as presented in Equation (1) [3].

$$k_\beta = \frac{H_\beta(300)}{H_\beta(300) + H_\alpha(110) + H_\alpha(040) + H_\alpha(130)} \qquad \text{Equation 1}$$

3.2.11 Scanning electron microscopy (SEM)

Scanning electron microscopy (SEM) analysis was conducted on powder and fibre samples, as well as on the fractured surfaces of polypropylene (PP) composites after tensile testing. The examination was carried out using a Hitachi S-4700 Field Emission Scanning Electron Microscope (FE-SEM) operating at 5 kV. Prior to imaging, the samples were dried, mounted on aluminium stubs using conductive tape, and coated with a 5 nm layer of platinum using a Quorum Q150V sputter coater to improve conductivity. Elemental analysis and filler distribution within the PP composites were evaluated using energy-dispersive X-ray spectroscopy (EDS) in combination with backscattered electron (BSE) imaging. BSE mode was specifically employed to observe the fractured surfaces of PP composites reinforced with both mussel shell particles and harakeke fibres. To minimise operator bias and ensure consistent observations, all BSE imaging was performed at an accelerating voltage of 15 kV and a working distance of 14.5 mm.

3.2.12 Contact angle measurement

Contact angle measurements were performed using the sessile drop method on compressed discs of untreated and treated mussel shell powder at room temperature (20 ± 3 °C). A 10 µL droplet of test liquid was carefully dispensed onto the surface of each sample using an auto-pipette. Images were captured within 20 seconds of droplet application using a smartphone camera, and the contact angle was calculated using the ImageJ contact angle plugin. For each sample, five measurements were taken at different positions, and the standard deviation was calculated.

The contact angle was defined as the angle formed through the liquid phase between the solid surface and the tangent to the droplet radius at the point of contact. Surface energy of the solid samples was determined based on contact angle measurements with two test liquids: distilled water and diiodomethane. The surface energy components required for these calculations are listed in Table 3-2.

Table3- 2: Polar and dispersive surface energy components of the test liquids[4].

	γ_l (mJ/m^2)	γ_l^p (mJ/m^2)	γ_l^d (mJ/m^2)
Water (W)	72.8	51.0	21.8
Diiodomethane (DIM)	50.8	0.0	50.8

Note: γ_l is denoted as the surface energy of the test liquid; γ_l^p and γ_l^d are denoted as polar and dispersive surface energy components of the test liquid, respectively.

3.2.13 Fourier transform infrared (FTIR) spectroscopy

Infrared spectra were obtained in transmission mode using a Perkin Elmer® Spectrum 100 FTIR spectrometer. Samples were prepared using a standard KBr pellet technique. All spectra were recorded over a wavelength range of 4000 - 400 cm^{-1} with 10 scans at 4 cm^{-1} resolution.

3.2.14 Ultraviolet - visible (UV-vis) spectroscopy

The UV–visible absorption characteristics of dopamine in solution and polydopamine in film form were examined using a Varian Cary100 UV–Visible spectrophotometer. Scans were carried out across a wavelength range of 200–800 nm. A 0.1 wt.% aqueous dopamine solution was used to obtain the UV–visible spectrum, with distilled water serving as the reference.

To analyse polydopamine, a film was formed on the outer surface of a cuvette using the same procedure as for mussel shell surface modification. A clean cuvette was immersed in a Tris-HCl buffer solution (20 mM, pH 8.5) containing 2 g/L dopamine and stirred vigorously at 600 rpm at 45 °C for 24 hours. This process produced a thin polydopamine coating on the cuvette. A separate clean cuvette was used as the reference.

3.2.15 Optical Microscopy

Optical microscopy observations were conducted with a BX53 Olympus optical microscope, and images were captured using OLYMPUS STREAM software.

3.2.16 Differential scanning calorimetry (DSC) analysis

The melting enthalpy and crystallinity of polypropylene (PP) composites were determined using a Netzsch DSC 3500 Sirius differential scanning calorimeter. Approximately 5–10 mg of each composite sample was placed in an aluminium pan with a pierced lid and scanned under a nitrogen atmosphere. Both heating and cooling rates were set at 10 °C/min.

The thermal protocol began by cooling the samples to –70 °C, followed by heating to 220 °C. The samples were held at 220 °C for 5 minutes to remove any prior thermal or mechanical history. They were then cooled from 220 °C to –70 °C and held at this temperature for another 5 minutes. Finally, the samples were reheated from –70 °C to 220 °C. This reheating step was used to analyse the melting behaviour of neat PP and PP composites, while the crystallisation behaviour was assessed based on the cooling curve. The temperature profile is illustrated in Figure 3-4.

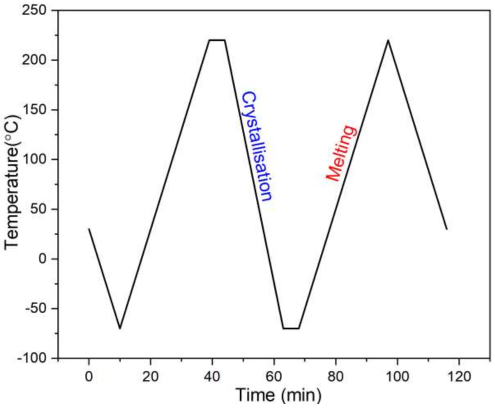

Figure 3- 4: Temperature profile for the differential scanning calorimetry analysis.

3.2.17 Thermogravimetric analysis (TGA)

Thermogravimetric analysis (TGA) was conducted using a Perkin Elmer STA 8000 to assess the thermal stability of untreated and surface-modified mussel shells, harakeke fibres, and polypropylene (PP) composites. The samples were dynamically heated from 30 °C to 800 °C at a rate of 10 °C/min under a 40 ml/min argon atmosphere. An empty crucible was used as the reference.

3.2.18 Tensile and Flexural tests

Tensile testing was performed in accordance with EN ISO 527 standard[5] using an Instron® 5982 equipped with a 5 kN load cell, operating at a speed of 5 mm/min. Flexural testing was conducted following ASTM D790-17 at a speed of 2 mm/min[6]. Before testing, specimens were conditioned in a chamber maintained at 23 °C and 50% relative humidity for 48 hours. To ensure robust statistical analysis, a minimum of four composite samples were tested for each condition, and the results were reported as averages.

3.2.19 Dynamic mechanical analysis (DMA)

Dynamic mechanical analysis (DMA) was conducted using a PerkinElmer DMA8000 Dynamic Mechanical Analyser. In this analysis, specimens measuring 120 mm in length, 4 mm in width, and 3 mm in height were evaluated in a single cantilever mode. The specimens were subjected to thermal evaluation by heating them at a rate of 2 °C/min, ranging from -80 °C to 120 °C. The displacement amplitude was set at 20 μm, and the tests were performed at a frequency of 1 Hz.

3.2.20 Creep and recovery tests

Creep and recovery tests were conducted in creep mode at various temperatures using a Perkin Elmer DMA8000 Dynamic Mechanical Analyser. The specimens measured 120 mm in length, 4 mm in width, and 3 mm in height. Creep and recovery strain were evaluated over a 30-minute duration for each phase at temperatures of 30, 50, and 70 °C, with applied stress levels of 3, 4, and 5 N. Initially, a 5-minute equilibration period was performed to stabilise the specimen at the specified temperature. Subsequently, creep measurements were initiated using machine settings designed to induce displacement at the designated stress level, which was determined based on the stress-strain diagrams obtained from tensile tests to ensure that the measurements remained within the linear viscoelastic deformation regime. Each measurement was replicated at least three times using three individual specimens, and the experimental curves presented represent typical data from the analysis. Additionally, cyclic creep-recovery tests were conducted, repeating the 60-minute creep-recovery process for a total of 10 cycles at 30 °C with a 3 N load applied.

3.2.21 Melt rheology analysis

The melt flow behaviour of the samples was evaluated using a Discovery Hybrid Rheometer DHR-2 (TA Instruments, New Castle, DE, USA). The measurements were conducted in a parallel-plate geometry with a diameter of 25 mm, at a temperature of 190 °C. The gap between the plates was maintained at 1000 μm during the measurements. Steady shear measurements were performed at a strain rate of 0.01 s^{-1}. Additionally, angular frequency sweep measurements were conducted over a range of 0.1 to 100 rad/s, with a constant strain of 10%. This strain is within the linear viscoelastic region of the materials, ensuring the reliability of the results obtained.

3.2.22 Accelerated weathering testing

Accelerated weathering testing was performed on neat polypropylene and two polypropylene composites, specifically 5% MAPP-MS/PP and 5% PDA/MAPP-MS/PP, using a QUV accelerated weathering tester (Q-Lab) in accordance with ASTM G 154-23 standard [7]. The testing employed eight UVA fluorescent lamps that emitted an irradiance of 1.55 W/m², simulating sunlight in the short wavelength range of 295 nm to 365 nm, with a peak emission at 340 nm.

The test cycles were designed to replicate natural weathering conditions, comprising 8 hours of UV irradiation at 60 °C, followed by 15 minutes of deionised water spray, and concluding with 3.75 hours of condensation at 50 °C. To assess the impact of accelerated weathering duration on the materials, samples were subjected to various exposure times: 120 hours, 240 hours, 480 hours, 740 hours, and 1000 hours. This structured approach facilitates a comprehensive evaluation of the weathering effects on the different polypropylene formulations.

3.3 Reference

1. Hemmatpour, H., De Luca, O., Crestani, D.*, et al.* (2023). New insights in polydopamine formation via surface adsorption. *Nat. Commun.*, *14*(1), 664.
2. Beckermann, G. (2007). *Performance of Hemp-Fibre Reinforced Polypropylene Composite Materials* The University of Waikato].
3. Jones, A. T., Aizlewood, J. M., & Beckett, D. R. (1964). Crystalline forms of isotactic polypropylene. *Die Makromolekulare Chemie*, *75*(1), 134-158.
4. Kozbial, A., Li, Z., Conaway, C.*, et al.* (2014). Study on the surface energy of graphene by contact angle measurements. *Langmuir*, *30*(28), 8598-8606.
5. International Organization for Standardization. (2019). *ISO 527-1:2019 Plastics — Determination of tensile properties*
6. ASTM International. (2017). *ASTM-D790-17:Flexural Properties of Unreinforced and Reinforced Plastics and Electrical Insulating Materials.* West Conshohocken.
7. ASTM International. (2023). *ASTM G 154-23 Standard Practice for Operating Fluorescent Ultraviolet (UV) Lamp Apparatus for Exposure of Materials*

Chapter 4

Characterisation of polydopamine and different mussel shell fillers

4.1 Introduction

This study aims to explore the potential of mussel shells as a biogenic filler and assess their suitability for application in polypropylene composite materials. To achieve this objective, it is imperative to investigate the fundamental properties of mussel shell particles, including particle size distribution, chemical composition, crystalline components and morphology.

Given the inherent low polarity and surface energy (approximately 35 mJ/m^2) of polypropylene (PP), surface modification to increase the hydrophobicity of mussel shell fillers is essential to enhance their compatibility with the polypropylene matrix. To prevent filler agglomeration and enhance the surface hydrophobicity of the filler, three surface modification methods were employed on the mussel shells: polydopamine coating, MAPP modification, and combined PDA/MAPP modification.

Among three modification methods, polydopamine coating, a facile method inspired by the super adhesion of mussel foot proteins, aims to introduce abundant functional groups onto the surface of mussel shells, including amine and hydroxyl groups [1-3]. Polydopamine coating on mussel shells involves an in situ self-polymerisation process starting from dopamine monomer under alkaline conditions. Assessing the successful synthesis of polydopamine under these conditions is essential. Investigating the changes in chemical structure between polydopamine and the dopamine monomer provides insights into the self-polymerisation process.

Polydopamine is generally acknowledged to consist of super-molecular structures composed of oligomer aggregates, rather than a well-defined polymeric structure. Due to this complexity, elucidating the exact structure of polydopamine remains challenging [4]. Meanwhile, functional groups, particularly catechol and amine groups, play a key role in the strong adhesive properties of polydopamine coatings on various materials. Identifying functional groups introduced by the polydopamine coating leads to a better understanding of the adhesive mechanism of polydopamine coatings on mussel shell particles, which is crucial for this surface modification. Furthermore, functional groups can enable polydopamine to serve as an active layer for further modifying mussel shells through interactions with MAPP. The differences in chemical structure and functional groups of dopamine and polydopamine were thoroughly investigated using Fourier-transform infrared spectroscopy (FTIR) and solid-state nuclear magnetic resonance spectroscopy (SS-NMR). FTIR and SS-NMR aimed to assess the self-polymerisation process of dopamine, contributing to a better understanding of the surface properties of polydopamine-coated mussel shell particles. UV-visible spectroscopy was also employed to confirm the formation of polydopamine through self-polymerisation of dopamine. Furthermore, the UV-visible behaviour of polydopamine facilitates exploration of its potential application as a UV absorber within PP composites. This aspect is addressed in Chapter 7, which examines the photo-degradation behaviour of polypropylene and its composites.All fillers incorporated into polymers are subjected to the same high-temperature processing procedures, including melt mixing and extrusion (160–185 °C), during compounding of PP composites. Therefore, the thermal behaviour of surface-modified fillers – specifically polydopamine, mussel shell, and polydopamine-modified mussel shell – was also evaluated using thermogravimetric analysis (TGA).In this chapter, contact angle measurements were carried out on unmodified mussel shell fillers and those subjected to various surface modifications. Consequently, their surface properties were assessed using two empirical models: the Fowkes and Owens-Wendt models. This analysis aimed to assess their hydrophobicity levels and predict tendencies for filler agglomeration and re-agglomeration upon incorporation into PP. The influence of surface modification on the macroscopic properties of PP incorporated with various mussel shell fillers will be evaluated in subsequent chapters.

4.2 Characterisation of polydopamine

4.2.1 Solid-state NMR (SS-NMR) spectroscopic investigations

Solid-state ^{13}C cross-polarisation/magic angle spinning (CP/MAS) NMR spectroscopy plays a pivotal role in enabling a comprehensive understanding of the structural evolution from dopamine to polydopamine (PDA) via self-polymerisation. Figure 4-1 presents the ^{13}C cross-polarisation (CP) MAS SS-NMR spectra of the dopamine monomer and polydopamine. In contrast to the well-resolved resonances observed for dopamine, the spectra of polydopamine predominantly exhibit broad and overlapped peaks. This not only signifies notable architectural distinctions from the dopamine monomer but also reveals the predominantly amorphous and disordered nature of polydopamine.

In the solid-state nuclear magnetic resonance (SS-NMR) spectra of the initial dopamine monomer (Figure 4-1A), the inset displays the chemical structure and numeration of carbon atoms of dopamine. Within the range of 40-60 ppm, two distinct resonances are observed, situated at 47 ppm and 56 ppm, respectively. These resonances are attributed to the protonated aliphatic carbons at positions 1 and 2 in dopamine, corresponding to the sp^3 carbons within the uncycled units. Additional resonances emerge within the unsaturated region (100-160 ppm), where the chemical shifts of carbons present in alkenes, aromatic compounds, and other groups containing π bonds can be ascribed. Specifically, two signals at 155 ppm and 160 ppm can be associated with quaternary carbons bonded to oxygen in the catechol form at positions 5 and 6, resonating within the range of 150-165 ppm. Additionally, a signal at 130 ppm may be attributed to aromatic carbons at positions 4 and 7 (some prior studies have reported the resonance at this position as split into two peaks [5; 6]), while the peak at 136 ppm corresponds to the carbon at position 8. Moreover, a signal around 145 ppm is indicative of the quaternary carbon at position 3 within the dopamine structure.

In Figure 4-1B, Solid-state ^{13}C CP/MAS NMR spectrum of polydopamine was deconvoluted to extract information regarding its chemical structure. The inset displays the chemical structure (as proposed in Chapter 3, Figure 3-1) with numbered carbon groups C1 to C4. This approach to visualisation of the peaks was necessitated by the broadening of signals and the significant overlap of individual resonances. Upon the polymerisation of dopamine to polydopamine, in the upfield region, a resonance centred at 37 ppm emerges, characterised by a broad shape, accompanied by smaller shoulders around 28, 33, 42, and 47 ppm (grouped as C1 in the chemical structure of polydopamine). These observations suggest an increased chemical disorder in the aliphatic region after self-polymerisation [1; 6], and V. Proks *et al.* proposed that this may be attributed to the cyclisation of primary amines, leading to the formation of CH_2-CH_2-N bonds [7]. In the aromatic region (100-170 ppm), a shoulder resonance positioned around 102 ppm can be attributed to the carbon in the indole (C2 group) of polydopamine. The broad peaks appearing at around 167 ppm can be attributed to the carbon (C3 group) in the catechol structure, while those at 197 ppm are characteristic of carboxyl groups (C4) [1; 6; 8; 9]. These results support the proposed chemical structure of polydopamine, indicating successful polymerisation of dopamine under alkaline conditions.

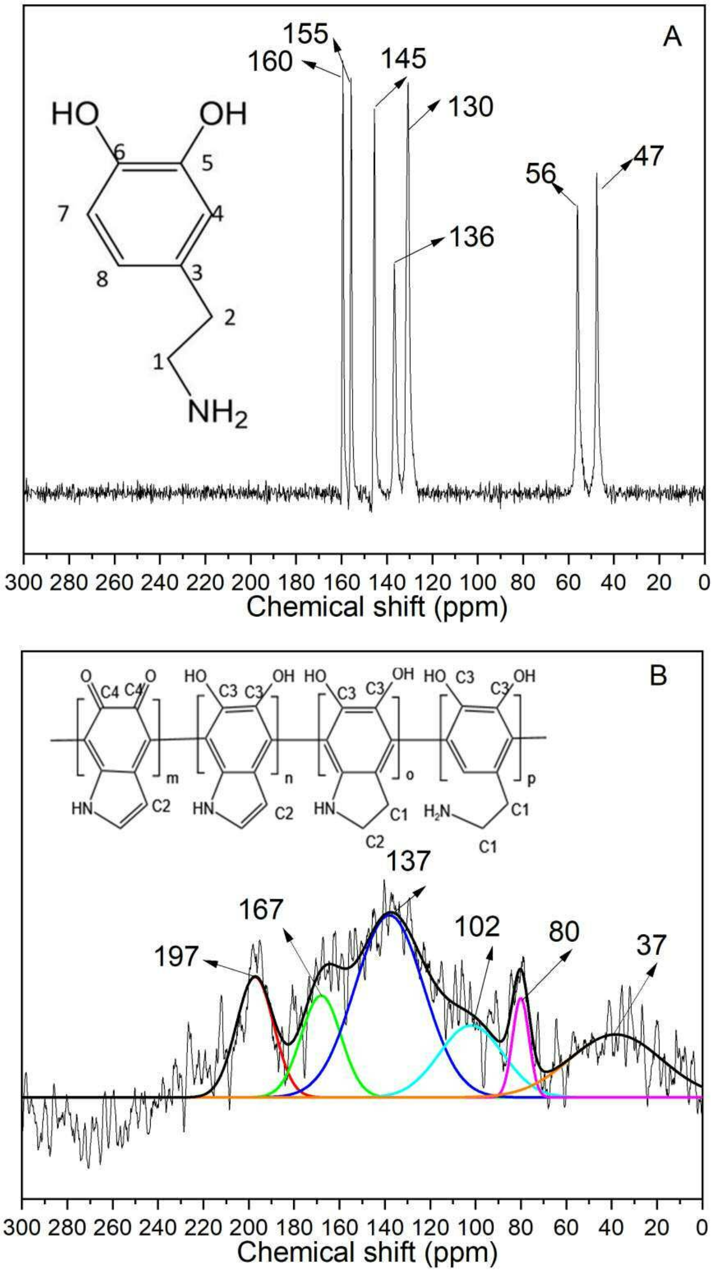

Figure 4- 1: ^{13}C SS-NMR spectra of (A) dopamine (inset-chemical structure of dopamine), (B) polydopamine (peaks deconvoluted, inset- simplified chemical structure of polydopamine).

4.2.2 Fourier transform infrared (FTIR) investigations

Fourier Transform Infrared Spectroscopy (FTIR) was utilised to investigate the molecular structure of both the monomer dopamine and polydopamine, as illustrated in Figure 4-2. Both dopamine and polydopamine display relatively broad and intense bands ranging from 3000 to 3400 cm^{-1}. This observation is consistent with the presence of hydroxyl groups and N-H bonds, stemming from primary amines, water, and catechol groups in both compounds. Additionally, moderate intensity bands are observed at 2850 cm^{-1}, 2920 cm^{-1}, and 2960 cm^{-1} which can be assigned to saturated C-H stretching vibrations. These spectral features closely correspond to the chemical structures of dopamine and specific units (containing C1) of polydopamine, as illustrated in Figure 4-2.

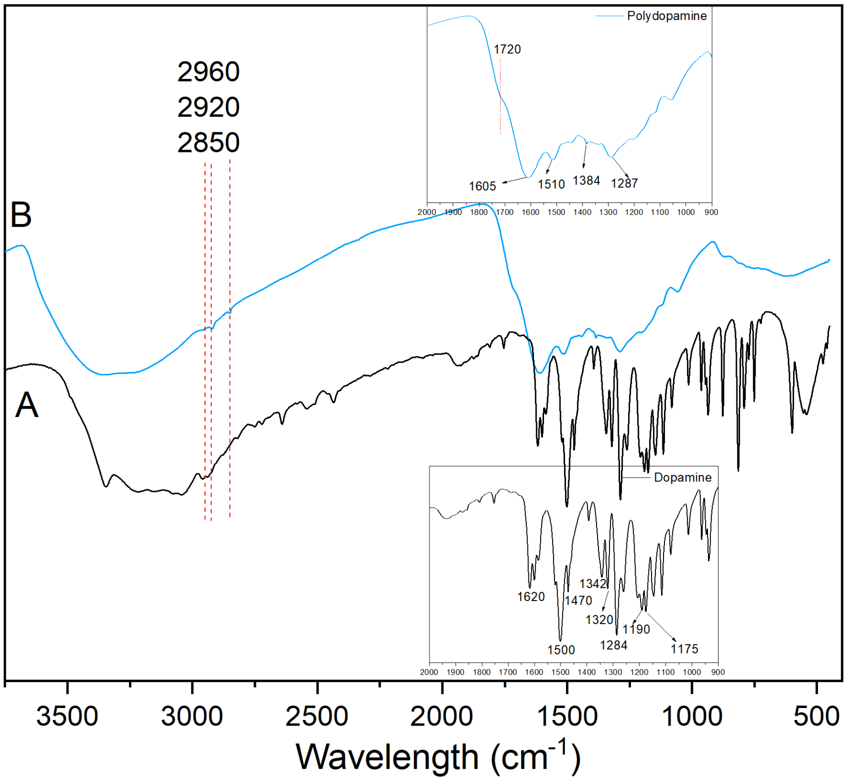

Figure 4- 2: FTIR spectra of (A)dopamine, (B)Polydopamine.

The difference between the FTIR spectra of dopamine and polydopamine becomes apparent in the 900-2000 cm^{-1} region, indicating changes in the chemical structure as dopamine undergoes self-polymerisation. The FTIR spectrum of dopamine, specifically in the 900-2000 cm^{-1} region as illustrated in the lower inset of Figure 4-2, exhibits several prominent absorption peaks. The strong peak centred around 1620 cm^{-1} is attributed to the C=C stretching mode of the aromatic ring, while a strong peak observed at approximately 1500 cm^{-1} is attributed to both the C-N stretching and N-H scissoring vibrations [10]. Additionally, a distinct absorption feature at 1342 cm^{-1} is assigned to the bending vibration of CH_2. Peaks at 1320 cm^{-1} and 1190 cm^{-1} correspond to the asymmetrical and symmetrical bending vibrations of C-O-H, respectively, while the absorption peak at 1176 cm^{-1} is linked to the stretching vibration of C-C bonds. A peak observed at 1100 cm^{-1} can be associated with a C-N stretching vibration [11]. These observations agree with what would be expected spectroscopically from the chemical structure of dopamine, which contains unsaturated aromatic phenol, $-CH_2$, and $-NH_2$ groups.

A close examination of the 900-1800 cm^{-1} region (higher inset in Figure 4-2) reveals distinct features within the FTIR spectrum of polydopamine. The intricate nature of polydopamine, consisting of numerous monomer units with varied oxidation states and chemical linkages, arranged into diverse hierarchical aggregates, poses a substantial challenge for accurate structural elucidation. Consequently, the FTIR spectrum of polydopamine lacks well-defined bands associated with single functional groups in distinct compounds. Instead, due to overlapping contributions from various functional units with similar absorption energies, broadened bands and fewer distinct features are instead evident. The prominent peaks centred at 1605 cm^{-1} and 1510 cm^{-1} are indicative of the ring C=C stretching vibration and ring C-N stretching vibration, respectively, suggesting the presence of indole or indoline structures in polydopamine. Unlike dopamine, the absence of features between 1340-1170 cm^{-1} in polydopamine indicates intramolecular cyclisation reactions, further implying the formation of indole derivatives from dopamine self-polymerisation. Solid-state nuclear magnetic resonance (SS-NMR) analysis revealed the presence of carbonyl groups in the quinone structure unit following the self-polymerisation of dopamine to form polydopamine. However, in the FTIR spectrum of polydopamine, only a shoulder peak at 1720 cm^{-1} was detected, which can be attributed to the C=O in quinone in polydopamine. The peak associated with the carbonyl group is likely obscured by the broad peak observed between 800-1750 cm^{-1} [1].

Overall, the FTIR analysis is in good agreement with SS-NMR results and confirmed that dopamine had successfully formed polydopamine through self-polymerization with some noticeable changes being observed considering the structure of polydopamine, such as the oxidation of catechol to quinone and the cyclization of primary amine.

4.2.3 Ultraviolet - visible (UV-vis) spectroscopic investigations

The solar ultraviolet (UV) light spectrum spans from 100 to 400 nm, with the ozone layer effectively filtering out UVC radiation (100–280 nm) and attenuating 95% of UVB (280–315 nm) and 5% of UVA (315–400 nm) radiation [12]. Predominantly, it is UVA radiation along with a minor fraction of UVB radiation that penetrates the Earth's atmosphere to reach the surface [13]. Polymer materials, such as polypropylene, are susceptible to photodegradation upon exposure to UV light, resulting in the deterioration of their material properties. To counteract this degradation, UV absorbers or stabilizers can be introduced into polypropylene. These agents operate by absorbing UV light and dissipating its energy through chromophores, such as phenol, quinone, -C=N, and -C=O groups. For example, melanin, characterised by its conjugated double bonds and aromatic quinone structures, exhibits a broad absorption in the UV region and confers brown-black pigmentation to human skin, offering natural protection of it against UV radiation [14]. Polydopamine, a synthetic compound mirroring melanin's structure, shares analogous physical and chemical characteristics. Investigating the UV behaviours of dopamine and polydopamine can aid in understanding the chemical structure disparities between the dopamine monomer before and after self-polymerization. This can then elucidate the photodegradation mechanism of polypropylene composites, with or without the polydopamine-modified mussel shell.

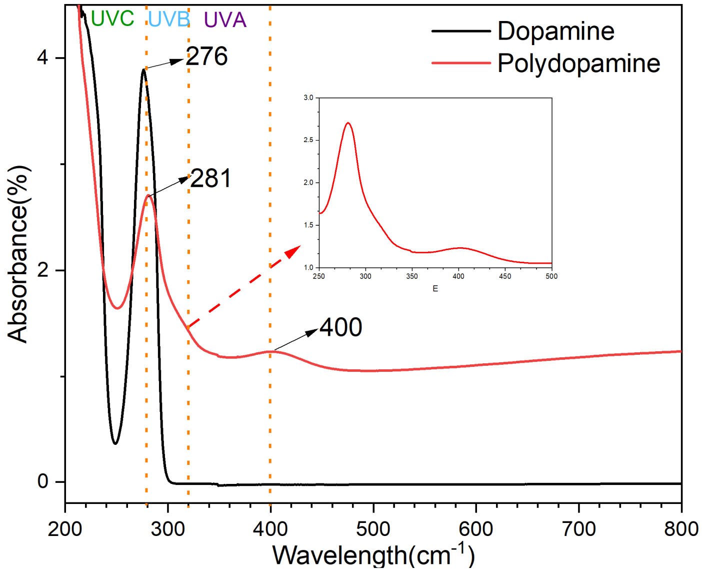

Figure 4- 3:UV-vis spectra of dopamine and polydopamine.

UV-visible absorption spectra of dopamine and polydopamine were conducted, as depicted in Figure 4-3.

In comparison to dopamine, the absorption spectrum of polydopamine displays broader characteristics. Specifically, the intensity of the sharp absorbance peak at 276 nm, associated with the catechol group present in dopamine, decreases noticeably. This reduction in intensity is coupled with a slight shift in the peak to 281 nm, suggesting the continued presence of the catechol structure within the polydopamine compound. Furthermore, shoulder peaks at 320 nm and broad peaks at 400 nm are evident in polydopamine which collectively demonstrate the oxidative transformation of dopamine, particularly the latter absorbance associated with the generation of ortho-quinone resulting from the oxidative transformation of dopamine monomer [15; 16].

The UV-visible spectrum of polydopamine confirms the successful self-polymerization of dopamine. The heightened absorption of polydopamine in the UVA and UVB regions may be linked to the chromophoric functional groups of polydopamine, suggesting its potential as a UV absorber when incorporated into polypropylene. The influence of the UV absorption behaviour of polydopamine on as-coated mussel shell-incorporated polypropylene composites will be discussed in Chapter 7, focusing on the effect of various mussel shell fillers and hybrid fillers on the UV resistance of polypropylene composites under accelerated weathering conditions.

4.3 Characterisation of mussel shells before and after surface modifications

4.3.1 Solid-state NMR (SS-NMR) spectroscopic investigations

Solid-state NMR is a well-established technique for identifying the crystalline polymorphs of calcium carbonate. The carbonate chemical shift indicates the local order, while the peak width indicates the uniformity or heterogeneity of local chemical environments, thus indicating crystalline order versus disorder. Compared to crystalline forms of calcium carbonate, which are aragonite and calcite, vaterite, the carbonate peak in the ^{13}C NMR spectrum of amorphous calcium carbonate (ACC) normally shows larger line width due to the more disordered structure [17].

Figure 4-4 illustrates the ^{13}C DP (direct polarisation) MAS NMR spectra of mussel shell, commercial calcium carbonate and polydopamine coated mussel shell. The spectra of unmodified mussel shell and polydopamine-coated mussel shell exhibit good similarity. Both show two peaks in the range of 165-175 ppm, with one at 171.1 ppm and another at 168.7 ppm. The chemical shifts agree well with reported results in publications, with the peak at 171.1 ppm indicating the typical carbonate salt present as the crystalline aragonite form, while the 168.7 ppm represents the calcite form [18; 19].

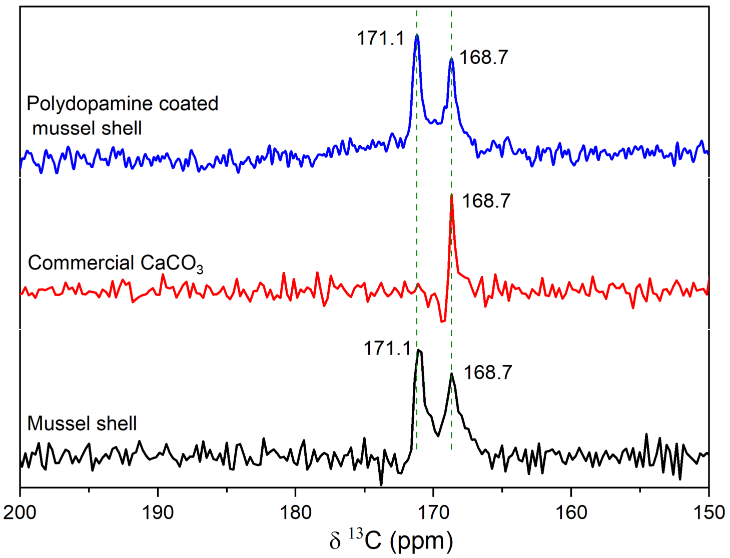

Figure 4- 4: ^{13}C DP SS-NMR spectra of mussel shell, commercial calcium carbonate, polydopamine coated mussel shell.

Notably, only one peak is present at 168.7 ppm for commercial calcium carbonate, confirming its identity as calcite exclusively. Compared to commercial calcium carbonate, the relatively broadened peaks at 168.7 ppm in untreated or PDA-coated mussel shell samples suggest that the calcite lattice may be disrupted by the occlusion of bioorganics and/or inorganics, such as Mg^{2+} with a chemical shift that is ca. 1.5 ppm less shielded than calcite. The presence of Mg^{2+} is often observed in biogenic calcite [18; 20].

Given the focus on investigating the crystal phases of both raw and polydopamine-coated mussel shells using 13C SS-NMR, single pulse and direct polarization were specifically chosen. The characteristic peaks of organic matter in mussel shells are not observed in the ^{13}C MAS NMR spectra. This is partly due to the low abundance of organic matter in these shells. Organic macromolecules in bivalve shells amount to less than 5 wt.%, as previous studies have revealed. For example, *Arctica islandica* shells have the lowest organic content at 1.65 wt.%, while *Hyriopsis cumingii* shells contain 3.14 wt.%, similar to *Diplodon chilensis* shells at 3.35 wt.% and Bufonaria shells at 3.8% [21]. *Pinctada fucata* exhibited the highest content in this sample suite at 4.13 wt.% [22]. Even 8.2 vol% organics were estimated from TGA results for *Haliotis laevigata* shells, the ^{13}C signals of protein/polysaccharide do not show up in the single pulse NMR spectrum [19]. Alternatively, multi cross polarization 13C MAS NMR can provide insights into proteins and polysaccharides. Resonances between 66 and 108 ppm correspond to carbons from sugar rings like chitin, while signals between 110 and 155 ppm are attributed to aromatic or alkene carbons, as documented by Fritzsching K. J. *et al.* [23].

4.3.2 Fourier transform infrared (FTIR) spectroscopic investigations

The carbonate ion exhibits four vibrational modes: two non-degenerate modes (symmetric stretching v_1 at approximately 1085 cm^{-1} and out-of-plane bending v_2 at approximately 860 cm^{-1}) and two doubly degenerate modes (asymmetric stretching v_3 at approximately 1475 cm^{-1} and in-plane bending v_4 at approximately 700 cm^{-1}) [24]. Among these, the v_4 band is the most useful for determining calcium carbonate polymorphs, as it is sharp and distinct for crystalline phases such as calcite, aragonite, and vaterite. In mollusc shells, calcite and aragonite phases are evident, whereas vaterite is rarely encountered and typically confined to sites of shell regeneration.

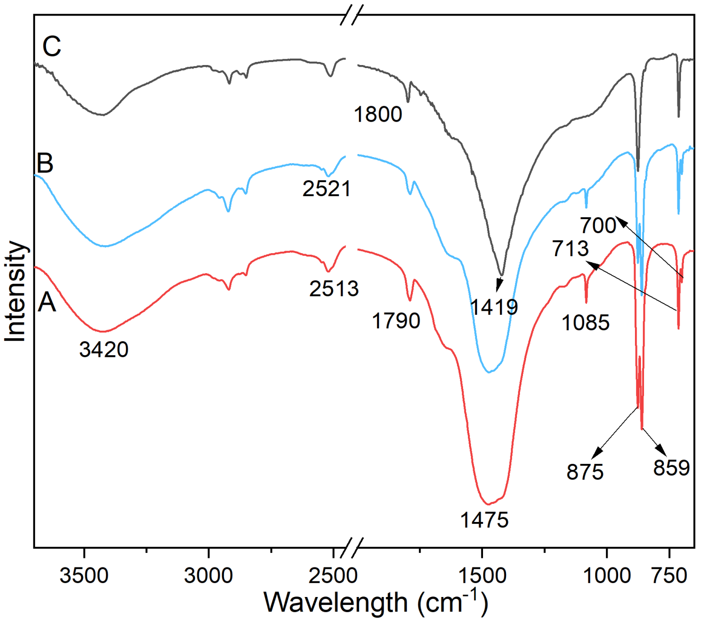

Figure 4- 5:FTIR spectra of (A)mussel shell, (B)PDA-MS and (C) commercial $CaCO_3$.

The infrared (IR) bands associated with aragonite and calcite are listed in Table 4-1 [24; 25]. The two split peaks at ~700 cm^{-1} are characteristic of the aragonite structure, whereas calcite shows only one sharp unsplit peak at this position. Additionally, the symmetric stretching (v_1) at 1085 cm^{-1} is more pronounced for aragonite, and the position of the out-of-plane bending v_2 is also slightly different; the peak at 877 cm^{-1} is characteristic of calcite, while the peak at 857 cm^{-1} is characteristic of aragonite. Ding *et al.* investigated the FTIR spectra of *C. farreri* and identified different polymorphs at the interface and nacre layer based on the ratio of the peaks at 857 and 877 cm^{-1}. This observation suggests the coexistence of aragonite and calcite crystal forms in *C. farreri* [26]. Lee *et al.* identified the exclusive presence of aragonite in the nacre, whereas the polymorph in the folia layer of oyster shells was identified as calcite based on the in-plane bending v_4 band, which split in the nacre sample but appeared as a single peak in the folia [27].

Table 4- 1:Infrared band assignments for aragonite and calcite[24; 25].

Crystal phases of $CaCO_3$	Assignment	Wavenumber (cm^{-1})
Aragonite	In-plane bending (ν_4)	713, 700
	Out of plane bending (ν_2)	859
	Asymmetric stretching (ν_3)	1475
	Symmetric stretching ($\nu1$)	1085
	Combination of ν_1 +ν_3	2521
	Combination of ν_1 +ν_4	1790
Calcite	In-plane bending (ν_4)	712
	Out of plane bending(ν_2)	875
	Asymmetric stretching mode (ν_3)	1419
	Symmetric stretching (ν_1)	-
	Combination of ν_1 +ν_3	2513
	Combination of ν_1 +ν_4	1800

The FTIR spectra of the mussel shell, polydopamine modified mussel shell, and commercial $CaCO_3$ are shown in Figure 4(a). Characteristic absorption peaks of calcium carbonate can be seen spanning 400 to 1700 cm^{-1}. In Figure4-5(c), commercial $CaCO_3$ shows typical characteristic peaks for calcite, as v_4 at 712 cm^{-1}, v_2 at 875 cm^{-1}, and v_3 at 1419 cm^{-1}, demonstrating the exclusive presence of the calcite polymorph in the commercial material. In contrast, the FTIR spectra of mussel shell (both pristine and polydopamine modified) display characteristic bands of both the calcite and aragonite phases. The in-plane bending (v_4) splits into two peaks, 700 and 713 cm^{-1}, together with the symmetric stretching (v_1) at 1085 cm^{-1}, indicating the presence of the aragonite structure [28; 29]. Additionally, the out-of-plane bending band (v_2) splits into two peaks, 859 and 875 cm^{-1}, representing aragonite and calcite structures, respectively. The intensity of the peak located at 859 cm^{-1} is relative stronger than that at 875 cm^{-1}, suggesting that aragonite is the predominant crystal form in mussel shells [26].

The strongest absorption band (1600-1100 cm^{-1}) observed in mussel shell is broad and lacks sharpness, contrasting with the sharp band at 1419 cm^{-1} in commercial $CaCO_3$. This difference is likely due to overlapping peaks arising from the asymmetric stretching (v_3) of aragonite (at 1475 cm^{-1}) and calcite (at 1419 cm^{-1}), along with the stretching vibration of C=C bonds, very likely originating from the organic matrix present in shells [26].The stretching vibration of C-O or C-N was identified at approximately 1630 cm^{-1}, while the stretching vibration of O-H or N-H was observed around 3415 cm^{-1}. These peaks correspond to the protein amide I (around 1650 cm^{-1}) and protein amide A (around 3415 cm^{-1}) peaks, indicating the presence of a protein matrix in mussel shells [26; 30].

It is worth noting that the FTIR spectra of pristine mussel shell and PDA-modified mussel shell are highly similar. According to the preparation method for polydopamine coating on mussel shell (Chapter 3.2.1), the weight ratio of polydopamine to mussel shell is approximately 1:4. This lower proportion of polydopamine results in weaker signals in the FTIR spectra compared to those of the mussel shell. More importantly, as discussed in Section 4.1.2, the characteristic peaks of polydopamine mainly appear in the 1100-1750 cm^{-1} range, which overlap with the broad and strong absorption band from the mussel shell in the 1600-1100 cm^{-1} region. These factors contribute to the challenges in revealing the characteristics of polydopamine on mussel shells through FTIR analysis.

Yao *et al.* compared two fillers for polypropylene composites: mineral $CaCO_3$ and a bio-based filler derived from shell waste. The latter fillers were found to disperse more easily in the polymer matrix., likely due to the presence of matrix protein in the shell waste [31]. Similarly, in the present study, improved dispersion of mussel shell in polypropylene can be expected, as indicated by the FTIR spectra revealing the coexistence of organic and mineral phases in the mussel shell.

4.3.3 Powder X-ray diffraction (XRD)

The crystal structures and phase compositions of mussel shell, polydopamine-modified mussel shell (PDA-MS), and commercial calcium carbonate ($CaCO_3$) can be further elucidated by their XRD patterns, as shown in Figure 4-6. The crystal phase of commercial $CaCO_3$ can be indexed to calcite (JCPDS PDF Card No. 47-1743). The characteristic planes of (012), (104), (110), (113), (202), (018), (116), (211), and (122) correspond to 2θ positions of 23.0°, 29.3°, 35.9°, 39.3°, 43.0°, 47.4°, 48.4°, 56.4°, and

57.3°, respectively, all of which are assigned to the calcite structure. Therefore, it can be concluded that the commercial $CaCO_3$ exclusively exhibits peaks attributed to the calcite phase. Both pristine mussel shell and PDA-MS revealed two main crystalline forms. In addition to the peaks corresponding to the calcite phase, peaks reflecting the aragonite phase were also detected at 2θ positions of 26.1°, 27.2°, 33.1°, 37.8°, and 38.4°, corresponding to the crystal planes (111), (021), (012), (200), (112), and (130), respectively (indexed to JCPDS PDF Card No. 41-1475). Notably, no peaks indicative of other non-CaCO3 phases were detected in either the mussel shell or PDA-MS samples, suggesting a high level of raw material purity. Furthermore, the surface modification with polydopamine did not appear to affect the crystalline phases of the mussel shell.

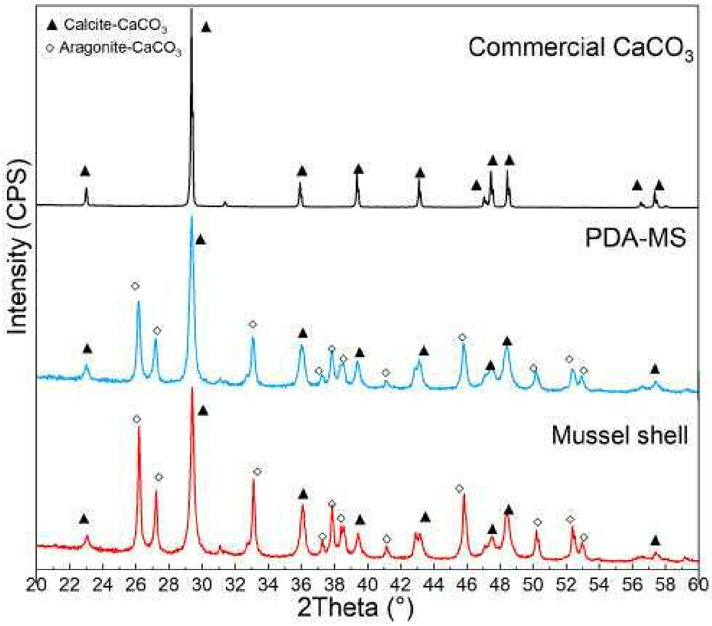

Figure 4- 6:Powder X-ray diffraction patterns of commercial CaCO3, mussel shell, PDA-MS.

4.3.4 Scanning electron microscopy (SEM)

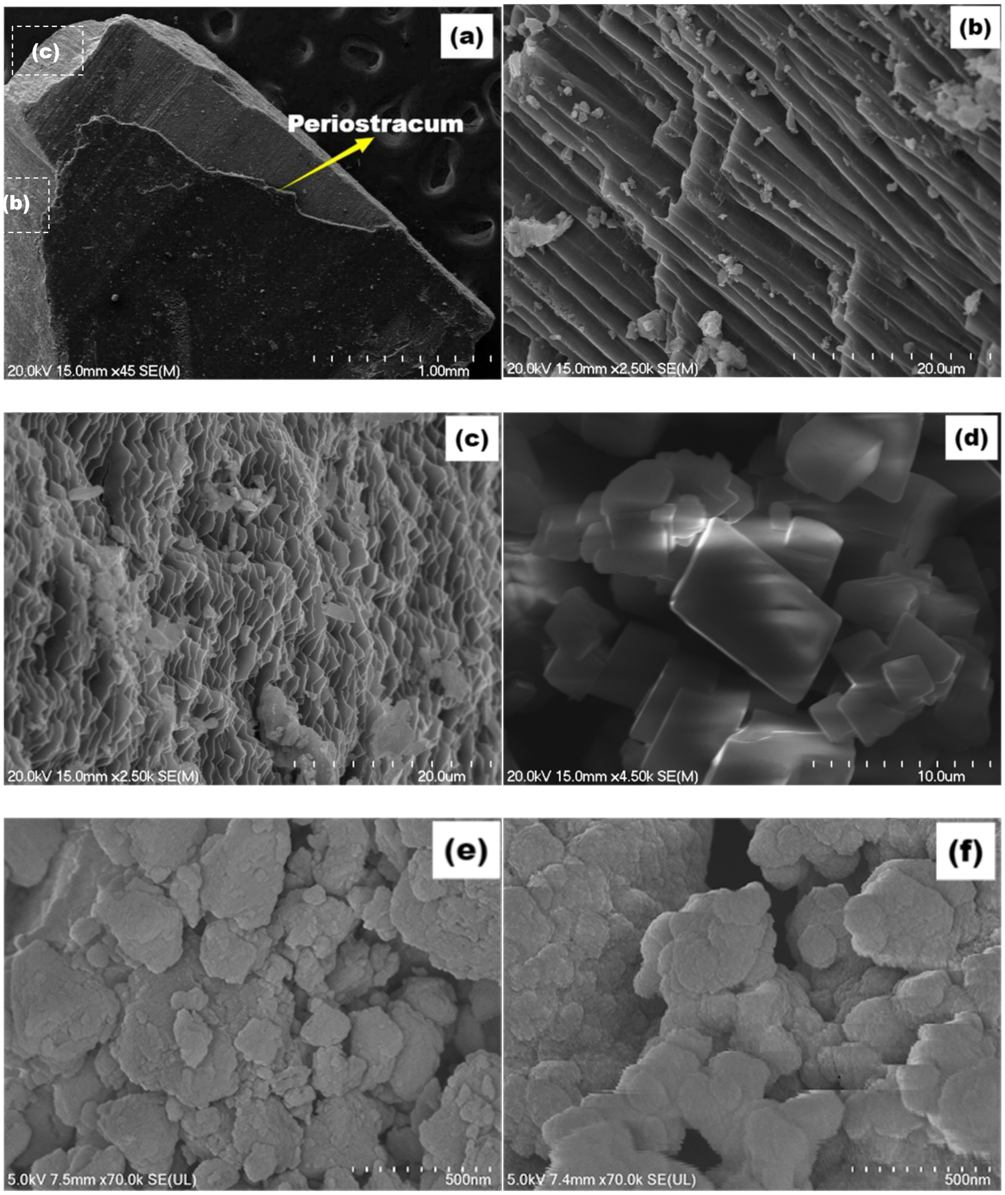

Figure 4- 7: SEM images of (a)mussel shell pieces, (b&c) cross section of mussel shell, (d) commercial calcium carbonate powder, (e) mussel shell powder after ball milling, and (f) polydopamine coated mussel shell powder.

SEM images depicting fractured mussel shell pieces and their cross sections are presented in Figure 4-7 (a)-(c). As depicted in Figure 4-8, mollusc shells typically exhibit a three-layered structure: the outermost layer, known as the periostracum, is composed of hardened protein; the middle layer, termed prismatic, comprises columnar calcite; and the inner layer, called nacre, consists of aragonite and a soft organic matrix [32]. Shell formation is predominantly a biomineralization process wherein the organic matrix plays a pivotal role. Previous studies have revealed that when both calcite and aragonite are present within the mollusc shell, they manifest as distinct layers [26].

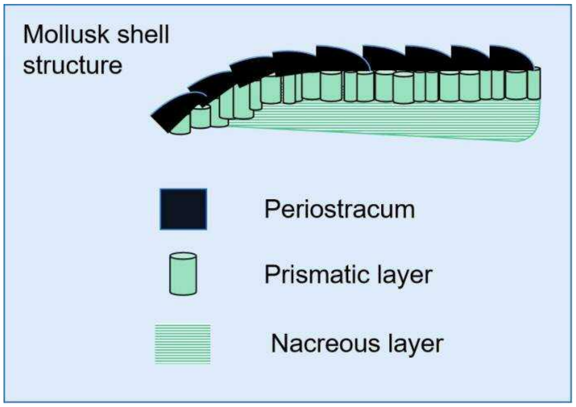

Figure 4- 8: Diagram of three layered mollusc shell structure (reproduced from [33]).

The layer-stacking structure of the mussel shell is clearly observable in Figure 4-7 (a)-(c). A brick-mortar-like structure is evident at the cross-section of a fractured mussel shell piece, with a thin outermost layer (darker colour) atop the shell piece.

The layered structure of the shell serves as the protective function of mollusc species by shielding their soft bodies from external aggression by predators. Each layer possesses distinct structures and serves unique mechanical functions. The brittle and hard exterior shell layers provide resistance against external impacts. The nacreous layer garners significant interest among researchers due to its remarkable mechanical properties, including strength, stiffness, and toughness, despite its predominantly high inorganic phase content, typically around 95% [19]. This extraordinary mechanical behaviour can mainly be attributed to the brick-mortar-like structure of nacre. Some researchers describe nacre as "ceramic plywood," where hard aragonite bricks are bonded together with soft organic layers in between. This unique structure of nacre helps mollusc shells resist slippage and provides toughness and impact resistance [33; 34].

The nacreous layer of mollusc shells typically consists of ordered layers of aragonite-rich platelets separated by a thin organic polymer matrix. Single platelets measure approximately 0.5 -1 μm thick [34; 35]. The estimated thickness of single platelets from Figure 4-7 (b)-(c) supports with this reported value. Figure 4-7 (e)-(f) depict mussel shell powders before and after polydopamine coating, both exhibiting non-uniform sizes and a flake-like morphology, likely resulting from thin aragonite platelets in mussel shells becoming broken during extensive mechanical ball milling. In comparison, commercial

$CaCO_3$ particles aggregate with cubic shapes of varying sizes, exhibiting conventional calcite crystal morphology, such as rhombohedral morphology [36].

4.3.5 Thermogravimetric analysis (TGA)

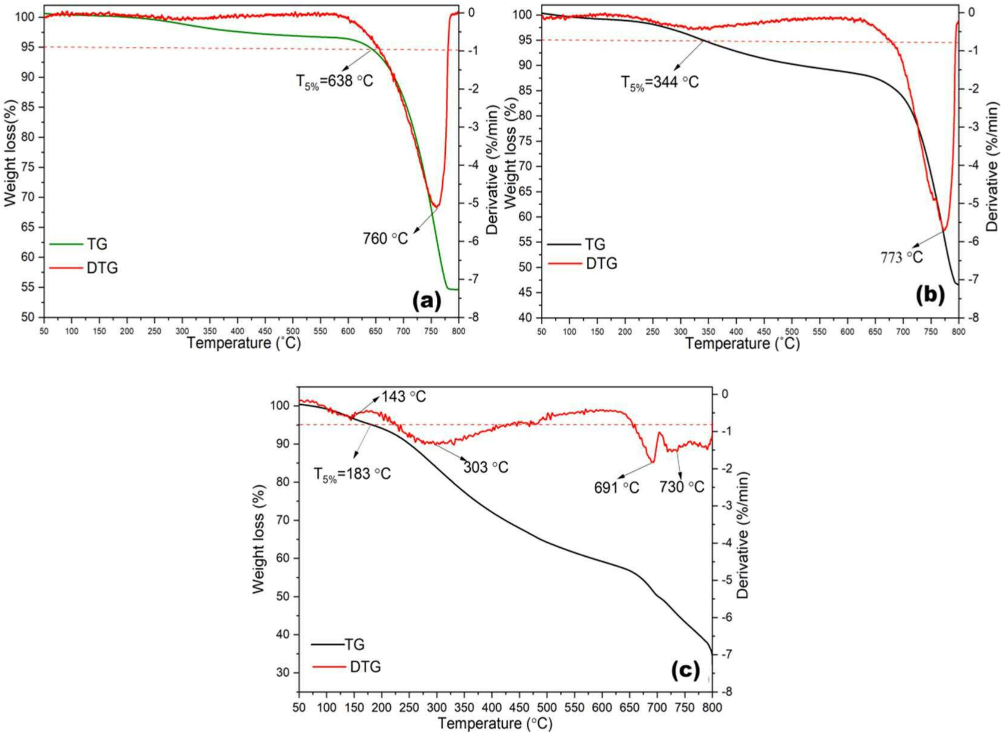

Figure 4- 9:TGA-DTG curves of (a)mussel shell, (b) polydopamine coated mussel shell (PDA-MS), (c) pure polydopamine.

Thermogravimetric analysis (TGA) is a crucial analytical technique used for assessing materials based on their mass loss within a defined temperature range. This technique offers valuable insights into various processes, including vaporization, adsorption, desorption, decomposition, degradation, oxidation, and reduction. Figure 4-9 illustrates the TGA-DTG curves of mussel shell (a), polydopamine coated mussel shells (b) and polydopamine. Both untreated and polydopamine-coated mussel shells exhibit three decomposition steps, as depicted in Figure 4-9 (a)-(b). The initial stage, occurring around 100 °C, involves the loss of adsorbed water. The subsequent decomposition, spanning 200 - 650 °C, can be attributed to the combustion of the organic matrix within the shells, comprising proteins, glycoproteins, and polysaccharides. Additionally, the transformation of aragonite to calcite, an endothermic process between 400 - 500 °C, contributes to the weight loss within this temperature range [37], The third decomposition step, spanning 650 - 800 °C, corresponds to the breakdown of calcium carbonate into calcium oxide and CO_2 [22].

In Figure 4-9 (c), the TG curve of polydopamine exhibits no sharp mass loss with increasing temperature, consistent with previous reports, owing to its heterogeneous structure and complex chemical composition, typically composed of physical and covalent oligomer-like units [38]. The DTG curve of polydopamine reveals multiple peaks and weak shoulder peaks, indicating overlapping reactions with increasing temperature. The gradual mass loss of polydopamine can be categorized into two temperature regimes: early mass loss between 100-300 °C due to the loss of adsorbed water and partial dihydroxylation, and later mass loss between 300-800 °C attributed to PDA carbonization [39]. According to the thermal decomposition pattern of polydopamine, the temperature of 5% weight loss ($T_{5\%}$) of polydopamine-coated mussel shells decreased from 638 °C for mussel shells to 344 °C , which can be attributed to the coexistence of polydopamine with the mussel shells.

Both pristine and polydopamine-coated mussel shells exhibit thermal stability within the temperature range of 160-200 °C, making them promising fillers for polypropylene composites. Furthermore, the maximum mass loss temperature shows a different trend, with mussel shells reaching a maximum mass loss at 760 °C, while polydopamine-coated mussel shells exhibit a higher maximum mass loss temperature at 773 °C. The increased thermal stability after polydopamine coating was observed in PDA coated $CaCO_3$ [40].

4.3.6 X-ray photoelectron spectroscopy (XPS)

XPS provides the surface elemental compositions, characteristics, chemical states, and distribution of functional groups in mussel shell, polydopamine (PDA), and PDA-modified surfaces (PDA-MS), as shown in Figure 4-10 and 4-11. Elemental compositions are shown in Table 4-2.

The X-ray photoelectron survey spectrum (Figure 4-10) of mussel shell and PDA-MS revealed the presence of the three elemental constituents of $CaCO_3$, namely Ca, C, and O. A weak signal due to N1s (atomic percentage of N = 1.56%) was also observed for the mussel shell due to the presence of the natural proteinaceous organic matrix in mussel shell.

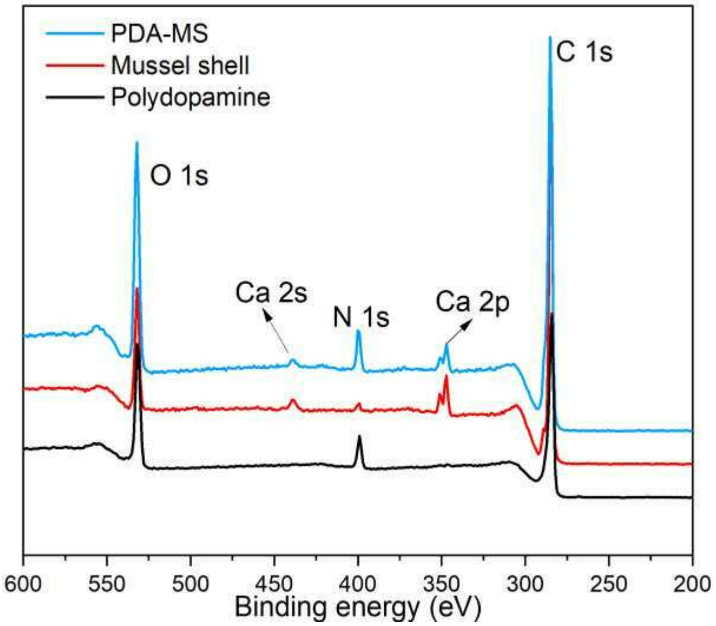

Figure 4- 10:XPS survey spectra of mussel shell, polydopamine, and polydopamine coated mussel shell (PDA-MS).

Table 4-2. XPS surface elemental-analysis parameters of mussel shell, PDA, and PDA-MS.

Sample	Elemental contents					
	C(%)	N(%)	O(%)	Ca(%)	N/O	N/C
MS	83.53	1.56	12.69	2.21	0.12	0.02
PDA	71.31	7.77	20.93	-	0.37	0.11
PDA-MS	69.1	4.32	23.54	3.04	0.18	0.06

According to the structural model of PDA as outlined in Scheme 1, XPS signals corresponding to C1s, N1s, and O1s were identified in the survey spectrum of polydopamine (Figure 4-11, black line). The atomic percentage of N1s was reported to be 7.77%, originating from the amine groups of PDA. The N/C atomic ratio (0.11) observed in the polydopamine (PDA) synthesized in this study is consistent with the reported value (N/C = 0.10) from a previous XPS investigation on PDA, suggesting a comparable structure for the obtained PDA [8].

In comparison to the N1s signal observed for the mussel shell alone, an enhanced signal for the N1s (atomic percentage of N = 4.32 %) was observed on the polydopamine-coated mussel shell (PDA-MS), This enhancement stems from the nitrogen-containing chemical groups introduced through the PDA coating. This observation provides evidence supporting the effective surface coating of polydopamine on the mussel shell. Furthermore, compared to the survey spectrum of PDA, the N/C ratio of PDA-MS decreased to 0.06, attributed to the incorporation of additional carbon atoms from carbonate and mussel protein.

To further elucidate the surface compositions of mussel shell, PDA, and PDA-MS, the narrow scan and curve fitting of the C 1s, N 1s, and O1s regions were acquired and presented in Figure 4-11.

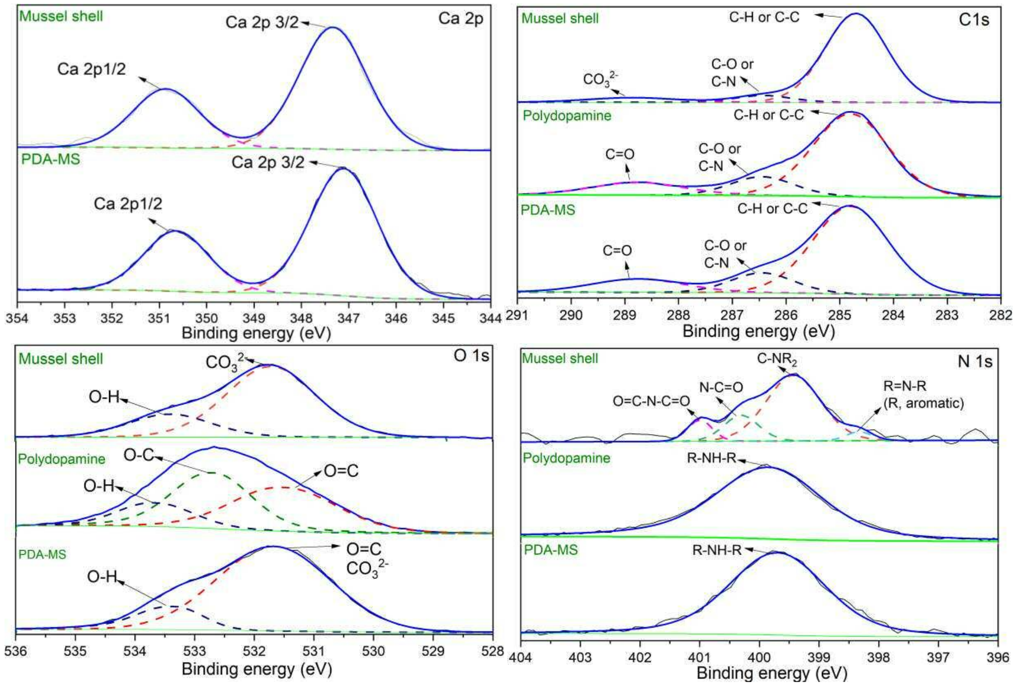

Figure 4- 11:High-resolution (narrow scan) XPS spectra of Ca 2p, C 1s, O 1s, and N 1s regions of mussel shell, polydopamine, and PDA-MS.

The high-resolution (narrow scan) spectrum of the Ca 2p core levels for both the mussel shell and PDA-MS samples can be fitted with two peaks, corresponding to the peak of Ca $2p_{3/2}$ and Ca $2p_{1/2}$, as shown in Figure 4-11. The chemical shifts between the Ca $2p_{3/2}$ and Ca $2p_{1/2}$ core level in both samples are approximately 3.5 eV, consistent with previous literature [41].

For the binding energy values and their corresponding assessments of mussel shell, PDA, PDA-MS, the C1s region narrow scan is able to have three similar components fitted to it but with different intensities. Notably, the narrow scan profiles acquired for PDA and PDA-MS are relatively more similar to each other while that of the mussel shell alone is more distinct in appearance. This indicates a comparable percentage of contribution from each functional group in these two samples. Specifically, discernible peaks corresponding to aliphatic carbon (or a hydrocarbon environment) were observed at a binding energy (BE) of 284.7 eV, while peaks attributable to C-O/C-N appeared at BE=286.4 eV, and those associated with C=O or carbonate groups were identified at BE=288.86 eV [42]. On comparison of pristine mussel shell and PDA-MS, the peaks at 286.4 and 288.86 eV were heightened for PDA-MS, indicating the presence of chemical groups containing C-O, C-N, and C=O which would have been introduced by the PDA coating. This XPS observation definitively confirms the successful surface coating of polydopamine onto the mussel shell substrate.

The O1s spectrum of the pristine mussel shell exhibits two main peaks: one attributed to CO_3^{2-} at a binding energy (BE) of 531.7 eV and another to O-H at 533.3 eV. Conversely, the O1s core-level spectrum of polydopamine (PDA) reveals three principal peaks following deconvolution: C=O (BE=531.5 eV) originating from quinone and catechol, C-O (BE=532.7 eV), and O-H (BE=533.6 eV), respectively [43]. Upon PDA coating, the O1s spectrum of PDA-MS shows two predominant contributions similar to those observed in the mussel shell [44].

The relatively weak N1s spectrum of the mussel shell can be deconvoluted into four components, including R=N-R (398.3 eV), C-NR_2 (399.4 eV), N-C=O (400.3 eV), and oxidized nitrogen groups such as O=C-N-C=O (401.00 eV). This complexity arises from the presence of a protein matrix in the mussel shell [45]. This finding is consistent with the results from FTIR analysis.

In line with the polydopamine (PDA) only sample examined by XPS, the PDA coated mussel shell exhibits a broad and strong peak centred at 399.7 eV, indicative of C-NR_2 from rich amine compounds containing polydopamine, thereby further confirming the successful coating of polydopamine on the mussel shell [4].

4.3.7 Particle size distribution

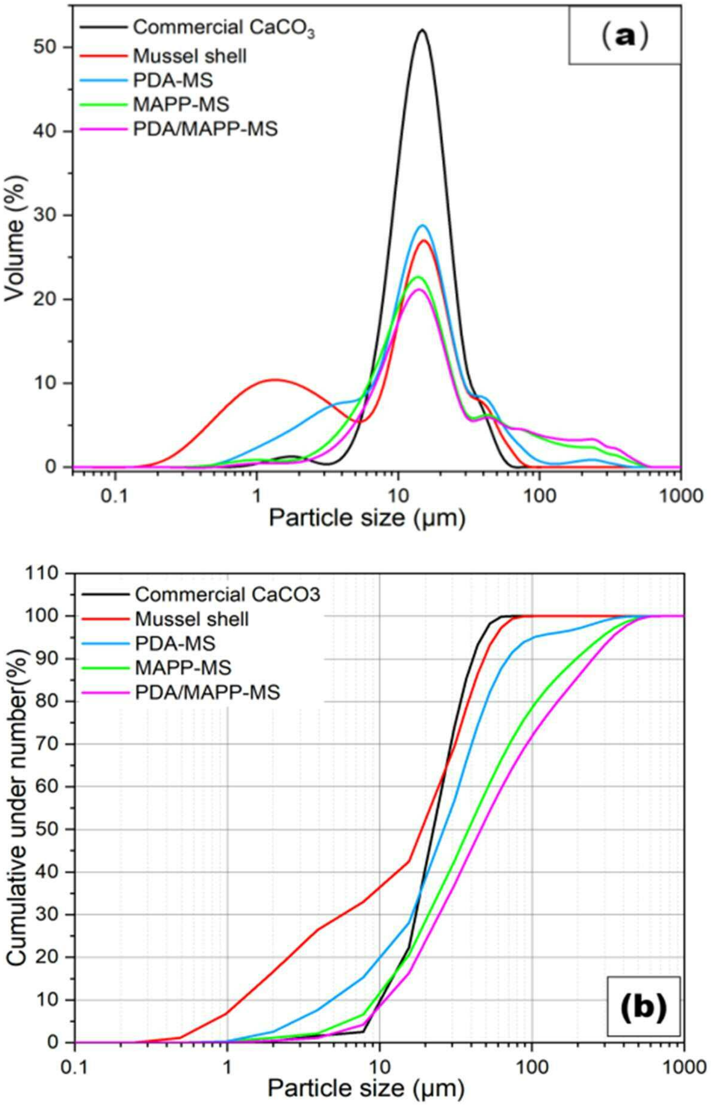

Figure 4- 12:The particle size distribution (a) and cumulative curves (b) of commercial $CaCO_3$ and different mussel shells.

Particle size distribution, adhesion at the particle-matrix interface, and the level of particle loading are key factors that significantly influence the mechanical properties of particulate-polymer composites[46-49]. Hence, it is imperative to investigate the size distribution of commercial $CaCO_3$ and untreated or surface-modified mussel shells.

Figure 4-12 illustrates the particle size distribution (a) and cumulative curves (b) of commercial $CaCO_3$ alongside various mussel shells. In the sample used in this study the commercial $CaCO_3$ exhibited a relatively narrow size distribution, with a range between 5-100 µm, where 100% of the population of grains was less than 100 µm. Similarly, 90% of grains in the pristine mussel shell and PDA-MS samples were also smaller than 100 µm, although this proportion drops to 80% of the total after MAPP or PDA/MAPP co-modification. The cumulative curve revealed that the majority of these fillers fall within the same size range (10 µm < D_{50} < 50 µm), which is deemed to be relatively small.

Larger particles, with a median particle size (D_{50}) of approximately 3 mm, have been observed in other studies to be efficiently integrated into polymers [50]. Conversely, smaller particles with higher surface area have a tendency to agglomerate due to increased particle-particle interactions [48]. This agglomeration can result in adverse dispersion and performance issues in the polymer composites.

The results from the particle size distribution studies in the present study indicate that all tested fillers tended to agglomerate. Hence, investigating the surface properties of these fillers is essential to understand their tendency for agglomeration, particularly during processing with the polymer matrix. Gaining insights into this will assist in determining the interfacial reactions between the filler and matrix, which are crucial for assessing their subsequent influence on the mechanical properties of the PP composites.

4.3.8 Contact angle measurement and surface energy calculation

According to thermodynamic principles, surface energy (γ) and its constituent components represent crucial surface characteristics of solids, influencing their interactions with other materials [51-54]. For instance, the weak adhesive properties of polypropylene (PP) to binders, particularly those featuring polar surfaces, can be attributed to its non-polar nature characterised by a low surface energy (≈32 mJ/m^2) [55; 56]. In the context of polymer composites, these surface energy parameters play a key role in governing filler dispersion and the adhesion between the filler and polymer matrix. Accordingly, to probe this in the case of materials being investigated in the present study, the surface energy values of mussel shells and modified mussel shells were calculated using contact angle experiment data. It is known that no exact algorithm exists for calculating solid surface energy from contact angle data. Therefore, various semi-empirical methods are utilized for this purpose. Here the Fowkes model was used to calculate the surface energy from contact angle measurement [57].

Using a nonpolar aprotic liquid, e.g., diiodomethane ($\gamma_l^p = 0$) , the dispersive component of the solid surface energy, γ_s^d, can be computed from Equation 1. Secondly, a polar protic liquid, e.g., water, is tested, and using γ_s^d and Equation 1, the polar component of the solid surface energy, γ_s^p, can be computed. In this context, the dispersive component denotes the interactions arising from London dispersion forces, while the polar component encompasses interactions induced by polar functional groups, such as hydroxyl, carboxyl, or amino moieties [57]. The Fowkes theory assumes that the total surface energy is the sum of the dispersive and polar components as expressed in Equation 2. This analysis aids in comprehending the surface properties of mussel shell fillers before and after the various surface modifications so allowing a prediction to be made of filler dispersibility within the PP matrix and assessing the potential for interfacial adhesion between the filler materials and the polymer matrix. The results of these analyses are summarized in Table 5.

With a PDA coating applied to the surface of mussel shells, the contact angles (CAs) obtained using two test liquids exhibit distinct trends in comparison to those on raw mussel shells. Specifically, after PDA coating, the contact angle from the water test (CA_w) decreased, while the contact angle from the diiodomethane test (CA_{DIM}) increased slightly.

$$\frac{\gamma_l(\cos\theta+1)}{2}=(\gamma_l{}^d)^{1/2}(\gamma_s{}^d)^{1/2}+(\gamma_l{}^p)^{1/2}(\gamma_s{}^p)^{1/2} \qquad \text{Eq1}$$

$$\gamma_s=\gamma_s{}^d+\gamma_s{}^p \qquad \text{Eq2}$$

Note: γ_l and γ_s is denoted as total surface energy of liquid and solid, respectively ; $\gamma_s{}^p$ and $\gamma_s{}^d$ are denoted as polar and dispersive surface energy components of solid, respectively while $\gamma_l{}^p$ and $\gamma_l{}^d$ are denoted as polar and dispersive surface energy components of liquid. θ is the contact angle measured using different test liquids.

These findings support previous research, which suggests that the observed changes result from the introduction of hydrophilic functional groups, such as catechol, amine, and imine, onto the surface of mussel shells through the PDA coating [53]. This increase in contact angle with diiodomethane and the decrease in water, is interpreted because of the introduction of hydrophilic functional groups, which enhances the surface hydrophilicity. Accordingly, the polar component of surface energy of untreated mussel shell is 24.6 mJ/m^2, while that of PDA coated mussel was slightly higher at 25.9 mJ/m^2. [26]

Table 4- 2:Contact angle measurements (average (standard deviation)) and dispersion, polar, and total components of surface energy.

Samples	Contact angle (°)		Surface energy (mJ/m^2)			cos θ	ΔWa (mJ/m^2)
	CA$_W$	CA$_{DIM}$	γ_s^p	γ_s^d	γ_s		
MS	29.3(2.2)	14.3(2.6)	24.6	49.2	73.8	0.13	46.44
PDA-MS	26.4(3.5)	15.4(2.4)	25.9	49.0	74.9	0.11	48.80
MAPP-MS	87.5(28)	49.1(3.6)	2.1	34.8	36.9	0.86	2.63
PDA/MAPP-MS	103.6(5.1)	48.9(2.4)	0.001	34.9	34.9	0.94	0.23
PP[56]	108		0.1	32.8	32.9		
PP[55]	98(2.3)	57(0.8)	0.5	31.6	32.1		

Note: γ_s is denoted as total solid surface energy; γ_s^p and γ_s^d are denoted as polar and dispersive surface energy components of solid, respectively.

The PDA coating did not enhance the hydrophobicity of the mussel shell surface, as evidenced by the value of surface energy calculated. This PDA surface modification method aims to facilitate the introduction of functional groups, such as amine and hydroxyl groups, onto the surface of the mussel shell. Once present, these additional functional groups, combined with other features like the massive aromatic structures, enable the PDA coating to act as a linking platform on the mussel shell to enable further surface modification reagents, such as MAPP to become attached. This bridging occurs through mechanisms such as hydrogen bonding, covalent bonding, π-π conjugation, and chemical bonds, like ester bonds.

In contrast to untreated mussel shells or PDA-MS, the dispersive and polar energies of the surface modified MAPP-MS sample decreased significantly, and further reduction is moreover realized with the PDA/MAPP co-modified mussel shell fillers, bringing their surface energies closer to the values reported for PP alone [55; 56]. In particular, the polarity component of surface energy decreased by over 90% for both MAPP-MS and PDA/MAPP-MS. This substantial decrease effectively represents an increased hydrophobicity achieved via attachment of MAPP alone or when the MAPP is combined with PDA-modified mussel shell fillers.

Aggregated fillers typically result in defects within polymer composites which act to weaken the interaction between the filler and matrix. Consequently, the mechanical properties of the composite materials are compromised. In order to evaluate the aggregate tendency of fillers during the initial processing steps to compound polymer composite, the Owens-Wendt model was applied to calculate *cosθ* (equivalent equilibrium contact angle) as presented in Equation 3 and 4 [51]. Here, γ_{PP} is denoted as the total solid surface energy of PP while γ_{Filler} is denoted as the total solid surface energy of filler, respectively. The superscripts *d* and *p* denote the dispersed and the polar part of the surface energy, respectively.

The work of adhesion (*W)* is the energy required to separate the two adjacent phases.

$$\cos\theta = -1 + 2\frac{\sqrt{\gamma_{PP}{}^{d}\gamma_{Filler}{}^{d}}}{\gamma_{Filler}} + 2\frac{\sqrt{\gamma_{PP}{}^{p}\gamma_{Filler}{}^{p}}}{\gamma_{Filler}} \qquad \text{Eq3}$$

$$\cos\theta = \begin{cases} -1+2\dfrac{W_{FP}}{W_{FF}} & \dfrac{W_{FP}}{W_{FF}} < 1 \\ 1 & \dfrac{W_{FP}}{W_{FF}} > 1 \end{cases} \qquad \text{Eq4}$$

W_{FF} represents the work of adhesion of two filler particles, while W_{PP} and W_{FP} denote the work of adhesion between polymer-polymer and filler-polymer, interactions respectively.

According to Equation 4, Natarajan, *et al.* proposed that when *cosθ* is < 1, the relative attraction between fillers (W_{FF}) is more significant than their attraction to the polymer matrix (W_{FP}*)* [58]. In such a case, the fillers tend to aggregate to minimize their interfacial energy, which means that the initial dispersion state of these fillers is lacking.

As shown in Table 5, when considering PP as the matrix, it is to be noted that the *cosθ* values for the four different fillers—untreated mussel shell fillers, PDA-MS, MAPP-MS, and PDA/MAPP-MS—are all less than 1. This indicates a propensity for these fillers to aggregate upon incorporation into the PP matrix. However, the *cosθ* value of MAPP-modified mussel shells (*cosθ* = 0.86) is seen to be significantly higher than that of untreated mussel shell fillers (*cosθ* = 0.13), indicating an improvement in initial dispersibility upon the introduction of MAPP onto the surface of mussel shells.

Furthermore, the highest *cosθ* value (*cosθ* = 0.94) obtained from PDA/MAPP-modified mussel shells indicates that the PDA coating before MAPP modification can act to further improve the dispersibility of mussel shells, an effect which is attributed to the bridging effect of the polydopamine coating between MAPP and the mussel shell.

According to thermodynamic theory, the initial dispersed fillers tend to re-agglomerate during subsequent processing for compounding the polymer composite. To evaluate the driving force behind filler re-aggregation within polymer matrix, evaluation of the potential energy difference (ΔWa) value between the filler-filler interface energy (W_{FF}) and the polymer-polymer interface (W_{PP}), formed by the filler-polymer interf*ace* (W_{FP}),

$$\Delta Wa = W_{FF} + W_{PP} - 2W_{FP} \qquad \text{Eq5}$$

$$\Delta Wa = 2\left(\sqrt{\gamma_{Filler}{}^{d}} - \sqrt{\gamma_{PP}{}^{p}}\right)^2 + 2\left(\sqrt{\gamma_{Filler}{}^{p}} - \sqrt{\gamma_{PP}{}^{p}}\right)^2 \qquad \text{Eq6}$$

is crucial, as illustrated in Equations 5 and 6 [59]. Essentially, the larger the value of ΔWa, the greater the potential for filler re-agglomeration when processed with polymer. Table 4-3 presents the ΔWa values of different mussel shell fillers in PP matrix.

In polypropylene (PP) composites, the ΔWa value for MAPP-MS fillers was calculated to be 2.63 mJ/m², representing a clear decrease compared to that of pristine mussel shell fillers (ΔWa =46.44 mJ/m²) or polydopamine-modified mussel shell fillers (ΔWa = 48.80 mJ/m²). The lowest ΔWa value (0.23 mJ/m²) was obtained for the PDA/MAPP-MS filler in the PP system, indicating a significantly reduced tendency for re-agglomeration of these fillers. This substantial reduction suggests a low propensity for re-agglomeration of MAPP-MS and PDA/MAPP-MS fillers within polypropylene. Consequently, improved compatibility can be anticipated between the polypropylene matrix and MAPP-modified mussel shell fillers, with further enhancement expected when mussel shells undergo MAPP modification after polydopamine coating.

4.4 Conclusions

In this chapter, the characterisation of polydopamine and various types of mussel shells provides foundational insights into their properties and potential applications. Specifically, the study aims to explore how surface modifications can enhance the suitability of mussel shells as fillers in polypropylene composites.

The successful self-polymerisation of dopamine into polydopamine under controlled conditions was confirmed through SS-NMR and FTIR analyses of dopamine and polydopamine. Furthermore, the UV-vis absorption behaviour of polydopamine suggests that incorporating polydopamine-coated mussel shells could potentially enhance the UV-resistance of polypropylene.

Analysis using SS-NMR, FTIR, and XRD identified the predominant crystal phases of mussel shells as aragonite and calcite. Thermal stability between 160-200 ℃ indicated that both pristine and polydopamine-coated mussel shells are promising biogenic fillers for polymer composites, as demonstrated by TGA.

Surface energy calculations based on the Fowkes model indicated that polydopamine-coated mussel shell fillers maintain comparable hydrophilicity to unmodified fillers. XPS analysis revealed that polydopamine coating introduces functional groups on the filler surface, facilitating effective surface modification with MAPP through chemical and hydrogen bonding. Moreover, surface energy values suggested improved hydrophobicity for MAPP-modified mussel shell fillers. The Owens-Wendt model showed reduced tendencies of filler agglomeration and re-agglomeration with additional PDA/MAPP co-modification.

Subsequent chapters will investigate the impact of these untreated or modified mussel shell fillers on the properties of prepared polypropylene composites.

4.5 References

1. Dreyer, D. R., Miller, D. J., Freeman, B. D., *et al.* (2012). Elucidating the Structure of Poly(dopamine). *Langmuir*, *28*(15), 6428-6435.
2. Fredi, G., Simon, F., Sychev, D., *et al.* (2020). Bioinspired polydopamine coating as an adhesion enhancer between paraffin microcapsules and an epoxy matrix. *ACS omega*, *5*(31), 19639-19653.
3. Lee, H., Dellatore, S. M., Miller, W. M., *et al.* (2007). Mussel-inspired surface chemistry for multifunctional coatings. *SCIENCE*, *318*(5849), 426-430.
4. Liebscher, J., Mrówczyński, R., Scheidt, H. A., *et al.* (2013). Structure of polydopamine: a never-ending story? *Langmuir*, *29*(33), 10539-10548.
5. Grosu, I.-G., Moț, A., Filip, X., *et al.* (2023). What Is Wrong with Hyaluronic Acid Chemistry? A 15N/13C Solid-State NMR Re-Evaluation of Its Dopamine Conjugates. *Polymers*, *15*(13), 2825.
6. Cîrcu, M., & Filip, C. (2018). Closer to the polydopamine structure: New insights from a combined 13 C/1 H/2 H solid-state NMR study on deuterated samples. *Polymer Chemistry*, *9*(24), 3379-3387.
7. Proks, V., Brus, J., Pop-Georgievski, O., *et al.* (2013). Thermal-Induced Transformation of Polydopamine Structures: An Efficient Route for the Stabilization of the Polydopamine Surfaces. *Macromolecular chemistry and physics*, *214*(4), 499-507.
8. Hemmatpour, H., De Luca, O., Crestani, D., *et al.* (2023). New insights in polydopamine formation via surface adsorption. *Nat. Commun.*, *14*(1), 664.

9. Alfieri, M. L., Panzella, L., Oscurato, S. L., *et al.* (2018). The Chemistry of Polydopamine Film Formation: The Amine-Quinone Interplay. *Biomimetics (Basel)*, *3*(3).
10. Yu, F., Chen, S., Chen, Y., *et al.* (2010). Experimental and theoretical analysis of polymerization reaction process on the polydopamine membranes and its corrosion protection properties for 304 Stainless Steel. *Journal of Molecular Structure*, *982*(1), 152-161.
11. Zangmeister, R. A., Morris, T. A., & Tarlov, M. J. (2013). Characterization of Polydopamine Thin Films Deposited at Short Times by Autoxidation of Dopamine. *Langmuir*, *29*(27), 8619-8628.
12. Wang, Y., Su, J., Li, T., *et al.* (2017). A Novel UV-Shielding and Transparent Polymer Film: When Bioinspired Dopamine-Melanin Hollow Nanoparticles Join Polymers. *ACS Appl Mater Interfaces*, *9*(41), 36281-36289.
13. Nikafshar, S., Zabihi, O., Ahmadi, M., *et al.* (2017). The effects of UV light on the chemical and mechanical properties of a transparent epoxy-diamine system in the presence of an organic UV absorber. *Materials*, *10*(2), 180.
14. Meredith, P., & Sarna, T. (2006). The physical and chemical properties of eumelanin. *Pigment cell research*, *19*(6), 572-594.
15. Sugumaran, M., Duggaraju, P., Jayachandran, E., *et al.* (1999). Formation of a New Quinone Methide Intermediate during the Oxidative Transformation of 3,4-Dihydroxyphenylacetic Acids: Implication for Eumelanin Biosynthesis. *Archives of Biochemistry and Biophysics*, *371*(1), 98-106.
16. Cheah, Y. S., Santhanakrishnan, S., Sullivan, M. B., *et al.* (2016). The chemical reactivities of DOPA and dopamine derivatives and their regioselectivities upon oxidative nucleophilic trapping. *Tetrahedron*, *72*(41), 6543-6550.
17. Nebel, H., Neumann, M., Mayer, C., *et al.* (2008). On the structure of amorphous calcium carbonate-a detailed study by Solid-State NMR spectroscopy. *Inorg. Chem.*, *47*(17), 7874-7879.
18. Ben Shir, I., Kababya, S., Katz, I., *et al.* (2013). Exposed and buried biomineral interfaces in the aragonitic shell of Perna canaliculus revealed by Solid-State NMR. *Chem. Mater.*, *25*(22), 4595-4602.
19. Jäger, C., & Cölfen, H. (2007). Fine structure of nacre revealed by solid state 13C and 1H NMR. *Cryst. Eng. Comm.*, *9*(12), 1237.
20. Papenguth, H. W., Kirkpatrick, R. J., Montez, B., *et al.* (1989). 13C MAS NMR spectroscopy of inorganic and biogenic carbonates. *Am. Min.*, *74*(9-10), 1152-1158.
21. Sampath, V., Huang, P., Wang, F., *et al.* (2019). Crystalline organization of nacre and crossed lamellar architecture of seashells and their influences in mechanical properties. *Materialia*, *8*, 100476.
22. Agbaje, O. B. A., Thomas, D. E., McLnerney, B. V., *et al.* (2017). Organic macromolecules in shells of Arctica islandica: comparison with nacroprismatic bivalve shells. *Marine Biology*, *164*(11), 208.
23. Fritzsching, K. J., Duan, P., Alberts, E. M., *et al.* (2019). Silk-Like Protein with Persistent Radicals Identified in Oyster Adhesive by Solid-State NMR. *ACS applied bio materials*, *2*(7), 2840-2852.
24. Vagenas, N. V., Gatsouli, A., & Kontoyannis, C. G. (2003). Quantitative analysis of synthetic calcium carbonate polymorphs using FT-IR spectroscopy. *Talanta*, *59*(4), 831-836.
25. Ševčík, R., Šašek, P., & Viani, A. (2018). Physical and nanomechanical properties of the synthetic anhydrous crystalline $CaCO_3$ polymorphs: vaterite, aragonite and calcite. *JOURNAL OF MATERIALS SCIENCE*, *53*(6), 4022-4033.

26. Zhu, Y., Sun, C., Song, Y., *et al.* (2016). The study of the adductor muscle-shell interface structure in three Mollusc species. *Acta Oceanologica Sinica*, *35*(8), 57-64.
27. Lee, S. W., Jang, Y. N., & Kim, J. C. (2011). Characteristics of the aragonitic layer in adult oyster shells, Crassostrea gigas: structural study of Myostracum including the adductor muscle scar. *J. Evid. Based Complementary Altern. Med.*, *2011*(1), 742963.
28. Melo, P. M. A., Macêdo, O. B., Barbosa, G. P., *et al.* (2019). High-density polyethylene/mollusk shell-waste composites: effects of particle size and coupling agent on morphology, mechanical and thermal properties. *Journal of Materials Research and Technology*, *8*(2), 1915-1925.
29. Essabir, H., Bensalah, M. O., Rodrigue, D., *et al.* (2017). A comparison between bio- and mineral calcium carbonate on the properties of polypropylene composites. *Constr. Build. Mater.*, *134*(1), 549-555.
30. Li, H. Y., Tan, Y. Q., Zhang, L., *et al.* (2012). Bio-filler from waste shellfish shell: preparation, characterization, and its effect on the mechanical properties on polypropylene composites. *J. Hazard. Mater.*, *217-218*(30), 256-262.
31. Yao, Z. T., Chen, T., Li, H. Y., *et al.* (2013). Mechanical and thermal properties of polypropylene (PP) composites filled with modified shell waste. *J. Hazard Mater.*, *262*(15), 212-217.
32. Sun, J., & Bhushan, B. (2012). Hierarchical structure and mechanical properties of nacre: a review [10.1039/C2RA20218B]. *RSC Advances*, *2*(20), 7617-7632.
33. Barthelat, F., s, J. E. R., & Espinosa., H. D. (2009). A Review on the Structure and Mechanical Properties of Mollusk Shells – Perspectives on Synthetic Biomimetic Materials. In B. B.; & F. H. (Eds.), *Applied scanning probe methods XIII.NanoScience and Technology* (pp. 17-44). Springer.
34. Kakisawa, H., & Sumitomo, T. (2011). The toughening mechanism of nacre and structural materials inspired by nacre. *Science and technology of advanced materials*, *12*(6), 064710-064710.
35. Rousseau, M., Meibom, A., Gèze, M., *et al.* (2009). Dynamics of sheet nacre formation in bivalves. *Journal of structural biology*, *165*(3), 190-195.
36. Chakrabarty, D., & Mahapatra, S. (1999). Aragonite crystals with unconventional morphologies [10.1039/A905407C]. *Journal of Materials Chemistry*, *9*(11), 2953-2957.
37. Perić, J., Vučak, M., Krstulović, R., *et al.* (1996). Phase transformation of calcium carbonate polymorphs. *Thermochimica Acta*, *277*, 175-186.
38. Ryu, J. H., Messersmith, P. B., & Lee, H. (2018). Polydopamine surface chemistry: a decade of discovery. *ACS applied materials & interfaces*, *10*(9), 7523-7540.
39. Tawiah, B., Yu, B., Cheung, W. Y., *et al.* (2018). Synthesis and application of synergistic azo-boron-BPA / polydopamine as efficient flame retardant for poly(lactic acid). *Polymer Degradation and Stability*, *152*, 64-74.
40. Zhang, X., Zhang, Y., Li, H., *et al.* (2023). Enhanced thermal conductivity and photothermal effect of microencapsulated n-octadecane phase change material with calcium carbonate-polydopamine hierarchical shell for solar energy storage. *Solar Energy Materials and Solar Cells*, *256*, 112336.
41. Ni, M., & Ratner B. D. . (2008). Differentiating calcium carbonate polymorphs by surface analysis techniques-an XPS and TOF-SIMS study. *SIA*, *40*(10), 1356-1361.
42. Xie, Y., & Sherwood, P. M. (1990). X-ray photoelectron-spectroscopic studies of carbon fiber surfaces. 11. Differences in the surface chemistry and bulk structure

of different carbon fibers based on poly (acrylonitrile) and pitch and comparison with various graphite samples. *Chem. Mater.*, *2*(3), 293-299.

43. Alkhouzaam, A., Qiblawey, H., & Khraisheh, M. (2021). Polydopamine functionalized graphene oxide as membrane nanofiller: spectral and structural studies. *Membranes*, *11*(2), 86.
44. Zhou, X., Liu, W., Tian, C., *et al.* (2018). Mussel-inspired functionalization of biological calcium carbonate for improving Eu(III) adsorption and the related mechanisms. *J. Chem. Eng.*, *351*(1), 816-824.
45. Gong, F. Y., Zhang, J. H., Ding, L., *et al.* (2017). Mussel-inspired coating of energetic crystals: A compact core–shell structure with highly enhanced thermal stability. *J. Chem. Eng.*, *309*(1), 140-150.
46. Fu, S. Y., Feng, X. Q., Lauke, B., *et al.* (2008). Effects of particle size, particle/matrix interface adhesion and particle loading on mechanical properties of particulate–polymer composites. *Compos. Part B Eng.*, *39*(6), 933-961.
47. Vollenberg, P., & Heikens, D. (1989). Particle size dependence of the Young's modulus of filled polymers: 1. Preliminary experiments. *Polymer*, *30*(9), 1656-1662.
48. Xanthos, M. E. (2010). Functional fillers for plastics. (M. Xanthos, Ed. Second ed.). WILEY-VCH Verlag GmbH & Co. KGaA, Weinheim.
49. Nwanonenyi, S., Obidiegwu, M., & Onuegbu, G. (2013). Effects of particle sizes, filler contents and compatibilization on the properties of linear low density polyethylene filled periwinkle shell powder. *Int. J. Eng. Sci.*, *2*(2), 1-8.
50. Ersoy, O., & Köse, H. (2020). Comparison of the effect of reactive and nonreactive treatments on the dispersion characteristics of a calcium carbonate (calcite) filler in a polypropylene matrix composite. *Polym. Compos.*, *41*(9), 3483-3490.
51. Stöckelhuber, K., Wießner, S., Das, A., *et al.* (2017). Filler flocculation in polymers–a simplified model derived from thermodynamics and game theory. *J. Soft Matter*, *13*(20), 3701-3709.
52. Taguet, A., Cassagnau, P., & Lopez-Cuesta, J. M. (2014). Structuration, selective dispersion and compatibilizing effect of (nano)fillers in polymer blends. *Prog. in Polym. Sci.*, *39*(8), 1526-1563.
53. Lin, C., Gong, F., Qian, W., *et al.* (2021). Tunable interfacial interaction intensity: Construction of a bio-inspired interface between polydopamine and energetic crystals. *Compos. Sci. Technol.*, *211*(28), 108816.
54. Ma, Q., Wang, Z., Liang, T., *et al.* (2022). Unveiling the role of filler surface energy in enhancing thermal conductivity and mechanical properties of thermal interface materials. *Compos. Part A: Appl. Sci. Manuf.*, *157*(1), 106904.
55. Khoshkava, V., & Kamal, M. R. (2013). Effect of surface energy on dispersion and mechanical properties of polymer/nanocrystalline cellulose nanocomposites. *Biomacromolecules*, *14*(9), 3155-3163.
56. Mirabedini, S. M., Rahimi, H., Hamedifar, S., *et al.* (2004). Microwave irradiation of polypropylene surface: a study on wettability and adhesion. *Int. J. Adhes. Adhes.*, *24*(2), 163-170.
57. Fowkes, F. M. (1963). Additivity of intermolecular forces at interfaces. I. determination of the contribution to surface and interfacial tensions of dispersion forces in various liquids1. *J. Phys. Chem.*, *67*(12), 2538-2541.
58. Natarajan, B., Li, Y., Deng, H., *et al.* (2013). Effect of interfacial energetics on dispersion and glass transition temperature in polymer nanocomposites. *Macromol.*, *46*(7), 2833-2841.

59. Wang, M. J. (1998). Effect of polymer-filler and filler-filler interactions on dynamic properties of filled vulcanizates. *Rubber Chem. Tech.*, *71*(3), 520-589.

Chapter 5

Effects of Mussel Shell Fillers on Mechanical, Thermal, and Morphological Properties of PP Composites

5.1 Introduction

This chapter investigates the influence of pristine and surface-modified mussel shell fillers on the properties of polypropylene (PP) composites. The study encompasses two types of surface modifications: maleic anhydride-grafted polypropylene (MAPP) and a combination of polydopamine and MAPP (PDA/MAPP). The research aims to elucidate the impact of these fillers on the thermal and mechanical properties of the resultant PP composites.

A comparative analysis is conducted, considering varying filler contents and surface properties of the different mussel shell fillers. This approach allows for a comprehensive understanding of how these factors affect the filler-matrix interactions within the composite system.

Given the inherent viscoelastic nature of polypropylene, this study places particular emphasis on examining the influence of filler types and contents on the viscoelastic properties of the composites. The investigation encompasses both short-term and long-term behaviours, as well as properties in both solid and melt states, providing a holistic view of the material's performance under various conditions.

Furthermore, the morphology of fracture surfaces of PP and its composites containing different mussel shell fillers is examined. This analysis offers direct observational evidence of filler-matrix compatibility, complementing the quantitative data obtained from thermal and mechanical tests.

By systematically exploring these aspects, this chapter aims to provide a comprehensive understanding of how mussel shell fillers, both pristine and surface-modified, influence the properties of PP composites. The findings from this study will contribute to the broader knowledge base on polymer composites and potentially inform future developments in this field.

5.2 The influence of different fillers on the thermal behaviour of PP composites -TG-DTG analysis

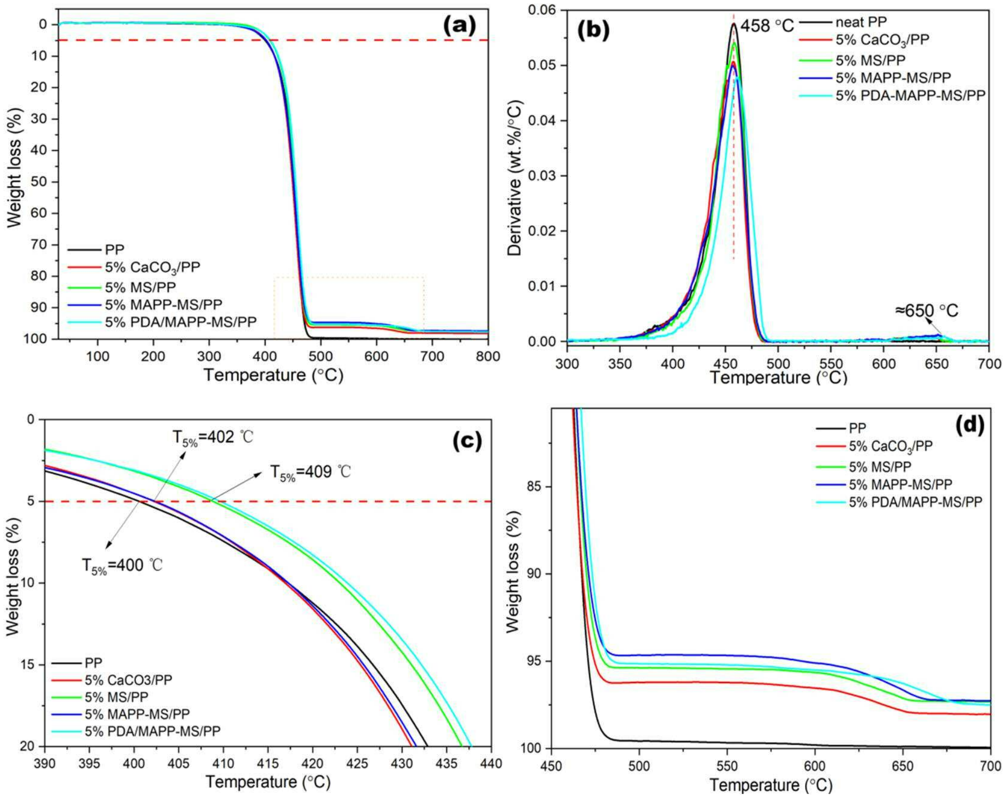

Figure 5- 1: (a) TGA, (b) DTG , and (c), (d) Enlargement of TGA curves of neat PP, PP composites incorporated with 5% different inorganic fillers.

5.2.1 Effect of 5 % different inorganic fillers

In Chapter 4, the Thermogravimetric (TG) and Differential Thermogravimetric (DTG) curves of mussel shell revealed that this rigid filler exhibits a high maximum decomposition temperature of approximately 760°C. This characteristic suggests that incorporating mussel shell filler into a polypropylene (PP) matrix has the potential to enhance the thermal stability of the resulting composite material.

TG and DTG analyses offer valuable insights into the thermal stability and degradation behaviour of neat PP and its composites. These analytical techniques provide crucial information about the material's response to thermal stress and can be utilised to determine the inorganic filler content from the residual percentage after thermal decomposition.

The influence of various mussel shell fillers on the thermal properties of polypropylene (PP) composites was initially investigated at a low filler loading level (5 %). Figure 5-1 presents the TG and DTG curves for neat PP and PP composites containing 5 % of different fillers, including untreated mussel shells, MAPP-modified mussel shells, and commercial calcium carbonate (CC).

Figures 5-1a and 5-1b demonstrate that neat PP undergoes a single-step thermal degradation process in an inert argon atmosphere. Specifically, the degradation of neat PP commences at approximately 340 °C and concludes at around 490 °C, with the maximum degradation occurring at 458 °C. At 660 °C, neat PP exhibits a weight loss of approximately 99.9%, leaving negligible ash content. This behaviour is consistent with the aliphatic hydrocarbon structure of PP, which is prone to rapid combustion and typically leaves no ash residues after pyrolysis [1]. These findings are consistent with previously reported literature [2].

In contrast, PP composites incorporating 5 % of various fillers exhibit a two-step degradation behaviour. The first degradation stage closely resembles that of neat PP, with the maximum degradation occurring at approximately 458°C. This similarity indicates that the predominant PP matrix governs the initial pyrolysis behaviour. A secondary mass loss stage, commencing at around 600 °C and concluding near 675 °C, is observed and can be attributed to the decarbonation reaction of calcium carbonate ($CaCO_3$) present in all three fillers.

The 5% weight loss temperature ($T_{5\%}$) serves as a crucial indicator of polymer thermal degradation [3]. Figure 5-1c shows that $T_{5\%}$ is 400 °C for neat PP, 402 °C for PP composites with 5% commercial calcium carbonate or MAPP-modified mussel shell fillers, and 409 °C for PP composites with 5% untreated or 5% PDA/MAPP-modified mussel shell fillers, respectively. It is noteworthy that the typical processing temperature range for polypropylene spans from 160°C to 185°C. The observed $T_{5\%}$ results confirm that both neat PP and its composites containing various mussel shell fillers maintain thermal stability well above the processing temperature range.

Furthermore, the maximum weight loss for PP composites incorporated with 5% fillers-whether commercial $CaCO_3$, untreated mussel shell, or MAPP-modified mussel shell—occurs at around 650 °C. This indicates that the influence of these three inorganic fillers on the thermal degradation behaviour of PP is negligible at a 5% loading level. However, the temperature of maximum weight loss for 5% PDA/MAPP-MS/PP shifts to 675 °C. This suggests a slightly improvement on the thermal stability of PP composite by adding PDA/MAPP-MS fillers.

As discussed in Chapter 4, a comparison of the surface properties of unmodified and modified mussel shells reveals that PDA and MAPP co-modification provides the most enhanced filler-matrix compatibility and improved filler dispersion. This enhancement in interfacial properties may contribute to the observed increase in thermal stability.

Inorganic fillers can absorb external thermal energy and restrict polymer chain mobility, thereby enhancing the thermal stability of the resulting polymer composite. The slight enhancement in thermal stability observed with PDA/MAPP-MS fillers is likely due to these effects. The co-modification with PDA/MAPP improves filler–matrix compatibility and dispersion, enabling more effective heat absorption and greater restriction of polymer chain movement. These findings agree with previously published studies[4; 5].

Unlike neat PP, the slightly higher residue content (approximately 2–3%) at 660 °C in these PP composites can be attributed to the residual CaO formed from the thermal decomposition of the mussel shell filler. This result matches with the known thermal degradation behaviour of mussel shells. The presence of residual CaO not only confirms successful filler incorporation but also provides insights into the composites' high-temperature behaviour, including potential thermal barrier effects and considerations for material reprocessing.

It is worth noting that the relatively small improvement in thermal stability at this low filler loading (5 %) suggests that higher filler concentrations or further optimisation of the modification process may be necessary to achieve more significant enhancements in thermal properties.

Having established the baseline thermal behaviour of PP composites with 5 % filler content, it is crucial to investigate the effects of varying filler types and concentrations on the thermal properties of PP composites. This comprehensive analysis will provide deeper insights into the thermal stability and degradation mechanisms of PP/mussel shell composites.

5.2.2 Effect of loading levels and different modified mussel shell fillers

Having established the baseline thermal behaviour of PP composites with 5 % filler content, it is evident that only PDA/MAPP-MS significantly impacts the thermal degradation behaviour of the PP matrix at this loading level. However, as filler content increases, interactions between filler particles and the filler-matrix interface become more pronounced, potentially altering the composite's thermal properties.

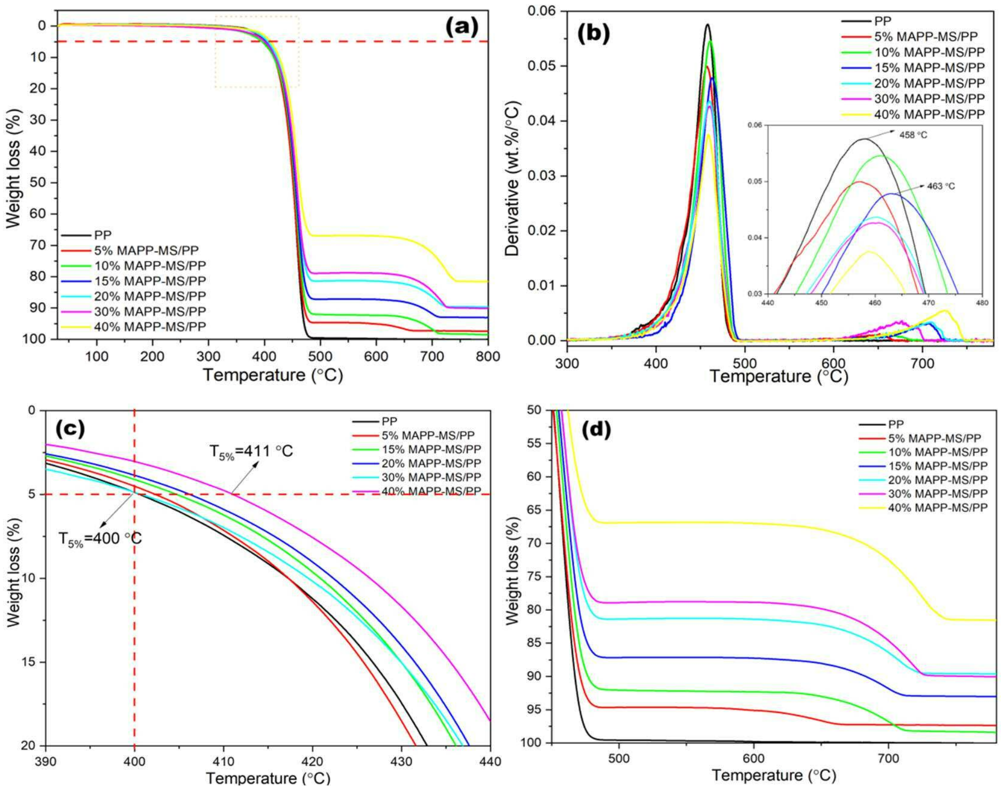

Figure 5- 2:(a) TGA, (b) DTG , and (c), (d) Enlargement of TGA curves of neat PP, PP composites incorporated with 5-40 % MAPP-MS fillers.

To gain deeper insights into the thermal stability and degradation mechanisms of PP/mussel shell composites, it is crucial to investigate the effects of varying filler types and concentrations. This is particularly important for surface-modified fillers such as MAPP-MS or PDA/MAPP-MS, which are designed to enhance filler dispersion and interfacial bonding in the polymer matrix, as discussed in Chapter 4.

Several studies have demonstrated that MAPP modification can enhance the thermal stability of polymer composites. In PP composites with MAPP-modified sisal fibres (SF), the degradation temperature at around 400°C was approximately 10°C higher than in composites with unmodified SFs [6]. This improvement was attributed to the cross-linking effect of MAPP between the PP matrix and SFs, or to molecular chain extension of the matrix itself, both leading to increased molecular weight. Similarly, MAPP-modified Alfa fibre composites exhibited slightly higher thermal stability compared to untreated or acetylation-modified counterparts, owing to enhanced compatibility and adhesion between the fibres and PP matrix [7]. The molecular weight of MAPP also influences thermal stability, as evidenced in wood flour-filled PP composites. Composites treated with higher molecular weight MAPP (Bondyram 1004, MW = 66,000; Polybond 3200, MW = 42,000) showed slightly lower weight loss compared to those treated with lower molecular weight MAPP (E-43, MW = 9,100), indicating that higher molecular weight MAPP contributes to greater thermal stability [8]. These findings collectively suggest that MAPP modification can be an effective strategy for improving the thermal stability of PP composites, with the extent of improvement dependent on factors such as fibre type, MAPP molecular weight, and the resulting interfacial interactions.

In this study, the thermal behaviour of PP composites filled with MAPP-modified mussel shell (MAPP-MS) fillers was investigated as the filler loading level increased from 5 to 40 %, as illustrated in Figure 5-2 (a)-(d). The results clearly demonstrate that PP composites with varying levels of MAPP-MS fillers undergo a two-stage thermal degradation process, as evidenced by the TG figures and corroborated by the DTG curves. At a 5% filler loading, the incorporation of commercial calcium carbonate, unmodified mussel shell, or MAPP-modified mussel shell resulted in negligible differences in thermal degradation behaviour compared to neat PP. However, as the MAPP-MS filler content increased from 10 to 40%, a modest enhancement in the thermal stability of the polymer matrix was observed. This improvement is manifested by an increase in the maximum degradation temperature.

For neat PP, the maximum degradation peak happens at 458°C. In contrast, PP composites containing 10-40% MAPP-modified mussel shell fillers exhibit an increase of approximately 2-5°C for the maximum degradation peaks. Notably, the highest maximum degradation peak at 463°C was observed in the PP composite with 15% MAPP-MS fillers, as depicted in the DTG curves in Figure 5-2(b). This observed enhancement in thermal stability with increasing MAPP-MS filler content is consistent with previous studies on MAPP-modified composites.

As the MAPP-MS filler loading increases, the 5% weight loss temperature ($T_{5\%}$) of PP composites shifts to higher temperatures, as illustrated in Figure 5-2(c). Whilst neat PP exhibits a $T_{5\%}$ of 400°C, this value increases to 411°C for PP composites containing 40% MAPP-MS fillers, indicating enhanced thermal stability. This behaviour matches with observations in graphene nanoplatelet- PP composites, where improved thermal degradation resistance was attributed to the fillers' ability to hinder oxygen diffusion and volatile product release [9].

Further evidence of enhanced thermal stability is provided by Figure 5-2(d), which shows that PP composites with 10-40% MAPP-modified mussel shell fillers experience maximum weight loss at temperatures exceeding 700 °C. This shift in the maximum weight loss temperature corroborates the overall improvement in thermal stability.

The enhanced thermal properties can be linked to the improved dispersion and compatibility of MAPP-MS fillers within the PP matrix, as discussed in the previous chapter. XPS analysis and thermodynamic calculations confirmed the increased hydrophobicity and reduced agglomeration tendency of mussel shell fillers following MAPP surface modification. Well dispersed mussel shell fillers with higher thermal stability act as physical barrier for heat diffusion, thereby contributing to the overall thermal stability of the PP composites.

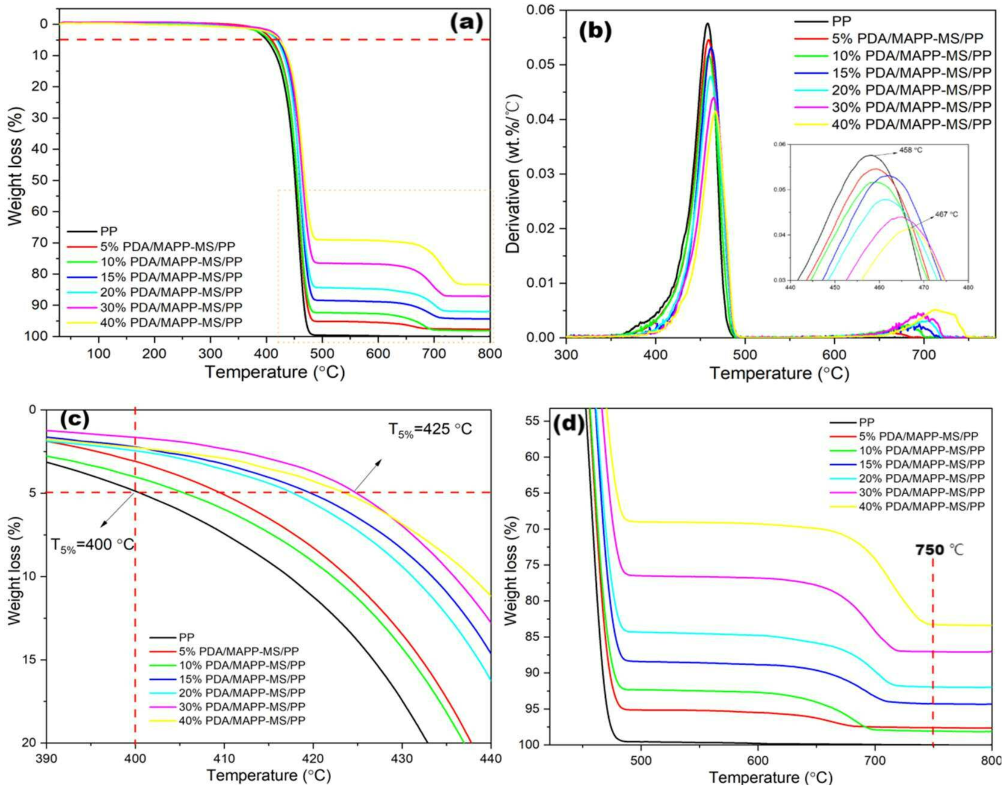

Figure 5- 3: (a) TGA, (b) DTG, and (c) (d) Enlargement of TGA curves of neat PP, PP composites incorporated with 5-40 % PDA/MAPP-MS fillers.

Moreover, the residue content exhibited a proportional increase with the amount of mussel shell filler added, ranging from 5-20 %. This observation is consistent with the presence of residual CaO resulting from the thermal decomposition of the calcium carbonate in the mussel shell fillers.

These findings collectively demonstrate that MAPP-modified mussel shell fillers effectively enhance the thermal stability of PP composites. The improvements in $T_{5\%}$, increased temperature of maximum degradation peak, and overall thermal resistance can be attributed to the synergistic effects of improved filler dispersion, enhanced filler-matrix compatibility, and the inherent thermal properties of the mussel shell fillers.

The thermal behaviour of PP composites containing varying amounts of PDA/MAPP co-modified mussel shell fillers (5–40 %) was investigated, with the TGA and DTG results presented in Figure 5-3(a–d).

PP composites with PDA/MAPP co-modified fillers exhibit thermal behaviour similar to those with MAPP-MS fillers across various loading levels. As the temperature increased from 30 to 800°C, a two-stage thermal degradation process was observed in both TGA and DTG curves (Figure 5-3 a-b). With increasing filler content from 5% to 40%, the maximum degradation temperature of PP composites increased by 2-9°C (maximum 467°C) compared to neat PP (458°C).

Figure 5-3(c) demonstrates higher $T_{5\%}$ values achieved with higher filler loading levels. Notably, the $T_{5\%}$ of PP composite filled with 30% PDA/MAPP-MS reached 425 °C, a significant 25°C increase compared to neat PP. The maximum weight loss temperature of PP composites shifted to a higher range (700-750°C), indicating further enhanced thermal stability for PP composites filled with PDA/MAPP-MS fillers.

As discussed in Chapter 4.2.8, calculated surface energies suggest that PDA/MAPP-MS fillers have values closer to PP than MAPP-MS fillers, indicating relative better compatibility with the polymer matrix. Additionally, the potential energy difference (ΔWa) reveals that PDA and MAPP co-modified mussel shell fillers have a lower tendency for re-agglomeration compared to MAPP-modified fillers, promoting better dispersion within the PP matrix. These factors contribute to the further improved thermal stability observed in PP composites incorporating various levels of PDA/MAPP-MS fillers.

5.3 The influence of different fillers on the crystalline structure of PP composites -XRD analysis

As discussed in Chapter 2, polypropylene (PP) exhibits significant complexity in its crystalline structure, manifesting three primary crystalline forms: α-monoclinic, β-trigonal, and γ-orthorhombic [10]. This polymorphism has attracted considerable research interest due to the distinct mechanical properties associated with each crystalline form.

The addition of fillers to the PP matrix can modify the polymer's crystallisation rate and alter its crystal structure by influencing polymer chain orientation or acting as nucleating agents [3; 11]. To directly investigate these effects, X-ray diffraction (XRD) analysis was conducted on injection-moulded samples of neat PP and PP composites containing various types and amounts of mussel shell fillers.

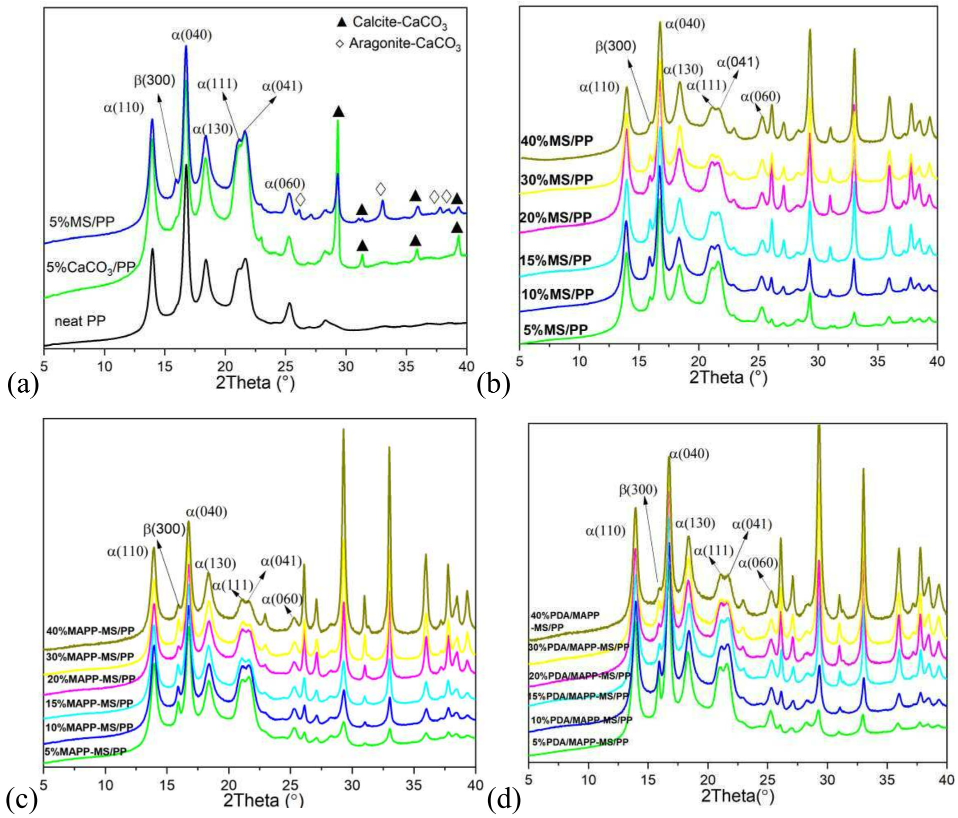

Figure 5- 4:X-ray diffractograms of (a) neat PP, 5%CC/PP, and 5% MS/PP; PP composites incorporated with different amounts of (b) untreated mussel shell fillers; (c) MAPP-MS fillers (d) PDA/MAPP-MS fillers.

Figure 5-4(a-d) presents the X-ray diffractograms of neat PP and PP composites with varying types and contents of mussel shell fillers. To facilitate comparison, the diffractograms were normalized to the intensity of the strongest α (040) peak.

The X-ray diffractograms (10-40 °) of neat PP and PP composites with 5% commercial calcium carbonate (CC) and mussel shell (MS) are shown in Figure 5-4 (a). Five characteristic diffraction peaks representing the α-crystalline form of PP are clearly identified in both neat PP and its composites with 5% CC or MS fillers, corresponding to

2θ values of 13.9º (110), 16.7º (040), 18.4º (130), 21.1º (111), 21.9º (041) and 25.3º (060) [3; 12]. Notably, a low-intensity peak indicating the β-crystal form of PP is detected at 2θ value of 15.9° (300) for 5% MS/PP composites. This observation confirms the coexistence of both α and β crystalline forms in 5% MS/PP, whilst only the α-crystalline form is present in neat PP and 5% CC/PP after injection moulding. These findings are in accordance with previous research by Kotek *et al.*, who reported that although pure β-PP cannot be produced by injection moulding, the presence of certain inorganic fillers, such as stearate-modified calcium carbonate, can influence the crystal phase of PP by acting as specific β-nucleants [13].

As illustrated in Figure 5-4(a), X-ray diffraction analysis reveals distinct peaks associated with calcite in PP composites containing 5% commercial calcium carbonate (CC), whilst both calcite and aragonite phases are detected in composites with 5% mussel shell (MS). These findings confirm the successful incorporation of both fillers and are consistent with the previously discussed crystal compositions of these inorganic materials (Chapter 4).

As illustrated in Figure 5-4(b-d), the XRD patterns of PP composites containing varying amounts of mussel shell fillers—whether untreated, MAPP-modified, or PDA-MAPP co-modified—exhibit similarities to those of PP composites filled with 5% mussel shell (MS). These diffractograms reveal reflection peaks indicative of the coexistence of α and β crystalline forms. However, the relative intensities of the characteristic peaks show subtle variations depending on filler type and loading level, necessitating further investigation into their impact on the crystal structure and composition of these PP composites.

To facilitate a more detailed analysis, peaks corresponding to α (110), α (040), α (130), and β (300) were selected. Figure 5-5(a-d) illustrates the peak heights and relative intensities of these four peaks for different samples, with the data summarised in Table 5-1.

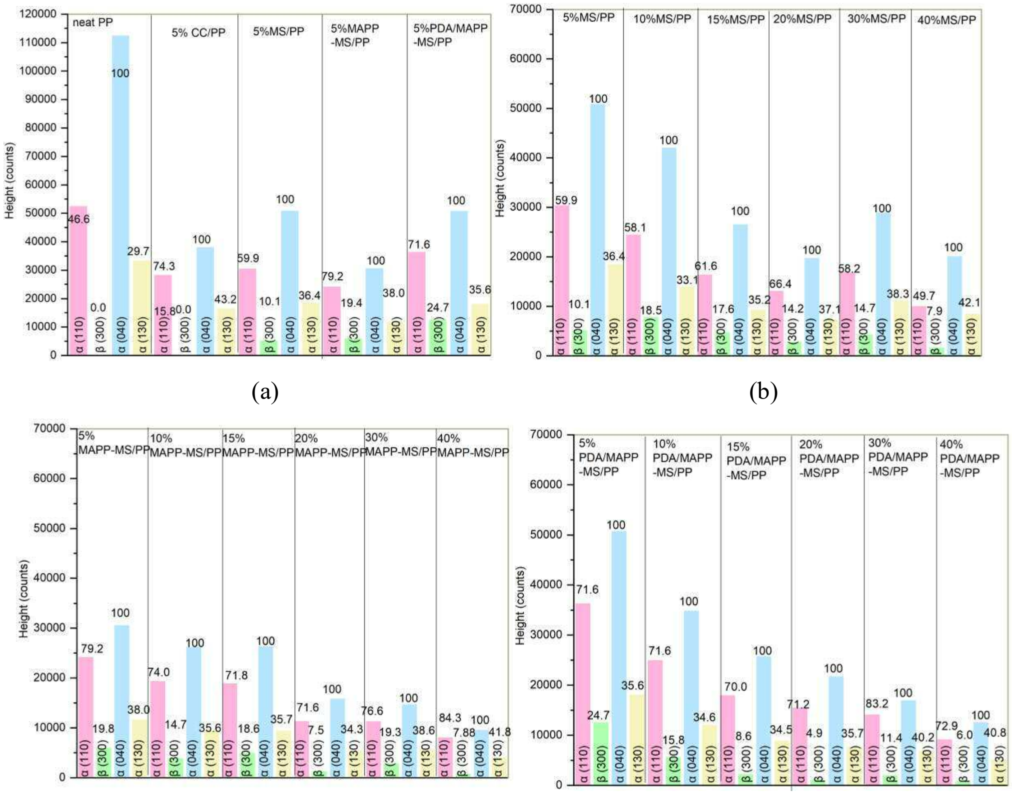

(a) (b)

(c) (d)

Figure 5- 5:Relative peak intensities from X-ray diffractograms of (a) neat PP and PP composites with 5% different fillers; PP composites incorporated with different amount of (b) untreated mussel shell fillers; (c) MAPP-MS fillers (d) PDA/MAPP-MS fillers.

Compared to pure PP, a significant reduction in peak intensities is observed across all PP composites. The heights of the three characteristic peaks for neat PP – α (110), α (040), and α (130)- are 52,436.9, 112,511.9, and 33,355.9 counts, respectively. Upon incorporation of 5% MS, these values decrease markedly to 30,406.67, 50,786.67 and

Table 5- 1:The intensity values of peaks reflecting different phase plane.

	Crystal Plane	Height (counts)	Rel. Int. (%)		Height (counts)	Rel. Int. (%)		Height (counts)	Rel. Int. (%)
neat PP	α (110)	52436.9	46.61	5%CaCO$_3$/PP	28266.88	74.33			
	β (300)	**0**	**0.00**		**0**	**0.00**			
	α (040)	112511.9	100		38026.88	100			
	α (130)	33355.9	29.65		16423.88	43.19			
5%MS/PP	α (110)	30406.67	59.87	5%MAPP-MS/PP	24206.61	79.23	5%PDA/ MAPP-MS/PP	36299.05	71.59
	β (300)	**5145.67**	**10.13**		**5920.61**	**19.38**		**12547.05**	**24.74**
	α (040)	50786.67	100		30552.61	100		50707.05	100
	α (130)	18493.67	36.41		11621.61	38.04		18063.05	35.62
10%MS/PP	α (110)	24442.11	58.14	10%MAPP-MS/PP	19365.2	73.95	10%PDA/MAPP-MS/PP	24945.72	71.59
	β (300)	**7790.11**	**18.53**		**3846.2**	**14.69**		**5507.72**	**15.81**
	α (040)	42039.11	100		26187.2	100		34843.72	100
	α (130)	13916.11	33.1		9335.2	35.65		12066.72	34.63
15%MS/PP	α (110)	16338.33	61.61	15%MAPP-MS/PP	18889.77	71.79	15%PDA/MAPP-MS/PP	17960.71	69.94
	β (300)	**4680.33**	**17.65**		**4903.77**	**18.64**		**2215.71**	**8.63**
	α (040)	26518.33	100		26311.77	100		25679.71	100
	α (130)	9343.33	35.23		9390.77	35.69		8876.71	34.57
20%MS/PP	α (110)	13103.37	66.45	20%MAPP-MS/PP	11323.03	71.63	20%PDA/MAPP-MS/PP	15464.46	71.22
	β (300)	**2791.37**	**14.16**		**1190.03**	**7.53**		**1062.46**	**4.89**
	α (040)	19719.37	100		15808.03	100		21713.46	100
	α (130)	7321.37	37.13		5427.03	34.33		7760.46	35.74
30%MS/PP	α (110)	16813.51	58.21	30%MAPP-MS/PP	11232.51	76.62	30%PDA/MAPP-MS/PP	14071.53	83.16
	β (300)	**4241.51**	**14.68**		**2823.51**	**19.26**		**1934.53**	**11.43**
	α (040)	28885.51	100		14659.51	100		16920.53	100
	α (130)	11068.51	38.32		5652.51	38.56		6799.53	40.19
40%MS/PP	α (110)	9978.19	49.72	40%MAPP-MS/PP	8026.07	84.27	40%PDA/MAPP-MS/PP	9136.75	72.86
	β (300)	**1589.19**	**7.92**		**750.07**	**7.88**		**751.75**	**5.99**
	α (040)	20069.19	100		9524.07	100		12539.75	100
	α (130)	8453.19	42.12		3980.07	41.79		5121.75	40.84

18,493.67, respectively. As filler content increases, peak intensities further diminish, irrespective of whether the mussel shell fillers are surface-modified or untreated. These reductions can be attributed to the smaller crystalline size of PP caused by the incorporation of mussel shell fillers, which likely act as nucleating agents. This influence of fillers on crystalline size agrees with observations from previous studies [3]. Another notable effect of fillers on the α-crystal structure of PP is associated with the α (110) plane. Whilst the α (040) peak remains the strongest among the three characteristic peaks (α (110), α (040), α (130)) for neat PP and PP composites with various types and amounts of mussel shell fillers, the relative intensities of the α (110) plane differ significantly. For neat PP, the peak height of α (110) is only 46.6% of α (040). However, with the addition of 5% untreated mussel shell, MAPP-MS, or PDA/MAPP-MS, the relative peak intensity of α (110) ($H_{\alpha110}$) increases to 59.9%, 79.2%, and 71.6%, respectively. The increase in the peak intensity of α (110) provides evidence for the formation of a cross-hatched structure in PP. This structural change is particularly significant, as the cross-hatched structure has been reported to increase the resistance of fibrils inside crazes, thereby enhancing the impact strength of PP composites [11].

With the increasing incorporation of different mussel shell fillers, the relative peak intensity of the α (110) plane changed accordingly. For PP composites with untreated mussel shell fillers, $H_{\alpha(110)}$ ranged from 49.7% to 66.4%. In comparison, PP composites with 5-40% PDA/MAPP-modified mussel shells exhibited $H_{\alpha(110)}$ values between 70.2% and 83.2%, while those with MAPP-modified mussel shells had slightly higher $H_{\alpha(110)}$ values, ranging from 71.6% to 84.3%. These results suggest that MAPP-MS is the most favourable filler among the three types for promoting the formation of the cross-hatched structure in PP.

Notably, the characteristic β-PP peaks in PP composites incorporating various types and amounts of mussel shell fillers are more intense compared to neat PP and PP composites with 5% commercial calcium carbonate (CC). The relative intensity of these β-PP peaks ranges from 7% to 25% of the strongest α (040) peak, providing further confirmation of the coexistence of α and β-PP in these composites after injection moulding. The ability of mussel shell fillers, especially when surface-modified, to simultaneously promote the formation of β-crystals and enhance the cross-hatched α-crystal structure suggests potential synergistic effects on the mechanical properties of the resulting composites.

5.4 The influence of different fillers on the melting and crystallisation behaviour of PP composites - Differential scanning calorimetry (DSC) analysis

Differential Scanning Calorimetry (DSC) is a valuable tool for observing phase transitions in polymers, including glass transition, melting, and cold crystallisation. As a typical semi-crystalline polymer, polypropylene (PP) can be described using a two-phase model: amorphous and crystalline phases. The incorporation of fillers, typically immiscible with the polymer and distributed within the amorphous fraction, increases the interfacial phase, especially when the surface area of the filler is increased. The behaviour of polymer chains at the interface differs from that in the bulk polymer phase, significantly affecting the formation of the crystalline structure.

It is noteworthy that the second melting curves were used in the DSC analysis. According to the DSC temperature program in Chapter 3, second melting curve better represents the melting behaviour of the specimens - their thermal history was removed at the first heating cycle then recrystallised under controlled cooling conditions. The findings on the crystalline structure do not necessarily correspond to the results obtained from XRD, which were based on samples produced through injection moulding.

The influence of mussel shell filler types and loading levels on the thermal behaviour, particularly melting and re-crystallisation, of the PP composites was investigated. The results are shown in Figure 5-6. The degree of crystallinity (X%, with subscripts α and β representing different crystalline phases of PP) was calculated from the melting enthalpy values using the following equation:

$$X\% = 100 \times \frac{\Delta Hm}{w\% \times \Delta H\alpha / \beta} \qquad \text{Equation1}$$

where H_m is the melting enthalpy of the specimens (J/g); $\triangle H_\alpha$ (177 J/g) and $\triangle H_\beta$ (168.5 J/g) are the enthalpy values for α- and β-PP, respectively [12]; and w% is the weight fraction of polymer in PP composites.

The thermal data obtained from the DSC curves are presented in Table 5-2. The DSC thermogram of neat PP showed a typical endothermic melting peak at 165 ℃ and an exothermic crystallisation peak at 121.5 ℃. This indicates that the dominant crystal form in neat PP is the α-phase, as the melting peak around 165 °C corresponds to the melting point of α-crystals. The crystalline structure of neat PP supports the results from XRD, suggesting that recrystallisation does not change the crystal phases of neat PP.

Table 5- 2: Melting and cooling behaviour of PP and PP composites.

Samples	**Melting behaviour**								**Cooling behaviour**	
	α crystal phase			**β crystal phase**			***Total Crystallinity***			
	$T_{\alpha\text{-peak}}$ (°C)	$\triangle H_m^{\alpha}$ (J/g)	X_α (%)	$T_{\beta\text{-peak}}$ (°C)	$\triangle H_m^{\beta}$ (J/g)	X_β (%)	$X_\alpha + X_\beta$ (%)	K_β (%)	T_c (°C)	$\triangle H_c$ (J/g)
neat-PP	165.0	83.83	47.36	-	-	-	47.36	-	121.5	-86.71
5 % CaCO₃/PP	165.0	76.40	45.44	-	-	-	45.44	-	118.9	-82.47
5 % MS/PP	165.1	80.24	47.72	-	-	-	**47.72**	-	120.6	-82.26
10 % MS/PP	165.0	68.71	34.93	150.9	7.06	4.65	39.59	11.8	121.0	-78.17
15 % MS/PP	165.4	63.62	30.55	151.3	6.06	4.23	34.78	12.2	120.9	-72.05
20 % MS/PP	164.8	66.80	30.19	151.2	2.34	1.74	31.93	5.4	122.3	-71.40
30%MS/PP	164.9	55.80	45.04	-	-	-	45.04	-	115.6	-64.50
40%MS/PP	164.7	53.50	50.38	-	-	-	**50.38**	-	115.8	-61.86
5 % MAPP-MS/PP	164.2	73.46	45.11	150.1	6.34	4.09	**49.20**	8.3	118.8	-79.68
10 % MAPP-MS/PP	163.7	65.42	42.49	149.9	7.39	5.04	**47.52**	10.6	120.2	-74.01
15 % MAPP-MS/PP	164.9	55.42	38.18	151.2	14.13	10.23	**48.41**	21.1	121.2	-69.76
20 % MAPP-MS/PP	165.4	59.01	43.30	151.0	8.68	6.69	**49.99**	13.4	117.8	-68.17
30% MAPP-MS/PP	164.0	59.72	**50.36**	-	-	-	**50.36**	-	119.6	-60.94
40% MAPP-MS/PP	164.6	53.86	**53.38**	-	-	-	**53.38**	-	119.2	-57.35
5% PDA/MAPP-MS/PP	165.0	73.64	45.22	151.0	6.51	4.20	**49.42**	8.5	120.4	-80.78
10%PDA/MAPP-MS/PP	165.4	73.77	47.91	151.4	3.16	2.15	**50.06**	4.3	121.5	-77.91
15%PDA/MAPP-MS/PP	165.1	70.34	48.46	151.4	2.25	1.63	**50.09**	3.2	122.0	-73.10
20%PDA/MAPP-MS/PP	165.6	67.09	49.22	151.9	1.35	1.04	**50.27**	2.1	122.3	-66.45
30%PDA/MAPP-MS/PP	165.5	56.16	**47.36**	-	-	-	**47.36**	-	123.1	-65.28
40%PDA/MAPP-MS/PP	165.3	51.12	**50.67**	-	-	-	**50.67**	-	124.8	-57.18

Notes: $T_{\alpha\text{-peak}}$ and $T_{\beta\text{-peak}}$ are denoted as the melting peak of α-PP and β-PP, respectively; T_c is denoted as the cooling peak of specimens; $\triangle H_m^{\alpha}$ and $\triangle H_m^{\beta}$ are denoted as the melt enthalpy of α-PP and β-PP in specimens, respectively; $\triangle H_c$ is denoted as the cooling enthalpy of specimens; X_α and X_β are denoted as the crystallinity of α-PP and β-PP, respectively; K_β is denoted as the β crystal phase percentage in the total crystal phase.

When 5 % CC or MS was added to PP, the melting peaks remained around 165 °C, indicating that the dominant crystal form in these PP composites did not change significantly, and the fillers did not alter the crystal structure. The crystallinity of the 5% CC/PP composite slightly decreased from 47.36% in neat PP to 45.44%, while the crystallinity of the 5 % MS/PP composite remained relatively unchanged at 47.72%.

These results suggest that at a 5% loading level, neither CC nor MS acts as a nucleating agent for crystallisation, meaning the lamellar size and crystal growth of polypropylene were unaffected. Instead, the reduction in crystallinity suggests an inhibitory effect on the

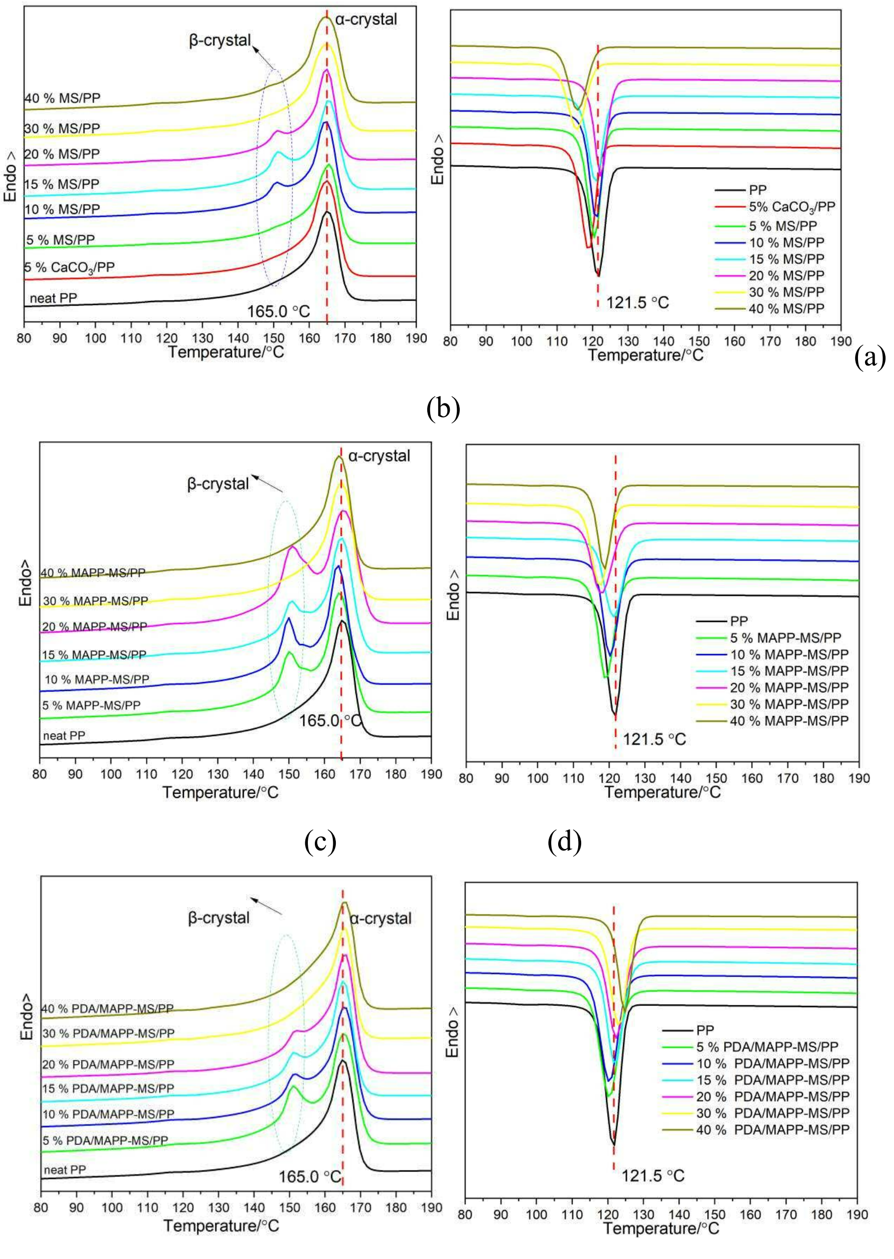

(a)

(b)

(c) (d)

(e) (f)

Figure 5- 6:DSC thermograms: (a) melting curves of neat PP, 5%CC/PP, and 5-40% MS/PP; (b) cooling curves of neat PP, 5%CC/PP, and 5-40% MS/PP; (c) melting curves of neat PP and 5-40%MAPP-MS/PP; (d) cooling curves of neat PP and 5-40%MAPP-MS/PP;(e) melting curves of neat PP and 5-40%PDA/MAPP-MS /PP;(f) cooling curves of neat PP and 5-40%PDA/MAPP-MS /PP.

crystallisation of PP when CC is added at 5% loading. This finding is consistent with previous reports in the literature [14].

The multiple-melting behaviour of polymers can be attributed to factors such as polymorphism, varying degrees of crystal perfection, and crystallisation phenomena during heating [12]. PP composites containing 5% MAPP-MS or 5% PDA/MAPP-MS exhibited two distinct melting peaks: one at approximately 165 °C, corresponding to the melting of α-PP, and another at around 151 °C, associated with β-PP. This indicates that both types of mussel shell fillers, at a 5% loading level, promote the formation of β-PP. The crystallinity of these composites increased slightly compared to neat PP, reaching 49.20% for MAPP-MS/PP and 49.42% for PDA/MAPP-MS/PP. This enhancement in crystallinity is likely due to improved dispersion and interfacial adhesion of the modified fillers within the PP matrix, as discussed in Chapter 4, which facilitates PP crystallisation.

Figure 5-6(a) reveals a notable difference in the melting behaviour of polypropylene (PP) composites with higher mussel shell filler content compared to 5%MS/PP. As the loading level of untreated mussel shell fillers increases to 10-20%, two distinct melting peaks emerge for the filled composites. The α-crystal melting peak remains dominant, whilst a secondary peak corresponding to β-crystal polypropylene (PP) becomes apparent. This observation indicates that higher concentrations of mussel shell fillers can significantly influence the recrystallisation process and promote the formation of β-crystal PP.

The emergence of β-crystal PP at higher filler loading is particularly noteworthy, as the β-form is known to impart enhanced impact strength and toughness to PP materials. The percentage of β-crystal (K_β) among the total crystallinity ($X_\alpha + X_\beta$) for 10%MS/PP, 15%MS/PP, and 20%MS/PP are 11.8%, 12.2%, and 5.4%, respectively. These values suggest a non-linear relationship between filler content and β-crystal formation, with an optimal concentration around 15% for maximising β-crystal content.

As illustrated in Figure 5-6 (c) and (e), PP composites incorporating MAPP-modified mussel shell (MAPP-MS) and PDA/MAPP-modified mussel shell (PDA/MAPP-MS) at loading levels of 10-20% exhibit melting peaks associated with both α- and β-crystal forms of PP. This observation confirms the coexistence of both crystal forms within these composites, conforming with previous findings for untreated mussel shell fillers.

Interestingly, a consistent trend emerges across all types of mussel shell fillers-whether untreated or modified with MAPP or PDA/MAPP. As filler loading increases to 30% and 40%, a notable reduction in the β-PP melting peak is observed.

The observed phenomena can be attributed to several interrelated factors. Firstly, the lower thermodynamic stability of β-PP compared to α-PP plays a crucial role. As filler content increases, the system may preferentially form the more stable α-crystals to minimise the overall energy required for crystallisation. This tendency is likely exacerbated during the heating stage, where a phase transformation from metastable β-PP to stable α-PP may occur due to crystallisation [15].

Secondly, the increased amount of mussel shell fillers causes significant disruption in the amorphous phase of polypropylene (PP). This disruption likely creates an environment less conducive to β-PP formation, as the β-form typically requires specific conditions and molecular arrangements to nucleate and grow. The presence of high filler concentrations may interfere with these necessary conditions, further inhibiting β-crystal development. This hypothesis agrees with previous research findings and provides a plausible explanation for the reduction in β-PP melting peaks observed at higher filler loading. [16].

The macroscopic properties of polymer composites are largely dependent on the crystallinity of the polymer matrix. A comprehensive understanding of the crystallisation characteristics can serve as a guide for tailoring the mechanical properties of the composites. To this end, a comparison of crystallinity between neat polypropylene (PP) and PP composites was conducted based on DSC results.

Upon the addition of untreated mussel shell fillers at loading levels of 10%, 15%, and 20%, the total crystallinity ($X\alpha + X\beta$) of PP composites decreased by 16.41%, 26.56%, and 32.59%, respectively. This significant reduction in crystallinity compared to neat PP can be attributed to the hydrophilic nature of mussel shell particles, which leads to poor compatibility with the hydrophobic PP matrix. Consequently, at increased loading levels, these particles tend to agglomerate, disrupting the polymer matrix, inhibiting the mobility of polymer chains, and resulting in less crystal formation.

Interestingly, as the loading level of untreated mussel shell filler increased to 30%, a less pronounced decrease in crystallinity (4.91%) was observed. Furthermore, at a loading level of 40%, the crystallinity increased by 6.37%. This unexpected trend can be explained by the nucleation effect- at higher filler concentrations, there are sufficient untreated mussel shell particles to act as nucleating sites, overcoming the initial inhibitory effects associated with agglomeration. This phenomenon facilitates increased crystal formation [17].

PP composites incorporated with different amounts of MAPP-MS and PDA/MAPP-MS fillers generally exhibit crystallinity levels that are either comparable to or higher than neat PP. The crystallinity of these PP composites increased by approximately 3-7%, with a notable exception for 40% MAPP-MS/PP, which experienced a significant increase of 12.72%. These results suggest that both MAPP-MS and PDA/MAPP-MS fillers facilitate the crystallisation of PP.

Interestingly, MAPP-MS fillers appear to exhibit a better β-PP nucleating effect than PDA/MAPP-MS fillers, as evidenced by the K_β values. This difference in nucleating efficiency can be attributed to the varying surface characteristics of the modified mussel shell fillers.

It is also notable that the amount of MAPP-MS or PDA/MAPP-MS incorporated does not show a clear, consistent relationship with the crystallinity of the resulting PP composites. The influence of different mussel shell fillers on PP crystallisation can be understood by considering the complex interplay between filler surface properties and polymer chain dynamics. Although the complete mechanism of polymer crystallisation remains an active area of research, it is generally accepted that crystallisation occurs through the alignment and folding of polymer chains, with the degree of crystallinity largely determined by chain mobility and the availability of nucleating sites. Fillers typically act as heterogeneous nucleating agents, where higher filler contents provide more nucleation sites. However, because nucleation occurs at the filler surface, the strength of polymer − filler interactions significantly affect the process. Weakly attractive surfaces tend to promote nucleation, while stronger interactions can reduce the crystallisation rate by restricting chain mobility through surface adsorption [17]. As discussed in Section 5.1, MAPP-MS enhances interfacial bonding between the filler and matrix, and the addition of a PDA coating further strengthens this interaction. Given the complexity of crystallisation, the crystallinity of PP composites with increasing amounts of MAPP-MS or PDA/MAPP-MS is generally higher than that of neat PP, but no clear trend can be directly related to filler loading levels.

For all PP composites studied, the melting peak of α-PP ranged from 163.7 to 165.6 °C, compared with 165.0 °C for neat PP, representing a narrow variation of −1.3 to +0.6 °C. In contrast, the crystallisation peak temperature from cooling curves showed a much wider range, from 124.8 to 155.6 °C, compared with 121.5 °C for neat PP. This broader variation indicates that the fillers exert a more substantial influence on the crystallisation process than on melting behaviour. These results are consistent with previous reports, which suggest that filler content has a more pronounced effect on crystallisation behaviour than on melting characteristics [18].

Crystallisation of polymers is an exothermic process, and the latent energy provides valuable insights into the crystallisation behaviour of polymer composites.

An intriguing observation in the PP composites with different mussel shell fillers is that the absolute value of cooling enthalpy (ΔHc) of all PP composites was lower than that of neat PP. Moreover, ΔHc decreased with increasing filler loading in the PP composites. This trend suggests that less energy was required to facilitate crystallisation in PP composites containing higher amounts of mussel shell fillers, which is consistent with findings reported in previous literature [1]. The observed phenomenon can be attributed to several interrelated factors. Different types of mussel shell fillers likely serve as heterogeneous nucleation sites for PP crystallisation, lowering the energy barrier for crystal formation and thus requiring less energy overall. As filler content increases, the proportion of PP decreases, resulting in less polymer available for crystallisation and contributing to lower crystallisation enthalpy. Additionally, fillers may restrict polymer chain mobility, leading to smaller, less perfect crystals that require less energy to form compared to the larger crystals in neat PP. Furthermore, interactions between the mussel shell fillers and the PP matrix can influence local chain motion and packing, facilitating easier crystal formation at less energy input. Collectively, these effects explain the reduction in cooling enthalpy with increasing filler content in PP/mussel shell composites.

Building on our findings regarding thermal behaviour and crystalline structure, it is crucial to explore how these microscopic changes translate into macroscopic properties of PP/mussel shell composites. The observed variations in crystallinity, polymorphism, and thermal stability are expected to significantly influence mechanical performance. Of particular interest is understanding how different mussel shell types (untreated, MAPP-modified, and PDA/MAPP-modified) and their varying concentrations affect these properties.

The next section will focus on the mechanical characteristics of these composites, presenting results from tensile and flexural tests.

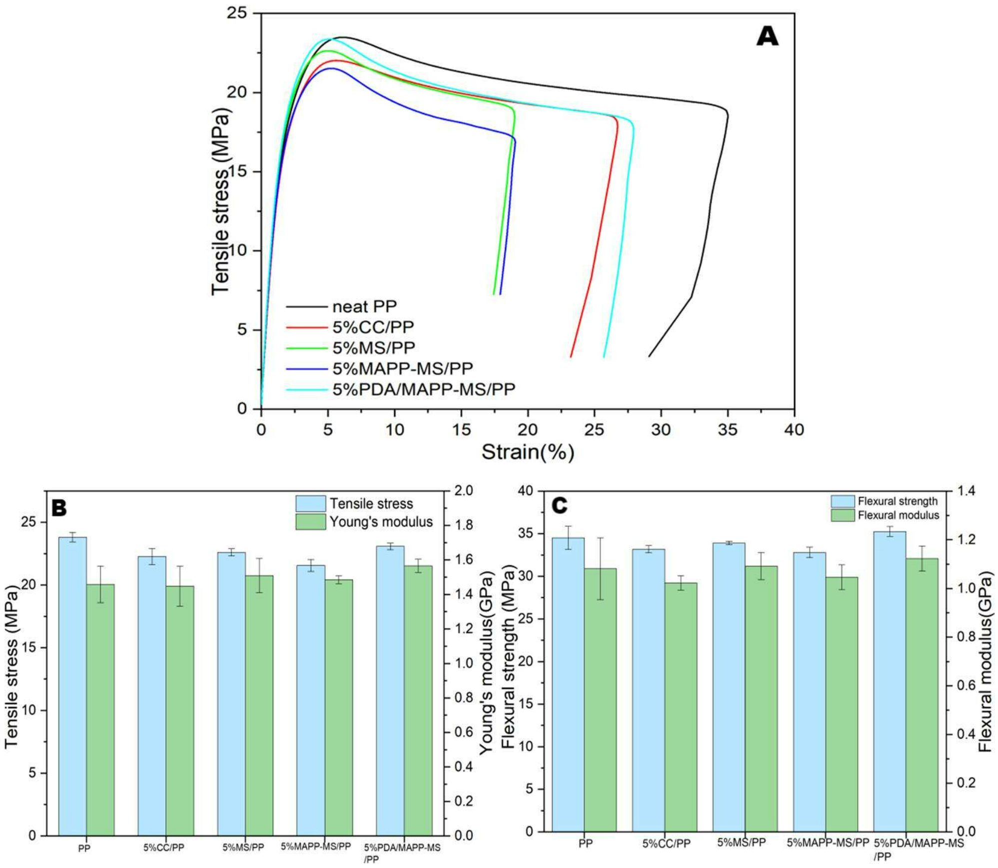

Figure 5- 7:(a) Stress-strain curves, (b) tensile behaviour, and (c) flexural behaviour of PP and PP composites with 5% different fillers.

5.5 The influence of different fillers on the mechanical properties of PP composites

5.5.1 Effect of 5% different fillers on the mechanical properties of PP composites

The influence of different fillers at 5% loading level on the mechanical properties of resultant PP composites was shown in Figure 5-7 and summarised in Table 5-3.

The tensile properties reflect both the characteristics of the polypropylene matrix and the influence of the filler. The stress-strain curves, as shown in Figure 5-7a, demonstrate that PP and PP composites with 5% various fillers exhibit similar behaviour, showing yield at maximum stress (necking) and post-yield drawing. This indicates that fracture energy is primarily consumed by matrix yielding, with negligible defects caused by the 5% filler loading [19].

Young's modulus, also known as the elastic modulus, quantifies a material's stiffness in the linear elastic region of a tensile test. It is defined as the ratio of stress to strain within this region, where the material exhibits reversible deformation [20]. From Figure 5-7 (b), the elastic moduli of the polymers can be found to follow the order: neat PP (1.46 GPa) ≈ 5%CC/PP (1.45 GPa) < 5%MAPP-MS/PP (1.48 GPa) < 5%MS/PP (1.51 GPa) < 5%PDA/MAPP-MS/PP (1.57 GPa, representing a 7.4% increase compared to neat PP). At a 5% filler loading level, the addition of rigid particles to the polymer matrix can improve the elastic modulus, as these hard particles possess higher stiffness values than the polymer matrix. Compared to commercial calcium carbonate, the introduction of 5% untreated mussel shell demonstrates an improvement in elastic modulus, suggesting better filler dispersion within the polymer matrix. This enhanced dispersion may be attributed to the co-existence of organic matter with inorganic calcium carbonate in mussel shells, as previously discussed in Chapter 4. The addition of PDA/MAPP co-modified mussel shell fillers results in PP composites with even more significant improvements in elastic modulus. This further enhancement can be ascribed to the superior filler dispersion achieved through surface modification. Notably, flexural moduli exhibit a similar trend across different fillers at the 5% loading level, corroborating the above observations.

Table 5-3 reveals, as anticipated, a higher variation in elongation at break values within each specimen. This variability stems from the challenge of reproducing terminal failure in polymer stress-strain curves, which is strongly dependent on flaw presence.

Table 5- 3:Mechanical properties of PP and PP composites with 5% different fillers.

Samples	**Tensile strength （MPa）**	**Young's modulus （GPa）**	**Elongation at break (%)**	**Flexural strength （MPa）**	**Flexural Modulus （GPa）**
PP	23.81±0.38	1.46±0.11	29.71±6.85	34.52±1.35	1.08±0.08
5%CC/PP	22.27±0.65	1.45±0.11	26.16 ±9.08	33.18±0.43	1.02±0.03
5%MS/PP	22.61±0.29	1.51±0.10	21.27±11.66	33.91±0.20	1.09±0.05
5%MAPP-MS/PP	21.56±0.48	1.48±0.02	27.43±9.20	32.80±0.61	1.05±0.05
5%PDA/MAPP-MS/PP	23.08±0.26	1.57±0.04	24.38±6.56	35.26±0.58	1.12±0.05

Considering the high data variability, the elongation at break values for neat PP and PP composites with 5% various fillers are comparable. Generally, elongation at break is closely related to the material's fracture behaviour and reflects structural flaws within the material [21]. The comparable values suggest that the addition of fillers at a 5% loading level does not significantly increase specimen defects.

However, tensile and flexural strengths decrease, as shown in Figures 5-7 (b) and (c). Table 5-3 indicates that neat PP has a tensile strength of 23.81 MPa and a flexural strength of 34.52 MPa. The tensile strengths of 5%CC/PP, 5%MS/PP, and 5%MAPP-MS/PP are 22.27, 22.61, and 21.56 MPa, respectively. Their flexural strengths are 33.18, 33.91, and 32.80 MPa, respectively. Their strength values are all lower compared to those of neat PP. Notably, 5%PDA/MAPP-MS/PP exhibits a tensile strength of 23.08 MPa, comparable to neat PP, and a flexural strength of 35.26 MPa, slightly higher than neat PP. Strength is sensitive to the filler-matrix interfacial interaction, as effective stress transfer between the matrix and particles is crucial for improving strength. The reduction in strength upon adding fillers indicates weak bonding between the matrix and fillers. In well-bonded composites, stress can be efficiently transferred to the particles, leading to enhanced strength. At 5% filler loading, the tensile strength results suggest insufficient bonding for commercial calcium carbonate, untreated mussel shell, and MAPP-modified mussel shell fillers with the PP matrix. In contrast, PDA/MAPP co-modification shows clear potential for enhancing interfacial interactions between mussel shell fillers and the PP matrix.

To fully elucidate the influence of surface modification of mussel shell fillers on PP composite's mechanical properties, further investigation with increased filler content is necessary.

5.5.2 Effect of different contents of untreated mussel shell fillers on the mechanical properties of PP composites

Figure 5-8(a) illustrates the stress-strain curves of PP composites as a function of untreated mussel shell filler content. In the initial stage (0-5% strain range) of these stress-strain curves, the slopes increase with higher filler content, indicating enhanced stiffness

Table 5- 4:Mechanical properties of PP and PP composites with different amounts of mussel shell fillers.

Samples	**Tensile strength （MPa）**	**Young's modulus （GPa）**	**Elongation at break (%)**	**Flexural strength （MPa）**	**Flexural Modulus （GPa）**
PP	23.81±0.38	1.46±0.11	29.71±6.85	34.52±1.35	1.08±0.08
5%MS/PP	22.61±0.29	1.51±0.10	21.27±11.66	33.91±0.20	1.09±0.05
10%MS/PP	21.86±0.44	1.62±0.12	20.47±8.06	33.52±1.02	1.16±0.06
15%MS/PP	21.36±0.57	1.82±0.10	17.97±8.75	33.30±1.01	1.20±0.08
20%MS/PP	21.16±0.17	1.98±0.11	12.85±4.35	33.61±0.78	1.28±0.09
30% MS/PP	21.72±0.29	2.02±0.05	12.24±2.97	32.99±0.31	1.27±0.03
40%MS/PP	20.14±0.24	2.18±0.18	9.48±3.44	32.82±0.18	1.38±0.12

(elastic modulus). Conversely, the yield strength (maximum stress observed at the peak of the stress-strain curve) of PP composites decreases with increasing untreated filler content. Furthermore, the tensile behaviour of these polymers is presented in Figure 5-8(b). The blue columns, representing tensile strength, demonstrate a decreasing trend, while the green columns, depicting Young's moduli, exhibit an opposite trend. These observations are corroborated by a detailed examination of the datasets in Table 5-4.

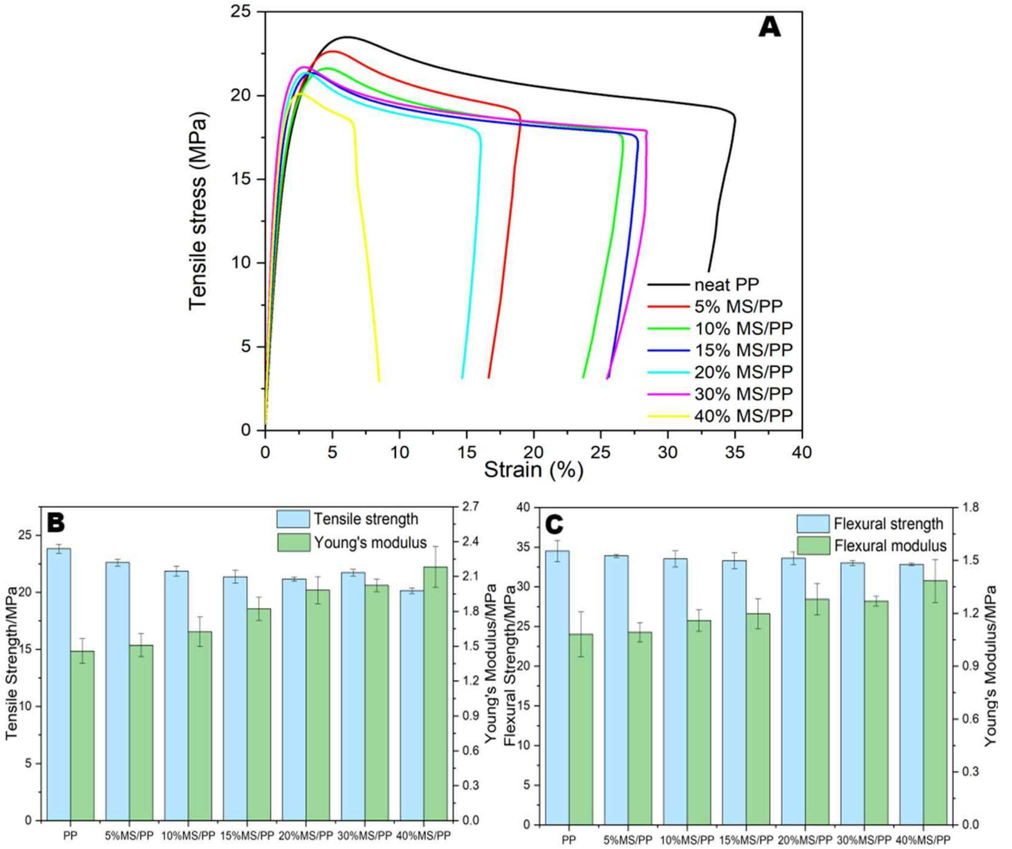

Figure 5- 8: (a) Stress-strain curves, (b) tensile behaviour, and (c) flexural behaviour of PP and PP composites with different amounts of untreated mussel shell fillers.

Tensile strength decreases continuously as the untreated mussel shell filler content increases from 5% to 40%. Notably, the tensile strength of 40% MS/PP is 20.14 MPa, representing a 15% decrease compared to neat PP (23.8 MPa). This detrimental trend in tensile strength with increasing untreated mussel shell filler content suggests filler-matrix debonding due to poor interfacial interaction between these components.

Conversely, elastic moduli increase monotonically with increasing untreated mussel shell filler content from 5% to 40%. With 40% untreated mussel shell filler, the elastic modulus of the composite reaches 2.18 GPa, a nearly 50% increase compared to neat PP. This suggests that the mobility and deformability of PP are reduced due to the inclusion of a large volume of mussel shell particles, significantly increasing the composite's stiffness. Similar increments in Young's moduli have been observed in other studies [1; 22; 23].

Moreover, the monotonic decrease in elongation at break with increasing untreated mussel shell filler content reveals increased defect creation, suggesting reduced ductility. This result further confirms the lack of sufficient interfacial interaction between the filler and PP matrix.

Flexural behaviour exhibits trends similar to tensile properties, albeit less pronounced as shown in Figure 5-8c. Flexural strength decreases gradually with increasing untreated mussel shell content from 5% to 40%, with 40% MS/PP showing a value of 32.82 MPa, a 5% decrease compared to neat PP. Flexural moduli increase continuously with 5-40% mussel shell incorporation into PP composites, with 40% MS/PP reaching 1.38 GPa, a 28% increase compared to neat PP.

5.5.3 Effect of different contents of MAPP modified mussel shell fillers on the mechanical properties of PP composites

Figure 5-9(a) illustrates the stress-strain curves of PP composites as a function of MAPP modified mussel shell filler content. Furthermore, tensile and flexural behaviour of these polymers were presented in Figure 5-9b and c, respectively. These observations are corroborated by a detailed examination of the datasets in Table 5-5.

Table 5- 5: Mechanical properties of PP and PP composites with different amounts of MAPP-MS fillers.

Samples	Tensile strength （MPa）	Young's modulus （GPa）	Elongation at break (%)	Flexural strength （MPa）	Flexural Modulus （GPa）
PP	23.81±0.38	1.46±0.11	29.71±6.85	34.52±1.35	1.08±0.08
5%MAPP-MS/PP	21.56±0.48	1.48±0.02	27.43±9.20	32.80±0.61	1.05±0.05
10%MAPP-MS/PP	21.93±0.23	1.58±0.03	19.58±8.79	32.43±0.48	1.11±0.05
15%MAPP-MS/PP	21.36±0.57	1.82±0.10	13.64±8.75	32.79±0.39	1.16±0.06
20%MAPP-MS/PP	21.95±0.27	1.80±0.06	10.19±1.84	33.78±0.57	1.23±0.04
30% MAPP-MS/PP	24.61±0.18	1.98±0.07	9.83±2.73	35.85±0.85	1.28±0.13
40%MAPP-MS/PP	24.47±0.09	2.24±0.04	6.45±1.26	38.2±0.45	1.52±0.10

Interestingly, the impact of MAPP-modified mussel shell filler on the stress-strain relationship of the resultant composites exhibits a different pattern to that of untreated

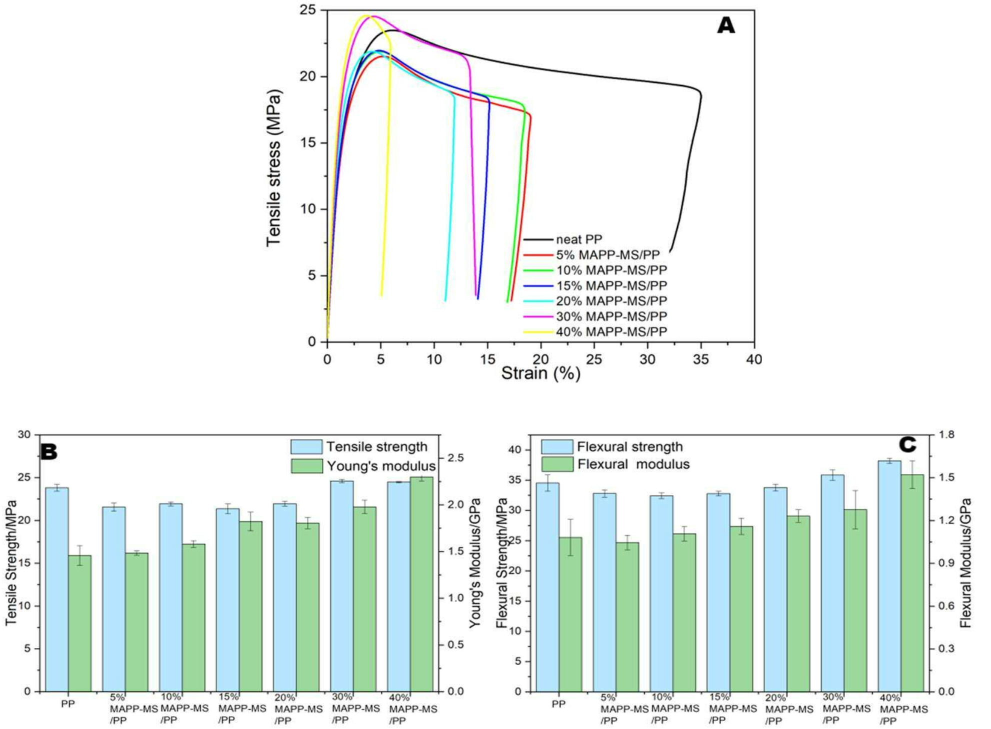

Figure 5- 9: (a) Stress-strain curves, (b) tensile behaviour, and (c) flexural behaviour of PP and PP composites with different amounts of MAPP modified mussel shell fillers.

mussel shell fillers: the yield strength decreases when 5-20% MAPP-MS fillers are incorporated into composites. However, further increasing the loading level of MAPP-MS to 30 or 40% results in PP composites yielding at higher stresses but at slightly smaller strains. As shown in Figure 5-9(b) and Table 5-5, the tensile strength of PP composites containing 5–20% MAPP-MS remained relatively constant, ranging from 21.36 to 21.95 MPa. These values are 7.8–10.2% lower than that of neat PP (23.81 MPa).In contrast, 30% and 40% MAPP-MS/PP composites exhibit higher tensile strengths of 24.61 and 24.47 MPa, respectively, representing increases of 3.3% and 3.5% compared to neat PP.

Compared to untreated mussel shell fillers, MAPP-MS fillers demonstrate a less detrimental effect on tensile strength, and even slightly increase it at higher loadings (30-40%). This can be attributed to the MAPP modification, which enhances both filler dispersion and filler-matrix interfacial bonding. These improvements facilitate more efficient stress transfer from the fillers to the matrix, consequently leading to improved tensile strength. Given the fixed MAPP to PP weight ratio of 3:97 in all MAPP-MS/PP composites, an optimal amount of mussel shell fillers is necessary to ensure sufficient surface modification. The increased surface area provided by a larger number of MAPP-modified fillers dispersed within the PP matrix allows for greater interaction with the matrix. Consequently, the enhanced effective stress transfer results in a slight improvement in tensile strength.

Young's moduli increase monotonically with increasing MAPP-MS filler content. At the maximum loading of 40% MAPP-MS/PP, the elastic modulus reaches 2.24 GPa, representing a 53.6% increase compared to neat PP. This value is slightly higher than that of 40% MS/PP, which can be attributed to further restricted polymer mobility due to enhanced filler-matrix interfacial bonding.

The elongation at break of these composites, as anticipated, decreases with increasing MAPP-MS filler loading levels. Despite MAPP surface modification, filler debonding within PP composites increases with increasing filler content, due to the difference in deformation rates between mussel shell fillers and the PP matrix. As the MAPP-MS filler content increases, defects and crazes become more prevalent and propagate more readily under stress, resulting in a progressive loss of ductility.

Flexural behaviour demonstrates trends similar to tensile properties, as illustrated in Figure 5-9c. Flexural strength initially decreases gradually with increasing MAPP-MS filler content from 5% to 20%. However, the flexural strength of 30% MAPP-MS/PP increases to 35.85 MPa. Furthermore, it reaches 38.20 MPa for 40% MAPP-MS/PP, representing a 10.7% increase compared to neat PP. Flexural moduli increase continuously with 5-40% MAPP-MS incorporation into PP composites. Notably, 40% MAPP-MS/PP exhibits a flexural modulus of 1.52 GPa, representing a 40.6% increase compared to neat PP. These enhanced flexural properties corroborate the hypothesis that an optimal MAPP-MS content enables the tailoring of mechanical properties, while simultaneously demonstrating that MAPP modification effectively enhances the interfacial adhesion between mussel shell fillers and the PP matrix.

5.5.4 Effect of different contents of PDA/MAPP co-modified mussel shell fillers on the mechanical properties of PP composites

The influence of various loading levels of PDA/MAPP co-modified mussel shell fillers on the mechanical properties of PP composites was investigated. The results are presented in Figure 5-10 a-c, with detailed data summarised in Table 5-6.

The stress-strain curves reveal that all samples yield at a lower strain compared to neat PP. PP composites containing 5-15% PDA/MAPP-MS fillers maintain yield stress values (ranging from 23.08 to 23.76 MPa) that are only marginally lower than those of neat PP.

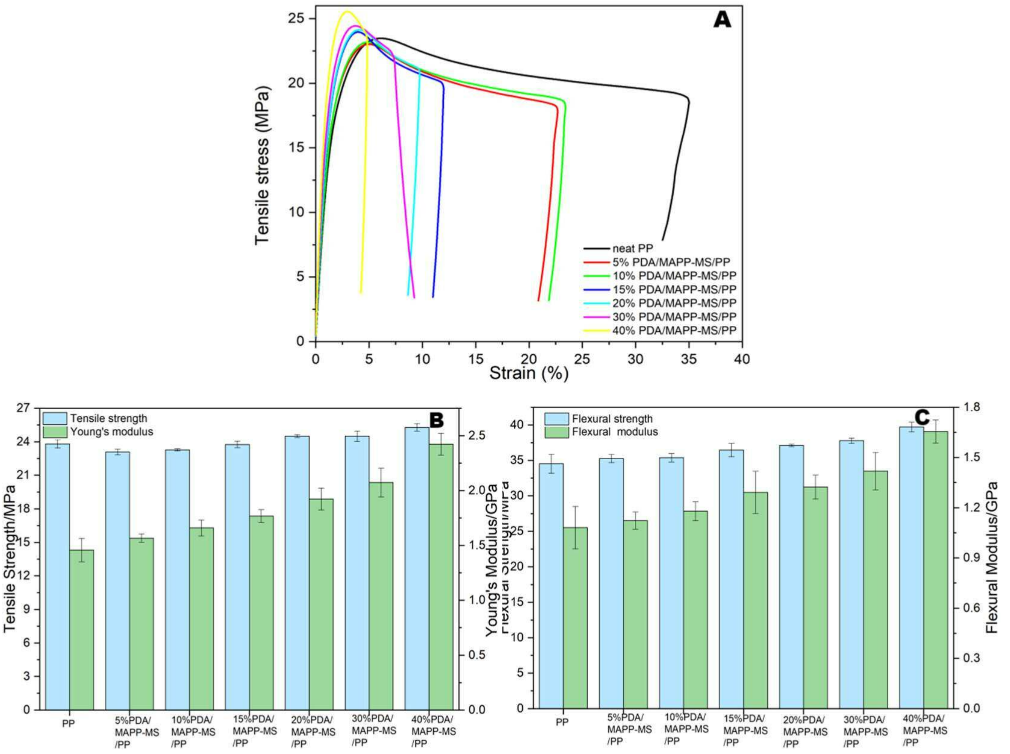

Figure 5- 10: (a) Stress-strain curves, (b) tensile behaviour, and (c) flexural behaviour of PP and PP composites with different amounts of PDA/MAPP co-modified mussel shell fillers.

However, higher yield strength is observed when the filler loading increases to 20% and above. Table 5-6 shows that composites with 20%, 30%, and 40% PDA/MAPP-MS yield at 24.51, 24.50, and 25.28 MPa, respectively. The maximum tensile strength, obtained from 40% PDA/MAPP-MS/PP, demonstrates a 6.2% increase compared to neat PP and a 2.6% increase relative to 40% MAPP-MS/PP. Compared to PP composites incorporating MAPP-modified mussel shell fillers, the integration of PDA-MAPP co-modified mussel shell results in enhanced tensile strength. This improvement demonstrates that the interfacial adhesion between filler and matrix is further enhanced by PDA-MAPP co-modification of the mussel shell filler surface. This enhanced interfacial adhesion facilitates improved stress transfer and distribution, enabling the composite to withstand higher stress before yielding.

Young's moduli of PP composites with 5-40% PDA/MAPP-MS increase with increasing filler content. The elastic modulus of 40% PDA/MAPP-MS/PP reaches 2.42 GPa, representing a 66.10% increase compared to neat PP and an 8.2% increase relative to 40% MAPP-MS/PP. This observation supportsthe proposed mechanism whereby PDA/MAPP co-modification enhances the adhesion between filler and matrix through chemical and hydrogen bonds, enabling relatively tighter polymer chain restraint upon the addition of 40% PDA/MAPP-MS fillers. Consequently, the stiffness increases further.

Analogous to PP composites with varying amounts of MAPP-MS, the elongation at break of PP composites decreases with increasing PDA/MAPP-MS content. This phenomenon can be ascribed to the disparity in the deformation rates between the filler and the polymer matrix, in conjunction with the intrinsic defects present within the composites, which become increasingly prominent with an augmented filler content.

Both flexural strength and modulus of PP composites increase monotonically with increasing PDA/MAPP-MS filler content. At the maximum loading of 40% PDA/MAPP-MS filler, the PP composite exhibits a flexural strength of 39.72 MPa, representing a 15.1% increase compared to neat PP and a 4.0% increase relative to 40% MAPP-MS/PP. The maximum flexural modulus is also achieved by 40% PDA/MAPP-MS/PP at 1.65 GPa, representing increases of 53.1% and 8.8% compared to neat PP and 40% MAPP-MS/PP, respectively. These results corroborate the analysis that PDA/MAPP co-modification enhances mechanical properties by enabling better filler dispersion in the polymer matrix and providing sufficient filler-matrix adhesion.

Table 5- 6:: Mechanical properties of PP and PP composites with different amounts of PDA/MAPP-MS fillers.

Samples	Tensile strength （**MPa**）	Young's modulus （**GPa**）	Elongation at break **(%)**	Flexural strength （**MPa**）	Flexural Modulus （**GPa**）
PP	23.81±0.38	1.46±0.11	29.71±6.85	34.52±1.35	1.08±0.08
5%PDA/MAPP-MS/PP	23.08±0.26	1.57±0.04	24.38±6.56	35.26±0.58	1.12±0.05
10%PDA/MAPP-MS/PP	23.28±0.11	1.66±0.07	13.24±6.83	35.38±0.59	1.18±0.06
15%PDA/MAPP-MS/PP	23.76±0.29	1.77±0.06	10.40±2.31	36.47±0.93	1.30±0.13
20%PDA/MAPP-MS/PP	24.51±0.14	1.92±0.09	8.42±1.83	37.12±0.16	1.33±0.07
30% PDA/MAPP-MS/PP	24.50±0.47	2.07±0.13	7.68±2.92	37.79±0.38	1.42±0.11
40%PDA/MAPP-MS/PP	25.28±0.34	2.42±0.10	4.63±0.42	39.72±0.68	1.65±0.07

5.6 Fracture morphology of PP composites incorporated with different mussel shell fillers

In the preceding chapter, contact angle measurements reveal that following MAPP or PDA/MAPP co-modification, the surface of mussel shell particles exhibits increased hydrophobicity, with surface energies approaching that of PP. This enhanced compatibility aligns with the principle of 'like dissolves like' [24].

SEM analysis provides insights into both the particle dispersion within the matrix and the potential adhesion between the two phases. The influence of surface modification on mussel shell fillers is directly observable from SEM analysis conducted on the fracture surfaces of the PP composites with different fillers; neat PP was examined for comparison. The tested specimens are obtained after tensile testing.

Figure 5-11(a) shows that the fracture surface of neat PP displays a typical brittle morphology, characterised by crazing and cracking that developed perpendicular to the tensile direction. These features are consistent with D. J. Dear's research comparing SEM studies on different polymers. The observed morphology corresponds tothe characteristic brittle failure mode of polymer, which is typically associated with low energy absorption during fracture [25]. Figures 5-11(b) and (c) depict SEM images of fracture surfaces of

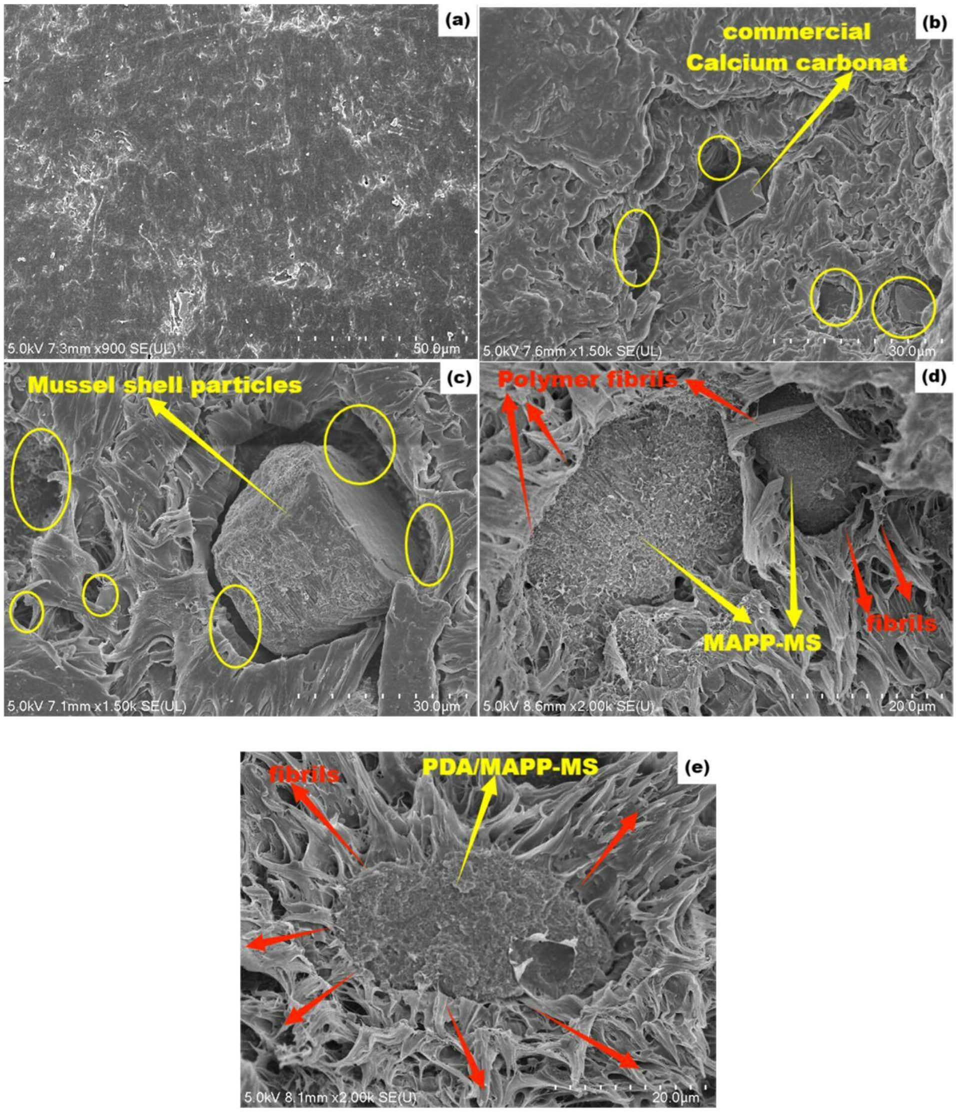

Figure 5- 11: SEM images of the fractural surface of (a) neat PP and PP composites incorporated with 5 % (b) commercial $CaCO_3$, (c) pristine mussel shell, (d) MAPP modified mussel shell fillers, (e) PDA and MAPP co-modified mussel shell fillers. Yellow arrow-filler particles; yellow circle-voids; red arrow- polymer fibrils.

PP composites incorporating 5 % commercial $CaCO_3$ and 5 % unmodified mussel shell fillers, respectively. Clear voids are observed between the fillers and the polymer, indicating extensive debonding of these fillers from the PP matrix due to a lack of total compatibility/adhesiveness. The absence of surface modification renders these fillers highly hydrophilic, resulting in poor adhesion with the hydrophobic PP matrix, as discussed in the previous section in Chapter 4.

The efficacy of surface modification on mussel shell fillers with MAPP or PDA/MAPP

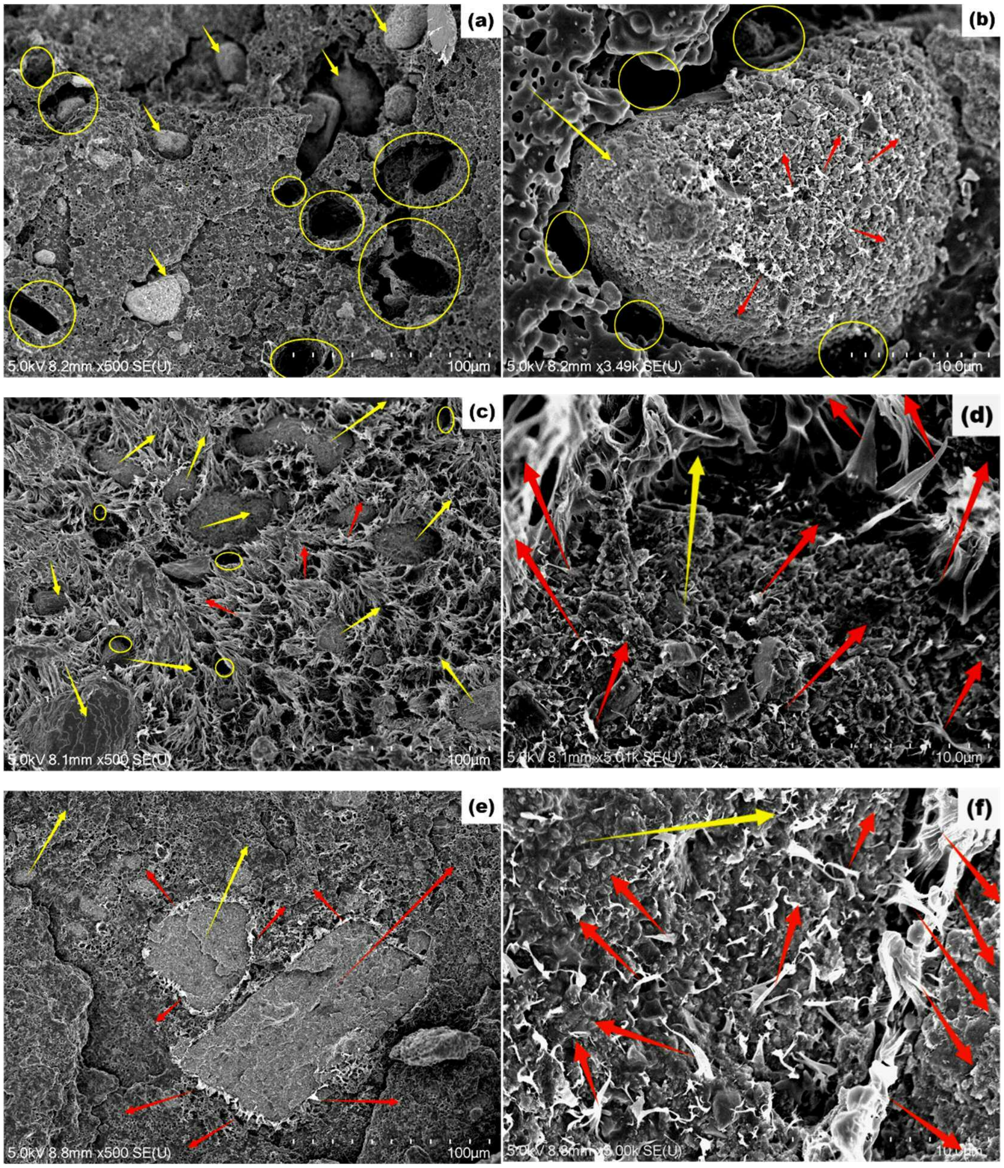

Figure 5- 12: SEM images of the fractural surface of (a) 40% MS/PP (×500), (b) 40% MS/PP(×3.49k), (c) 40% MAPP-MS/PP(×500), (d) 40% MAPP-MS/PP (×5.01k), (e) 40%PDA/MAPP-MS/PP (×500), and (f) 40%PDA/MAPP-MS/PP(×5.00k).

Yellow arrow-filler particles; yellow circle-voids; red arrow- polymer fibrils.

co-modification is clearly demonstrated in Figure 5-11(d) and (e), where a notable enhancement in filler/matrix wettability supporting the potential for increased adhesion is observed, indicated by the absence of holes and debonding of the fillers. Furthermore, polymer fibrils are observed adhering to the filler surfaces, manifesting as pulled-out fragments on the aggregated filler morphology.

Figure 5-12 (a)-(f) depict the SEM images of tensile deformed fracture surfaces of PP composites with 40% different mussel shell fillers. At this loading level, both untreated and modified mussel shell fillers were successfully incorporated into the PP matrix, showing surface interactions between the polymer and fillers. The filler sizes for all types of mussel shells were under 100 µm, consistent with the particle size distribution results (Chapter 4, Figure 4-12).

The fracture surface of 40% MS/PP composite exhibits a typical brittle morphology, as shown in Figure 5-12 (a) and (b). Numerous voids are visible in the SEM images, with sizes and shapes comparable to those of mussel shell particles, likely caused by filler debonding from the polymer. At higher magnification, clear gaps (marked in yellow circles) are observed around the fillers, indicating poor adhesion between the filler and matrix. Small polymer fibrils (red arrows) can be seen attached to the surface of mussel shell particles; a phenomenon not observed in PP composites with 5% mussel shell fillers. This phenomenon can be explained by the increased filler content, which enhances the probability of polymer adhesion to the irregular surfaces of mussel shell particles, likely occurring during melt mixing.

In polypropylene composites containing 40% MAPP-modified mussel shell (MAPP-MS) filler (Figure 5-12 c-d), fracture surface analysis revealed reduced void formation and increased polymer fibril formation, particularly surrounding the particles and at their interfaces with the matrix. These fibrils effectively bridge the filler-matrix interface. Under tensile deformation, the enhanced interfacial adhesion resulting from MAPP modification promotes efficient stress transfer between phases while restricting crack propagation perpendicular to the tensile axis. Furthermore, this strong interfacial bonding improves composite toughness through crack pinning, deflection and bridging mechanisms. These morphological observations correlate well with the enhanced tensile properties reported in Section 5.5.3.

Similarly, polypropylene composites filled with 40% PDA/MAPP-MS (Figure 5-12 e-f) also demonstrate strong bonding between the filler and the polymer matrix. Polymer fibrils can be observed attached to the surface of the fillers, and these fibrils act as bridges at the edges of the fillers to bind them to the polymer matrix. The fractured surface of

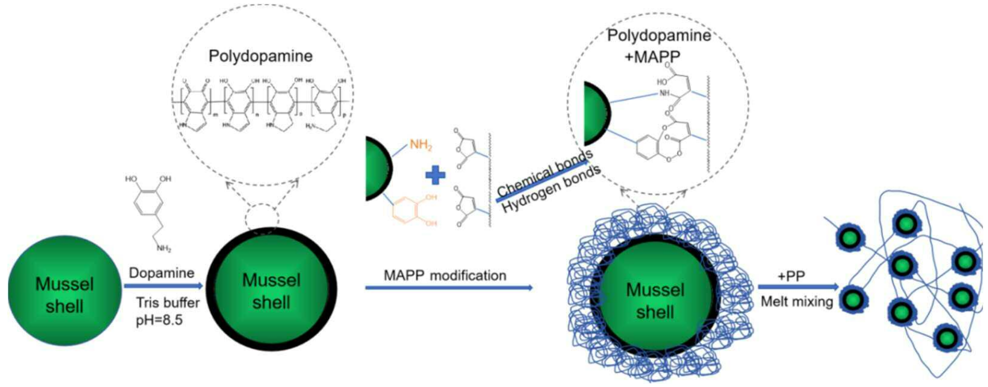

Figure 5- 13: Surface modification of mussel shell through PDA coating and MAPP modification.

these composites appears smoother and more brittle, indicating enhanced filler-matrix adhesion, which reduces chain mobility and ductility.

The SEM observations support the findings from mechanical tests, showing that improved interfacial adhesion in modified composites contributes to enhanced mechanical properties.

Based on the SEM observations and previous mechanical results, we can propose mechanisms for MAPP modification and PDA/MAPP co-modification of mussel shell fillers in PP composites. These mechanisms explain the improved mechanical properties and can be schematically represented in Figure 5-13.

MAPP functions as a highly effective polymer composite compatibilizer, enhancing the interfacial adhesion between filler and matrix. The grafted maleic anhydride on the polypropylene chain facilitates the formation of strong interfacial adhesion by creating covalent ester bonds with the hydroxyl groups present on the fillers. Furthermore, during the melt processing stage, the polypropylene backbone of MAPP forms entanglements with the PP matrix, further improving compatibility. This mechanism has been documented in previous literature [26-28]. While MAPP is widely recognised as an effective polymer compatibilizer, direct spectroscopic evidence of esterification between MAPP and fillers - even with hydroxyl-rich cellulosic fillers - remains experimentally challenging to obtain. This difficulty stems from two key factors: firstly, commercial MAPP formulations typically contain only 1-3% maleic anhydride functional groups. Secondly, when incorporated as a compatibilizer at standard loading levels (3-5 %), the effective concentration of reactive acid groups in the composite system falls below 1%, making their detection analytically problematic [29].

In this study, both pristine and polydopamine (PDA) coated mussel shells underwent MAPP modification through dry ball-milling. Subsequently, these modified fillers were incorporated into a polypropylene (PP) matrix through melt mixing, followed by extrusion and injection moulding processes. Dry ball-milling, utilised for MAPP modification in this study, is a solid-state mechano-chemical treatment known for its ability to generate local high-pressure spots and facilitate closer contact between reacting species, potentially leading to novel chemical reactions. Previous reports have indicated the functionalization of multiwalled carbon nanotube fillers with MAPP to enhance its compatibility with PP [30]. Another study revealed that ball milling cellulose with MAPP has been shown to facilitate the release of -OH groups in crystalline cellulose, thereby inducing efficient esterification between cellulose hydroxyl groups and maleic anhydride groups in MAPP [31].

In the case of MAPP-MS, given that $CaCO_3$ is the primary chemical constituent of mussel shells, it is not surprising that functional groups such as -OH are absent. Consequently, the possibility of esterification between MAPP and mussel shells presents significant challenges. It is more probable that the process of coating MAPP onto the shells involves physical dispersion and surface coverage during the assisted-intensive ball milling process. The improved interfacial bonding between MAPP-MS and PP observed from SEM images is more likely to be attributed to the entanglement of PP and the PP backbone of MAPP during the subsequent melt mixing and extrusion process at high temperature (161-185 °C), as the mobility of polymer chains can be achieved above its melting temperature (melt point of PP is 140 °C in this study).

In PDA/MAPP-MS, the mussel shell surface is initially coated with polydopamine through self-polymerisation, introducing functional groups like amines and catechols from PDA. During the ball-milling process, these functional groups on the surface of mussel shell can be effectively activated by localised high-pressure spots and close contact with maleic anhydride groups in MAPP, then these functional groups may react with maleic anhydride groups from MAPP through ring-opening reactions, leading to the formation of strong chemical bonding between the mussel shell and MAPP interfaces. Furthermore, during high-temperature melt mixing and extrusion (160-185 °C) procedures for compounding PP composites, the maleic anhydride groups readily undergo ring-opening to convert into dicarboxylic acid groups. This transformation potentially allows for hydrogen bonding with the amine groups present between the PDA-coated mussel shell and the matrix, thereby enhancing the interfacial adhesion of the composites.

5.7 Dynamic mechanical properties

The viscoelastic characterisation of composite systems is inherently more complex than that of neat polypropylene due to their multicomponent nature, which includes: (1) the filler phase, (2) the polymer matrix, (3) the interfacial region, and (4) potential interfacial chemical reactions. This complexity arises from the interplay between these distinct components and their respective contributions to the overall viscoelastic response.

Dynamic mechanical analysis (DMA) offers insights into viscoelastic behaviour under dynamic conditions. For heterogeneous polymer composites, DMA analysis is a sensitive measurement to provide information on interfacial characteristics. Consequently, the influence of filler, filler-matrix interfacial reactions can be evaluated. Additionally, DMA reflects the different hierarchical levels of molecular chain motions in both amorphous and crystalline phases; the relaxation/transition processes can be evaluated as well. In this section, the effects of untreated and modified mussel shell fillers on the dynamic mechanical behaviour of PP composites were investigated.

5.7.1 Effect of 5% different inorganic fillers on the dynamic mechanical properties of PP composites

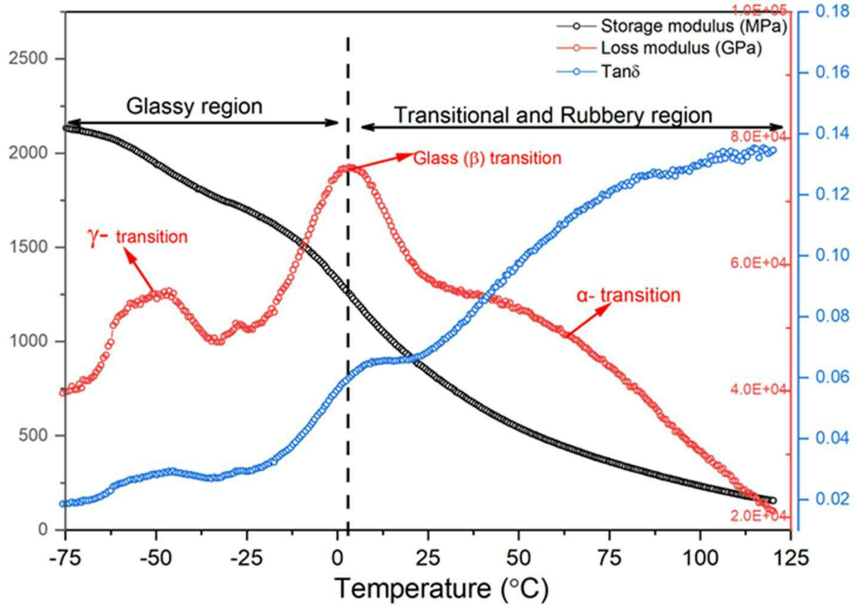

Figure 5- 14: DMA curves of neat PP.

The temperature dependence of the dynamic mechanical properties of neat PP, including storage modulus (E'), loss modulus (E''), and damping factor (tan δ), is illustrated in

Figure 5-14As established in polymer science, the temperature-dependent storage modulus (E') typically exhibits three characteristic regions: (1) the glassy state at low temperatures, (2) the glass transition region, and (3) the rubbery plateau at elevated temperatures. A clear descending trend in the storage modulus of neat PP is observed as temperature increases from -75°C to 120°C. Storage modulus contributes to the elastic behaviour of the polymer and relates to the material's stiffness, representing its resistance to deformation under stress. As temperature increases, the molecular mobility of the

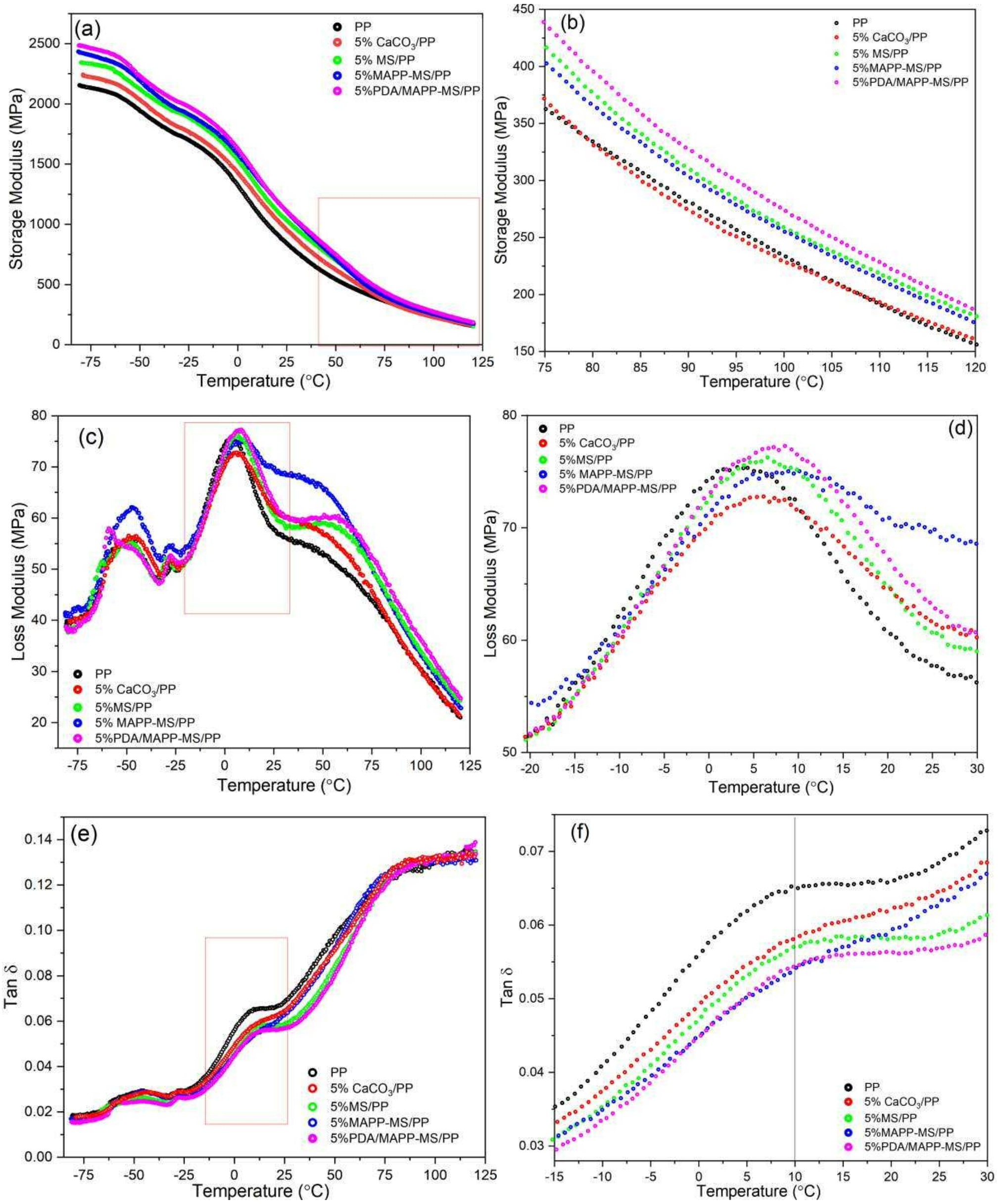

Figure 5- 15: DMA curves of PP composites incorporated with 5% different fillers as functions of temperature, (a) storage moduli, (b) enlargement of storage moduli; (c) loss moduli,(d) enlargement of loss moduli;(e) damping factors, (f) enlargement of damping factors.

polymer chains also increases. This leads to reduced resistance to deformation, increased chain flexibility, and weakened intermolecular forces. These factors collectively contribute to the decrease in storage modulus with increasing temperature [32].

Three distinctive transitions are evident in both the loss modulus and Tan δ (damping) curves. The γ-transition occurs at approximately -50 °C, the β-transition is more pronounced at around 3.2 °C, and the α-transition occurs at a higher temperature range of 50-80 °C, below the melting point, without a distinct peak.

At 5% filler loading, all formulations showed higher storage moduli than neat PP over the entire temperature range (Figure 5-15a and b), while retaining a similar decreasing trend.At glassy region, the storage modulus is high as PP and PP composites are rigid due to the close-packed polymer molecular chains. During the glass transition region, the storage modulus shows a rapid decrease around the glass transition temperature (T_g) because of a large segmental PP chain movement. With the incorporation of 5% untreated or modified mussel shell fillers, storage moduli of PP composites are all increased, revealing that the stiffness of PP composites are improved due to the addition of rigid fillers. The order of increasing storage modulus was as follows: PP < 5% CC/PP < 5% MS/PP < 5% MAPP-MS/PP < 5% PDA/MAPP-MS/PP. As shown in Table 5-7, the storage moduli (E') at -50°C for increased by 4.4% for 5% CC/PP, 9.3% for 5% MS/PP, 13.0% for 5% MAPP-MS/PP, and 14.5% for 5% PDA/MAPP-MS/PP, respectively, compared to neat PP. At a higher temperature (120°C), the relative increase in storage modulus for 5% CC/PP, 5% MS/PP, 5% MAPP-MS/PP, and 5% PDA/MAPP-MS/PP remained at a slightly higher but the same level as observed at -50°C. The addition of these various fillers at a 5% loading level demonstrates similar positive effects on the storage modulus in the rubbery region, where the mobility of polymer chains is dramatically enhanced due to the increased temperature. These results corroborate the

Table 5- 7: Comparison of neat PP and PP with 5% different fillers (DMA data).

Samples	**Storage modulus (MPa)**				**T_g (°C)**	**Loss modulus (MPa)**	**C (60 °C)**
	-50 °C	Change %	120 °C	Change %	/		
PP	1951.09		198.34		3.2	75.39	
5%CC/PP	2037.40	4.4%	161.7	3.63	6.1	72.78	0.95
5%MS/PP	2132.78	9.3%	180.83	15.9	6.6	76.26	0.90
5%MAPP-MS/PP	2204.15	13.0%	174.29	11.71	8.3	75.03	0.91
5%PDA/MAPP-MS/PP	2234.14	14.5%	185.16	18.67	8.5	77.17	0.90

findings from tensile tests, suggesting that the stiffness of PP composites is enhanced by the addition of rigid filler particles.

Interestingly, PP composites with 5% untreated or modified mussel shell fillers show higher storage moduli than those of neat PP and PP filled with 5% $CaCO_3$. These can be attributed to a better filler dispersion of different mussel shells within PP matrix, which leads to the reduced mobility of PP molecules. Similar observations were reported in previous publications [33].

To evaluate the impact of fillers on the viscoelastic properties of polymer composites across different temperature regions, the effectiveness coefficient (C) is introduced as a useful parameter [34]. This coefficient compares the storage modulus (E') of the composite in the glassy and rubbery states to that of the neat polymer. The effectiveness coefficient can be calculated using the following equation:

$$C = \frac{E'g / E'r(composite)}{E'g / E'r(PP)} \qquad \text{Eq 5-1}$$

where E' denotes the storage modulus, with subscripts g and r referring to the glassy and rubbery regions, respectively. A lower C value indicates greater effectiveness of the filler in maintaining the composite's stiffness during the transition from the glassy to the rubbery state [35]. Based on the storage moduli at -10 °C in the glassy region, 60 °C was chosen to evaluate the effectiveness coefficients (C) of these PP composites. Table 5-7 shows that the C values of PP with 5% various mussel shell fillers are close to 0.90, while 5% CC/PP is slightly higher at 0.95. These results indicate that at a 5% loading level, mussel shell fillers, whether raw or modified, are more effective at improving the stiffness of PP than commercial calcium carbonate fillers.

The loss modulus curves (Figure 5-15c&d) indicate a slight increase in glass transition temperatures, while the changes in loss moduli upon the addition of 5% various fillers are negligible. On the contrary, the incorporation of 5 % filler induces distinct changes in the rubbery region, most notably through the appearance of a weak transition peak at approximately 70°C. This contrasts with the neat PP matrix, which exhibits merely a shoulder-like transition feature near 50°C. This is associated with α-transition [36].

The tan δ curves (Figure 5-15e&f) show that PP composites with 5% of various fillers exhibit lower values than neat PP at the glass transition temperature. It is important to note that the damping behaviour of hybrid composites is influenced by two competing mechanisms. On one hand, well-dispersed fillers can interact with more polymer chains, increasing interfacial friction and potentially raising tan δ. On the other hand, when interfacial bonding is strong, energy dissipation is reduced, resulting in a lower tan δ [37]. Therefore, the overall damping response reflects a balance between filler dispersion and interfacial bonding. At a 5% loading level, lower damping factor was achieved with MAPP-MS and PDA/MAPP-MS, implying an enhanced filler-matrix bonding by surface modification. Further investigations into the influence of increased filler content on the viscoelastic behaviour are discussed in the following sections.

5.7.2 Effect of different contents of untreated mussel shell fillers on the dynamic mechanical properties of PP composites

The relationship of DMA properties with untreated mussel shell filler loading levels was presented in Figure 5-16 a-f.

A similar descending trend in storage modulus is observed for PP composites with 5-40% untreated mussel shell fillers as temperature increases. As the loading levels of mussel shell fillers increase from 5 to 15%, the storage modulus of the filled PP composites remains relatively similar. Data from Table 5-8 indicate that at -50℃, their storage modulus increases by approximately 7-9.5% compared to neat PP. With the addition of 20 and 30 wt.% mussel shell filler, the E' of resultant composites increases by 22.05% and 23.96%, respectively. At 40 wt. % loading, the mussel shell-filled PP composites exhibit only a modest 15.19% increase in storage modulus (E') compared to lower filler contents. This limited enhancement may be attributed to compromised filler dispersion at high loading levels, particularly in the glassy region, where particle agglomeration likely reduces the composite's stress transfer efficiency.

Table 5- 8: Comparison of neat PP and PP composites with different amounts of untreated mussel shell fillers (DMA data).

Samples	**Storage modulus (MPa)**				**T_g (°C)**	**Loss modulus (MPa)**	**C (60 °C)**
	-50 °C	Change %	120 °C	Change %	/		
PP	1951.09		198.34		3.2	75.39	
5%MS/PP	2132.78	9.31	180.83	15.90	6.6	76.26	0.90
10%MS/PP	2103.38	7.81	186.80	19.72	6.3	76.20	0.90
15%MS/PP	2136.59	9.51	179.80	15.23	7.5	83.11	0.93
20%MS/PP	2381.21	22.05	202.89	30.03	8.6	86.60	0.87
30%MS/PP	2418.59	23.96	207.79	33.18	12.2	86.66	0.81
40%MS/PP	2247.37	15.19	193.08	23.75	9.1	83.35	0.82

A similar trend of increasing storage modulus for PP composites with varying mussel shell filler content is observed in the rubbery region (120℃), with the rate of increase being higher compared to that in the glassy region (50℃). The storage modulus of

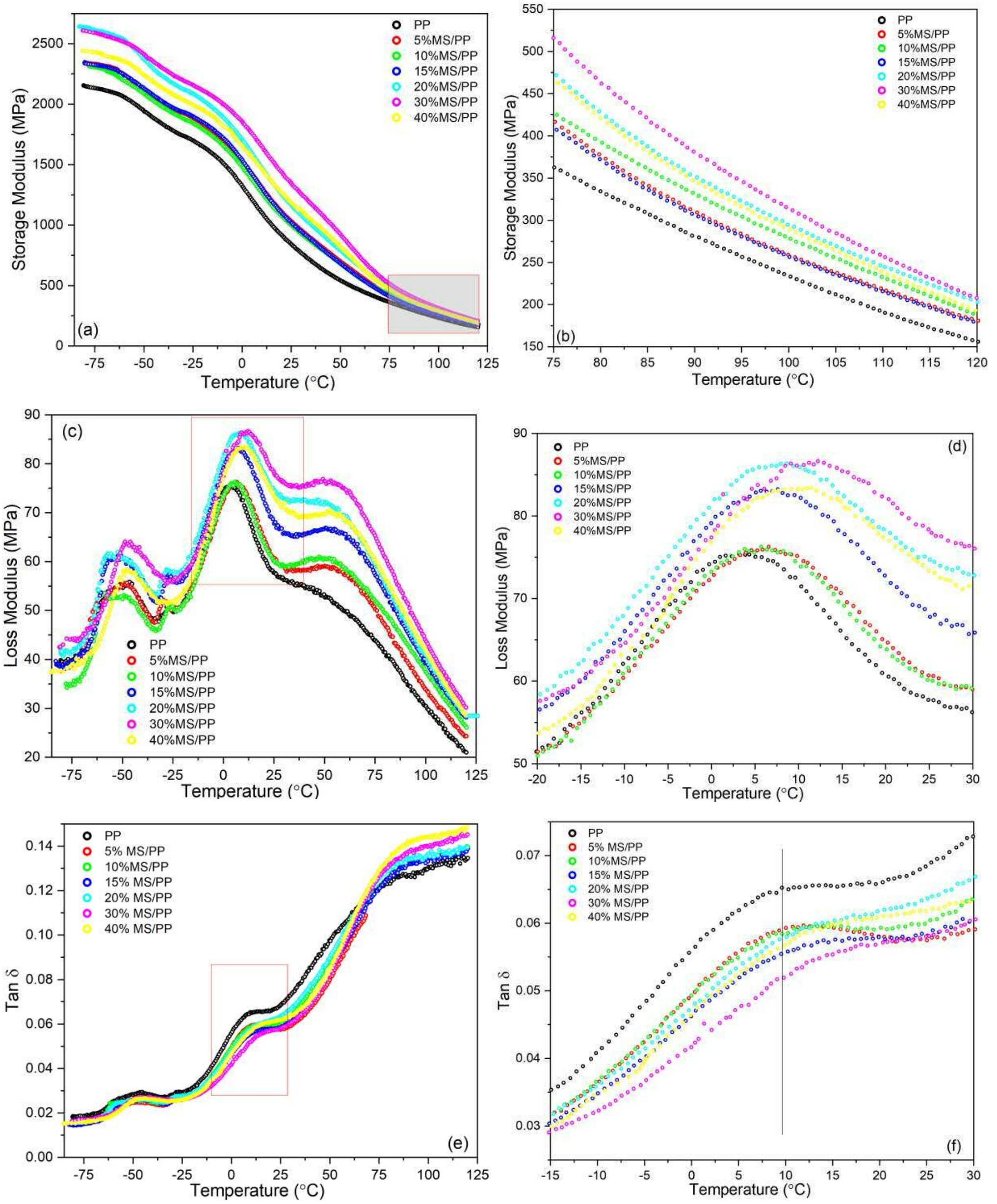

Figure 5- 16: DMA curves of PP composites incorporated with 5-40% untreated mussel shell fillers as functions of temperature, (a) storage moduli, (b) enlargement of storage moduli; (c) loss moduli,(d) enlargement of loss moduli;(e) damping factors, (f) enlargement of damping factors.

polypropylene is heavily dependent on the strength of intermolecular forces and the packing arrangement of polymer chains. Unlike the closely packed polymer chains in the glassy state, the mobility of polymer chains is much higher in the rubbery region. Increasing the filler content leads to a higher proportion of immobilised polymer chains, consequently resulting in a greater increase in storage modulus. However, a lower rate of storage modulus increase is observed when 40% mussel shell fillers are added to the polymer composite, which can be attributed to poor mussel shell filler dispersion.

Glass transition temperatures (T_g) obtained from loss modulus curves and the peaks of damping factor curves at β-transition also exhibit a similar trend. The T_g of PP composites filled with 5-15% mussel shell fillers ranges from 6.3-7.5℃, higher than that of neat PP at 3.2℃. The T_g of 20% MS/PP increases to 8.6℃, while that of 30% MS/PP further increases to 12.2℃. However, the T_g of 40% MS/PP drops to 9.1℃. The higher T_g can be attributed to the lower mobility of polymer segment chains resulting from the restraining effect by adding fillers. If the filler dispersion is more uniform, the movement of chains decreases effectively and T_g moves to higher temperature, resulting in the improvement of the thermal stability of composites The loss modulus at T_g follows the order of PP < 5% MS/PP ≈ 10% MS/PP < 15% MS/PP ≈ 40% MS/PP < 20% MS/PP < 30% MS/PP. The loss modulus is associated with the viscous behaviour of polymers and measures energy dissipation. A higher loss modulus indicates greater energy dissipation in the filler-polymer system [33; 35]. The addition of a substantial amount of filler to the polymer creates an extensive filler-polymer interface, which facilitates energy dissipation. Consequently, it is reasonable to expect that energy dissipation increases with increasing mussel shell filler content, especially in the system with the weak filler-matrix adhesion. However, when the mussel shell filler content reaches 40%, poor filler dispersion and possible agglomeration of untreated mussel shell particles lead to a decrease in the effective filler-matrix interface for energy dissipation. Consequently, the loss modulus decreases accordingly. The peak of the damping factor curves at the β-transition decreases gradually with increasing mussel shell filler content. These results indicate that the poor dispersion of untreated mussel shell filler leads to reduced effectiveness of filler. The value of effectiveness coefficient ($C_{60℃}$) for PP composites decreases with increasing mussel shell filler content. Values of 0.90 are observed for both 5% and 10% MS/PP, 0.93 for 15% MS/PP, and 0.87, 0.81, and 0.82 for 20%, 30%, and 40% MS-incorporated PP composites, respectively. Given that the effectiveness coefficient considers the behaviour of materials in both glassy and rubbery regions, it can be concluded that the overall impact of mussel shell fillers on the viscoelastic properties of the resultant composites increases with increasing filler content.

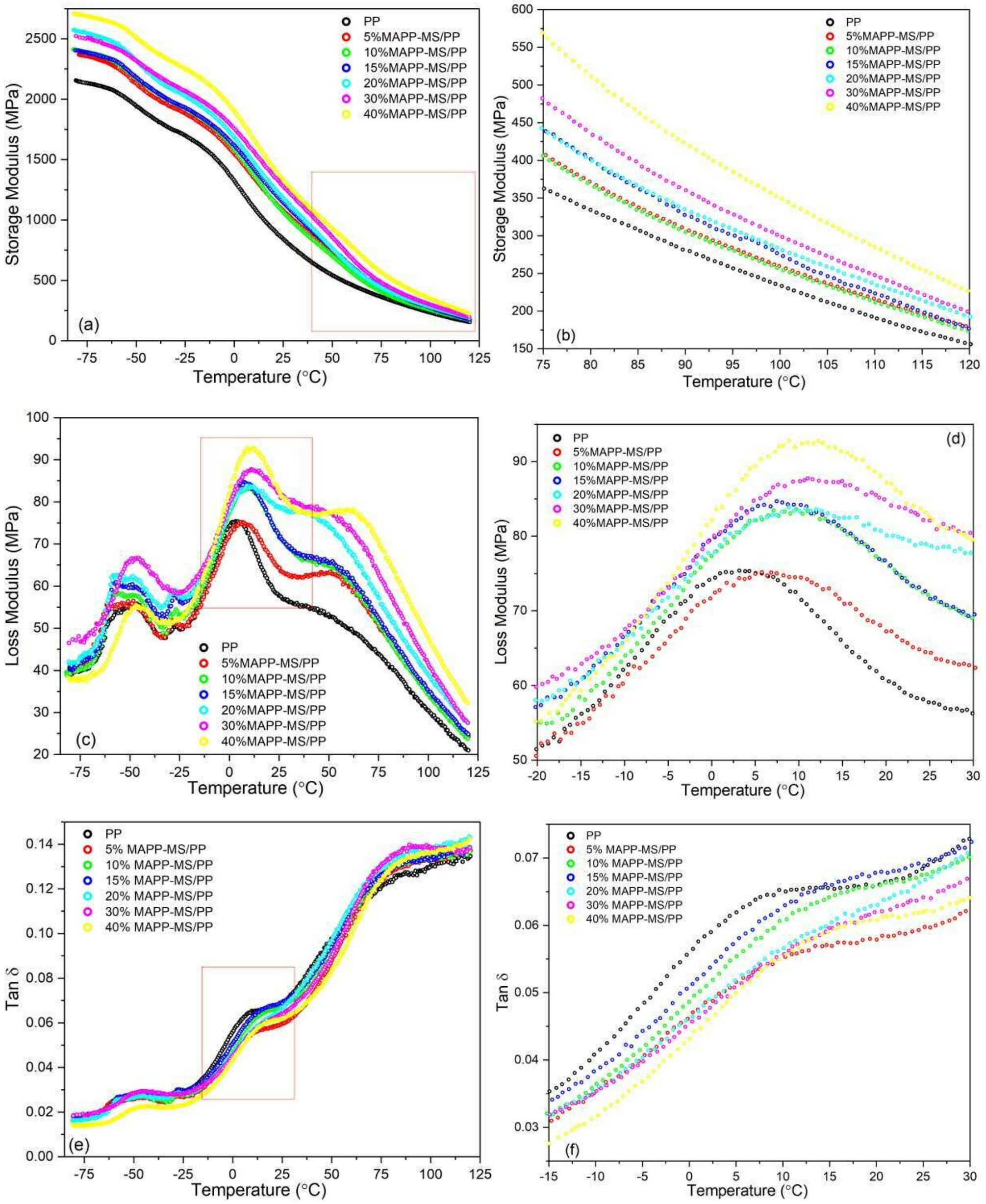

Figure 5- 17: DMA curves of PP composites incorporated with 5-40% MAPP-MS as functions of temperature, (a) storage moduli, (b) enlargement of storage moduli; (c) loss moduli,(d) enlargement of loss moduli;(e) damping factors, (f) enlargement of damping factors.

5.7.3 Effect of different contents of MAPP modified mussel shell fillers on the dynamic mechanical properties of PP composites

Generally, enhanced filler/matrix bonding with surface-modified filler can improve dynamic mechanical properties. Rana *et al.* reported that the storage modulus of jute fibre reinforced PP composites increases as the fibre content increasing, and further increase was observed with the addition of MAPP modified jute fibre [38].

The influence of different amounts of MAPP modified mussel shell fillers on the viscoelastic properties of PP composites was investigated, and the results are shown in Figure 5-17 and Table 5-9.

The PP composites containing 5-40 % MAPP-modified mussel shell (MAPP-MS) fillers demonstrate comparable storage modulus trends to their unmodified counterparts. Notably, composites with higher filler loading exhibit systematically enhanced storage moduli, consistent with the expected reinforcement effect from increased rigid filler content. Compared with neat PP, the E' values of the composites show higher increase rates in both the glassy region and the rubbery region, with the magnitude of increase rising alongside filler content. The increase in storage modulus is more pronounced in the rubbery region compared to the glassy region for equivalent MAPP-MS loading levels. In contrast to untreated mussel shell fillers, the addition of 40% MAPP-MS continues to increase the storage modulus of the resultant composite in both glassy and rubbery regions, with a notable 45.35% increase observed for PP in the rubbery state. This suggests that MAPP modification improves filler dispersion and enhances interfacial adhesion between mussel shell fillers and the polymer matrix, effectively restraining polymer chain motion. From Figure 5-17 c&d, the glass transition temperature and loss modulus can be seen to increase with the increasing content of MAPP-MS, at 40% loading level, its glass transition temperature rises to 12.4°C, and loss modulus increased by 23.2% to that of neat PP. The persistently elevated loss modulus with increasing MAPP-MS content indicates increased energy dissipation at the filler-matrix interface, suggesting that the efficacy of

Table 5- 9: Comparison of neat PP and PP composites with different amounts of MAPP-MS fillers (DMA data).

Samples	**Storage modulus (MPa)**				**T_g (°C)**	**Loss modulus (MPa)**	**C (60 °C)**
	-50 °C	Change %	120 °C	Change %	/		
PP	1951.09		198.34		3.2	75.39	
5%MAPP-MS/PP	2135.96	9.48	177.45	13.73	8.3	75.03	0.94
10%MAPP-MS/PP	2181.34	11.8	176.59	13.18	9.8	83.72	0.95
15%MAPP-MS/PP	2186.95	12.09	176.62	13.2	10.3	84.31	0.89
20%MAPP-MS/PP	2325.22	19.18	194.47	24.64	10.7	83.92	0.90
30%MAPP-MS/PP	2325.36	19.18	199.25	27.7	11.5	87.84	0.85
40%MAPP-MS/PP	2524.78	29.40	226.78	45.35	12.4	92.85	0.81

interfacial adhesion achieved through MAPP modification diminishes with increasing MAPP-MS content.

Upon the addition of 5% MAPP-MS, the loss modulus is comparable to that of neat PP, indicating preserved viscous properties of PP. However, as the MAPP-MS content further increases, the interfacial adhesion becomes insufficient and the loss moduli of resultant composites increase accordingly. This phenomenon becomes more pronounced as the filler content approaches 40%. The underlying mechanism can be explained as follows: As discussed in Section 5.5, the MAPP content in PP composites remains constant (3 %) regardless of the increasing mussel shell filler content. Consequently, as the filler content increases, the amount of MAPP available per mussel shell particle decreases, resulting in a reduction of the interfacial adhesion effect. Peaks associated with the α-transition in loss modulus curves can be observed to shift towards higher temperatures. For neat PP, this peak appears around 50°C. Notably, the peak for 40% MAPP-MS/PP shifts to 75°C. This more intense α-transition peak and higher temperature suggest increased energy dissipation due to internal friction, likely resulting from poor interfacial bonding between the filler and polymer.

The damping factor is generally more sensitive to interfacial adhesion than either the storage modulus or the loss modulus. This is because it is independent of sample geometry. As shown in Figure 5-17(e) and (f), the addition of MAPP-MS fillers caused the glass transition temperature (Tg) to shift to higher values in the damping curves. Furthermore, the damping peaks around the β-transition became broader and lower for PP composites compared with neat PP. The lowest tan δ peak was recorded for the composite containing 5 % MAPP-MS, indicating that the mobility of polymer chain segments was most effectively restricted at this filler loading. When the MAPP-MS content exceeded 5%, tan δ at Tg increased, suggesting a reduction in filler-matrix bonding.

The effectiveness coefficient ($C_{60°C}$) values for composites containing 5–40% MAPP-MS decreased with increasing filler content, further indicating that the overall influence of MAPP-modified mussel shell fillers on the viscoelastic properties becomes more pronounced as the filler loading increases.

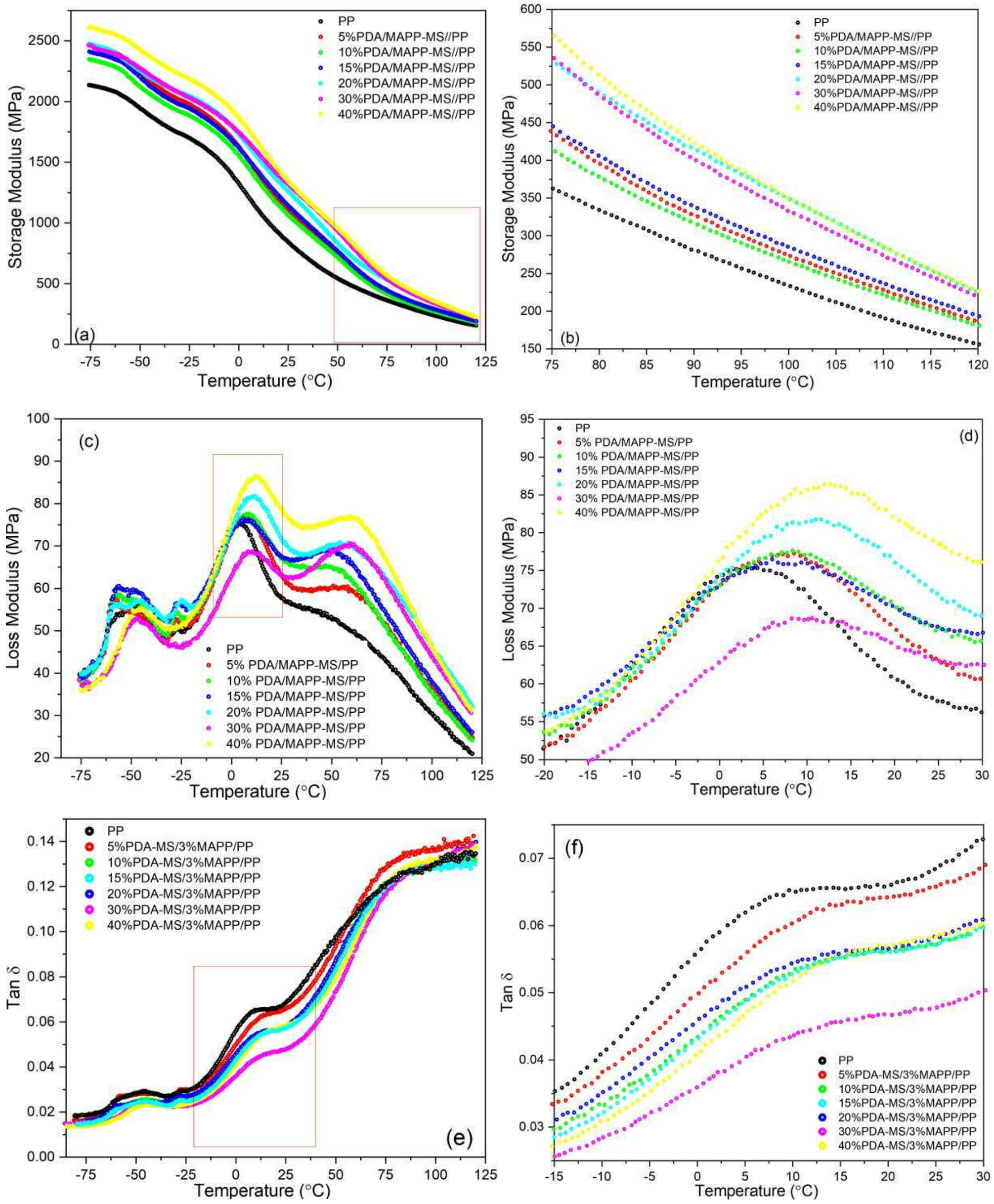

Figure 5- 18: DMA curves of PP composites incorporated with 5-40% PDA/MAPP-MS as functions of temperature, (a) storage moduli, (b) enlargement of storage moduli; (c) loss moduli,(d) enlargement of loss moduli;(e) damping factors, (f) enlargement of damping factors.

5.7.4 Effect of different contents of PDA/MAPP co-modified mussel shell fillers on the dynamic mechanical properties of PP composites

As illustrated in Figure 5-3, the PDA coating introduced abundant functional groups onto the mussel shell fillers, which facilitated interactions with MAPP through chemical and hydrogen bonding, thereby enhancing the interfacial bonding between the filler and the PP matrix..

The effect of PDA/MAPP co-modified mussel shell fillers on the viscoelastic deformation of PP composites was evaluated, with results shown in Figure 5-18 and summarised in Table 5-10. The storage modulus of the composites increased with rising PDA/MAPP-MS content, although all curves showed a general decline with increasing temperature. This trend is consistent with that observed for PP composites containing MAPP-MS fillers. Notably, in the glassy region, the rate of increase in storage modulus was comparable to that of MAPP-MS-filled composites. However, in the rubbery region (120 °C), the enhancement was more pronounced. Specifically, the storage modulus increased by 45.04%, 41.86%, and 45.25% for the 20%, 30%, and 40% PDA/MAPP-MS/PP composites, respectively, relative to neat PP. This pronounced improvement in the rubbery region is attributed to stronger interfacial adhesion between the PDA/MAPP-MS fillers and the PP matrix, which effectively restricted polymer chain mobility through enhanced filler–matrix interactions.

Table 5- 10: Comparison of neat PP and PP composites with different amounts of PDA/MAPP-MS fillers (DMA data).

Samples	**Storage modulus (MPa)**				**T_g (°C)**	**Loss modulus (MPa)**	**C (60 °C)**
	-50 °C	Change %	120 °C	Change %			
PP	1951.09		198.34		3.2	75.39	
5%PDA/MAPP-MS/PP	2234.14	14.51	185.16	18.67	8.5	77.17	0.90
10%PDA/MAPP-MS/PP	2126.41	8.99	180.94	15.97	9.0	77.76	0.92
15%PDA/MAPP-MS/PP	2211.4	13.34	193.23	23.84	9.1	77.30	0.88
20%PDA/MAPP-MS/PP	2257.6	15.71	226.31	45.04	11.5	81.86	0.84
30%PDA/MAPP-MS/PP	2275.69	16.64	221.34	41.86	11.9	68.2	0.75
40%PDA/MAPP-MS/PP	2432.74	24.69	226.64	45.25	12.6	86.4	0.77

Glass transition temperatures (Tg) derived from loss modulus (E”) curves increased with the incorporation of PDA/MAPP-MS fillers, as shown in Figure 5-18c and d. The loss modulus peaks at Tg rose by approximately 2 ‒ 3% compared to neat PP for composites containing 5-15% PDA/MAPP-MS, with the maximum increase observed at 40% loading.

Interestingly, the E” value of the 30% PDA/MAPP-MS/PP composite decreased by 9.55% relative to neat PP. As discussed previously, stronger interfacial adhesion reduces interfacial regions available for energy dissipation, resulting in lower loss modulus values. This suggests that 30% PDA/MAPP-MS provides an optimised interfacial interaction with the PP matrix. The overall reduction in damping curves across all PDA/MAPP-MS loading levels, particularly the pronounced drop for the 30% composite, further supports this conclusion.

The effectiveness coefficient ($C_{60°C}$) of PP composites containing 5–40% PDA/MAPP-MS fillers decreased with increasing filler content, indicating that the overall influence of PDA/MAPP-MS fillers on the viscoelastic properties of the composites becomes more pronounced at higher loading.

5.8 Creep-recovery properties

The addition of fillers significantly influences the viscoelastic behaviour of the polymer matrix, particularly its creep response. Creep, defined as time-dependent deformation under constant stress (typically below the yield stress), occurs through two primary mechanisms at the molecular level [39]. Firstly, under constant stress, polymer chains can untangle and slip passing each other, involving the breaking and reforming of weak intermolecular forces, such as Van der Waals forces and hydrogen bonds. Secondly, as the polymer chains slip, they reorient themselves in the direction of the applied stress, contributing to the overall deformation of the material [40]. Additionally, the free volume theory provides further insight into the observed creep behaviour. This theory posits that matrix deformation induced by stress increases local free volume within the polymer structure. This increase in free volume, in turn, facilitates local chain mobility and drives plasticity [41]. Upon the removal of stress, these chains reorient at their original position but not fully recover, which may result in permanent creep strain (residue strain, ε_p). These molecular processes result in creep behaviour, which becomes more pronounced with increasing temperature and stress levels.

Creep recovery, also known as the material's ability to return to its original shape after stress removal, is of particular importance in engineering applications. Insufficient recovery ratios or substantial unrecovered strain upon stress removal may lead to unpredictable material damage, affecting the long-term reliability of polymer-based components [42]. In the preceding sections, the addition of various mussel shell fillers was shown to affect the intermolecular interactions within polymer chains and restrict the mobility of polymer molecules. Consequently, the impact of different mussel shell fillers and the filler contents on the creep behaviour of PP composites is of particular interest and is investigated in this section.

5.8.1 Creep-recovery behaviour of neat PP

The creep-recovery behaviour of neat polypropylene (PP) was investigated at three distinct stress levels and temperatures. The applied stresses of 2, 3, and 4 N were carefully selected based on the stress-strain curve obtained at 30°C, as illustrated in Figure 5-19(a). Crucially, these stress levels fall within the linear viscoelastic region, where stress and strain exhibit a proportional relationship without inducing structural yielding.

The importance of conducting creep-recovery measurements within the linear viscoelastic region cannot be overstated. This regime ensures that the material's response to applied stress is reversible and does not involve permanent deformation or structural changes. Consequently, the observed behaviour directly reflects the material's intrinsic viscoelastic properties, allowing for a more accurate assessment of its micro-structural characteristics [40].

The response of neat polypropylene (PP) to the application and removal of stress over time is presented in Figure 5-19 (b-d). Three distinct sections are evident in all creep-recovery curves across various temperatures and stress levels, as illustrated in Figure 5-

19 (f). The first section corresponds to the elastic/instantaneous strain ($\varepsilon_{elastic}$) of PP, representing the fully recoverable stretching movement of polymer chains. The second section, known as the primary creep strain region, is characterised by elastic-predominant viscoelastic deformation. As the constant stress continues to be applied, viscous deformation becomes more pronounced whilst elastic deformation decreases in the secondary creep region (third section). Upon stress removal, the elastic deformation

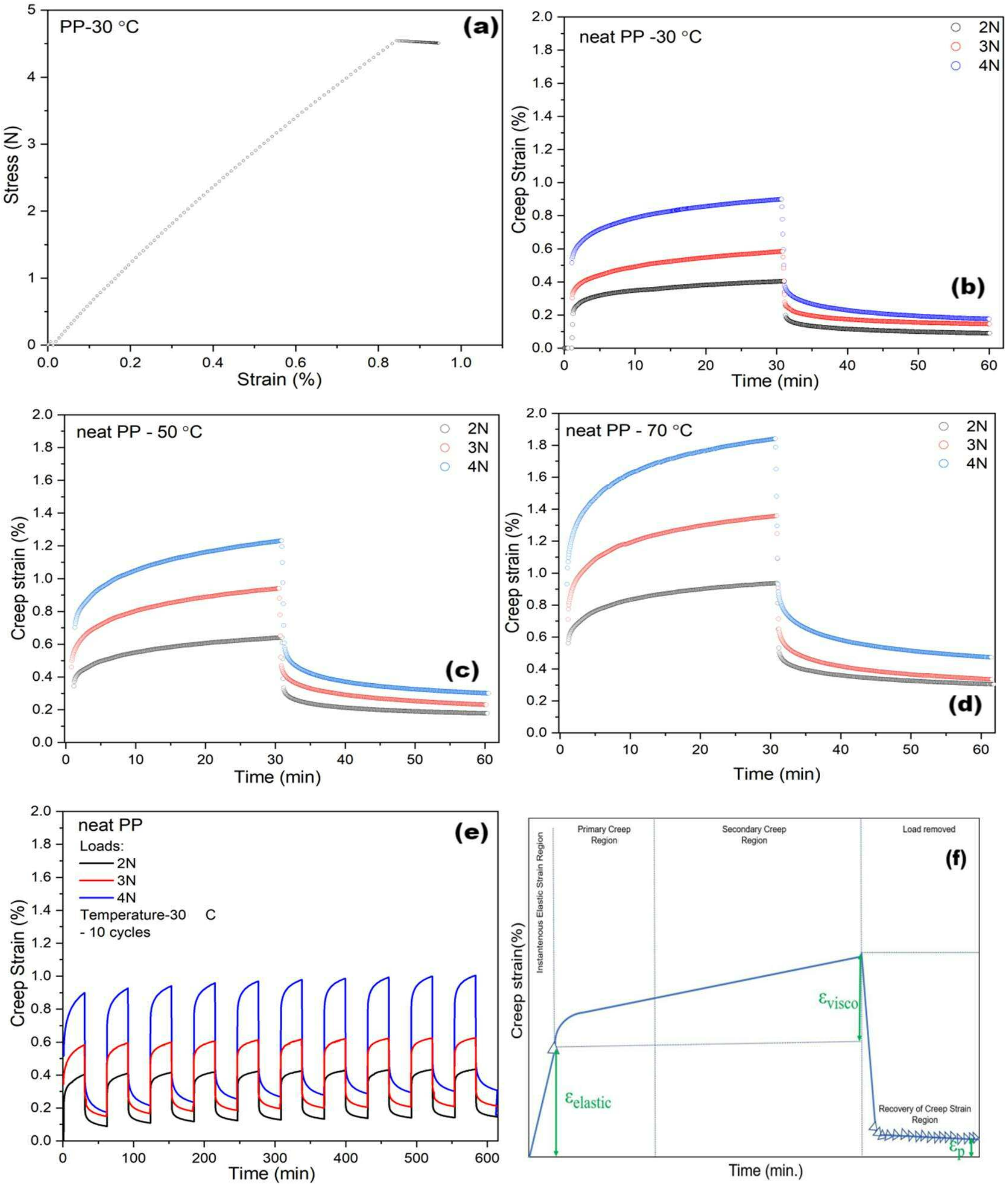

Figure 5- 19: (a) The stress-strain curve of neat PP obtained at 30 ℃; creep recovery curves of neat PP at different temperature (b) 30 ℃; (c) 50 ℃; (d) 70 ℃ under different stress levels; and its (e) cyclic creep recovery curves at different loads (30 ℃);(f) Typical creep-recovery curve.

recovers instantaneously, whilst the purely viscous deformation remains due to unrecoverable chain reorientation, defined as permanent deformation (ε_p).

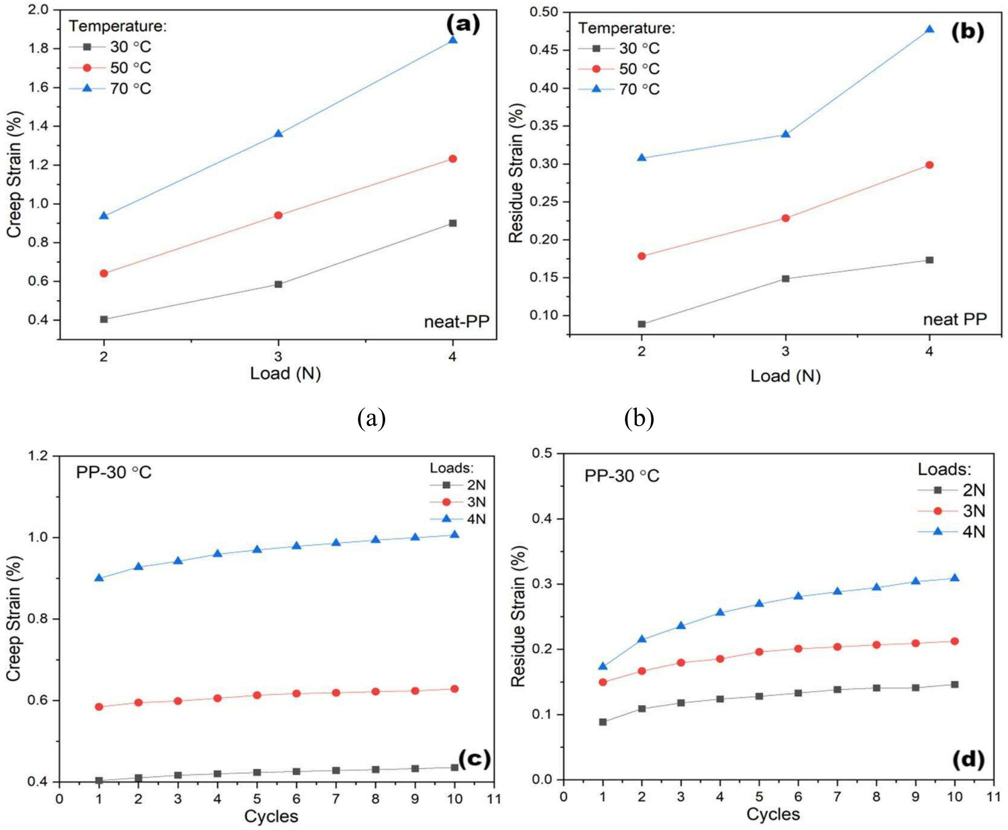

(a) (b)

Figure 5- 20: (a) The maximum strain of neat PP obtained at different temperatures and different stress levels; (b) the permanent strain of neat PP obtained at different temperatures and different stress levels; (c) the maximum strain of neat PP after different cycles; (d) the residue strain of neat PP after different cycles.

A clear temperature- and stress-dependent trend is observed. At 2 N, ε_{max} increased from 0.40% at 30°C to 0.94% at 70°C, while ε_p rose from 0.08% to 0.31%. Similarly, as stress increased from 2 N to 4 N, εmax increased by factors of 2.22, 1.92, and 1.96 at 30°C , 50°C, and 70°C, respectively. Permanent strain exhibited a similar trend, increasing by factors of 1.95, 1.67, and 1.55 across these temperatures. These results demonstrate that both ε_{max} and ε_p increase with stress and temperature, with greater sensitivity observed at higher temperatures (Figure 5-20a–b).

The creep-recovery behaviour of polypropylene (PP) is significantly influenced by temperature and stress level, owing to its complex molecular architecture and semi-crystalline structure. When subjected to stress, PP's response is governed by its molecular configuration, temperature, time allowed for chain rearrangement mobility, and crucially, the interplay between its amorphous and crystalline regions [43]. Upon application of stress, the initial deformation occurs primarily in the amorphous phase through elastic molecular chain rearrangements. However, this chain mobility is constrained by the presence of the crystalline phase. As stress persists, progressive alterations in the crystalline region can ensue, including inter-lamellar separation, rotation and twisting of lamellae, lamellar block slip, chain slip through crystals, and sliding and separation of tie molecules [44].

Temperature plays a key role in modulating PP's creep behaviour. As the temperature increases, the proportion of mobile chain segments in the polymer increases correspondingly. Concurrently, the intermolecular forces, such as van der Waals interactions and hydrogen bonds, which maintain the cohesion between polymer chains, are weakened. This weakening of intermolecular bonds facilitates greater chain mobility, allowing the polymer chains to slide past one another more readily. Additionally, the free volume within the polymer expands, facilitating greater chain segment movement [41]. Notably, when the temperature exceeds the α-transition point (typically >50°C for PP , as revealed by DMA in Figure 5-14), chain motions in the rigid amorphous phase become more pronounced. This enhanced molecular mobility leads to an increase in creep strain due to more active chain movements. The stress level also significantly impacts the creep-recovery response of PP. Higher stress levels induce greater deformation as the material attempts to relieve and redistribute the applied stress. This increased deformation results in a larger viscous strain component, ultimately leading to higher permanent strain after stress removal.

In real-world applications, plastic components are frequently subjected to repetitive loads and mechanically aggressive forces over extended periods. Understanding the time-dependent deformation of polymers under such conditions is crucial for assessing their long-term performance and durability. Cyclic creep-recovery tests provide valuable insights into this behaviour, offering a more comprehensive evaluation of a material's mechanical lifetime under various stress levels and thermomechanical deformation rates. Cyclic testing involves a repeating pattern of loading and unloading, which can reveal the accumulation of permanent strain in polymers. This permanent deformation can be attributed to several interrelated factors, including plastic deformation mechanisms and damage accumulation [45]. By subjecting materials to multiple cycles of stress, researchers can observe how these mechanisms evolve over time and under repeated loading conditions.

To investigate these phenomena in polypropylene (PP), cyclic creep-recovery tests were conducted. The experiments were performed at 30°C, with ten loading and unloading cycles applied at forces of 2, 3, and 4 N. Both creep and recovery periods were set at 30 minutes for each cycle. The resulting cyclic creep and recovery curves for neat PP are presented in Figure 5-19 (e) and Figure 5-20 c&d.

The results demonstrate that the total maximum strain or deformation increased progressively with the number of cycles. Both ε_{max} (maximum strain) and ε_p (permanent strain) increased with stress growth, indicating a more pronounced rate of deformation. Comparing the first cycle of creep to the tenth cycle, ε_{max} at 2 and 3 N both increased by approximately 7%, whilst ε_{max} at 4 N increased by 11.8%. The changes in permanent strain were more pronounced; at the tenth recovery cycle, ε_p increased by 65%, 42%, and 78% for 2, 3, and 4 N, respectively.

These findings highlight the time-dependent viscoelastic characteristics of PP and demonstrate accumulated damage due to unrecoverable strain under repeated loading and unloading. This behaviour underscores the importance of considering cyclic loading conditions when assessing the long-term performance of PP components in practical applications.

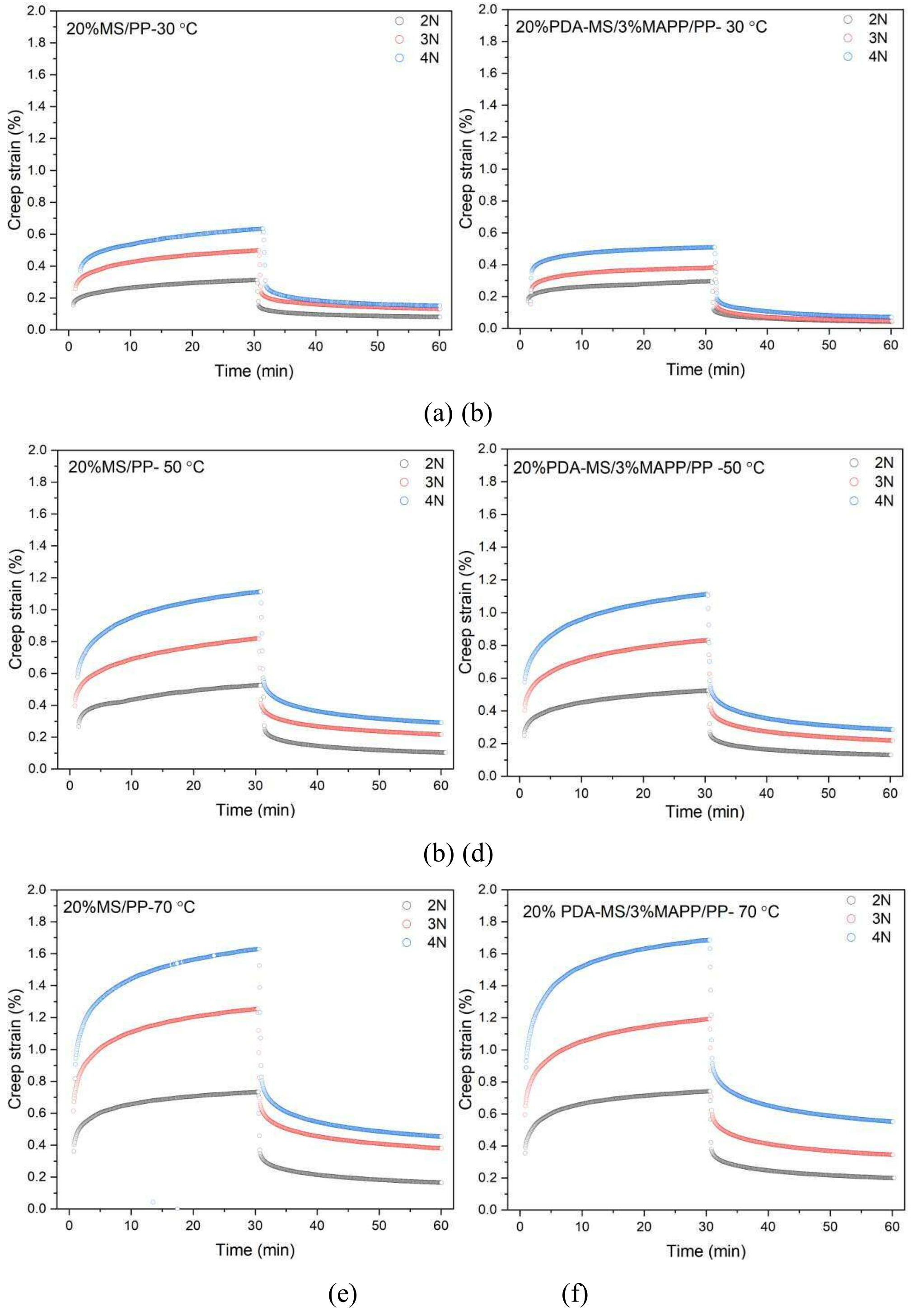

(a) (b)

(b) (d)

(e) (f)

Figure 5- 21: Creep-recovery curves of (a) 20%MS/PP and (b) 20%PDA/MAPP-MS/PP at 30℃ under 2/3/4 N stress; Creep-recovery curves of (c) 20%MS/PP and (d) 20%PDA/MAPP-MS/PP at 50 ℃ under 2/3/4 N stress; Creep-recovery curves (e) 20%MS/PP and (f) 20%PDA/MAPP-MS/PP at 70 ℃ under 2/3/4 N stress.

5.8.2 Comparison of creep-recovery behaviours of 20%MS/PP and 20% PDA/MAPP-MS/PP

Figure 5-21 (a)-(f) illustrates the creep-recovery curves of PP composites containing 20% untreated and PDA/MAPP co-modified mussel shell fillers at various stress levels and temperatures. Both PP composites exhibit time, temperature, and stress-dependent behaviour similar to neat PP, indicating that the viscoelastic nature of the matrix predominantly governs the creep properties. The composites demonstrate increased maximum creep strain with elevated temperature and stress levels, with higher permanent strain correlating to higher maximum creep strain, as can be seen from Figure 5-22.

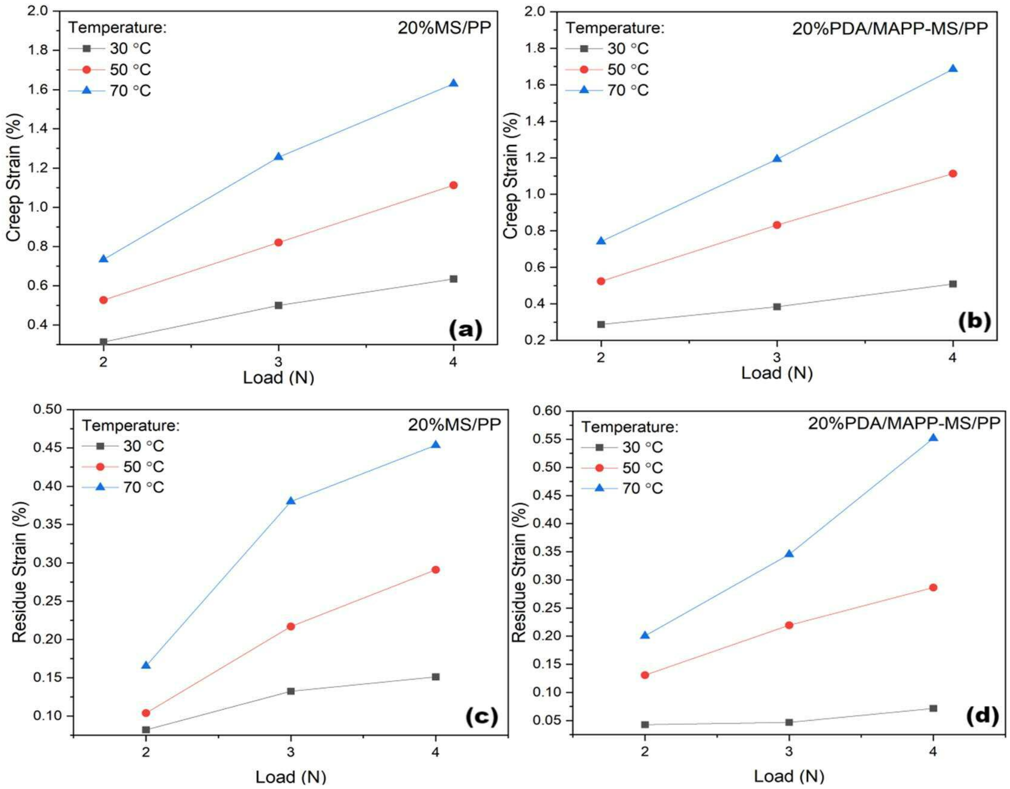

Figure 5- 22: Maximum creep strains of (a) 20% MS/PP and (b) 20%PDA/MAPP-MS/PP under different stresses and temperature; Permanent strains of (c) 20% MS/PP and (d) 20%PDA/MAPP-MS/PP under different stresses and temperature.

Table 5-11 compares the maximum creep strain (ε_{max}) and permanent strain (ε_p) of neat PP with the two PP composites. At 30℃, the incorporation of untreated MS fillers improved creep resistance by reducing ε max by 22.5%, 14.5%, and 29.4% at 2, 3, and 4 N, respectively, compared to neat PP. Permanent strain decreased by 7.45%, 9.07%, and 12.76% under the same stresses. PDA/MAPP-MS fillers yielded much greater improvements: ε_{max} decreased by 29.0%, 34.2%, and 43.4%, while ε_{p} decreased by 51.69%, 67.86%, and 58.66%, respectively. These results demonstrate that PDA/MAPP modification substantially enhances creep resistance beyond what is achieved by untreated fillers.

The improved performance of untreated MS/PP arises from the rigid filler particles restricting chain mobility in the amorphous regions of PP. In contrast, PDA/MAPP co-modification introduces abundant functional groups that promote stronger filler－matrix adhesion. This enhanced interfacial interaction restricts chain slippage and rearrangement more effectively, resulting in significantly reduced deformation and permanent strain.

At higher temperatures (50°C and 70°C) under 3 and 4 N stress, however, the benefits of PDA/MAPP modification diminish. Under these conditions, PP enters the rubbery region, as shown by DMA results. Chain mobility of the polymer in the rubbery region is enhanced by increased free volume and thermal energy, overriding the restraining effects of interfacial adhesion from surface-modified fillers. Localised interfacial debonding may also occur under high stress, further reducing the effectiveness of PDA/MAPP modification. Thus, while PDA/MAPP-MS fillers improve creep resistance at ambient conditions, their relative advantages become less pronounced at elevated temperatures and stresses.

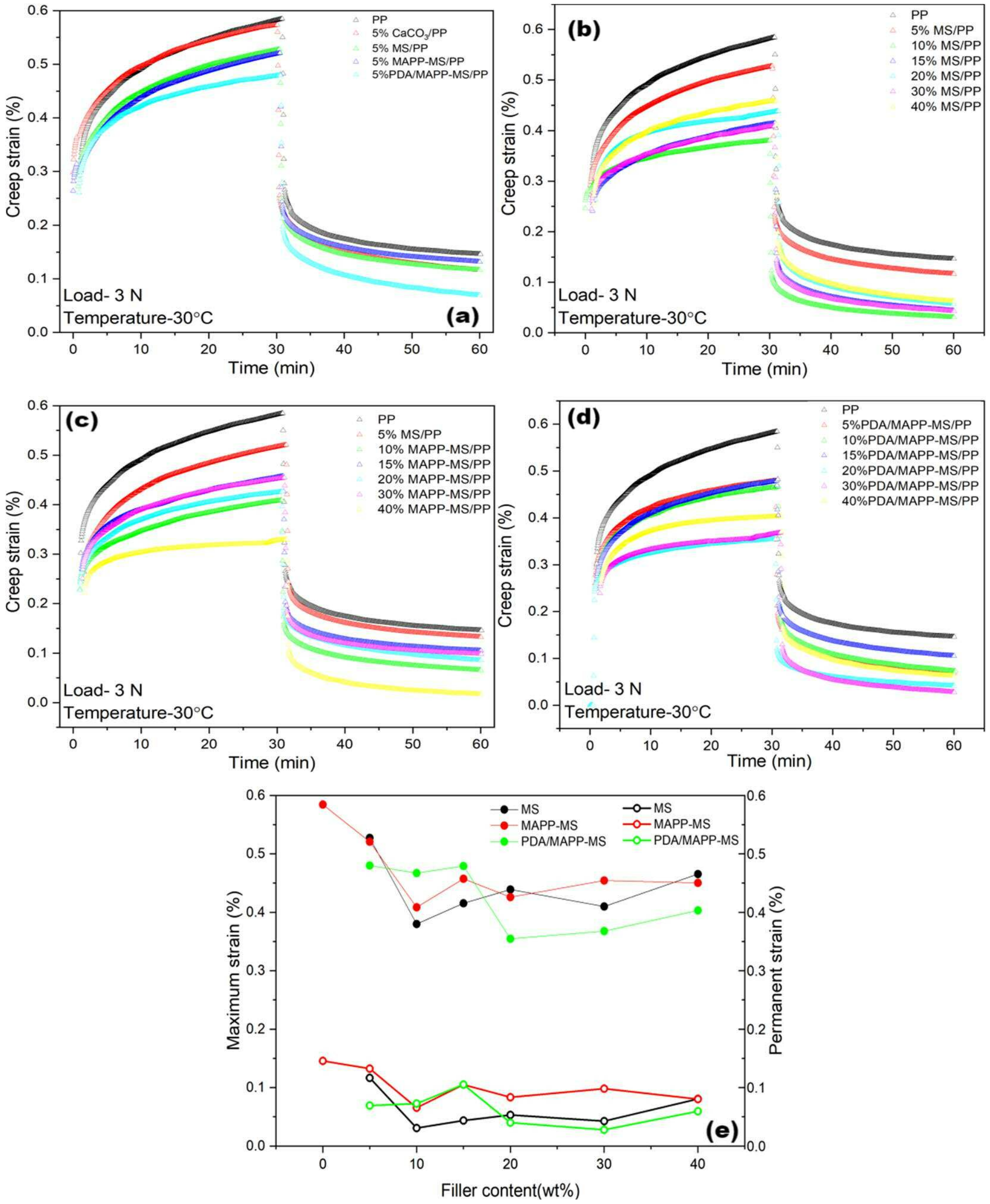

Figure 5- 23: Creep-recovery curves of (a) neat PP and PP composites with 5% different fillers; (b) neat PP and PP composites with various amount mussel shell fillers; (c) neat PP and PP composites with various amount MAPP-MS fillers;(d)neat PP and PP composites with various amount PDA/MAPP-MS fillers;(e) Comparison of maximum strain(solid symbols) and permanent strain(hollow symbols) of neat PP and PP composites

5.8.3 Creep-recovery behaviours of PP composites with various filler types and filler amounts

Building on the insights gained from the creep-recovery behaviour of PP composites with 20% mussel shell fillers, it is essential to explore how varying filler amounts and types influence creep resistance. The following section will compare the creep-recovery behaviour of PP composites containing different amounts of mussel shell fillers (ranging from 5% to 40%) and various surface modifications—untreated, MAPP-modified, and PDA/MAPP co-modified—under controlled conditions of 30° C and 3N stress. This focused analysis will provide a clearer understanding of how filler content and interfacial adhesion affect the viscoelastic response of these materials, informing future composite design strategies.

As illustrated in Figure 5-23 (a), neat polypropylene (PP) exhibits the highest maximum strain and permanent strain, indicating that the creep resistance improved by incorporating 5% different rigid fillers. The addition of 5% commercial $CaCO_3$ only improves the permanent strain (lower value), whilst the incorporation of 5% untreated or MAPP-modified mussel shell fillers enhances both maximum and permanent strain. Notably, enhanced creep resistance is achieved through the addition of 5% PDA/MAPP-modified mussel shell (MS) fillers.

These observations can be elucidated by considering the filler surface properties and filler-matrix interactions, as discussed in the preceding section. Commercial $CaCO_3$ is an inorganic filler with a highly hydrophilic surface; therefore, it is inherently incompatible with the hydrophobic PP matrix. Although the surface of the mussel shell remains hydrophilic, it may achieve better dispersion within the PP matrix due to the presence of trace organic components (e.g., proteins and polysaccharides). The most favourable fillers, demonstrating superior compatibility and interfacial adhesion, were successfully produced via PDA/MAPP co-modification.

Figures 5-23(b – d) reveal a consistent trend across all composites: increasing filler content (5 – 40%) reduced both ε_{max} and ε_p, confirming that higher rigid filler loading levels improve creep resistance by restricting chain motion. Figure 5-23(e) highlights the strong positive correlation between ε_{max} and ε_p. At loadings above 20%, PDA/MAPP-MS fillers consistently outperformed untreated and MAPP-MS fillers, demonstrating the importance of interfacial adhesion at higher concentrations. Quantitatively, compared to neat PP, the ε max of 20%, 30%, and 40% PDA/MAPP-MS/PP decreased by 39%, 37%, and 31%, while ε p decreased by 72%, 81%, and 59%, respectively.

The creep-recovery behaviour of polymer composites is inherently complex, governed by multiple interdependent variables. Maximum strain is a function of applied stress, loading duration, and material-specific factors, including filler concentration, morphology, aspect ratio, filler-matrix interfacial properties, and inherent structural heterogeneities [45]. Starkova et al. observed that permanent strain exhibited a positive correlation with both stress magnitude and loading duration, while demonstrating an inverse relationship with MWCNT filler content. Furthermore, cyclic loading data corroborated these trends [45]. The improved creep resistance with PDA/MAPP-MS fillers arises from a combination of efficient stress transfer and restricted chain mobility due to enhanced filler dispersion and stronger interfacial bonding. In contrast, untreated MS fillers, despite some inherent heterogeneity aiding dispersion, showed inferior performance due to weaker matrix interactions.Polypropylene (PP) composites incorporating different mussel shell fillers at

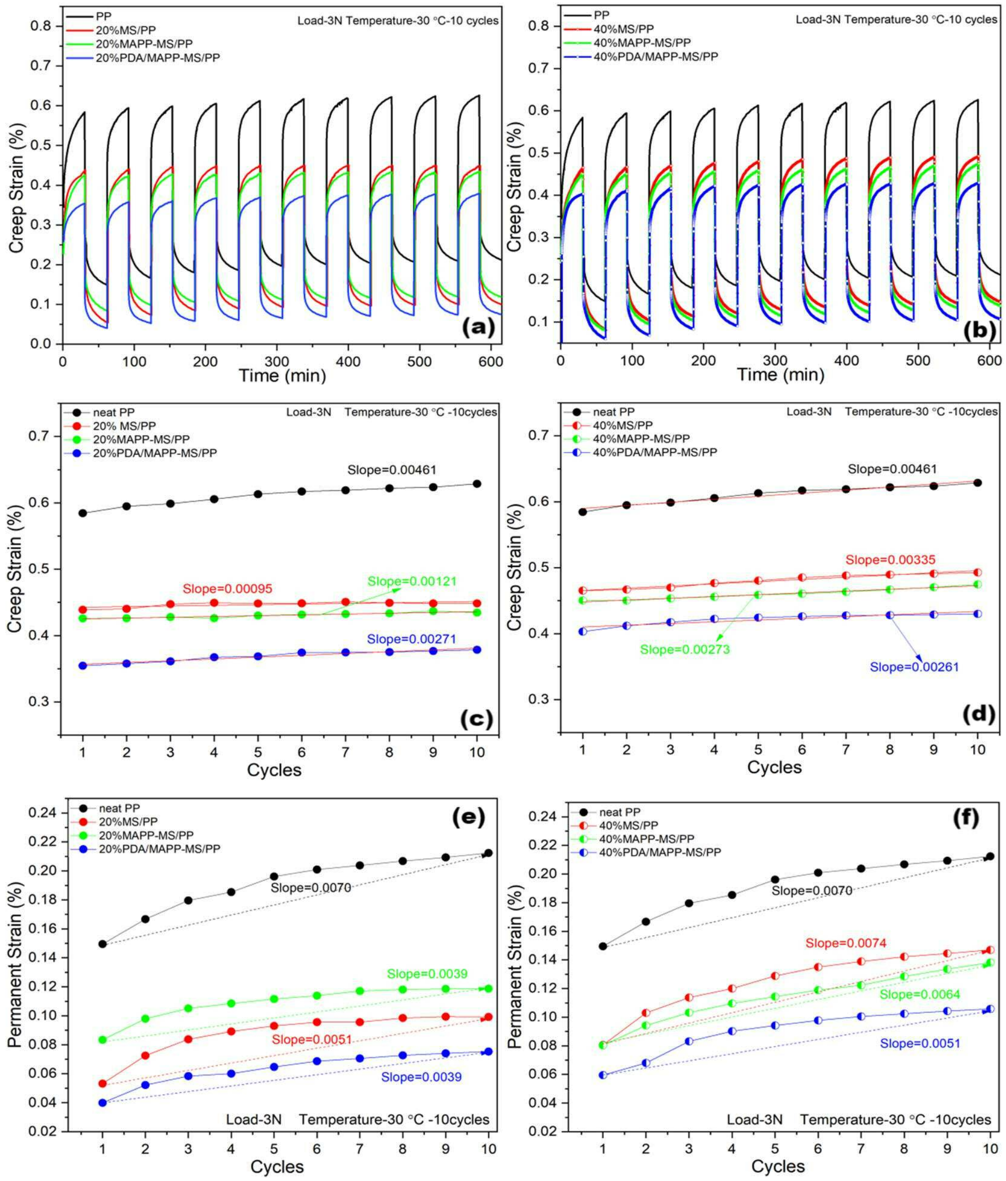

Figure 5- 24: Cyclic creep-recovery curves of neat PP and PP composites with (a) 20% different mussel shell fillers and (b) 40% different mussel shell fillers; Comparison of creep strains of (c) 20% different mussel shell fillers and (d) 40% different mussel shell fillers; Comparison of permanent strains of (e) 20% different mussel shell fillers and (f) 40% different mussel shell fillers.

20% and 40% loading levels were subjected to cyclic stress loading and unloading, with results presented in Figure 5-24(a-f). Neat PP was included for comparison. After 10 cycles of creep-recovery tests at 30°C under a 3N load, PP composites with 20% of three different mussel shell fillers demonstrated superior creep resistance compared to neat PP, consistent with observations from single creep-recovery tests. Notably, PP composites with 20% PDA/MAPP-MS fillers exhibited the most significant improvement in creep resistance relative to composites containing 20% untreated or MAPP-modified mussel shell fillers, as evident from the creep-recovery curves in Figure 5-24(a).

As filler content increased to 40%, the maximum creep strain and permanent strain of PP composites slightly increased, indicating reduced creep resistance compared to composites with 20% filler. However, the overall improvement in creep resistance remained evident with the addition of 40% mussel shell fillers, as illustrated by the 10-cycle creep-recovery curves in Figure 5-24(b).

The maximum strain and permanent strain values were plotted against cycle number, as shown in Figure 5-24(c-f). Linear fitting slopes for maximum strain indicate a subtle accumulation effect during repeated stress loading and unloading, although changes over cycles were minimal. Comparing slopes between 20% and 40% filler content for untreated and MAPP-modified mussel shell fillers revealed slight increases. The slope for 20% MS/PP maximum strain plots against cycle number was 0.0095, increasing to 0.00335 for 40% MS/PP. Similarly, the slope for 20% MAPP-MS/PP increased from 0.00121 to 0.00273 at 40% filler content. Interestingly, the slope for PDA/MAPP-MS/PP remained nearly constant between 20% and 40% filler content.

The accumulation of creep strain can be attributed to the viscous characteristics of the PP matrix and defects introduced by filler addition due to filler-matrix incompatibility, resulting in unrecoverable deformation. Consequently, PDA/MAPP-modified mussel shell fillers, with improved dispersion and interfacial adhesion, exhibited less pronounced creep strain accumulation under cyclic stress.

Permanent strain plots against cycle number demonstrated less linearity. Slopes calculated from the first and tenth permanent strain values indicated that PP composites with higher (40%) filler content exhibited slightly steeper increase trends (higher slopes) compared to their 20% counterparts.

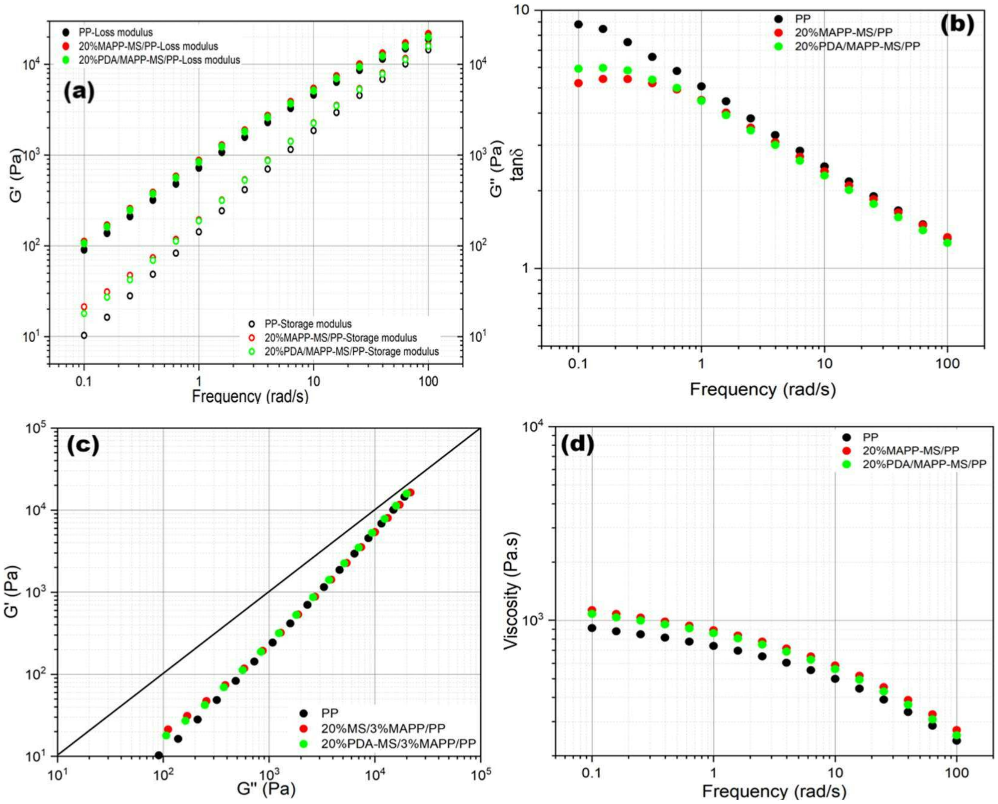

Figure 5- 25: Rheological properties of PP and its composites. (a) Storage moduli and loss moduli, (b) damping factor, (c) Han plots for PP, 20% MAPP-MS/PP, and 20% PDA/MAPP-MS/PP composites, (d) shear viscosity as a function of angular frequency.

5.9 Melt rheological analysis

Polymer processing typically occurs at elevated temperatures in the molten state. A characteristic feature of polymer melts is their non-Newtonian behaviour, exhibiting shear-thinning properties where viscosity decreases with increasing shear rate. This shear-thinning behaviour is relevant to processing phenomena such as die swell post-extrusion and influences end-use properties, including warpage and stress cracking resistance.

The introduction of fillers into a polymer melt alters its rheological behaviour, affecting both processability (e.g., extrusion and injection moulding) and end-product properties. Key factors influencing these changes include filler size, shape, size distribution, concentration, and surface chemistry [46]. Understanding the impact of fillers on melt rheological behaviour is particularly crucial for optimising production processes.

This section presents the melt rheological behaviour of PP composites incorporating 20% surface-modified mussel shell fillers (MAPP-MS and PDA/MAPP-MS) as a function of angular frequency, comparing them with neat PP. The results are presented in Figure 5-25 (a)-(d).

The characteristic curves of storage modulus (G'), loss modulus (G"), damping factor (tan δ), and shear viscosity all exhibit frequency-dependent behaviour, as shown in Figure 5-25 (a-b) and (d). The effect of fillers is more pronounced at low frequencies, corresponding to longer relaxation regimes. At low angular frequencies, there is sufficient time for chain entanglements to unravel, resulting in lower storage moduli values. Generally, composite melts demonstrate reduced frequency dependence in the low-frequency region due to the restrictive effect of filler particles on chain mobility [47].

As illustrated in Figure 5-25(a), both storage (G') and loss (G") moduli increase with frequency for neat PP and its composites. Across all frequencies, the moduli of PP composites exceed those of neat PP, with loss moduli consistently higher than storage moduli for all samples. In the lower frequency range (0.1-10 rad/s), PP composites containing 20% MS or PDA/MAPP-MS fillers exhibit slightly higher storage and loss moduli compared to neat PP, with the difference more pronounced for storage modulus. This observation agrees with the understanding that storage modulus is a more sensitive rheological indicator of structural changes in multi-component polymeric systems such as composites. At low frequencies, neat PP and all PP composites demonstrate typical liquid viscoelastic behaviour (G" > G'). Conversely, in the high-frequency region, the values of G' and G" converge for neat PP and both PP composites. This convergence suggests that at higher frequencies, the behaviour of the composites is predominantly governed by the matrix, with the contribution of filler particles becoming less significant [48].

The damping factor (tanδ= G"/G') serves as an indicator of the viscous and elastic components in polymers, with perfect viscous fluids exhibiting tanδ=∞ and elastic solids showing tanδ=0. Figure 5-25(b) illustrates the damping factor curves for neat PP and PP composites containing 20% MAPP-MS or PDA/MAPP-MS. Neat PP demonstrates a rapid descent in tanδ across the entire frequency range, approaching 1, which is characteristic of terminal behaviour in liquid-like melt materials. In contrast, PP composites with 20% MAPP-MS or PDA/MAPP-MS fillers exhibit a plateau at low frequencies before transitioning to a rapid descent as frequency increases. This behaviour indicates that both fillers significantly alter the rheological properties, inducing a transition from melt-like to solid-like behaviour. Similar observations have been reported in melt rheological analyses of Polypropylene/Novolac Blends [49] and long-chain branched PP[50]. These studies attributed the phenomenon to increased terminal relaxation times resulting from the addition of Novolac and MAPP, or the grafting of long-chain branches, respectively. In the present study, the extended terminal relaxation time can be attributed to the restricted polymer chain motions caused by the introduction of surface-modified mussel shell fillers.

Han plots (G' vs G") in Figure 5-25(c) provide a comparative analysis of the elastic (G') and viscous (G") behaviours of the specimens. The diagonal line represents the relationship G' = G". Across the entire modulus range, viscous characteristics dominate for both neat PP and the two PP composites, with this dominance more pronounced in the lower modulus region.

Figure 5-25(d) illustrates the shear viscosity obtained from frequency sweep tests for neat PP and the two PP composites. All samples exhibit similar characteristic flow curves, featuring a Newtonian (constant viscosity) plateau at low shear frequencies (0.1-0.5 rad/s), followed by a transition to non-Newtonian (shear-thinning) behaviour. The incorporation of 20 % MAPP or PDA/MAPP modified mussel shell fillers results in higher viscosities compared to neat PP across the entire frequency range.

Shear viscosity, representing resistance to shear force, increases with the addition of surface-modified mussel shell fillers. This elevation in viscosity suggests that the fillers restrict polymer chain mobility, likely due to physical obstruction by dispersed filler particles and potential filler-matrix interactions. Consequently, these PP composites are expected to exhibit reduced die swell during processing.

The transition from Newtonian to non-Newtonian behaviour is characterized by the critical shear rate (γ_c). For polypropylene (PP), γ_c is typically observed at approximately 0.5 s^{-1}, as evidenced by the clear Newtonian plateau at low shear rates [47]. As illustrated in Figure 5-25(d), the critical shear rate for the PP composites with 20% MAPP-MS or PDA/MAPP-MS fillers remains largely unchanged compared to neat PP. Shear viscosities generally decrease with increasing shear frequency, a phenomenon known as shear thinning. At lower frequencies, the entanglement of polymer chains impedes shear flow, resulting in higher viscosity. As shear frequency increases, molecular alignments and disentanglement of the long polymer chains occur, leading to lower viscosity [48].

Notably, at higher shear rates, the effect of the filler diminishes, and the matrix contributions become dominant. This observation is consistent with the convergence of viscosity curves for neat PP and its composites at high frequencies, as seen in Figure 5-25(d). The reduced influence of fillers at high shear rates can be attributed to the breakdown of filler networks and the overwhelming effect of polymer chain alignment in the flow direction.

5.10 Conclusion

This chapter demonstrates that the incorporation of mussel shell fillers, particularly when surface-modified, significantly enhances the properties of polypropylene (PP) composites across multiple dimensions. The effects vary depending on filler type, surface modification, and loading level, with PDA/MAPP co-modification consistently showing the most promising results.

MAPP and PDA/MAPP modified mussel shell fillers substantially improve the thermal stability of PP composites. The 5% weight loss temperature ($T_{5\%}$) increased from 400 ℃ for neat PP to 425 ℃ for 40% PDA/MAPP-MS/PP, with similar improvements in maximum degradation temperature. This enhancement is attributed to improved filler-matrix compatibility and dispersion, facilitating more efficient heat absorption and polymer chain movement restriction.

The introduction of mussel shell fillers induces the formation of both α- and β-crystalline forms in PP composites, compared to only α-form in neat PP. MAPP-MS fillers were most effective in promoting the cross-hatched structure in PP. At higher filler loadings (30-40%), β-PP diminished for all composites, indicating that excessive filler content inhibits β-crystalline formation. Both MAPP and PDA/MAPP modifications enhanced PP crystallisation through improved interfacial adhesion.

PDA/MAPP co-modified mussel shell fillers demonstrated the most significant improvements in both stiffness and strength across all loading levels. At 40% loading, PDA/MAPP-MS/PP composites exhibited a 66.10% increase in Young's modulus, a 6.2% increase in tensile strength, and a 15.1% increase in flexural strength compared to neat PP. These improvements are attributed to enhanced interfacial adhesion, improved stress transfer, and better filler dispersion within the PP matrix.

Dynamic Mechanical Analysis (DMA) revealed that PDA/MAPP co-modified fillers provided the best improvement in storage modulus, particularly at higher temperatures, indicating enhanced filler-matrix interaction and restricted polymer chain mobility. Creep-recovery tests showed that PDA/MAPP-MS/PP composites exhibited superior creep resistance, especially at lower temperatures and stress levels. Melt rheology studies indicated that the addition of surface-modified mussel shell fillers increased shear viscosity and altered the viscoelastic behaviour of PP composites, transitioning from melt-like to more solid-like behaviour at low frequencies.

SEM observations corroborated the mechanical and viscoelastic findings, showing that PDA/MAPP co-modified fillers demonstrated the strongest bonding with the PP matrix. This was evidenced by polymer fibrils acting as bridges at filler edges and a smoother, more brittle fractured surface, indicating enhanced filler-matrix adhesion.

In conclusion, this study highlights the effectiveness of surface modification strategies, particularly PDA/MAPP co-modification, in optimising the overall performance of PP/mussel shell composites. This approach achieves a favourable balance between strength and stiffness, addressing the trade-off frequently encountered in filled polymer systems. The PDA/MAPP co-modification strategy emerges as the most promising approach for enhancing thermal stability, mechanical strength, and viscoelastic properties, especially at higher filler loadings.

These findings contribute significantly to the development of high-performance, bio-based polymer composites and offer valuable insights into the structure-property relationships in filled polymer systems. Future work should focus on optimising processing conditions and exploring potential applications for these enhanced PP/mussel shell composites in various industrial sectors, particularly where improved thermal stability, mechanical strength, and creep resistance are required.

5.11 References

1. Das, O., Bhattacharyya, D., Hui, D.*, et al.* (2016). Mechanical and flammability characterisations of biochar/polypropylene biocomposites. *Composites Part B: Engineering*, *106*, 120-128.
2. Părpăriţă, E., Nistor, M. T., Popescu, M.-C.*, et al.* (2014). TG/FT–IR/MS study on thermal decomposition of polypropylene/biomass composites. *Polymer Degradation and Stability*, *109*, 13-20.
3. Davachi, S. M., Heidari, B. S., Sahraeian, R.*, et al.* (2019). The effect of nanoperlite and its silane treatment on the crystallinity, rheological, optical, and surface properties of polypropylene/nanoperlite nanocomposite films. *Composites Part B: Engineering*, *175*, 107088.
4. García, P. G., Ramírez-Aguilar, R., Torres, M.*, et al.* (2018). Mechanical and thermal behavior dependence on graphite and oxidized graphite content in polyester composites. *Polymer*, *153*, 9-16.
5. Zhou, Q., & Xanthos, M. (2009). Nanosize and microsize clay effects on the kinetics of the thermal degradation of polylactides. *Polymer Degradation and Stability*, *94*(3), 327-338.

6. ASTM International. (2022). *Standard Test Method for Tensile Properties of Plastics* West Conshohocken.
7. Hamour, N., Boukerrou, A., Djidjelli, H., *et al.* (2015). Effects of MAPP Compatibilization and Acetylation Treatment Followed by Hydrothermal Aging on Polypropylene Alfa Fiber Composites. *International journal of polymer science*, *2015*, 1-9.
8. Kim, H.-S., Lee, B.-H., Choi, S.-W., *et al.* (2007). The effect of types of maleic anhydride-grafted polypropylene (MAPP) on the interfacial adhesion properties of bio-flour-filled polypropylene composites. *Composites Part A: Applied Science and Manufacturing*, *38*(6), 1473-1482.
9. Ahmad, S. R., Xue, C., & Young, R. J. (2017). The mechanisms of reinforcement of polypropylene by graphene nanoplatelets. *Materials Science and Engineering: B*, *216*, 2-9.
10. Jones, A. T., Aizlewood, J. M., & Beckett, D. R. (1964). Crystalline forms of isotactic polypropylene. *Die Makromolekulare Chemie*, *75*(1), 134-158.
11. do Nascimento, E. M., Eiras, D., & Pessan, L. A. (2016). Effect of thermal treatment on impact resistance and mechanical properties of polypropylene/calcium carbonate nanocomposites. *Composites Part B: Engineering*, *91*, 228-234.
12. Bhuiyan, M. K. H., Rahman, M. M., Mina, M. F., *et al.* (2013). Crystalline morphology and properties of multi-walled carbon nanotube filled isotactic polypropylene nanocomposites: Influence of filler size and loading. *Composites. Part A, Applied science and manufacturing*, *52*, 70-79.
13. Kotek, J., Kelnar, I., Baldrian, J., *et al.* (2004). Tensile behaviour of isotactic polypropylene modified by specific nucleation and active fillers. *European Polymer Journal*, *40*(4), 679-684.
14. Cangiotti, J., Scatto, M., Araya-Hermosilla, E., *et al.* (2022). Valorization of seashell waste in polypropylene composites: An accessible solution to overcome marine landfilling. *European Polymer Journal*, *162*, 110877.
15. Labour, T., Gauthier, C., Séguéla, R., *et al.* (2001). Influence of the β crystalline phase on the mechanical properties of unfilled and CaCO3-filled polypropylene. I. Structural and mechanical characterisation. *Polymer*, *42*(16), 7127-7135.
16. Yuan, Q., Jiang, W., & An, L. (2004). Study of β–α recrystallization of the polypropylene. *Colloid and Polymer Science*, *282*, 1236-1241.
17. Majerczak, K., Wadkin-Snaith, D., Magueijo, V., *et al.* (2022). Polyhydroxybutyrate: a review of experimental and simulation studies of the effect of fillers on crystallinity and mechanical properties. *Polymer international*, *71*(12), 1398-1408.
18. Sahraeian, R., Davachi, S. M., & Heidari, B. S. (2019). The effect of nanoperlite and its silane treatment on thermal properties and degradation of polypropylene/nanoperlite nanocomposite films. *Composites Part B: Engineering*, *162*, 103-111.
19. Zebarjad, S. M., Tahani, M., & Sajjadi, S. A. (2004). Influence of filler particles on deformation and fracture mechanism of isotactic polypropylene. *Journal of materials processing technology*, *155-156*, 1459-1464.
20. Callister Jr, W. D., & Rethwisch, D. G. (2020). Materials science and engineering: an introduction. John wiley & sons.
21. Fu, S.-Y., Feng, X.-Q., Lauke, B., *et al.* (2008). Effects of particle size, particle/matrix interface adhesion and particle loading on mechanical properties of particulate–polymer composites. *Composites Part B: Engineering*, *39*(6), 933-961.

22. Peceño, B., Alonso-Fariñas, B., Arenas, C., & Leiva, C. (2021). Influence of particle size of mussel shells in physical, mechanical and insulating properties of fireproof materials Procedia Environmental Science, Engineering and Management,
23. Owuamanam, S., & Cree, D. (2020). Progress of bio-calcium carbonate waste eggshell and seashell fillers in polymer composites: a review. *J. Compos. Sci.*, *4*(2).
24. Li, H. Y., Tan, Y. Q., Zhang, L*., et al.* (2012). Bio-filler from waste shellfish shell: preparation, characterization, and its effect on the mechanical properties on polypropylene composites. *J. Hazard. Mater.*, *217-218*(30), 256-262.
25. Dear, D. J. (1999). A study of polymer fracture surface features and their relationship to toughness. *JOURNAL OF MATERIALS SCIENCE*, *34*, 4897-4907.
26. Kim, H. S., Lee, B. H., Choi, S. W*., et al.* (2007). The effect of types of maleic anhydride-grafted polypropylene (MAPP) on the interfacial adhesion properties of bio-flour-filled polypropylene composites. *Compos. Part A: Appl. Sci. Manuf.*, *38*(6), 1473-1482.
27. Lu, J. Z., Wu, Q., & Negulescu, I. I. (2005). Wood-fiber/high-density-polyethylene composites: Coupling agent performance. *J. Appl. Polym. Sci.*, *96*(1), 93-102.
28. Pickering, K. L., Efendy, M. G. A., & Le, T. M. (2016). A review of recent developments in natural fibre composites and their mechanical performance. *Compos. Part A: Appl. Sci. Manuf.*, *83*(1), 98-112.
29. Niwa, S., Ogawa, T., Ogoe, S*., et al.* (2019). Wetting and localization of compatibilizers in biocomposites: A nanoscale evaluation and effects on physical properties. *Polymer*, *185*(17), 121963.
30. Ambrogi, V., Gentile, G., Ducati, C*., et al.* (2012). Multiwalled carbon nanotubes functionalized with maleated poly(propylene) by a dry mechano-chemical process. *Polymer*, *53*(2), 291-299.
31. Qiu, W., Endo, T., & Hirotsu, T. (2004). Interfacial interactions of a novel mechanochemical composite of cellulose with maleated polypropylene. *J. Appl. Polym. Sci.*, *94*(3), 1326-1335.
32. Seshweni, M. H. E., Makhatha, M. E., Botlhoko, O. J*., et al.* (2023). Evaluation of Mechanical and Thermal Properties of Polypropylene-Based Nanocomposites Reinforced with Silica Nanofillers via Melt Processing Followed by Injection Molding. *Journal of Composites Science*, *7*(12), 520.
33. Bashir, M. A. (2021). Use of dynamic mechanical analysis (DMA) for characterizing interfacial interactions in filled polymers. *Solids*, *2*(1), 108-120.
34. Senturk, O., Senturk, A. E., & Palabiyik, M. (2018). Evaluation of hybrid effect on the thermomechanical and mechanical properties of calcite/SGF/PP hybrid composites. *Composites. Part B, Engineering*, *140*, 68-77.
35. Etaati, A., Pather, S., Fang, Z*., et al.* (2014). The study of fibre/matrix bond strength in short hemp polypropylene composites from dynamic mechanical analysis. *Composites. Part B, Engineering*, *62*, 19-28.
36. Granda, L. A., Méndez, J. A., Espinach, F. X*., et al.* (2016). Polypropylene reinforced with semi-chemical fibres of Leucaena collinsii: Thermal properties. *Composites. Part B, Engineering*, *94*, 75-81.
37. Izwan, S. M., Sapuan, S. M., Zuhri, M. Y. M*., et al.* (2021). Thermal stability and dynamic mechanical analysis of benzoylation treated sugar palm/kenaf fiber reinforced polypropylene hybrid composites. *Polymers*, *13*(17), 2961.

38. Rana, A. K., Mitra, B. C., & Banerjee, A. N. (1999). Short jute fiber-reinforced polypropylene composites: Dynamic mechanical study. *Journal of Applied Polymer Science*, *71*(4), 531-539.

39. Jia, Y., Peng, K., Gong, X.-l.*, et al.* (2011). Creep and recovery of polypropylene/carbon nanotube composites. *International Journal of Plasticity*, *27*(8), 1239-1251.

40. Kurt, G., & Kasgoz, A. (2021). Effects of molecular weight and molecular weight distribution on creep properties of polypropylene homopolymer. *Journal of Applied Polymer Science*, *138*(30), 50722.

41. Bowman, A. L., Mun, S., Nouranian, S.*, et al.* (2019). Free volume and internal structural evolution during creep in model amorphous polyethylene by Molecular Dynamics simulations. *Polymer*, *170*, 85-100.

42. Starkova, O., Aniskevich, K., Sevcenko, J.*, et al.* (2021). Relationship between the residual and total strain from creep-recovery tests of polypropylene/multiwall carbon nanotube composites. *Journal of Applied Polymer Science*, *138*(10), 49957.

43. Genovese, A., & Shanks, R. A. (2007). Time-Temperature Creep Behaviour of Poly(propylene) and Polar Ethylene Copolymer Blends. *Macromolecular materials and engineering*, *292*(2), 184-196.

44. Kasgoz, A., Akın, D., & Durmus, A. (2016). Quantifying Structural and Solid-State Viscoelastic Properties of Poly(propylene) (PP)/Poly(oxymethylene) (POM) Blend Films. *Macromolecular materials and engineering*, *301*(11), 1402-1414.

45. Starkova, O., Aniskevich, K., Sevcenko, J.*, et al.* (2021). Relationship between the residual and total strain from creep-recovery tests of polypropylene/multiwall carbon nanotube composites. *Journal of Applied Polymer Science*, *138*(10), n/a.

46. Shenoy, A. V. (1999). Rheology of filled polymer systems. Springer Science+Business Media.

47. Alanalp, M. B., Durmus, A., & Aydin, I. (2019). Quantifying effect of inorganic filler geometry on the structural, rheological and viscoelastic properties of polypropylene-based thermoplastic elastomers. *Journal of Polymer Research*, *26*(2), 1-14.

48. Zdiri, K., Harzallah, O., Elamri, A.*, et al.* (2018). Rheological and thermal behavior of Tunisian clay reinforced recycled polypropylene composites. *Advances in Polymer Technology*, *37*(8), 3759-3768.

49. Cui, L., Zhou, Z., Zhang, Y.*, et al.* (2007). Rheological behavior of polypropylene/novolac blends. *Journal of Applied Polymer Science*, *106*(2), 811-816.

50. Tian, J., Yu, W., & Zhou, C. (2006). The preparation and rheology characterization of long chain branching polypropylene. *Polymer*, *47*(23), 7962-7969.

Chapter 6

Effects of hybrid fillers on the mechanical, thermal, and morphological properties of PP composites

6.1 Introduction

The incorporation of hybrid fillers in polymer composites has gained significant attention due to their potential to enhance material properties beyond what can be achieved with single fillers. This chapter builds upon the findings from Chapter 5, which explored the effects of various mussel shell fillers on polypropylene (PP) composites. While these fillers improved certain properties such as stiffness and thermal stability, they generally compromised mechanical strength, except for the polydopamine and maleic anhydride-grafted polypropylene co-modified mussel shell (PDA/MAPP-MS) fillers.

Hybrid composites offer a unique opportunity to synergise the individual advantages of different reinforcements, potentially leading to enhanced performance and reduced production costs [1-5]. The combination of geometrically different fillers, such as particulate inorganic fillers and natural fibres, can expand the limitations of single fillers and allow for tailored properties to meet specific application requirements [6]. Particulate inorganic fillers, including calcium carbonate, talc, and wollastonite, are known to reduce polymer material costs [6]. On the other hand, natural fibres have gained popularity as reinforcement fillers for PP composites due to their low cost, low density, high specific strength, and biodegradability.

Harakeke, a native New Zealand flax (Phormium tenax), is of particular interest due to its cultural significance and impressive mechanical properties [7]. This fibre is lightweight with a density of approximately 1.3 g/cm^3. Harakeke also possesses superior strength (0.8 GPa) and modulus (21 GPa) [8] compared to polypropylene. For reference, PP has a tensile strength of approximately 24 MPa and a Young's modulus of 1.5 GPa (see Chapter 5). These mechanical properties suggest harakeke's potential application as a reinforcement fibre in PP-based composites.

The hybridisation of mussel shell fillers and harakeke fibres presents an intriguing avenue for research, as these materials possess distinct shapes and properties. The selection of these specific materials is motivated by their local availability, sustainability, and potential for synergistic effects. Previous studies have demonstrated that the combination of glass fibres with particulate fillers can yield unique properties unattainable with single fillers [6].

However, the properties of hybrid composites are heavily influenced by the ratio of fillers in the mixture [9]. For instance, optimising the proportion of SiC particles (2%, 4%, 6%) in Kevlar fibre-reinforced epoxy composites has been shown to enhance mechanical properties [10]. Therefore, a comprehensive study of the possible synergistic effects and influences of hybrid fillers is necessary to build a thorough understanding of these complex systems.

In this chapter, PP composites reinforced with hybrid fillers consisting of harakeke fibres and modified mussel shell fillers (MAPP-MS and PDA/MAPP-MS) are investigated. The total filler content is maintained at 40 %, with varying combinations of the two filler types. The thermal properties, morphology, and chemical composition of harakeke fibres are first characterised. Subsequently, the influence of these hybrid fillers on the thermal properties, crystal structure, mechanical properties, fracture morphology, and viscoelastic properties of PP composites in both solid and molten states is examined. For comparison, PP composites with 20% or 40% harakeke fibre are also studied. This comprehensive analysis aims to elucidate the complex interactions and potential synergistic effects of hybrid fillers in PP composites, providing valuable insights for tailoring material properties for specific applications.

6.2 Basic properties of harakeke fibres

Characterisation of harakeke fibres (HF) is crucial for understanding their potential influence and possible synergistic effects when incorporated into mussel shell/PP composite systems. To comprehensively analyse the fibres' properties before and after treatment, a suite of analytical techniques was employed. Scanning Electron Microscopy (SEM), Thermogravimetric Analysis (TGA), X-ray Diffraction (XRD), and Fourier-Transform Infrared Spectroscopy (FTIR) were used to investigate the morphological, thermal, crystalline, and chemical characteristics of the harakeke fibres. Analyses were conducted on both untreated fibres and fibres treated by alkaline digestion and subsequent fibrillation using a super-mass-colloider..

6.2.1 Morphological properties of untreated and treated harakeke fibre-SEM analysis

The SEM images of untreated and treated (post-digestion/fibrillation) harakeke fibres are presented in Figure 6-1. Untreated harakeke fibres appeared as bundles, as shown in Figure 6-1A and at higher magnification (×500) in Figure 6-1B. This observation agrees with previous studies, which generally indicate that the primary cell wall comprises cellulose fibrils, hemicelluloses, and lignin embedded in a polysaccharide matrix, with the relatively smooth appearance attributed to waxes and pectins. The waxy substance on natural fibre surfaces impedes effective fibre-to-polymer matrix bonding and surface wetting [11]. Moreover, the presence of free water and hydroxyl groups in untreated fibres, particularly in amorphous regions, diminishes the ability of plant fibres to develop adhesive characteristics with most hydrophobic polymer matrices.

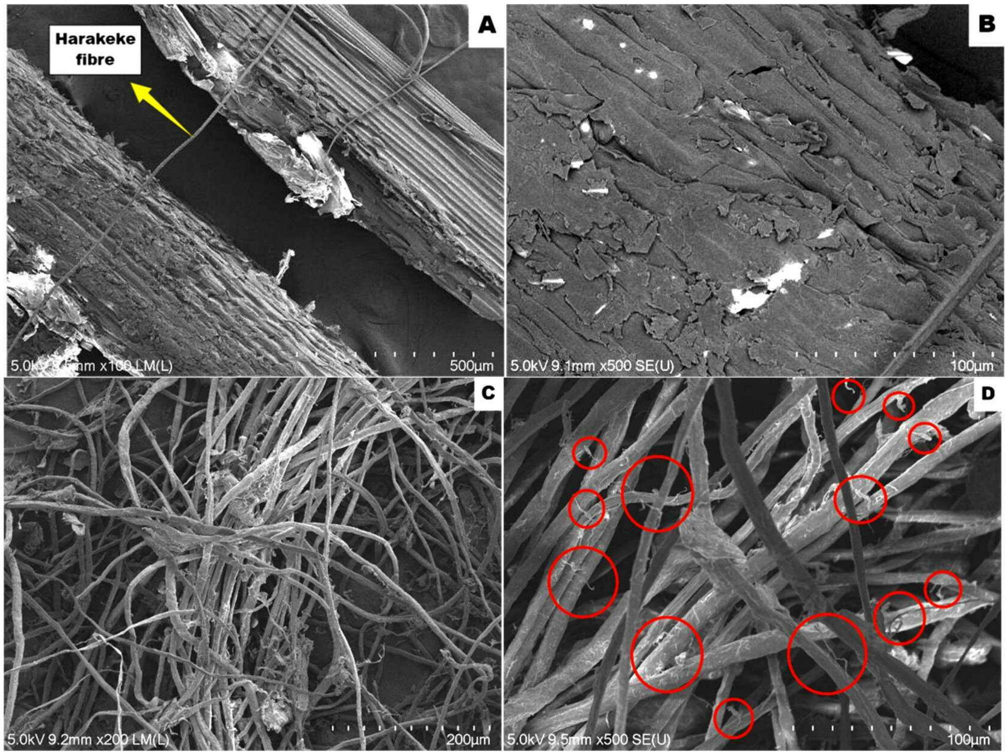

Figure 6- 1: Scanning electron micrograph images of (A) untreated harakeke fibres (× 100), (B) untreated harakeke fibres (× 500), and (C) treated harakeke fibres (× 200), (D) treated harakeke fibres (× 500).

Alkaline digestion has proven effective in enhancing the surface adhesion of natural fibres to matrices [12; 13]. Alkali treatment effectively removes non-structural components such as fats, waxes, lignin, and pectin from fibres. This process exposes more functional groups on cellulose surfaces, facilitating improved chemical bonding. Moreover, mild alkali treatment can enhance the crystallinity of natural fibres by optimising cellulose chain packing and stress relaxation through the removal of amorphous constituents. Consequently, this treatment improves the thermal stability of fibres and enhances mechanical interlocking between fibres and matrices by increasing surface roughness [14].

Figure 6-1C illustrates the effects of combined alkali digestion and fibrillation treatment on harakeke fibres. The image reveals largely separated fibres with diameters of approximately 10 µm, exhibiting notably rougher surfaces accompanied by extensive fibrils, as highlighted by the red circle in Figure 6-1D. This effective separation of fibres from bundles and increased surface roughness are expected to result in improved fibre dispersion within the matrix. Furthermore, enhanced interfacial bonding through increased physical interlocking and reduced surface tension can be anticipated.

6.2.2 Thermal properties of untreated and treated harakeke fibre -TGA-DTG analysis

Thermogravimetric analysis (TGA) measures weight loss as a function of temperature over time, enabling the quantification of volatile fractions released and solid residue remaining after thermal treatment. Derivative thermogravimetry (DTG), the first derivative of TGA data, offers enhanced sensitivity to subtle changes, making it particularly valuable for kinetic studies. While TGA provides comprehensive thermal decomposition profiles, DTG allows for more precise identification of distinct decomposition stages and rates.

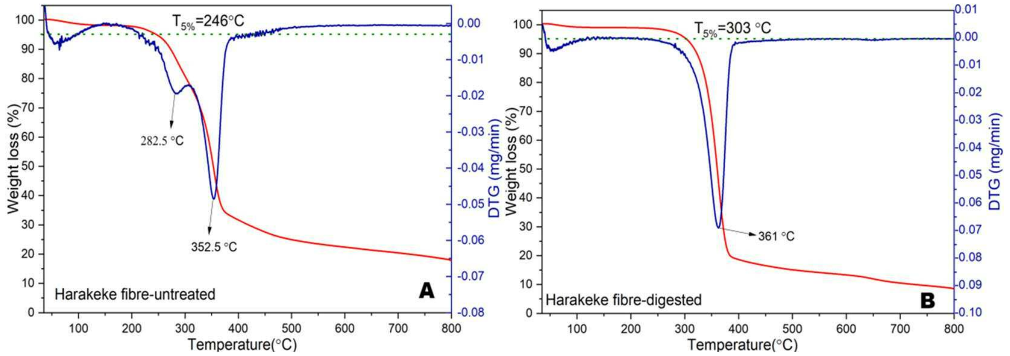

Figure 6- 2: TGA-DTG curves of (A) untreated harakeke fibres and (B) treated harakeke fibres.

Figure 6-2A and B illustrate the decomposition behaviours of harakeke fibre before and after treatment, respectively. In natural fibres, degradation typically initiates in the amorphous regions before progressing to the crystalline regions. Lignin degradation begins at approximately 160 °C and spans a wide temperature range due to its structural complexity. Hemicellulose degradation initiates at about 220 °C, whereas cellulose degradation starts around 315 °C [12; 15].

The TGA curves (red lines) reveal higher decomposition temperatures for the alkaline-digested and fibrillation-treated fibres compared to the untreated fibres. The $T_{5\%}$ (temperature at 5% weight loss) of harakeke fibres increased from 246°C for untreated fibres to 303°C after treatment. Given that the $T_{5\%}$ of harakeke fibres, both before and after treatment, significantly exceeds the typical processing temperature range of polypropylene (PP), which spans 160-210°C, it can be concluded that these fibres demonstrate sufficient thermal stability for incorporation into PP composites.

The residue for untreated harakeke fibre after thermal degradation (16.9%) exceeds that of treated fibre (7.9%). This difference can be attributed to lignin in the untreated fibre, which promotes char formation. The resulting char layer acts as thermal insulation, leading to a higher residue amount [12].

DTG curves for both untreated and treated harakeke fibres display a small peak at approximately 100 °C, attributable to the loss of absorbed moisture. The DTG curve of untreated harakeke fibre (Figure 6-2A, blue line) exhibits two peaks: a broader shoulder peak at 282.5 °C corresponding to hemicellulose decomposition, and a sharp peak at approximately 350 °C indicating cellulose and lignin decomposition. Conversely, the treated fibre (Figure 6-2B, blue DTG curve) shows only one sharp peak at 361 °C. The absence of a peak near 280 °C indicates substantial removal of hemicellulose and lignin.

These findings support previous research demonstrating that alkali treatments remove hemicellulose and lignin constituents from fibres. Consequently, the decomposition of treated fibres primarily involves cellulose, resulting in an elevated overall degradation temperature [12; 15].

6.2.3 Crystalline structures of untreated and treated harakeke fibre -XRD analysis

Figure 6-3 presents the X-ray diffractograms of untreated and treated harakeke fibres, illustrating their crystalline structure. Detailed parameters were presented in Table 6-1. It is noteworthy that all these two fibres exhibit a typical X-ray diffractogram of cellulose I , characterised by a crystallographic plane (002) peak centred around 22.3°, a (110) peak at 15.3°, a (110) peak proximate to 16.9°, and a (004) peak around 34.8°. While literature indicates the potential transformation of cellulose I to cellulose II or amorphous cellulose under thermal or alkaline conditions, this experiment did not observe such changes, which is likely due to the mild treatment conditions (5% NaOH and 2% Na_2CO_3) employed.

The percentage of crystallinity (Cr%) of untreated and treated harakeke fibres was calculated with the Segal method (peak height empirical method), equation 6-1 as below.

$$Cr\% = \frac{I_{002} - I_{am}}{I_{002}} \times 100 \qquad \text{Equation 6-1}$$

where I_{002} represents the intensity of the peak corresponding to the crystalline plane 002; I_{am} gives the intensity of diffraction of the non-crystalline material (amorphous band), which is taken as the valley between the crystalline peaks. Results are presented in Table 6-1.

Table 6- 1: XRD Properties of harakeke fibres

Parameters	Untreated fibre	Treated fibre
Peak position (°)	22.3	22.6
FWHM	2.69	1.77
d (Å)	3.97	3.92
Crystallinity Index (Cr %)	73.84	76.45

As shown in Table 6-1, the crystallinity index (Cr%) of harakeke fibre increased from 73.84% in the untreated sample to 76.45% following combined alkali treatment and fibrillation. In contrast, the interplanar spacing (d-spacing) of the (002) plane decreased slightly from 3.97 Å to 3.92 Å after treatment, accompanied by a reduction in the full width at half maximum (FWHM) of the corresponding XRD peaks. These changes

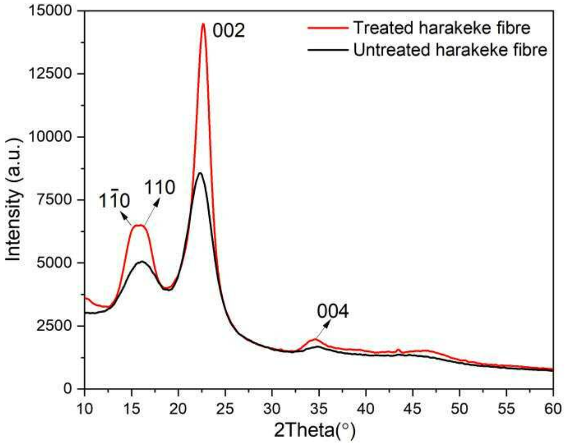

Figure 6- 3: X-ray diffractograms of untreated harakeke fibres and treated harakeke fibres.

suggest enhanced crystalline packing, which is attributed to the removal of non-cellulosic components during alkali treatment, allowing cellulose chains to align more closely and form denser crystal structures. [16].

6.2.4 Fourier transform infrared spectroscopy (FTIR) of untreated and treated harakeke fibre

The FTIR spectra in Figure 6-4 reveal significant structural changes in harakeke fibres following alkali treatment, particularly in the removal of hemicellulose and lignin components.

The most prominent indicator of hemicellulose removal is the disappearance of the carbonyl band at 1736 cm^{-1} in the treated fibres. This band, widely recognised as a signature of hemicellulose presence in natural fibres, is clearly visible in the untreated harakeke fibres but absent in the alkali-treated samples [11; 16]. The absence of this peak represents a key distinguishing feature between treated and untreated harakeke fibres, strongly suggesting the effective removal of hemicellulose during the alkali treatment process.

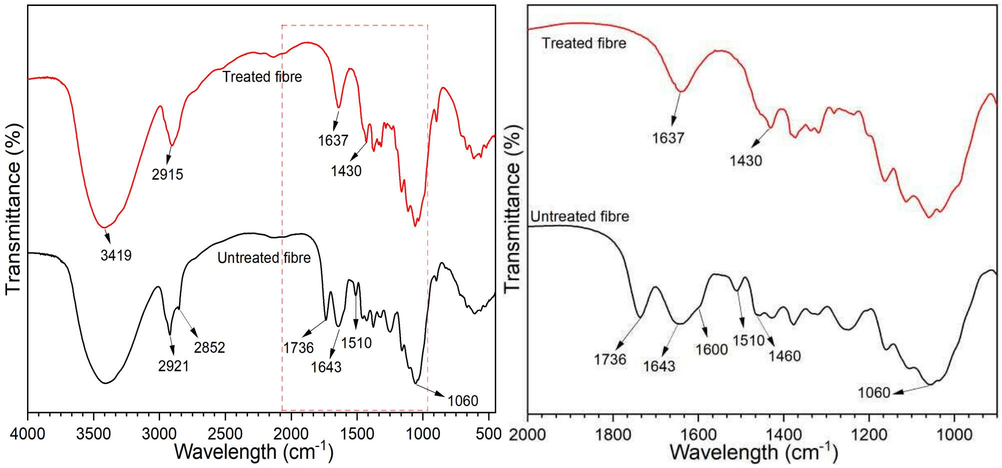

Figure 6- 4: FTIR spectra of untreated harakeke fibres and treated harakeke fibres., (A) 4000-500 cm^{-1}, (B) 2000-800cm^{-1}.

In untreated fibres, the bands at 2920 and 2850 cm^{-1}, attributed to C-H stretching in lignin, are prominent [17]. After alkali treatment, these peaks diminish, while the band at approximately 2900 cm^{-1}, associated with C-H stretching in cellulose, becomes dominant. The characteristic lignin bands at 1510 and 1600 cm^{-1}, assigned to aromatic skeletal vibrations of lignin, are clearly visible in untreated fibres. These bands are notably absent in the FTIR spectrum of alkali-treated harakeke fibres. The band at 1460 cm^{-1}, attributed to C-H deformations in lignin, is present in untreated fibres but not observed in the treated samples.

The alkali treatment results in a more pronounced cellulose signature in the FTIR spectrum. The relative intensity of the cellulose-associated peak at 2900 cm^{-1} increases, becoming the dominant feature in this region for treated fibres. The overall spectral profile of treated fibres shows a higher resemblance to pure cellulose, indicating an increased cellulose content relative to other components.

These spectral changes collectively demonstrate the efficacy of alkali treatment in removing hemicellulose and lignin from harakeke fibres, resulting in a more cellulose-rich material. This structural modification is consistent with the improved thermal stability and crystalline changes often observed in alkali-treated natural fibres.

6.3 Effects of hybrid fillers on the properties of PP composites

The significant improvements observed in harakeke fibres following alkali treatment and fibrillation, including enhanced thermal stability, increased crystallinity, and improved surface properties, present a compelling opportunity for their application in advanced composite materials. Building upon these findings, it is crucial to explore the synergistic potential of combining these treated harakeke fibres with other sustainable fillers, such as mussel shell powder, to create high-performance hybrid composites. By varying the ratio between treated harakeke fibres and modified mussel shell fillers -MAPP modified or PDA/MAPP co-modified- within a fixed total filler content of 40% in PP composites, we can systematically investigate the optimal balance of these two materials. This approach allows for a comprehensive examination of how different hybrid filler ratios and modification techniques influence the thermal, mechanical, and morphological properties of the resulting PP composites.

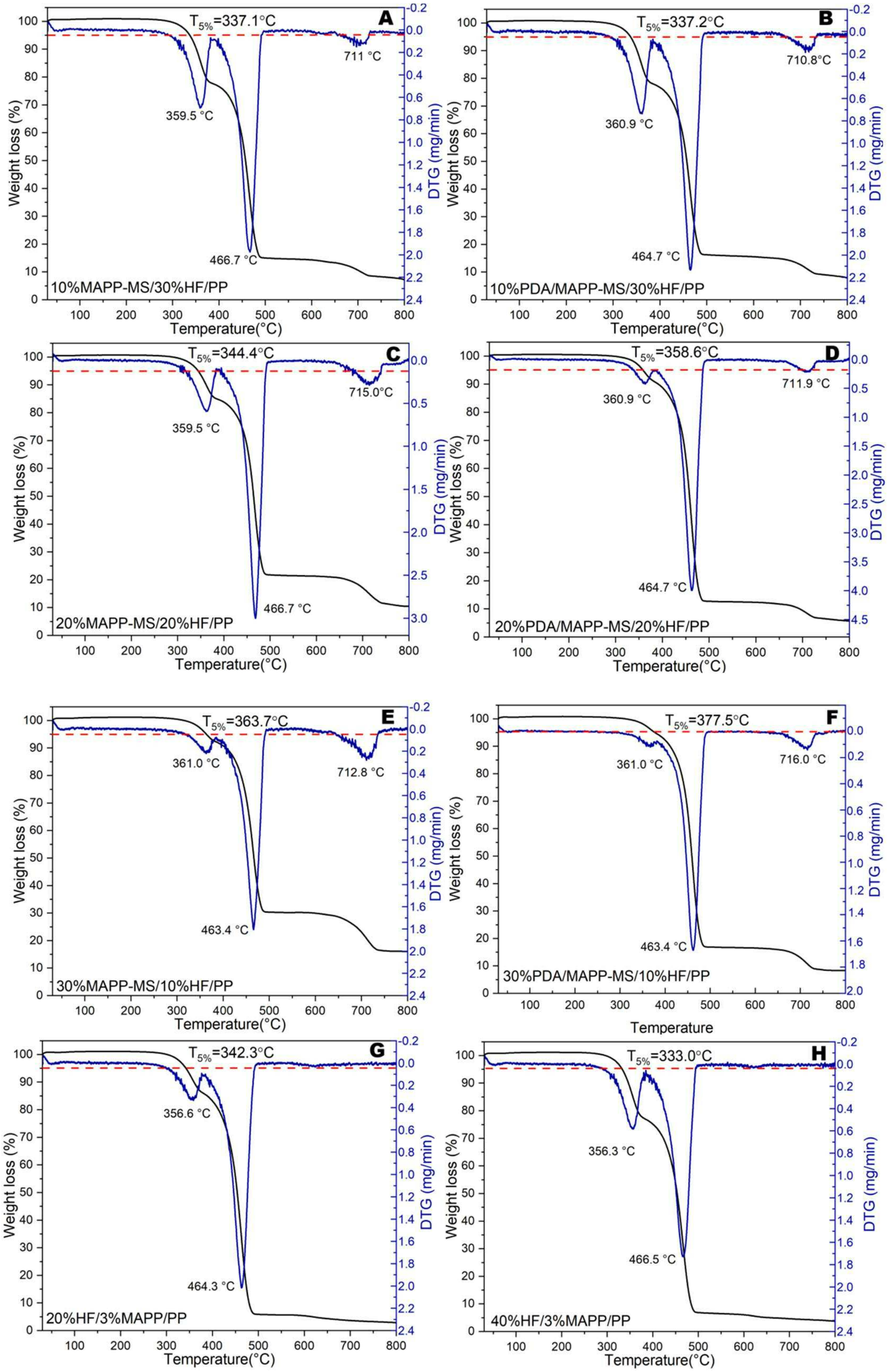

Figure 6- 5: TGA-DTG curves of (A) 10% MAPP-MS/ 30%HF/ PP, (B) 10% PDA/ MAPP-MS/ 30%HF/ PP, (C) 20% MAPP-MS/ 20%HF/ PP, (D) 20% PDA/MAPP-MS/ 20%HF/PP, (E) 30% MAPP-MS/ 10%HF/PP,(F) 30% PDA/MAPP-MS/ 10%HF/PP, (G) 20%HF/3%MAPP/PP, (H) 40%HF/3%MAPP/PP.

6.3.1 The influence of hybrid fillers on the thermal behaviour of PP composites- TGA-DTG analysis

Figure 6-5 and Table 6-2 present the TGA-DTG results for various PP composites, including those with different combinations of hybrid fillers (treated harakeke fibres and modified mussel shell) and composites with 20% and 40% harakeke fibres.

Table 6- 2: TGA results of PP and PP composites.

Sample	$T_{5\%}$ (°C)	T_{max} (°C)	Sample	$T_{5\%}$ (°C)	T_{max} (°C)
PP	400	458			
20%HF/3%MAPP/PP	342	464.3	20%HF/3%MAPP/PP	333	467
10% MAPP-MS/30% HF/PP	337	466.7	10% PDA/MAPP-MS/30% HF/PP	337	465
20% MAPP-MS/20% HF/PP	344	466.7	20% PDA/MAPP-MS/20% HF/PP	359	465
30% MAPP-MS/10% HF/PP	364	463.4	30% PDA/MAPP-MS/10% HF/PP	378	463

For PP composites incorporating treated harakeke fibres only (Figure 6-5G&H), the TGA-DTG curves consistently demonstrate the absence of a shoulder peak at approximately 282 °C, which is typically associated with hemicellulose decomposition. This observation agrees with our previous conclusion regarding the successful removal of hemicellulose from harakeke fibres following alkali treatment.

For comparative analysis, two key temperatures were examined: the 5% weight loss temperature ($T_{5\%}$) and the maximum decomposition temperature. Neat PP exhibited a $T_{5\%}$ of 400°C, whereas PP composites with varying harakeke fibre (HF) content (20 or 40%) showed significantly lower $T_{5\%}$ values. Specifically, 20% HF/PP and 40% HF/PP composites demonstrated $T_{5\%}$ values of 342 and 330 °C, respectively, indicating an inverse relationship between HF content and $T_{5\%}$. The $T_5\%$ values for the hybrid composites were recorded as follows: 337°C for both 10% MAPP-MS/30% HF/PP and 10% PDA/MAPP-MS/30% HF/PP; 344°C for 20% MAPP-MS/20% HF/PP; 358 °C for 20% PDA/MAPP-MS/20% HF/PP; 364 °C for 30% MAPP-MS/10% HF/PP; and 377 °C for 30% PDA/MAPP-MS/10% HF/PP. These results indicate that a higher proportion of modified mussel shell (MS) fillers in the hybrid composite formulation delays the onset of thermal decomposition. This enhancement in thermal stability is attributed to the improved interfacial adhesion achieved through the combined incorporation of surface-modified mussel shell fillers and harakeke fibres, as well as the inherently higher thermal stability of the mussel shell component.

Regarding the maximum decomposition temperature, all PP composites showed a slight increase compared to neat PP (458°C). The values for the composites were: 464°C (20% HF/PP), 466°C (40% HF/PP), 468°C (10% MAPP-MS/30% HF/PP), 464°C (10% PDA/MAPP-MS/30% HF/PP), 467°C (20% MAPP-MS/20% HF/PP), 465°C (20% PDA/MAPP-MS/20% HF/PP), and 463°C for both 30% MAPP-MS/10% HF/PP and 30% PDA/MAPP-MS/10% HF/PP.

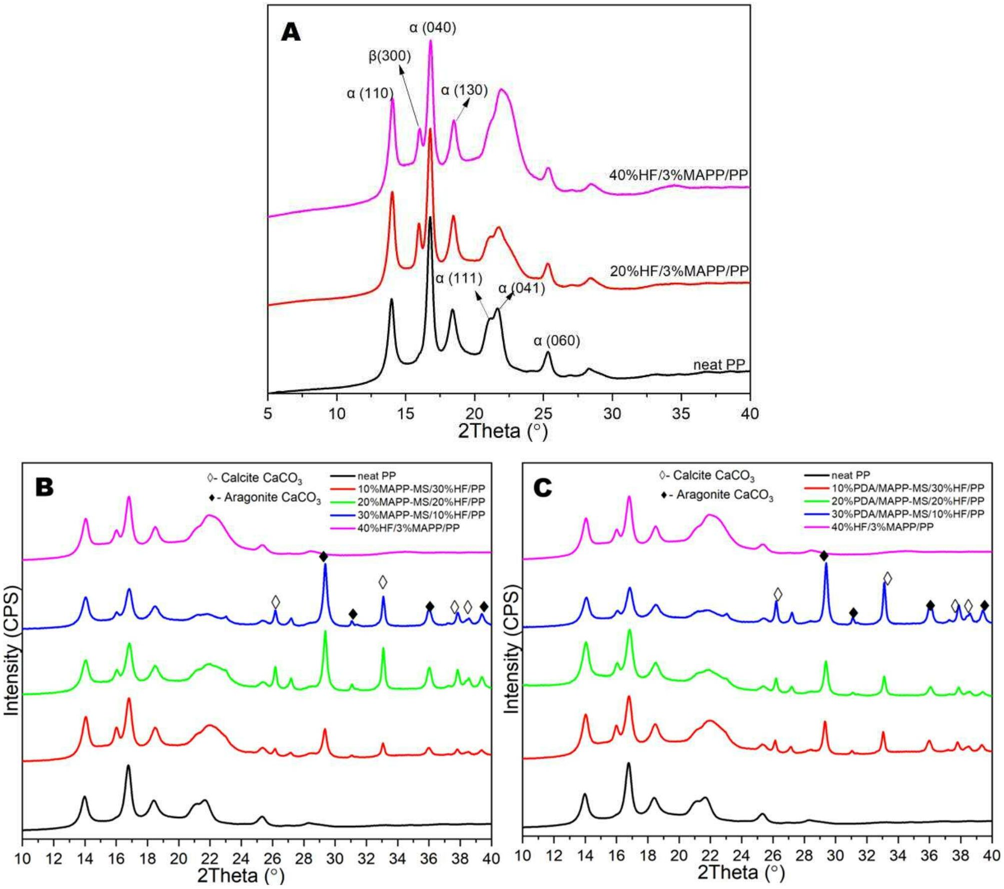

Figure 6- 6: X-ray diffractograms of (A) neat PP, 20%HF/3%MAPP/PP, and 40%HF/3%MAPP/PP; (B) neat PP and PP composites with different ratio of MAPP-MS and HF fillers, and (C) neat PP and PP composites with different ratio of PDA/MAPP-MS and HF fillers.

In conclusion, while the decrease in $T_{5\%}$ suggests an earlier onset of decomposition in the composites compared to neat PP, which may be due to the decomposition of cellulose from harakeke fibres, the incorporation of harakeke fibres or their combination with modified mussel shell in various ratios contributes to the thermal stabilisation of the

Table 6- 3: The intensity values of peaks reflecting different phase planes.

		Height (counts)	Rel. Int. (%)	K_β (%)		Height (counts)	Rel. Int. (%)	K_β (%)
neat PP	α (110)	52436.9	46.61					
	β (300)	**0**	**0.00**	**0.00**				
	α (040)	112511.9	100					
	α (130)	33355.9	29.65					
20%HF/3%MAPP /PP	α (110)	58941.26	61.35		40%HF/3%MAPP/ PP	41235.89	64.93	
	β (300)	**32421.26**	**33.75**	**14.59**		**21817.89**	**34.36**	**14.65**
	α (040)	96070.26	100			63503.89	100	
	α (130)	34808.26	36.23			22351.89	35.2	
10%MAPP-MS/30%HF/PP	α (110)	22305.91	70.56		10%PDA/MAPP-MS/30%HF/PP	19127.51	72.31	
	β (300)	**13909.91**	**44.00**	**17.32**		**11262.51**	**42.58**	**16.71**
	α (040)	31614.91	100			26451.51	100	
	α (130)	12467.91	39.44			10568.51	39.95	

composites. This is evidenced by the higher maximum decomposition temperatures observed in all composites relative to unfilled PP.

6.3.2 The influence of hybrid fillers on the crystalline structure of PP composites- XRD analysis

This section investigates the influence of fillers on the crystalline structure of polypropylene (PP) composites, specifically focusing on those containing harakeke fibres at two different loadings and the fillers' potential synergistic effects when combined with various mussel shell fillers. X-ray diffraction (XRD) analysis was employed to examine these effects, with the results presented in Figure 6-6. Table 6-2 lists the intensities of selected peaks, namely α (110), α (040), α (130), and β (300), which are crucial for understanding the crystalline structure of the PP composites.

6.3.2.1 Effect of harakeke fibres on PP crystalline structure

XRD analysis reveals significant changes in the crystalline structure of PP upon the addition of harakeke fibres (HF). Figure 6-6A demonstrates that the incorporation of either 20% or 40% HF results in XRD diffractograms exhibiting characteristic peaks of the α-crystalline form of PP at 2θ values of 13.9º (α_{110}), 16.7º (α_{040}), 18.4º (α_{130}), 21.1º (α_{111}), 21.9º (α_{04}1) and 25.3º (α_{060}) [18; 19]. Notably, an additional peak at the 2θ value of 15.9° (β_{300}) indicates the co-existence of β-PP, which is absent in neat PP. This observation leads to the conclusion that both 20% and 40% HF can induce the formation of β-PP.

As discussed in Chapter 5, with the strongest peak for α(040) denoted as 100% relative intensity, the XRD results indicate that the relative intensity of the β(300) peak ranges from 4.89% to 24.74% for PP composites with varying types and amounts of mussel shell fillers. Importantly, Table 6-3 shows that the relative intensity of the β(300) peak in 20%HF/3%MAPP/PP and 40%HF/3%MAPP/PP is 33.75% and 34.36%, respectively. This remarkable increase in the β-crystalline form of PP suggests that harakeke fibres are particularly effective in inducing the formation of β-PP.

These findings resonate with previous research by Yongli *et al.*, who reported that natural fibres derived from bamboo can serve as a stronger β-crystal nucleator for PP, especially when combined with MAPP. This effect might be attributed to the improved interfacial adhesion between fibre and matrix, as well as the development of transcrystallinity around the bamboo fibre [20].

6.3.2.2 Effects of harakeke fibres and mussel shell hybrid fillers on PP crystalline structure

With the total filler amount fixed at 40%, the XRD patterns in Figures 6-2B and 6-2C reveal that PP composites with varying ratios of MAPP-MS or PDA/MAPP-MS fillers to harakeke fibres all demonstrate the co-existence of β-PP and α-PP. This co-existence is particularly significant as different crystal forms of PP possess unique properties: α-PP provides superior tensile strength and stiffness, whilst β-PP offers enhanced toughness, better elongation at break, and a higher heat distortion temperature [21]. Consequently, the mechanical properties of PP composites may benefit from this synergistic combination of α-PP and β-PP.

Furthermore, corresponding peaks in the XRD diffractograms at 2θ values between 25-40° indicate the presence of both calcite and aragonite phases in composites containing different modified mussel shell (MS) fillers. These findings confirm the successful incorporation of both MAPP and PDA/MAPP modified mussel shell fillers, consistent with the crystal compositions of mussel shell discussed in Chapter 4.

6.3.2.3 Quantitative analysis of β-PP content

To quantitatively compare the relative β-PP fraction in all crystal phases, Equation 6-2 was employed [22],

$$K\beta = \frac{H\beta(300)}{H\beta(300)+H\alpha(110)+H\alpha(040)+H\alpha(130)} \qquad \text{Equation 6-2}$$

where K_β denotes the relative content of β-PP, and *H* represents the relative peak intensity.

Analysis of the data in Table 6-2 reveals that 30%MAPP-MS/10%HF/PP and 30%PDA/MAPP-MS/10%HF/PP exhibit the lowest β-crystal content at 11.57% and 11.45%, respectively, which is lower than PP composites with 20% or 40% HF (approximately 15%). Conversely, 10%MAPP-MS/30%HF/PP and 10%PDA/MAPP-MS/30%HF/PP exhibit the highest β-crystal content at 17.32% and 16.71%, respectively. The β-crystal contents for 20%MAPP-MS/ 20%HF/PP and 20%PDA/ MAPP-MS/ 20%HF/PP are approximately 14.66% and 14.57%, respectively, which are comparable to PP composites with 20% or 40% HF.

These results suggest that the optimal synergistic effect for promoting the formation of β -phase polypropylene (β -PP) may be achieved through the combination of 10% modified mussel shell fillers and 30% harakeke fibres. The two predominant crystalline forms of polypropylene, α and β , exhibit distinct mechanical properties. While α -PP is the most thermodynamically stable form, offering high tensile strength and rigidity, β -PP is characterised by superior toughness, increased elongation at break, lower density, improved transparency, and enhanced impact and tear resistance [23]. This finding highlights the potential of tailoring the crystalline structure of PP composites through hybridisation of mussel shell fillers with harakeke fibres to achieve targeted mechanical performance.

6.3.3 The influence of hybrid fillers on the melting and recrystallisation of PP composites- DSC analysis

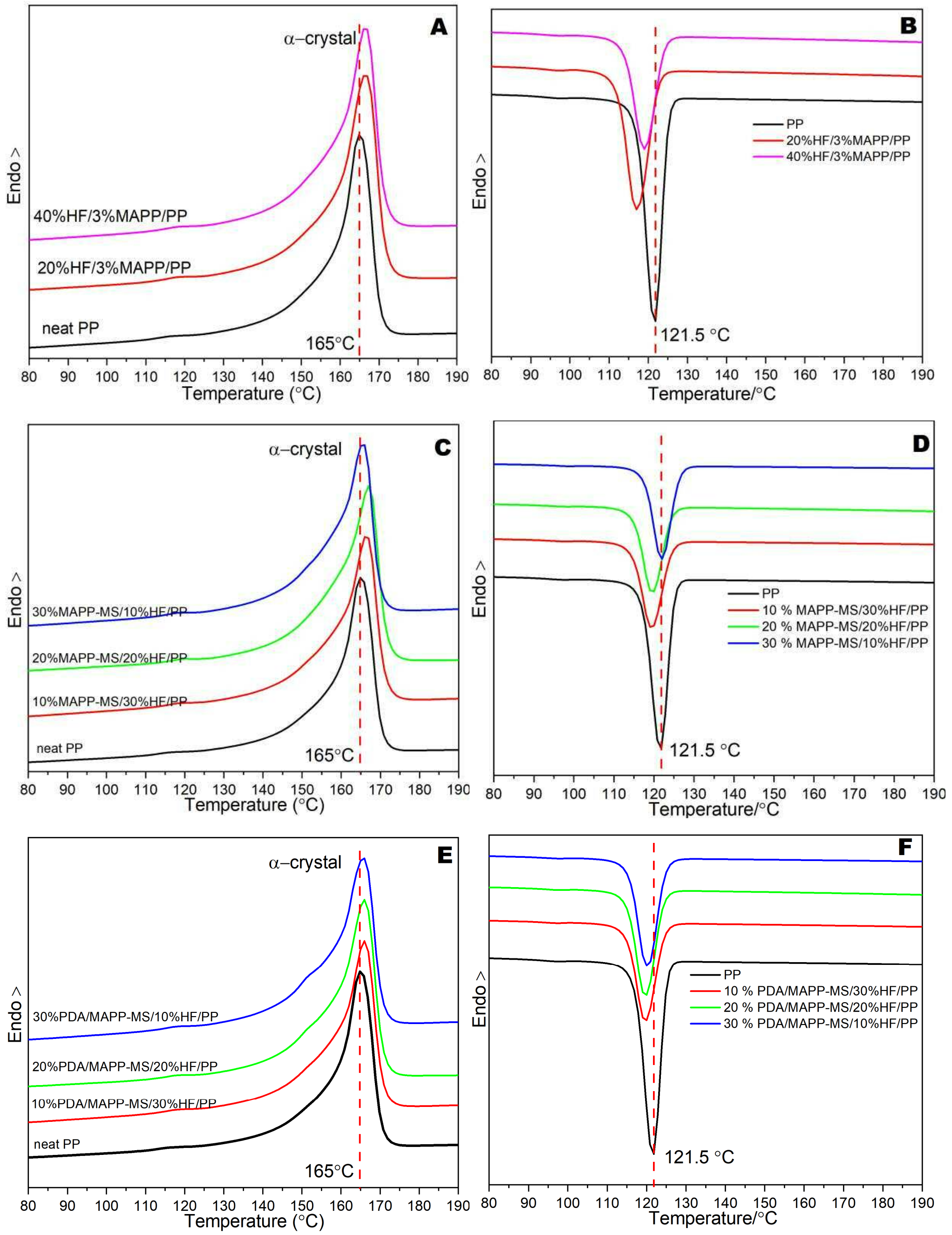

Figure 6- 7: DSC thermograms: (A) melting curves and (B) cooling curves of neat PP, 20%HF/3%MAPP/PP, and 40%HF/3%MAPP/PP; (C)melting curves and (D)cooling curves of neat PP and PP composites with different ratios of MAPP-MS and HF hybrid fillers;(E)melting curves and (F)cooling curves of neat PP and PP composites with different ratios of PDA/MAPP-MS and HF hybrid fillers

The incorporation of foreign materials, particularly fillers and fibres, into polymer matrices can significantly influence their crystallisation and melting behaviour. This study employs differential scanning calorimetry (DSC) to analyse polypropylene (PP) composites reinforced with harakeke fibres at 20% and 40% loadings, as well as combinations with modified mussel shell fillers (MAPP or PDA/MAPP).

Previous X-ray diffraction (XRD) results, obtained from samples directly after injection moulding, provided insights into the initial crystalline structure of the composites. The data indicated that introducing harakeke fibres alone, or in combination with MAPP-MS or PDA/MAPP-MS, facilitates the formation of β-PP, resulting in polymorphic composites characterised by the coexistence of α- and β-crystalline forms.

Building upon these findings, the current DSC analysis focuses on the influence of filler on the crystallisation behaviour of the composites. By using the second melting curves for analysis, this approach examines the thermal properties after controlled cooling, eliminating the thermal history effects from initial processing. The melting and cooling curves of PP composites are presented in Figure 6-7, with the derived parameters listed in Table 6-3.

The combination of harakeke fibres with modified mussel shell fillers may lead to complex interactions affecting the crystallisation and subsequent melting behaviour of the PP matrix. These interactions could result in unique thermal properties, potentially enhancing the material's performance in various applications.

This comprehensive analysis, combining XRD data of the initial structure with DSC insights into crystallisation behaviour, provides a thorough understanding of the thermal and crystalline properties of these hybrid composites. The information gained is crucial for optimising the composition and processing conditions of PP composites for specific applications.

6.3.3.1 Effect of harakeke fibres

The incorporation of harakeke fibres at 20% and 40% levels significantly influenced the crystallinity and crystal phase composition of polypropylene (PP) composites, as evidenced by differential scanning calorimetry (DSC) melting curves in Figure 6-7A. Table 6-3 reveals that PP composites with these harakeke fibre contents exhibited higher degrees of crystallinity (X%) compared to neat PP (47.36%), suggesting that harakeke fibres promote the crystallisation of PP.

A comparative analysis with PP composites incorporating different mussel shell fillers further underscores the efficacy of harakeke fibres. At 20% filler loading, the total X% for 20% MS/PP, 20% MAPP-MS/PP, and 20% PDA/MAPP-MS were 31.93%, 49.99%, and 50.27%, respectively, while the X% of 20% HF/3% MAPP/PP reached 57.58%. Similarly, at 40% filler loading, 40% MS/PP, 40% MAPP-MS/PP, and 40% PDA/MAPP-MS showed total X% values of 50.38%, 53.38%, and 50.67%, respectively, compared to 54.73% for 40% HF/3% MAPP/PP. These results demonstrate that harakeke fibres are more efficient in promoting PP crystallisation at both loading levels.

The endothermic melting peaks of both 20% HF/3% MAPP/PP and 40% HF/3% MAPP/PP composites appeared as single peaks at 166.5 ° C, slightly higher than the peak observed for neat PP at 165.0 ° C. This shift indicates the predominance of the α-phase crystals in the composites, as melting peaks near 165 ° C are characteristic of α-crystalline polypropylene. In contrast, XRD results presented in Section 6.3.2.1 revealed the co-existence of both α- and β-crystalline forms. The discrepancy between XRD and DSC outcomes arises from the differences in analytical conditions. The DSC curves reported here reflect the second heating cycle, in which any prior thermal history is eliminated during the initial heating phase. As a result, these curves represent the melting behaviour of PP composites after controlled crystallisation during cooling (refer to Chapter 3, Figure 3-4, Temperature profile for DSC analysis). In contrast, XRD analysis captures the crystalline structure of PP and its composites immediately after extrusion and injection moulding. Therefore, in addition to the effect of fillers, processing conditions—particularly shear flow and temperature gradients—also play a significant role in determining the crystal form observed.

The reduced presence of β-crystals in DSC results is attributed to a phase transformation process. The β-crystalline form is thermodynamically metastable and can convert into the more stable α-form during heating. This transformation typically requires complete melting of the β-structure, followed by recrystallisation into the α-phase [24].

The incorporation of harakeke fibres may facilitate this process by influencing nucleation, molecular folding, and the rearrangement and packing of PP chains. Consequently, crystallisation favours α-phase formation, particularly as overall crystallinity increases and the metastable β-phase diminishes due to thermal transformation [25].

When compared with the DSC data of PP composites containing mussel shell fillers (see Chapter 5), an interesting trend emerges. The transformation from β- to α-phase was more apparent at higher mussel shell filler loadings (30 – 40%). However, harakeke fibre induced a similar transition towards α-phase crystallinity at a lower loading of 20%. This suggests that harakeke fibres are more effective than mussel shell fillers in promoting α-phase formation under controlled crystallisation conditions.

Examination of the cooling curves provided further insights into the crystallisation behaviour of the PP composites. The exothermic crystallisation peak (T_C) of 20% HF/3% MAPP/PP (117.0 °C) and 40% HF/3% MAPP/PP (119.0 °C) were both lower than that of neat PP (121.5 °C). Additionally, a reduction in cooling enthalpy (ΔH_c) was observed with increasing harakeke fibre content. The ΔH_c values for 20% HF/3% MAPP/PP and 40% HF/3% MAPP/PP were 70.39 J/g and 55.83 J/g, respectively, both lower than that of neat PP (86.71 J/g).

These findings can be explained by two primary factors. Firstly, the nucleating effect of harakeke fibres led to a lowered energy barrier for PP crystallisation, resulting in less energy required for the crystallisation process. Secondly, the increased harakeke fibre content reduced the amount of PP available for crystallisation, contributing to the lower cooling enthalpy requirement. Together, these factors account for the observed decrease in crystallisation temperature and cooling enthalpy in the harakeke fibre-reinforced PP composites.

In conclusion, the incorporation of harakeke fibres significantly alters the crystallisation behaviour and thermal properties of PP composites, promoting α-phase crystallinity, facilitating phase transformation, and modifying the crystallisation process. These changes have important implications for the material's properties and potential applications, particularly in comparison to other fillers such as mussel shells. The superior efficiency of harakeke fibres in promoting crystallisation and phase transformation at lower loadings offers potential advantages in composite design and manufacturing.

6.3.3.2 Effects of harakeke fibres and mussel shell hybrid fillers -DSC analysis

Figures 6-7 C and E illustrate the melting behaviour of polypropylene (PP) composites with varying ratios of MAPP-MS to harakeke fibre and PDA/MAPP-MS to harakeke fibre, respectively. With the total filler content fixed at 40%, the ratios were adjusted to 1:3, 2:2, and 3:1, respectively. The differential scanning calorimetry (DSC) melting curves for all composites displayed a single melting peak between 165.5°C and 166.5°C, slightly higher than the melting peak of neat PP at 165.0°C. These peaks are indicative of the melting of α-PP, confirming the dominance of the α-crystal form in these composites.

The degrees of crystallinity (X%) for the various hybrid PP composites were as follows: 10% MAPP-MS/30% HF/PP: 56.28%; 20% MAPP-MS/20% HF/PP: 49.51%; 30% MAPP-MS/10% HF/PP: 53.65%; 10% PDA/MAPP-MS/30% HF/PP: 53.57%; 20% PDA/MAPP-MS/20% HF/PP: 53.66%; and 30% PDA/MAPP-MS/10% HF/PP: 55.84%. All values are higher than that of neat PP (47.36%) and exceed those observed for PP composites containing 40% untreated or modified mussel shell fillers. Additionally, they are comparable to the crystallinity level achieved in PP composites with 40% harakeke fibres.

The increase in crystallinity can be attributed to the synergistic effect of hybrid filler incorporation at high loadings. Harakeke fibres contribute to improved dispersion of mussel shell fillers within the PP matrix, resulting in a more homogeneous microstructure. This enhanced dispersion facilitates the role of the fillers as effective nucleating agents and restricts the mobility of PP chains, thereby promoting the formation of crystalline regions and leading to higher overall crystallinity. Notably, similar to PP composites containing 40% mussel shell fillers, these hybrid filler composites exhibited a diminished β-crystal form of PP, supporting the hypothesis that high filler content favours the thermodynamically stable α-crystal form, as evidenced by increased crystallinity of the α-crystal form. The potential phase transformation from β- to α-form also contributes to the increased α-crystal phase, further emphasising the impact of high filler content on the crystalline structure of PP composites.

The cooling curves for these composite series, presented in Figures 6-7 D and F, exhibited smaller crystallisation peaks compared to neat PP, with all peaks shifting towards lower temperatures. As shown in Table 6-3, the crystallisation temperatures (Tc) and absolute cooling enthalpies (ΔHc) for the PP composites containing hybrid fillers were as follows: T_C = 119.4 °C and ΔHc = 54.91 J/g for 10% MAPP-MS/30% HF/PP; T_C = 119.6 °C and ΔHc = 52.21 J/g for 20% MAPP-MS/20% HF/PP; and T_C = 121.9 °C and ΔHc = 53.02 J/g for 30% MAPP-MS/10% HF/PP. For the PDA/MAPP-MS/HF/PP composites, T_C = 119.7 °C and ΔHc = 53.19 J/g for 10% PDA/MAPP-MS/30% HF/PP; T_C = 119.6 °C and ΔHc = 55.03 J/g for 20% PDA/MAPP-MS/20% HF/PP; and T_C = 120.2 °C and ΔHc = 57.46 J/g for 30% PDA/MAPP-MS/10% HF/PP.

These cooling enthalpies are comparable to those of the PP composites filled with 40% harakeke fibres (55.83 J/g) or different mussel shell fillers (ranging from 57.18 to 61.86 J/g). As discussed earlier, lower crystallisation enthalpy and temperature values are indicative of a facilitated crystallisation process. The hybrid fillers at high loadings demonstrated a similar promoting effect on PP crystallisation.

In conclusion, the DSC results suggest that at a total filler loading of 40%, the crystallisation behaviour of hybrid-filled PP composites closely resembles that of composites reinforced solely with harakeke fibres. This indicates that at high filler contents, the influence of the harakeke fibres becomes dominant, regardless of the presence of additional inorganic fillers. All hybrid composites exhibited increased formation of α -crystals, reduced β -phase content, and similar levels of overall crystallinity. Moreover, the crystallinity enhancement observed in hybrid-filled PP composites, relative to those filled only with mussel shell particles, supports the presence of a synergistic effect arising from the combination of harakeke fibre and inorganic mussel shell fillers.

6.3.4 The influence of hybrid fillers on the mechanical properties of PP composites

6.3.4.1 Effect of harakeke fibres on the mechanical properties of PP composites

The influence of harakeke fibre (HF) content with the existence of MAPP compatibilizer on the mechanical properties of PP composites was investigated. Figure 6-8 A-C presents the results, with detailed data summarised in Table 6-4.

Stress-strain curves (Figure 6-8A) reveal that at strains below 0.5%, the slope of PP composites steepens with increasing HF content, indicating a transition from ductile neat PP to stiffer composite materials. Both tensile strength and Young's modulus of HF/PP composites surpass those of neat PP (Figure 6-8B).

Table 6- 4: Mechanical properties of PP and PP composites with different amounts of HF or hybrid fillers.

Samples	**Tensile strength** （**MPa**）	**Young's modulus** （**GPa**）	**Elongation at break** **(%)**	**Flexural strength** （**MPa**）	**Flexural Modulus** （**GPa**）
PP	23.81±0.38	1.46±0.11	29.71±6.85	34.52±1.35	1.08±0.13
20%HF/ 3%MAPP/PP	30.10±0.19	2.27±0.04	6.81±0.71	44.93±0.67	1.70±0.04
40%HF/ 3%MAPP/PP	45.57±0.79	2.93±0.07	4.20±0.57	65.80±1.01	3.39±0.17
40%MS/PP	20.14±0.24	2.18±0.18	9.48±3.44	32.82±0.18	1.38±0.12
40%MAPP-MS/PP	24.47±0.09	2.24±0.04	6.45±1.26	38.2±0.45	1.52±0.10
40%PDA/MAPP-MS/PP	25.28±0.34	2.42±0.10	4.63±0.42	39.72±0.68	1.65±0.07
10%MAPP-MS/30%HF/PP	40.20±0.77	3.27±0.13	4.65±0.54	59.80±0.88	2.91±0.05
20%MAPP-MS/20%HF/PP	34.81±0.40	3.09±0.07	6.18±0.48	50.79±2.02	2.22±0.20
30%MAPP-MS/10%HF/PP	27.19±0.36	2.67±0.14	6.54±0.41	47.40±1.03	2.11±0.12
10%PDA/MAPP-MS/30%HF/PP	40.06±0.53	3.69±0.12	4.48±0.42	60.97±0.75	2.30±0.16
20%PDA/MAPP-MS/20%HF/PP	35.43±0.98	3.79±0.17	5.18±0.37	54.60±1.43	2.82±0.12
30%PDA/MAPP-MS/10%HF/PP	28.75±0.78	3.15±0.19	6.13±0.46	48.62±1.07	2.40±0.07

The tensile strength of 20%HF/3%MAPP/PP (30.1MPa) and 40%HF/3%MAPP/PP (45.57MPa) increased by 26.4% and 91.6%, respectively, compared to neat PP (23.8MPa). This significant enhancement suggests good fibre wetting and strong fibre-matrix adhesion, attributable to two key factors: the mercerisation treatment of harakeke fibres and the addition of MAPP compatibilizer. Mercerisation removes amorphous regions, separates fibres, and creates a rough surface with visible fibrils, improving wettability and physical bonding. The MAPP compatibilizer further enhances fibre-matrix interaction, facilitating stress transfer and hindering fibre pull-out.

The surface treatment with MAPP significantly contributes to the interfacial bonding between fibres and the continuous phase (PP matrix). The 3% MAPP compatibilizer effectively improves the interaction between fibre and matrix, supporting stress transfer from the matrix to the reinforcing fibres. This enhanced adhesion consequently improves the overall mechanical performance of the composite. These findings are consistent with previous research, where 2 wt.% maleated polypropylene (MAPP) significantly enhanced the flexural strength of PP composites reinforced with sisal, jute, and flax fibres [26].

The Young's moduli of PP composites exhibit a marked increase with the incorporation of harakeke fibre (HF) content. Specifically, the Young's modulus rose by 58% for the 20%HF/3%MAPP/PP composite and by 101% for the 40%HF/3%MAPP/PP composite, relative to neat PP. This significant enhancement can be attributed to the substantially higher elastic modulus of harakeke fibres (approximately 21 GPa) [27] compared to that of neat PP (1.46 GPa). These results corroborate Shao-Yun's findings, which revealed that fibres with higher elastic moduli exhibit a reinforcement effect on the resultant polymer composite, and increasing fibre content has a positive impact on the modulus [28]. This phenomenon underscores the efficacy of harakeke fibres as reinforcing components in PP composites.

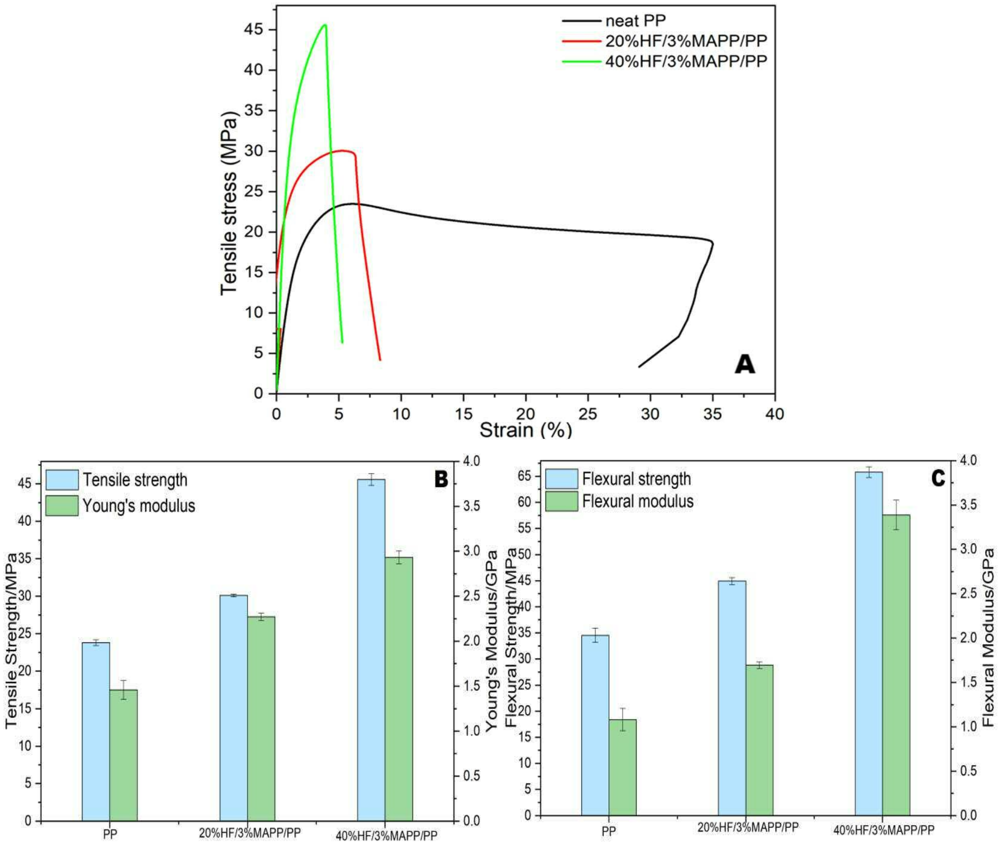

Figure 6- 8: :(A) Stress-strain curves, (B) tensile behaviour, and (C) flexural behaviour of PP and PP composites with 20% and 40% harakeke fibre.

Conversely, elongation at break decreases with increasing HF content, reducing from 29.7% for neat PP to 6.8% and 4.2% for 20% and 40% HF composites, respectively. This reduction is attributed to defect development and decreased composite ductility with fibre addition.

Both flexural strength and modulus of PP composites increase monotonically with increasing harakeke fibre content (Figure 6-8C). The flexural strength of 20%HF/3%MAPP/PP and 40%HF/3%MAPP/PP are 44.93 and 65.80 MPa, representing 30% and 90.6% increases from neat PP, respectively. More pronounced improvements are observed for flexural modulus, with 56.9% and 213.3% increases compared to neat PP for 20%HF and 40%HF incorporation, respectively.

These results demonstrate that incorporating harakeke fibres with MAPP compatibilizer significantly enhances the mechanical properties of PP composites. The improvements stem from effective fibre-matrix adhesion, facilitated by fibre mercerisation and MAPP coupling, enabling superior stress transfer and distribution within the composite.

6.3.4.2 Effect of harakeke fibres and mussel shell hybrid fillers on the mechanical properties of PP composites

This section investigates the influence of different compositions of hybrid fillers on the tensile and flexural properties of composites. The total filler content was maintained at 40%, the ratio of MAPP or PDA/MAPP modified mussel shell filler to harakeke fibre were changed between 1:3, 2:2, and 3:1. The mechanical properties of PP composites with 40% HF(and 3%MAPP), 40% different mussel shell fillers, namely MS, MAPP-MS, PDA/MAPP-MS, were listed as well, providing comparison of influence between composites with single fillers to those with hybrid fillers. Detailed results were presented in Table 6-4.

Stress–strain curves for PP composites incorporating different combinations of MAPP-MS or PDA/MAPP-MS with harakeke fibre (HF) are shown in Figures 6-9A and 6-10A.

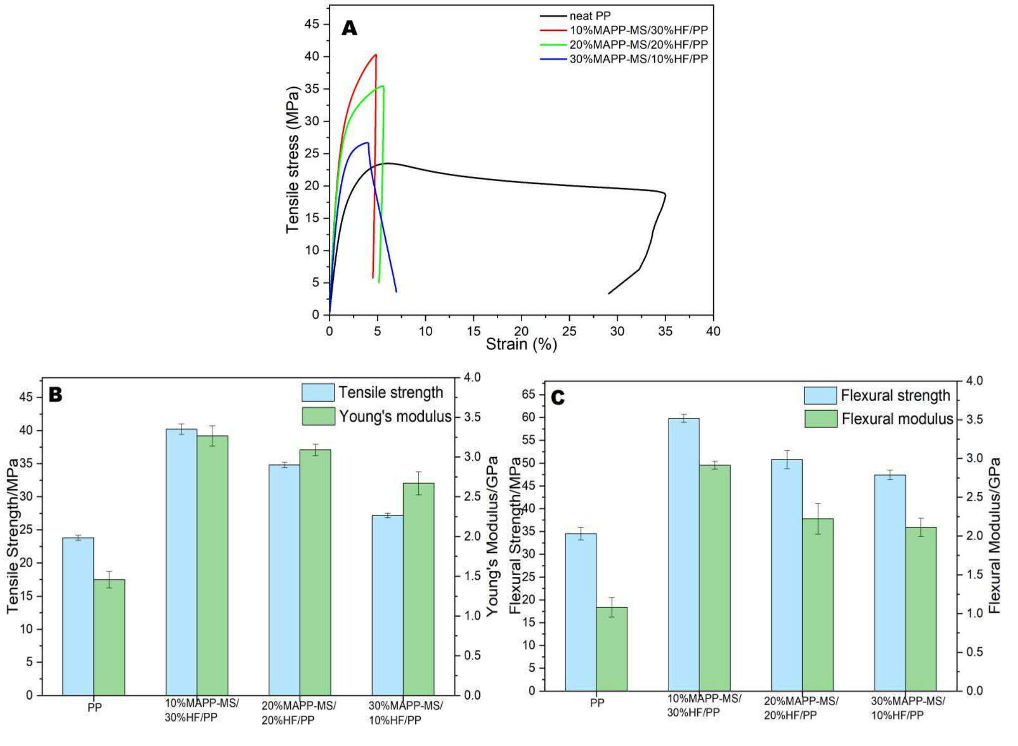

Figure 6- 9: (A) Stress-strain curves, (B) tensile behaviour, and (C) flexural behaviour of PP and PP composites with different ratios of MAPP-MS and HF hybrid fillers.

As the HF content increases, the slopes of the stress–strain curves within the 0.5% strain region become steeper. Correspondingly, the Young's moduli increase, as shown in Figures 6-9B and 6-10B. This indicates that stiffness is more strongly influenced by the amount of harakeke fibre than by the presence of modified mussel shell fillers.

According to Table 6-4, at a total filler loading of 40%, the composite containing 40% HF with 3% MAPP (40% HF/3% MAPP/PP) exhibited a higher Young's modulus than PP composites containing 40% mussel shell fillers alone. However, when hybrid filler systems were used—combining MAPP-MS or PDA/MAPP-MS with HF at the same total loading—the resulting PP composites displayed even higher elastic moduli than the 40% HF/3% MAPP/PP composite. This suggests a synergistic effect between the hybrid fillers in enhancing the stiffness of the composite.

The observed improvement in modulus can be attributed to better filler dispersion achieved through hybridisation. The combination of fillers with different shapes and particle sizes allows smaller mussel shell particles to occupy the voids between the polymer matrix and the larger harakeke fibres. This reduces the formation of defects and improves packing density in the composite material [29]. As a result, the well-dispersed rigid fillers within the matrix contribute to a stiffer composite structure.

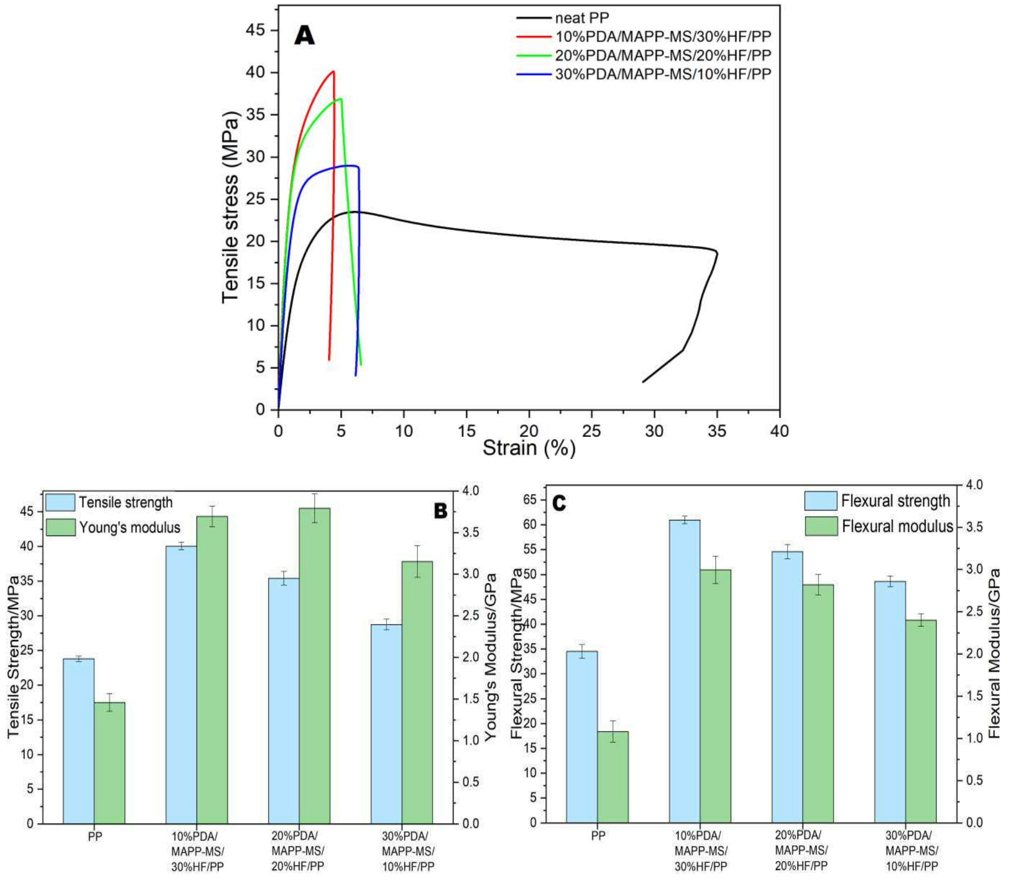

Figure 6- 10: (A) Stress-strain curves, (B) tensile behaviour, and (C) flexural behaviour of PP and PP composites with different ratios of PDA/MAPP-MS and HF hybrid fillers.

The surface properties of mussel shell fillers have a significant impact on the elastic modulus of polypropylene hybrid composites. At equivalent ratios of modified mussel shell to harakeke fibre, composites incorporating PDA/MAPP-MS consistently exhibited higher elastic moduli than those with MAPP-MS alone. For example, at a 10% mussel shell and 30% fibre ratio, PDA/MAPP-MS increased the elastic modulus to 3.69 GPa (a 153% improvement over neat PP), compared with 3.27 GPa (124%) for MAPP-MS. At a 30% mussel shell and 10% fibre ratio, the modulus rose from 2.67 GPa (83%) to 3.15 GPa (116%) with PDA/MAPP-MS. For instance, at a 10% mussel shell and 30% fibre ratio, the elastic modulus increased from 3.27 GPa (a 124% improvement over neat PP) with MAPP-MS to 3.69 GPa (153% improvement) with PDA/MAPP-MS. At a 20%:20% ratio, the modulus rose from 3.09 GPa (112%) to a peak of 3.79 GPa (160%), while at a 30% mussel shell and 10% fibre ratio, the modulus increased from 2.67 GPa (83%) to 3.15 GPa (116%) with PDA/MAPP-MS. These results indicate that PDA/MAPP modification contributes to a more substantial reinforcement effect. This enhancement is likely due to improved interfacial adhesion between the mussel shell fillers and the PP matrix, facilitated by the presence of PDA. In combination with harakeke fibres, this better adhesion reduces the number of voids and defects in the final composite, thereby enhancing stiffness.

Among all the PP composites with 40% fillers, 40%HF/3%MAPP/PP exhibited the highest tensile strength (45.6MPa), while all the composites with 40% hybrid fillers (tensile strength ranging from 27.2-40.2MPa) performed better in tensile strength measurements than PP composited only with 40% different mussel shell (single) fillers (tensile strengths for these ranged from 20.1-25.3MPa). It seems that a synergistic effect is leading to tensile strength improvement by incorporating both MS particulate and fibrous fillers into the PP matrix.

As can be observed from Figure 6-9B and Figure 6-10B, the higher the amount of harakeke fibre incorporated into the composite, the higher the tensile strength that resulted for the hybrid-filled PP composites. The values of tensile strength measured were 40.20 MPa for 10%MAPP-MS/30%HF/PP, 34.81 MPa for 20%MAPP-MS/20%HF/PP, and 27.19 MPa for 30%MAPP-MS/10%HF/PP, showing a 68.8%, 46.2%, and 14.2% increase compared to measurements executed on neat PP. The values of tensile strength were 40.06MPa for 10%PDA/MAPP-MS/30%HF/PP, 35.43 MPa for 20%PDA/MAPP-MS/20%HF/PP, and 28.75 MPa for 30%PDA/MAPP-MS/10%HF/PP. This showed increases of 68.3%, 48.8%, and 20.8% compared to neat PP. It is important to note that in the combination of harakeke fibres, PDA/MAPP modified mussel shell fillers, especially at higher filler contents (20% or 30%), had better enhancement effects on the tensile strength behaviour of the resultant composites over those modified with MAPP alone. This can be explained by the improved adhesion and dispersion of mussel shell filler within PP, which leads to stress transfer from the matrix to hybrid fillers upon tensile loading.

All elongation-at-break values for PP composites containing various hybrid filler combinations are either comparable to or slightly higher than those measured for PP reinforced solely with 40% harakeke fibres. However, all show a significant reduction compared to neat PP. This decline in ductility is attributed to the introduction of rigid fillers—such as harakeke fibres and mussel shell particles—into the soft polypropylene matrix. These materials differ markedly in their deformation behaviour from PP. As a result, stress concentration and interfacial defects become more pronounced, leading to premature failure during stretching. The presence of such rigid inclusions inevitably reduces the polymer's ability to undergo plastic deformation, thereby lowering the elongation at break.

Flexural strength and modulus in polypropylene (PP) composites containing hybrid fillers were primarily influenced by the content of harakeke fibres rather than mussel shell fillers. The PP composite with 40% harakeke fibre exhibited the highest flexural strength and modulus, reaching 65.80 MPa and 3.39 GPa, respectively. A clear trend was observed: both flexural strength and modulus decreased as the harakeke fibre content was reduced in the hybrid composites. This trend was consistent across composites modified with either MAPP or PDA/MAPP.

For comparison, the flexural strength and modulus of PP composites containing 40% mussel shell fillers alone ranged between 32.8–39.7 MPa and 1.38–1.65 GPa, respectively. In contrast, the PP composites incorporating various combinations of hybrid fillers showed improved performance, with flexural strength ranging from 47.4 to 61.0 MPa and modulus from 2.11 to 2.91 GPa. These values were significantly higher than those of composites reinforced solely with mussel shell fillers, whether untreated or surface modified.

Overall, the use of hybrid fillers resulted in superior mechanical performance compared to single mussel shell filler systems, highlighting the reinforcing role of harakeke fibre in enhancing flexural properties.

6.3.5 Fracture morphology of PP composites incorporated with hybrid fillers-

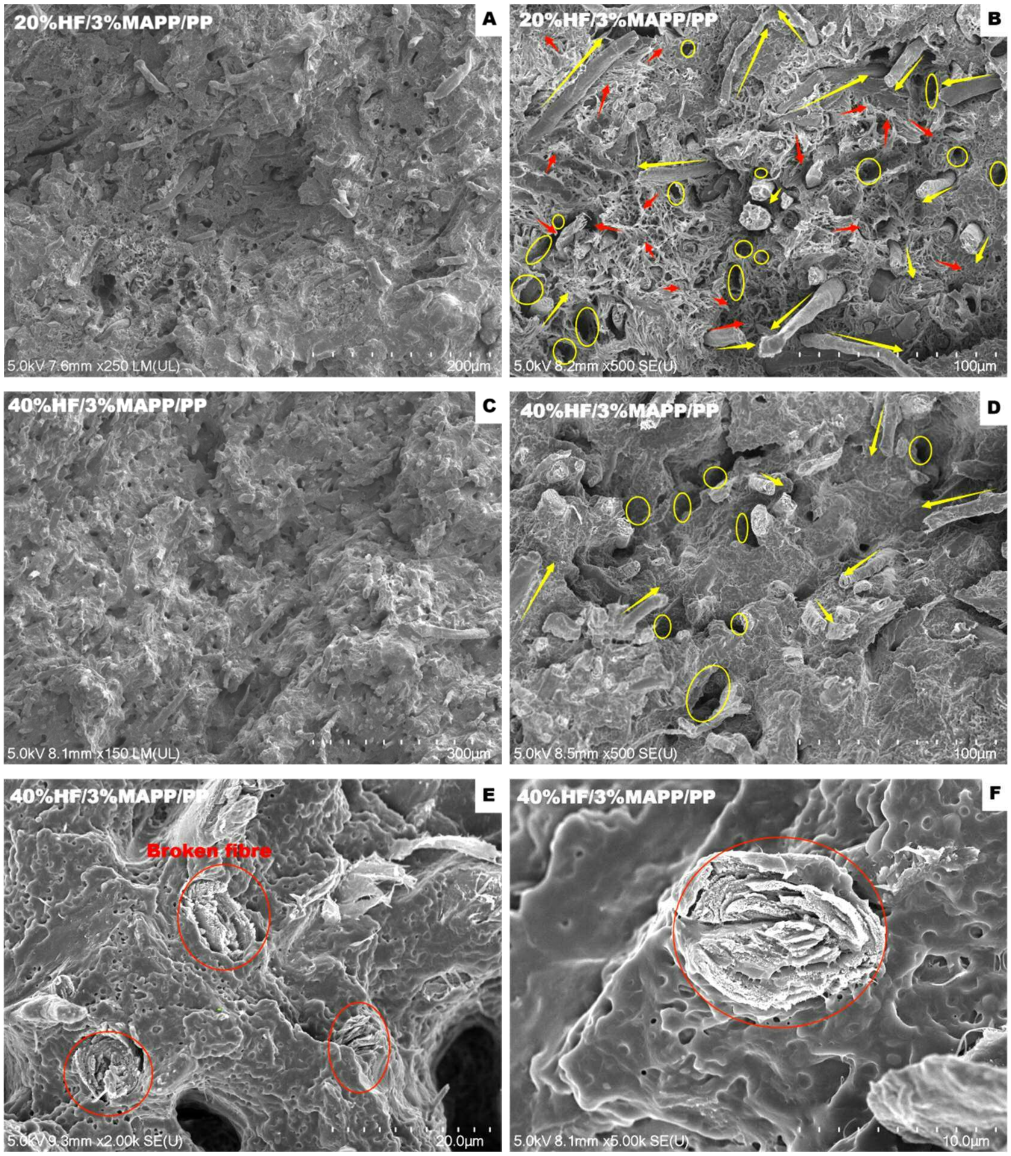

Figure 6- 11: SEM image of fracture surface of (A) 20%HF/ 3%MAPP/ PP (×250); (B) 20%HF/ 3%MAPP/ PP (×500); (C) 40%HF/ 3%MAPP/ PP (×150); (D) 40%HF/ 3%MAPP/ PP (×500); (E) 40%HF/ 3%MAPP/ PP (×2000); (F) 40%HF/ 3%MAPP/ PP (× 5000).

Yellow arrows indicate the orientation of harakeke fibres; yellow circles highlight voids within the matrix. The red arrow points to polymer fibrils pulled out during fracture, while red circles mark broken harakeke fibres.

SEM

6.3.5.1 SEM analysis of PP composites incorporated with harakeke fibres

Scanning electron microscopy (SEM) was employed to examine the morphological features of fracture surfaces in polypropylene (PP) composites incorporating 20% and 40% harakeke fibres (Figure 6-11A-F). The analysis revealed key characteristics of fibre-matrix interactions and their influence on composite properties.

Low magnification (×250) SEM images of 20% HF/3% MAPP/PP composite (Figure 6-11A) showed well-separated and distributed fibres within the matrix, indicating effective fibre wetting. However, the presence of voids resulting from fibre pull-out and debonding suggested insufficient interfacial bonding between harakeke fibres and the PP matrix. Similar observations were made in the 40% HF/3% MAPP/PP composite at low magnification (×150), with a notably higher concentration of harakeke fibres able to be seen from Figure 6-11C.

Higher magnification analysis of 20% HF/3% MAPP/PP (Figure 6-11B) provided detailed insights into the fibre-matrix interface. Harakeke fibres were embedded in the PP matrix with clear attachment, though lacking consistent alignment (as indicated by yellow arrows pointing in different directions reflecting this). The fibre-matrix bonding, attributed to MAPP-improved compatibility and interfacial adhesion, supported stress transfer and restraint in polymer deformation. This enhanced interfacial bonding explains the improved mechanical properties observed as discussed in previous sections, including the increased tensile strength and modulus, as well as flexural strength and modulus.

However, visible gaps around some fibres indicated a state of partial debonding, suggesting areas of insufficient interfacial bonding persist. This observation is consistent with challenges reported in other studies on natural fibre composites [30].

The presence of both well-bonded areas and regions of partial debonding highlights the complex nature of interfacial interactions in natural fibre composites.

At 40% fibre content, more intense fibre-matrix bonding was observed, with fibres exhibiting greater matrix coverage and increased fibre-top breakage (Figure 6-11D). This suggests improved fibre-matrix interaction at higher fibre content. The observed fibre breakage indicates mechanical failure of some harakeke fibres under applied stress, likely due to more effective stress transfer from matrix to fibre. Clear evidence of fibre breakage is visible in Figures 6-11E and F.

The enhanced fibre-matrix bonding at higher fibre content can be attributed to two factors: (1) MAPP's effectiveness in improving fibre wetting and adhesion, and (2) closer fibre-matrix interaction during melt compounding at higher fibre concentrations.

Fracture surface comparison revealed distinct differences between 20% and 40% fibre content composites. The 20% HF/3% MAPP/PP exhibited ductile features, evidenced by polymer fibril pull-out. In contrast, 40% HF/3% MAPP/PP showed more brittle characteristics, including smooth surfaces, crazing, and cracks perpendicular to the tensile direction. These observations explain the improvement in mechanical properties, i.e. the higher stiffness and reduced ductility in the 40% fibre content composite.

6.3.5.2 SEM analysis of PP composites incorporated with hybrid fillers

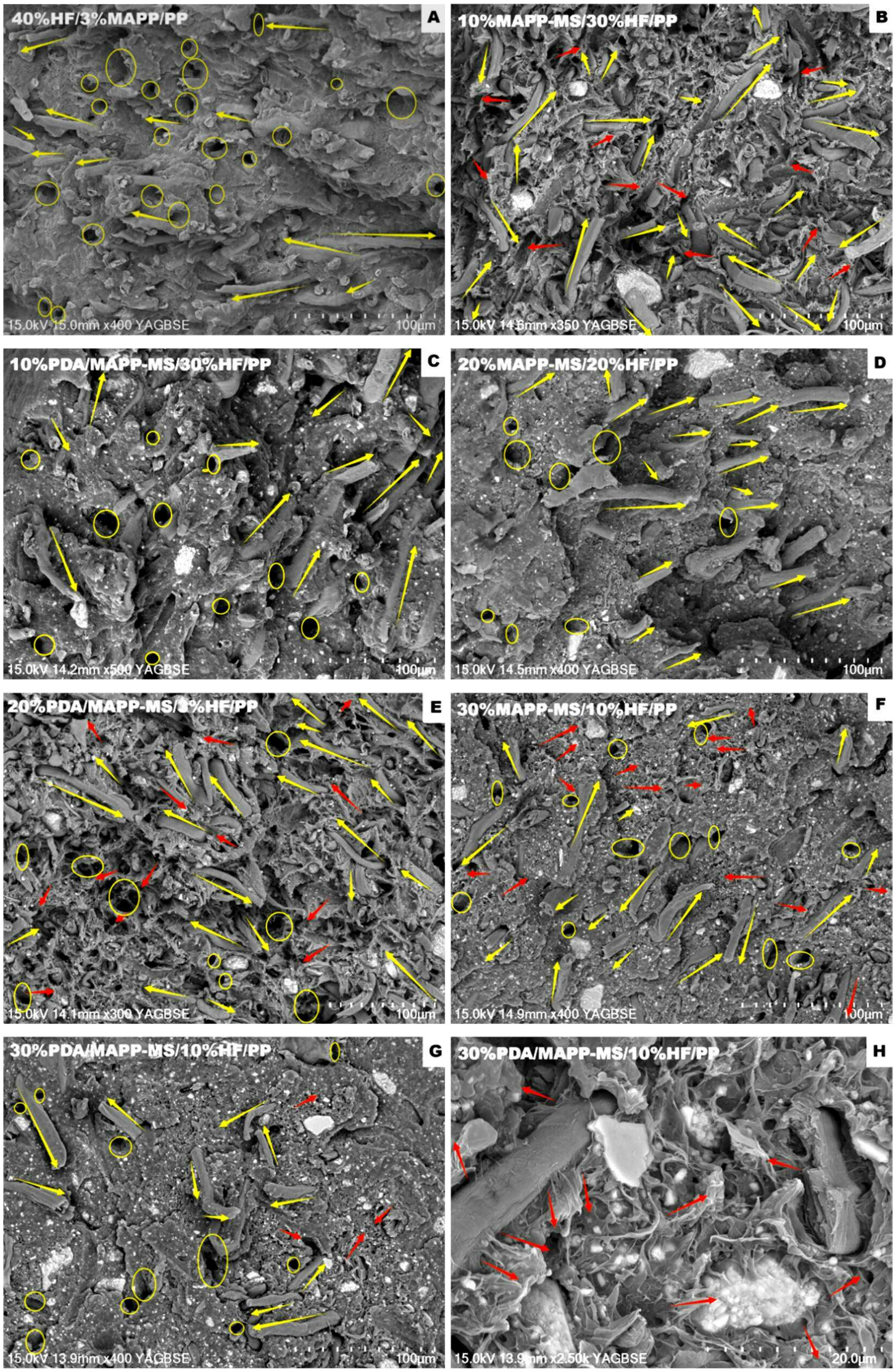

Figure 6- 12: BSE image of fracture surface of (A) 40% HF/ 3% MAPP/ PP; (B) 10% MAPP- MS/ 30% HF/ PP; (C) 10% PDA/ MAPP- MS/ 30% HF/ PP; (D) 20% MAPP- MS/ 20% HF/ PP; (E) 20% PDA/ MAPP- MS/ 20% HF/ PP; (F) 30% MAPP- MS/ 10% HF/ PP;(G) 30% PDA/ MAPP- MS/ 10% HF/ PP; (H) 30% PDA/ MAPP- MS/ 10% HF/ PP (×2500).

The fracture surfaces of polypropylene (PP) composites incorporating hybrid fillers were characterised using scanning electron microscopy (SEM) in Backscattered Electron (BSE) mode, as shown in Figure 6-12 B-H. BSE imaging relies on the reflection of incident electrons from the specimen, providing contrast based on atomic number (Z) differences; elements with higher atomic numbers scatter more electrons, appearing brighter in BSE images [31].

As a comparison, PP composite with a single filler, 40% harakeke fibres, is presented in Figure 6-12 A. Due to the similar carbon-rich composition of harakeke fibres and PP matrix, the BSE image shows uniform greyscale intensity without high contrast areas. Voids (marked with yellow circles) and non-aligned fibres are observed, providing similar information to conventional SEM imaging.

BSE images of PP composites with hybrid fillers (Figure 6-12 B-H) offer enhanced differentiation between organic and inorganic components, improved visibility of filler distribution, and insights into interfacial adhesion. Bright spots reveal the distribution of mussel shell particles, appearing brighter due to calcium's higher atomic number (Z_{Ca}=20) compared to carbon-rich PP (Z_C=6) and harakeke fibres. Mussel shell fillers, ranging from several micrometres to about 100 µm, are well-distributed in the matrix with irregular shapes. This size range confirms the particle size distribution results presented in Chapter 4, indicating good compatibility between the modified mussel shell particles and the PP matrix, with no severe agglomeration occurring during material processing. As the ratio of modified mussel shell filler to harakeke fibre increases from 1:3 to 3:1, a noticeable reduction in harakeke fibres is observed.

While voids from fibre pull-out and gaps between fillers persist, small mussel shell particles appear to fill some fibre-matrix debonding gaps, contributing to enhanced mechanical properties of hybrid filler composites compared to those with 40% mussel shell fillers alone. MAPP-enhanced filler-matrix interactions are evidenced by polymer fibrils bridging harakeke fibres and mussel shell fillers, which is particularly clear in Figure 6-13 H (30%PDA/MAPP-MS/10%HF/PP). These observations correlate with the improved tensile and flexural strength and modulus values measured for the hybrid filler composites.

The distribution of the filler through the composites can be further elucidated through EDS mapping performed on the same fracture surface (upon which attention was focused earlier). This effectively provides visualisation of the elemental distribution. Figure 6-13

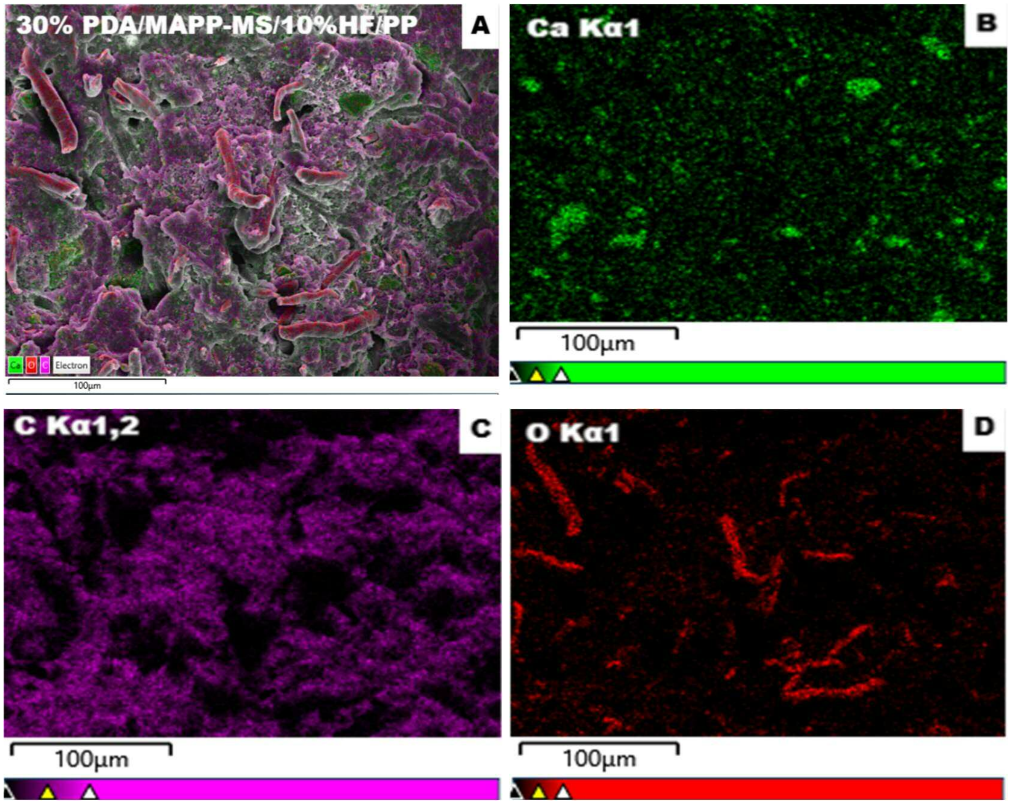

Figure 6- 13: Energy dispersive spectroscopy (EDS) mapping of 30% PDA/ MAPP- MS/ 10% HF/ PP (A) and elements mapping of (B) Ca Kα1, (C) C Kα1,2, and (D) O Kα1.

A-D presents EDS mapping results for 30% PDA/MAPP-MS/10%HF/PP, with colour codes of green for calcium, purple for carbon, and red for oxygen. The calcium distribution (green areas) closely corresponds to the bright regions observed in the BSE image (Figure 6-12G), confirming the shape, size, and distribution of the mussel shell particles in the composite. Carbon (shown by the purple areas) is expectedly ubiquitous in the composites, representing both the PP matrix and the harakeke fibres. Notably, the oxygen mapping distinctly reveals the shape and distribution of the harakeke fibres, attributable to their cellulose-rich composition following mercerisation. This oxygen-rich signature of the fibres provides a very clear differentiation from the otherwise non-oxygenated PP matrix, offering valuable insights into fibre dispersion and orientation within the composite. The EDS mapping thus complements the BSE imaging, providing a comprehensive understanding of the spatial arrangement of different components within the composite structure.

6.3.6 The influence of hybrid fillers on the dynamic mechanical properties of PP composites

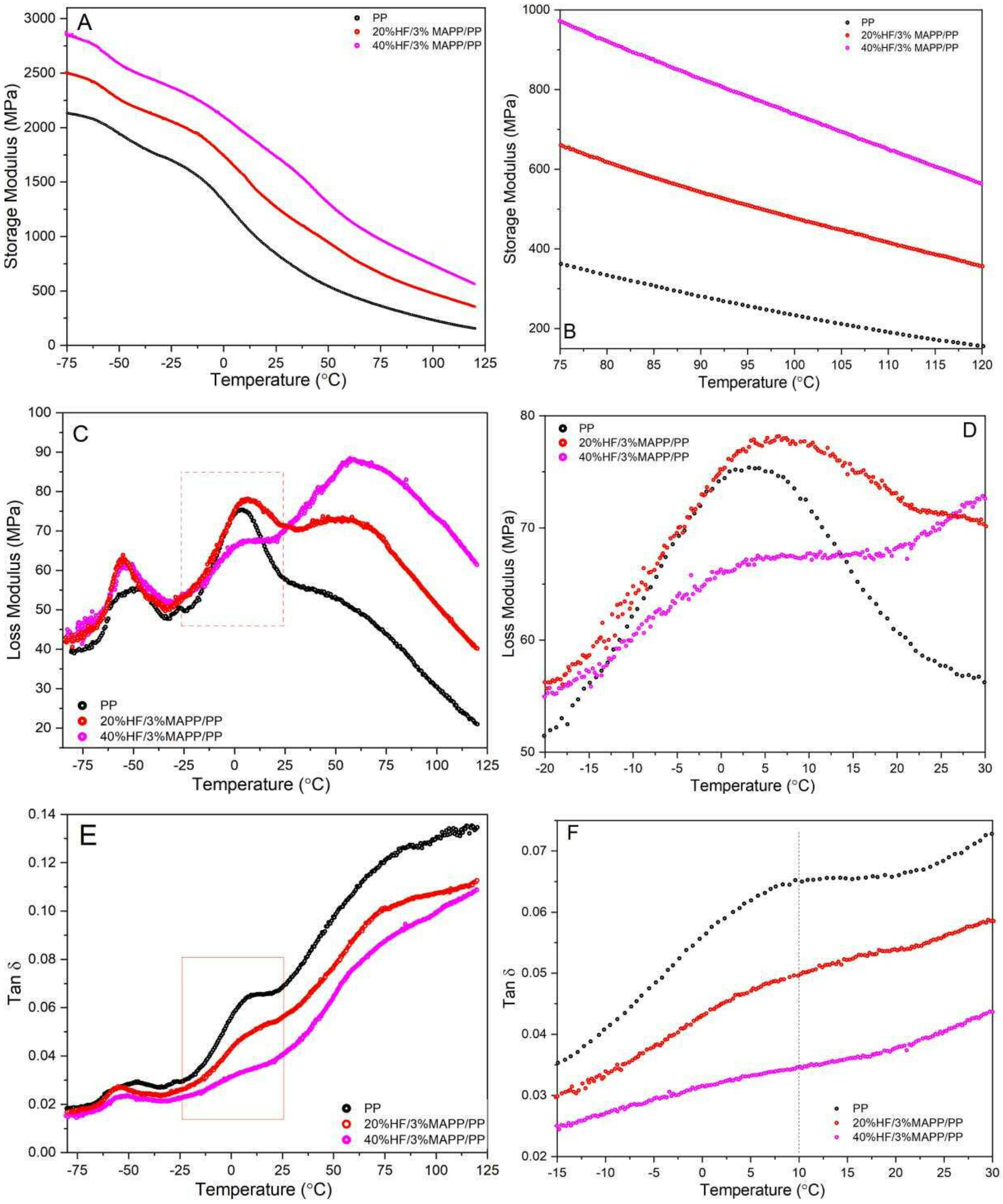

Figure 6- 14: DMA curves of PP composites incorporated with 20% and 40% HF as functions of temperature, (A) storage (B) enlargement of storage moduli, (C) loss moduli,(D) enlargement of loss moduli, (E) damping factors, (F) enlargement of damping factors.

Harakeke fibre or harakeke fibre combined with different modified mussel shell fillers incorporated into PP composites may exhibit varying viscoelastic responses to dynamic loading, so potentially revealing synergistic effects of these hybrid fillers. Dynamic Mechanical Analysis (DMA) is a powerful tool to investigate these viscoelastic properties and to explore such synergistic interactions. This technique reveals how the incorporation of these fillers affects the composite's stiffness, energy dissipation mechanisms, and filler-matrix interactions. By examining the storage modulus (E'), loss modulus (E"), and damping factor (tan δ), valuable insights can be gained intothe material's response to dynamic loading, its heterogeneity, and the effectiveness of filler-matrix adhesion. Furthermore, DMA elucidates how these properties evolve with temperature, providing a comprehensive understanding of the composite's performance under various conditions. In the following section, we present DMA results for PP composites containing 20% or 40% harakeke fibres, as well as various combinations of harakeke fibres and modified mussel shell fillers.

6.3.6.1 Effect of harakeke fibres on the dynamic mechanical properties of PP composites

The temperature dependence of the dynamic mechanical properties of PP composites incorporated with 20 or 40% harakeke fibres, including (Tc), is illustrated in Figure 6-14 A-F.

Table 6- 5: Comparison of neat PP and PP composites with different amounts of untreated mussel shell fillers (DMA data).

Samples	**Storage modulus (MPa)**				**T_g (°C)**	**Loss modulus (MPa)**	**C (60 °C)**
	-50 °C	Change %	120 °C	Change %	/		
PP	1951.09	-	156.03	-	3.2	75.39	
20%HF/ 3%MAPP/PP	2263.30	16.00	356.59	128.54	6.55	78.18	0.71
40%HF/ 3%MAPP/PP	2587.68	32.63	564.45	261.76	3.91	67.53	0.59
10%MAPP-MS/30%HF/PP	2860.69	46.62	592.99	280.05	7.72	83.11	0.63
20%MAPP-MS/20%HF/PP	2794.85	43.25	493.90	216.54	3.52	83.44	0.65
30%MAPP-MS/10%HF/PP	2693.29	38.04	382.40	145.08	5.88	88.79	0.72
10%PDA/MAPP-MS/30%HF/PP	2948.04	51.10	614.38	293.76	7.84	82.29	0.61
20%PDA/MAPP-MS/20%HF/PP	2487.70	27.50	301.10	92.97	8.20	89.64	0.68
30%PDA/MAPP-MS/10%HF/PP	2539.43	30.15	388.43	148.95	9.13	91.74	0.71

The temperature dependence of the dynamic mechanical properties of PP composites incorporated with 20 or 40% harakeke fibres at solid state, including storage modulus (E'), loss modulus (E"), and damping factor (tan δ), is illustrated in Figure 6-14 A-F. The storage moduli at selected temperatures (-50, 120 °C), glass transition (β-transition) temperature (T_g) from loss modulus curves and the loss moduli at β-transition were presented in Table 6-5. Furthermore, to evaluate the impact of fillers, the effectiveness coefficient (C) calculated using Equation 5-1 based on the storage modulus at -10°C in the glassy region was also included in Table 6-5.

The storage modulus curves of both 20% HF/3% MAPP/PP and 40% HF/3% MAPP/PP composites exhibit the typical decreasing trend with increasing temperature, consistent with the behaviour observed in neat PP and PP composites containing mussel shell fillers. Throughout the entire temperature range, the storage modulus of 20% HF/3% MAPP/PP remains higher than that of neat PP, with a further increase seen at the 40% harakeke fibre loading. This indicates that the stiffness of the composites improves with higher fibre content, particularly at 40 %, reflecting a clear correlation with the measured Young's moduli. The improvement in stiffness is attributed to the high elastic modulus of harakeke fibres.

Moreover, the presence of MAPP significantly enhances interfacial bonding between the harakeke fibres and the PP matrix, contributing to the improved storage modulus. The increase in storage modulus varies between the glassy and rubbery regions. At －50 ℃ (glassy region), 20% HF/3% MAPP/PP and 40% HF/3% MAPP/PP exhibit increases of 16.0% and 32.6%, respectively, relative to neat PP. In contrast, in the rubbery region, dramatic increases of 128.5% and 261.8% are observed for 20% and 40% HF/3% MAPP/PP, respectively.

This pronounced reinforcing effect at elevated temperatures is consistent with previous findings on hemp fibre-reinforced PP composites [32]. The storage modulus of PP is strongly influenced by the strength of intermolecular interactions and the packing of polymer chains. In the glassy state, polymer chains are tightly packed, restricting mobility. As the temperature rises into the rubbery region, chain mobility increases. However, the incorporation of harakeke fibres restricts this movement through interfacial interactions, leading to a greater proportion of immobilised chains and, consequently, a more significant increase in storage modulus.

Loss modulus, representing the viscous component of the material, reflects energy dissipation under stress, likely through interfacial friction. The addition of 20% or 40% harakeke fibres to polypropylene (PP) composites significantly enhances the γ- and α-transition peaks in the loss modulus curves (Figure 6-14 C&D), indicating a pronounced influence on molecular mobility and hence on these two relaxation processes. In neat PP, only the β-transition peak is observed, showing a maximum at 3.2°C, while the γ- and α-transitions appear as broad or merely shoulder peaks. The results also show that the loss moduli of composites with 20 or 40% harakeke fibres at γ- and α-transitions are both higher than those observed for neat PP, reflecting possible increased interfacial friction created by the introduction of fibres, leading to more energy dissipation in both the glassy and rubbery regions.

The β-transition peak occurs at around 6.6°C for the 20% HF composite and decreases to 3.91°C for the 40% HF composite. The β-transition, which reflects the unrestricted amorphous portions in polymers, exhibits more complex behaviour. At the β-transition, the loss moduli follow the order of 40%HF/3%MAPP/PP (67.53 MPa) < PP (75.39 MPa) < 20%HF/3%MAPP/PP (78.18 MPa). Upon the addition of 20% HF, the slightly increased loss modulus (compared to neat PP) indicates that the presence of harakeke fibres creates a filler-matrix interface where energy may dissipate. Increasing the HF content to 40% resulted in a pronounced decrease in loss modulus, indicating strong fibre-matrix interfacial adhesion due to the higher fibre loading. This finding is consistent with the SEM observations discussed earlier.

Figure 6-14 E – F shows a reduction in the damping factor (tan δ) for PP composites containing 20% and 40% harakeke fibres across the entire temperature range, compared to neat PP. Tan δ , defined as the ratio of loss modulus to storage modulus, is widely regarded as a more reliable indicator of interfacial bonding than either modulus alone, as it is independent of sample geometry [33] Higher tan δ values typically suggest weaker interfacial adhesion due to greater energy dissipation from interfacial friction, whereas lower values indicate stronger bonding at the fibre – matrix interface. Between the two fibre-reinforced composites, a further reduction in the damping factor was observed with increased fibre content. This trend indicates improved interfacial adhesion in the 40% harakeke fibre composite, likely due to both the higher fibre loading and the use of maleic anhydride-grafted polypropylene (MAPP) as a compatibilizer. These results are consistent with SEM observations, which also showed better fibre – matrix interaction in composites with greater fibre content.

The effectiveness coefficient (C) was found to decrease with increasing harakeke fibre content. A C value of 0.71 was recorded for the 20% HF/3% MAPP/PP composite, while a lower value of 0.59 was obtained for the 40% HF/3% MAPP/PP composite. A lower coefficient indicates a higher reinforcing efficiency, suggesting that 40% harakeke fibre provides a stronger reinforcement effect on the PP matrix than the 20% fibre content. This trend is consistent with results previously reported for hemp fibre-reinforced PP composites [32].

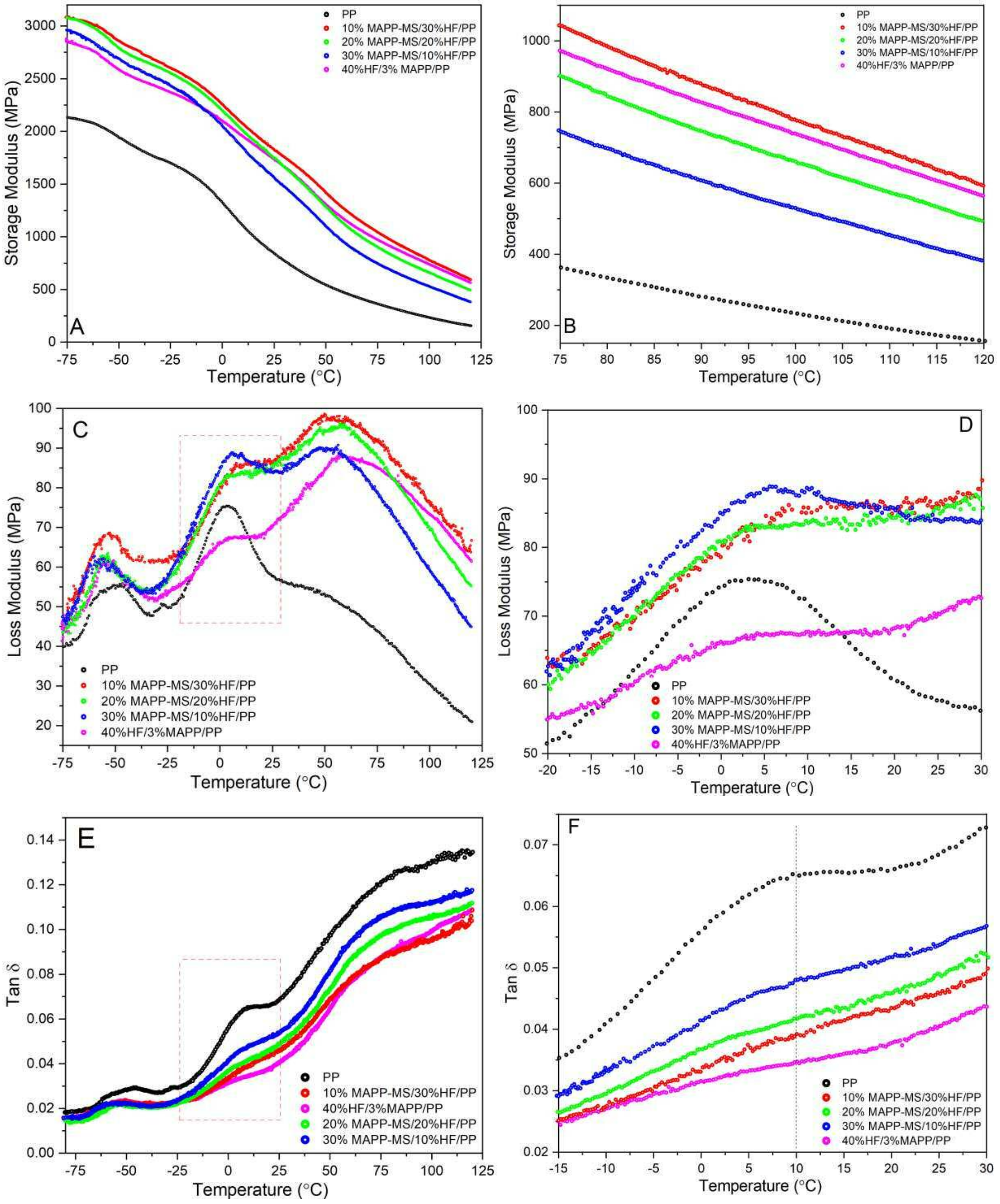

Figure 6- 15: DMA curves of PP composites incorporated with different combinations of MAPP-MS and HF fillers as a function of temperature, (A) storage moduli, (B) enlargement of storage moduli;(C) loss moduli, (D) enlargement of loss moduli; (E) damping factors, (F) enlargement of damping factors.

6.3.6.2 Effect of hybrid filler on the dynamic mechanical properties of PP composites

With the total filler content was fixed at 40 %, the potential synergistic effects of varying ratios of MAPP-MS or PDA/MAPP-MS fillers combined with harakeke fibres on the dynamic mechanical properties of PP composites were investigated. As the viscoelastic properties are primarily governed by the polymer matrix, the amount of polypropylene was kept constant across all composite formulations to match that of the 40% HF/3% MAPP/PP reference. Therefore, this section focuses on the influence of filler type, hybrid filler composition, the intrinsic properties of the fillers, and their interactions with the PP

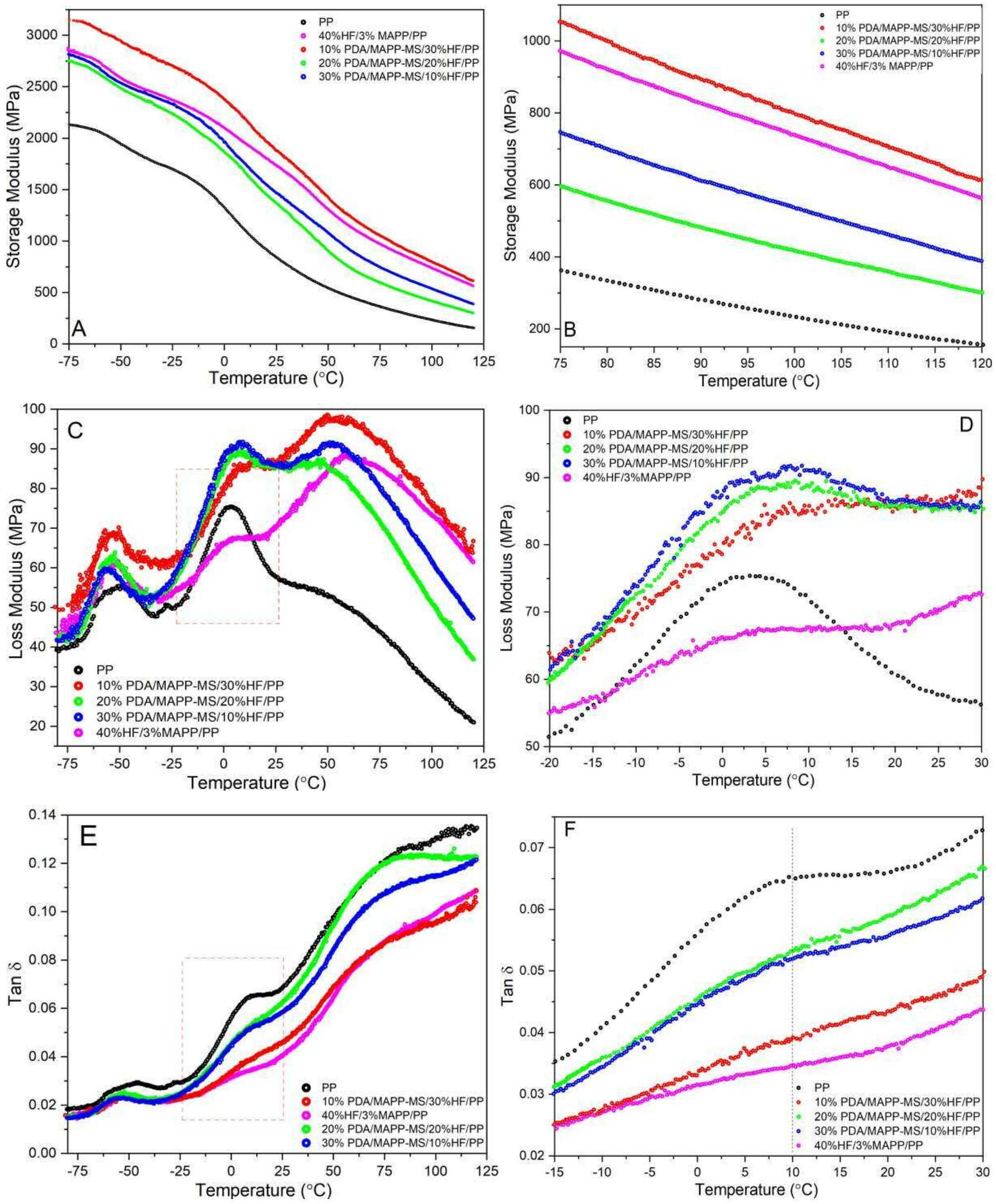

Figure 6- 16: DMA curves of PP composites incorporated with different combination of PDA/MAPP-MS and HF fillers as functions of temperature, (A) storage (B) enlargement of storage moduli;(C) loss moduli,(D) enlargement of loss moduli; (E) damping factors, (F) enlargement of damping factors.

matrix on the viscoelastic behaviour of the composites.

Dynamic mechanical analysis (DMA) curves for PP composites containing different combinations of MAPP-MS and harakeke fibres, as well as PDA/MAPP-MS and harakeke fibres, are presented in Figures 6-15 and 6-16, respectively.

Figures 6-15 and 6-16A – B show that the storage modulus curves for all polypropylene (PP) composites containing hybrid fillers exhibit a typical decreasing trend with increasing temperature. This temperature-sensitive behaviour is predominantly governed by the polymer matrix, as elevated temperatures increase chain mobility and expand the free volume within the material [34]. Across the entire temperature range, the storage moduli of all hybrid-filled composites are higher than that of neat PP, indicating enhanced stiffness.

As summarised in Table 6-5, at –50 °C (glassy region), the relative increase in storage modulus (E′) compared to neat PP follows the order: 40% HF/3% MAPP/PP (32.63%) < 30% MAPP-MS/10% HF/PP (38.04%) < 20% MAPP-MS/20% HF/PP (43.25%) < 10% MAPP-MS/30% HF/PP (46.62%). In the rubbery region at 120 °C, where the polymer chains exhibit greater mobility, the reinforcing effect becomes more pronounced: 30% MAPP-MS/10% HF/PP (145.08%) < 20% MAPP-MS/20% HF/PP (216.54%) < 40% HF/3% MAPP/PP (261.76%) < 10% MAPP-MS/30% HF/PP (280.05%). Among all composites, the combination of 10% MAPP-MS with 30% harakeke fibres demonstrated the most substantial enhancement in storage modulus in both temperature regions, suggesting an optimal synergistic effect from this hybrid filler ratio.

Generally, the higher storage modulus can be associated with 1) higher stiffness, resulting from the restrained and closer packed polymer chains, 2) higher crystallinity, and 3) introduction of rigid fillers [35]. In hybrid filler incorporated PP composites, both harakeke fibre and MAPP or PDA/MAPP modified mussel shell fillers are harder materials compared to soft PP. Moreover, in the glassy region, where molecular motion is highly constrained, the differing morphologies of MAPP-MS and HF effectively suppress chain mobility and reduce free volume. In the rubbery region, with higher thermal energy, these interactions remain effective, particularly with increased harakeke fibre content, supporting a higher proportion of immobilised chains.

A similar trend is observed for composites containing PDA/MAPP-MS and harakeke fibres. The highest storage modulus is achieved by the 10% PDA/MAPP-MS/30% HF/PP composite, reaffirming the effectiveness of a 1:3 hybrid filler ratio. In both temperature regions, the storage modulus follows the order: 20% PDA/MAPP-MS/20% HF/PP < 30%

PDA/MAPP-MS/10% HF/PP < 40% HF/3% MAPP/PP < 10% PDA/MAPP-MS/30% HF/PP, confirming the trends observed in Table 6-5.

Figures 6-15 and 6-16C – D present the loss modulus curves, showing three distinct transitions for all hybrid-filled composites. Across the entire temperature range, loss moduli exceed those of neat PP. This enhancement is due to increased interfacial friction between fillers and matrix, where energy dissipation occurs. The glass transition temperatures (Tg) of all hybrid-filled composites shift to higher values with broader transition peaks, indicating a greater energy requirement for molecular motion at Tg, and confirming the inhibitory effect of hybrid fillers on chain mobility.

Figures 6-15 and 6-16E–F depict the damping factor (tan δ) behaviour. All hybrid-filled composites exhibit reduced and broadened tan δ peaks compared to neat PP. At a total filler loading of 40%, the various hybrid combinations show synergistic effects in lowering the damping factor, though the lowest value is still observed for the 40% HF/3% MAPP/PP composite. Among the hybrid systems, tan δ of PP incorporated with MAPP-MS and harakeke fibres follows the order: 30% MAPP-MS/10%HF/PP>20% MAPP-MS/20% HF/ PP> 10% MAPP-MS/30% HF/PP>40% HF/3% MAPP/PP, similarly, 30% PDA/MAPP-MS/10% HF/PP ≈ 20% PDA/MAPP-MS/20% HF/PP > 10% PDA/MAPP-MS/30% HF/PP > 40% HF/3% MAPP/PP.

It is important to note that the damping behaviour of hybrid composites is influenced by two competing mechanisms. On one hand, well-dispersed fillers can interact with more polymer chains, increasing interfacial friction and potentially raising tan δ. On the other hand, when interfacial bonding is strong, energy dissipation is reduced, resulting in a lower tan δ [35]. Therefore, the overall damping response reflects a balance between filler dispersion and interfacial bonding. In the present study, the reduced tan δ values, particularly in composites with high fibre content and effective surface modification, suggest that strong interfacial adhesion dominates, leading to improved damping behaviour.

The effectiveness coefficient (C) was calculated based on the storage modulus at –10 °C, varied across different combinations of hybrid fillers in PP composites. For MAPP-MS-based hybrids, the C values were 0.72 for 30% MAPP-MS/10% HF/PP, 0.65 for 20% MAPP-MS/20% HF/PP, and 0.63 for 10% MAPP-MS/30% HF/PP. Similarly, for PDA/MAPP-MS-based hybrids, the values were 0.71 for 30% PDA/MAPP-MS/10%

HF/PP, 0.68 for 20% PDA/MAPP-MS/20% HF/PP, and 0.61 for 10% PDA/MAPP-MS/30% HF/PP.

Notably, in both hybrid systems, the 1:3 ratio of modified mussel shell filler to harakeke fibre yielded the lowest effectiveness coefficient. This result suggests that, at this specific ratio, the reinforcing efficiency was optimised due to the synergistic interaction between the two filler types. The lower C value reflects a more substantial improvement in stiffness relative to filler content, supporting the conclusion that filler synergy is most effective at this composition.

It is worth noting that the improvement in mechanical properties attributed to enhanced interfacial adhesion from PDA/MAPP co-modification, as compared to MAPP modification alone, was not observed in the hybrid filler PP composites. This can be attributed to the inherent complexity of the hybrid filler system, where both filler – matrix and filler – fibre interactions play significant roles. As a result, the specific advantage provided by surface modification becomes less dominant within the overall composite behaviour.

6.3.7 The influence of hybrid fillers on the creep-recovery behaviour of PP composites

Creep-recovery behaviour reflects the time-dependent viscoelastic properties of polymeric materials. In this study, polypropylene (PP) composites containing 20% and 40% harakeke fibres, along with various combinations of modified mussel shell (MS) and harakeke fibres, were subjected to cyclic stress loading and unloading. Tests were conducted at 30 ℃ using a constant 3 N load over 10 cycles, each lasting 30 minutes. The resulting cyclic creep and recovery curves are presented in Figure 6-17A – C.

The creep-recovery curves demonstrate that all PP composites exhibited lower creep and residual strain than neat PP across all cycles. Lower creep strain indicates reduced deformation under sustained load, while lower residual strain suggests improved elastic recovery.

Comparing 20%HF/3%MAPP/PP with 40%HF/3%MAPP/PP, the latter displayed reduced creep and residual strain, indicating enhanced long-term deformation resistance with higher fibre content. Among hybrid composites, the formulation with MAPP-MS and harakeke fibres achieved the lowest creep and residual strains when 10% MAPP-MS and 30% harakeke fibre were incorporated, outperforming both 20% MAPP-MS/20%

HF/PP and 30% MAPP-MS/10% HF/PP. This highlights an optimised hybrid filler ratio (MAPP-MS:HF = 1:3) for enhanced creep resistance. A similar trend was observed in hybrid filler PP composites with PDA/MAPP-MS and harakeke fibre, where the 10% PDA/MAPP-MS/30% HF/PP composite exhibited the best performance, while 20% PDA/MAPP-MS/20% HF/PP and 30% PDA/MAPP-MS/10% HF/PP showed comparable results.

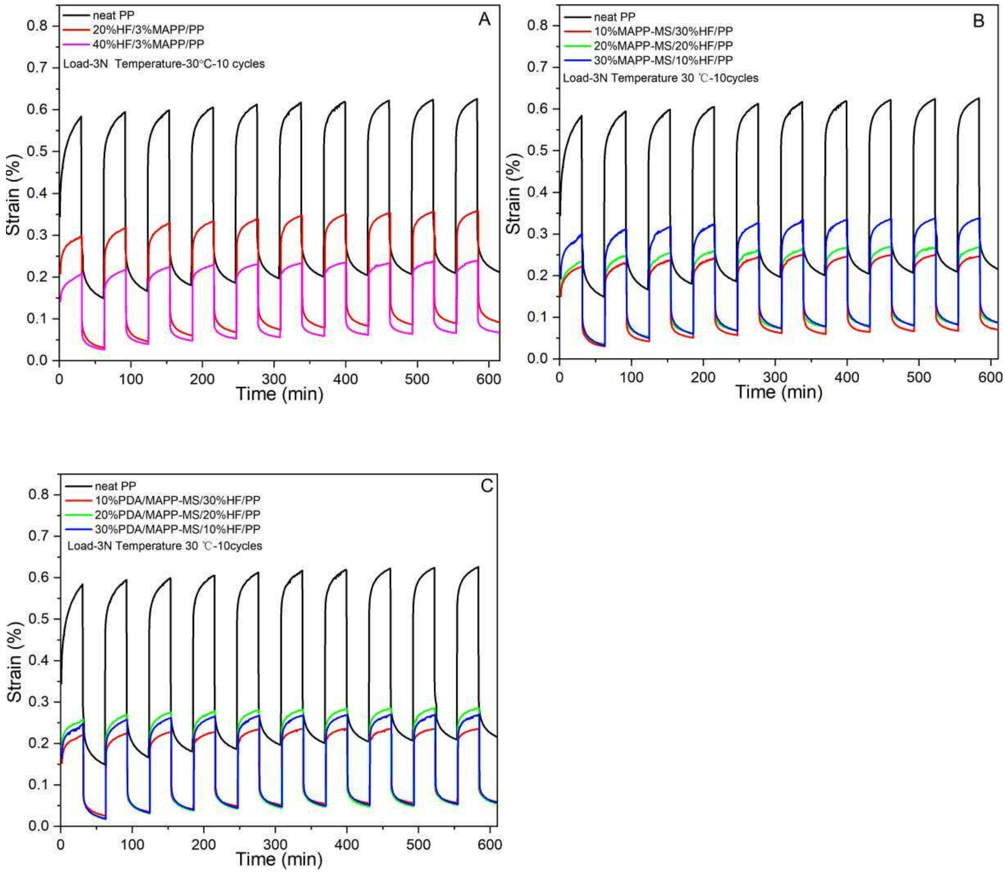

Figure 6- 17: Cyclic creep-recovery curves of neat PP and PP composites with (A) 20 and 40 % HF; (B) different combinations of MAPP-MS and HF; (C)different combinations of MAPP-MS and HF.

Table 6-7 summarises the maximum and residual strain values from the first cycle, showing that all fibre-reinforced and hybrid-filled composites recorded lower values than neat PP. Compared to neat PP, the maximum strain was reduced by 48.8% to 64.5%, and the residual strain by 75.5% to 88.6%. The greatest improvement in both metrics was observed for the 40%HF/3%MAPP/PP composite, followed closely by 10% MAPP-MS/30% HF/PP and 10% PDA/MAPP-MS/30% HF/PP, both of which showed maximum strain reductions of approximately 62%.

These improvements are attributed to several mechanisms. As detailed in Chapter 5, creep strain depends on applied stress, duration, and material characteristics such as filler morphology, concentration, interfacial properties, and structural heterogeneity [36]. Given that all samples were subjected to identical conditions, differences in performance stem from filler characteristics and matrix interactions. The addition of fillers restricts polymer chain mobility, thereby reducing slippage and reorientation. This explains the better performance of 40% harakeke fibre over 20%. Furthermore, improved dispersion and interfacial adhesion in hybrid systems enhance stress transfer and distribution. The superior performance of composites with 10% MAPP-MS or PDA/MAPP-MS and 30% harakeke fibre is consistent with dynamic mechanical analysis (DMA) results, which identified this ratio as providing optimal reinforcing efficiency.

Table 6- 6: Comparison of maximum creep strain and residual strain at the first cycle.

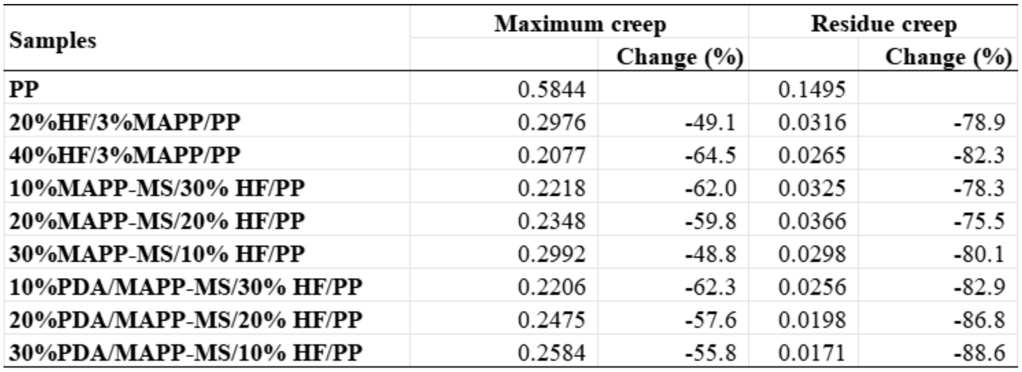

Samples	Maximum creep		Residue creep	
		Change (%)		Change (%)
PP	0.5844		0.1495	
20%HF/3%MAPP/PP	0.2976	-49.1	0.0316	-78.9
40%HF/3%MAPP/PP	0.2077	-64.5	0.0265	-82.3
10%MAPP-MS/30% HF/PP	0.2218	-62.0	0.0325	-78.3
20%MAPP-MS/20% HF/PP	0.2348	-59.8	0.0366	-75.5
30%MAPP-MS/10% HF/PP	0.2992	-48.8	0.0298	-80.1
10%PDA/MAPP-MS/30% HF/PP	0.2206	-62.3	0.0256	-82.9
20%PDA/MAPP-MS/20% HF/PP	0.2475	-57.6	0.0198	-86.8
30%PDA/MAPP-MS/10% HF/PP	0.2584	-55.8	0.0171	-88.6

Table 6- 7: Comparison of maximum creep strain and residual strain on the tenth cycle.

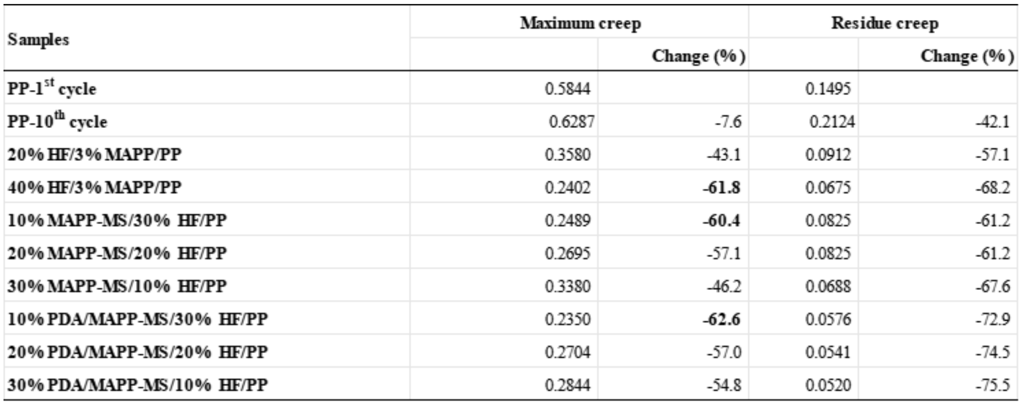

Samples	Maximum creep		Residue creep	
		Change (%)		Change (%)
PP-1st cycle	0.5844		0.1495	
PP-10th cycle	0.6287	-7.6	0.2124	-42.1
20% HF/3% MAPP/PP	0.3580	-43.1	0.0912	-57.1
40% HF/3% MAPP/PP	0.2402	**-61.8**	0.0675	-68.2
10% MAPP-MS/30% HF/PP	0.2489	**-60.4**	0.0825	-61.2
20% MAPP-MS/20% HF/PP	0.2695	-57.1	0.0825	-61.2
30% MAPP-MS/10% HF/PP	0.3380	-46.2	0.0688	-67.6
10% PDA/MAPP-MS/30% HF/PP	0.2350	**-62.6**	0.0576	-72.9
20% PDA/MAPP-MS/20% HF/PP	0.2704	-57.0	0.0541	-74.5
30% PDA/MAPP-MS/10% HF/PP	0.2844	-54.8	0.0520	-75.5

Table 6-8 presents creep and residual strain at the tenth cycle, comparing neat PP with different PP composites. After 10 cycles, neat PP exhibited a 7.6% increase in maximum strain compared to the value at first cycle, indicating cumulative deformation and a loss of dimensional stability. By contrast, all PP composites showed significant reductions in creep and residual strain. For example, 20%HF/3%MAPP/PP reduced maximum and residual strain by 43.1% and 57.1%, respectively. When fibre content was increased to 40%, these reductions reached 61.8% and 68.2%. Similarly, the hybrid formulations with a 1:3 filler ratio performed comparably to 40%HF/3%MAPP/PP. Specifically, 10% MAPP-MS/30% HF/PP achieved 60.4% and 61.2% reductions, while 10% PDA/MAPP-MS/30% HF/PP achieved even greater reductions of 62.6% and 72.9%, respectively. These results underscore the ability of hybrid fillers to mitigate long-term deformation under cyclic loading.

Additionally, the maximum and residual strain values for each cycle were plotted against the cycle number, as shown in Figure 6-18A–F. The slopes derived from linear fitting of the maximum strain data indicate a slight accumulation effect under repeated stress loading and unloading; however, all slope values remained below 0.01, suggesting minimal long-term deformation. For creep strain, neat PP exhibited a slope of 0.00461 over 10 cycles. The highest slope (0.00605) was observed for 20% HF/ 3% MAPP/PP, while 40% HF/3%MAPP/PP showed a reduced slope of 0.00298, indicating that higher harakeke fibre content resulted in less creep strain accumulation over 10 cycles. Notably, the lowest slope (0.00160) was recorded for the 10% PDA/MAPP-MS/30%HF/PP composite, followed by 10% MAPP-MS/30%HF/PP with a slope of 0.00292—

comparable to that of the 40%HF/3%MAPP/PP composite. These findings suggest that incorporating 10% PDA/MAPP-MS with 30% harakeke fibre offers the most effective reduction in creep strain accumulation under cyclic loading.

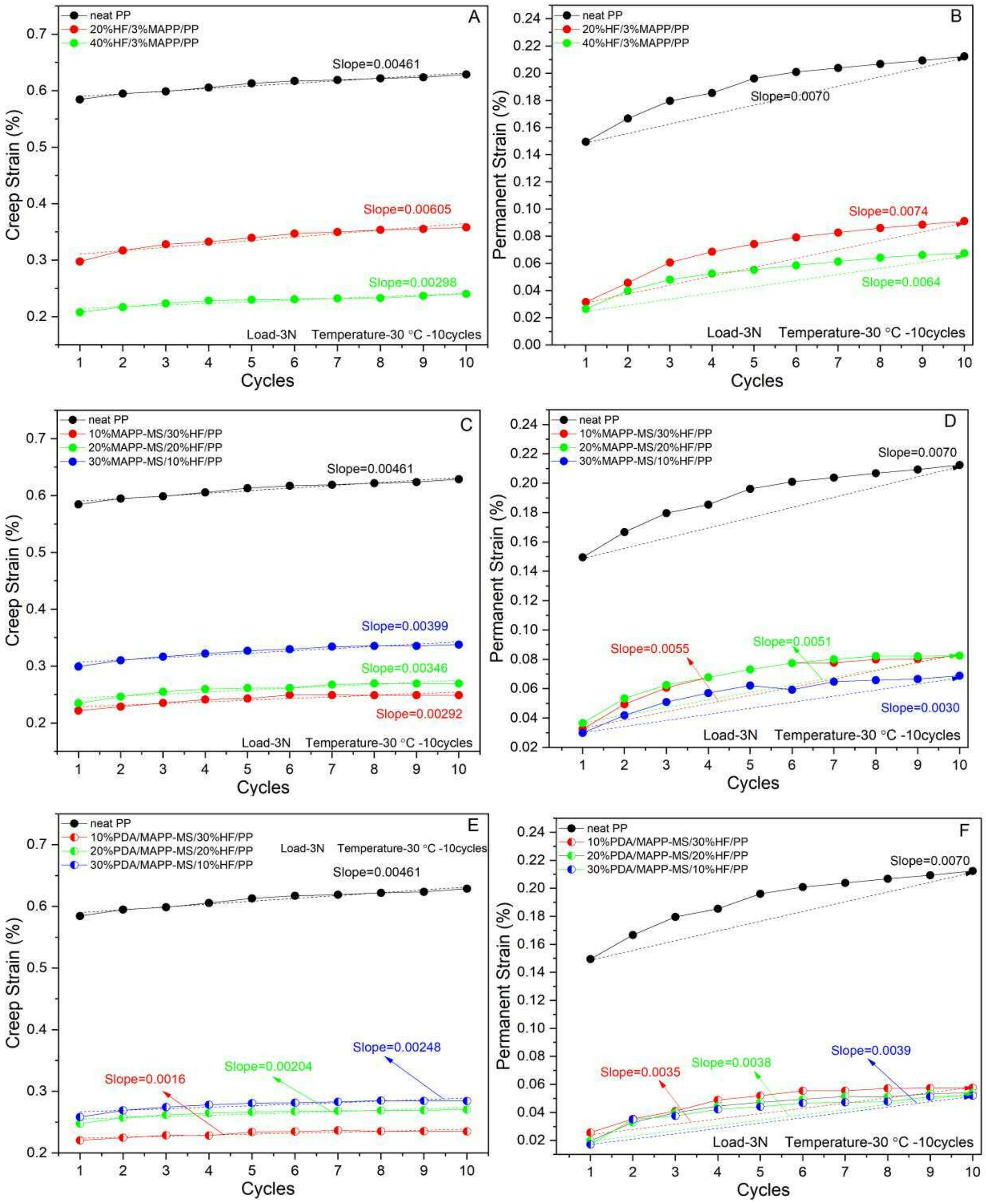

Figure 6- 18: Comparison of maximum creep strains of neat PP and PP composites with (A) 20 and 40 % HF; (C) different combinations of MAPP-MS and HF; (E) different combinations of MAPP-MS and HF; comparison of residue strains of neat PP and PP composites with (B) 20 and 40 % HF; (D) different combinations of MAPP-MS and HF; (F) different combinations of MAPP-MS and HF.

The residual strain plots exhibited a lower degree of linearity. Slope values calculated between the first and tenth cycle permanent strain values further confirmed that the 10% PDA/MAPP-MS/30%HF/PP composite had the lowest slope, indicating reduced defect accumulation and better structural integrity throughout cyclic deformation. These results collectively support the conclusion that hybrid filler systems, particularly with a 1:3 ratio

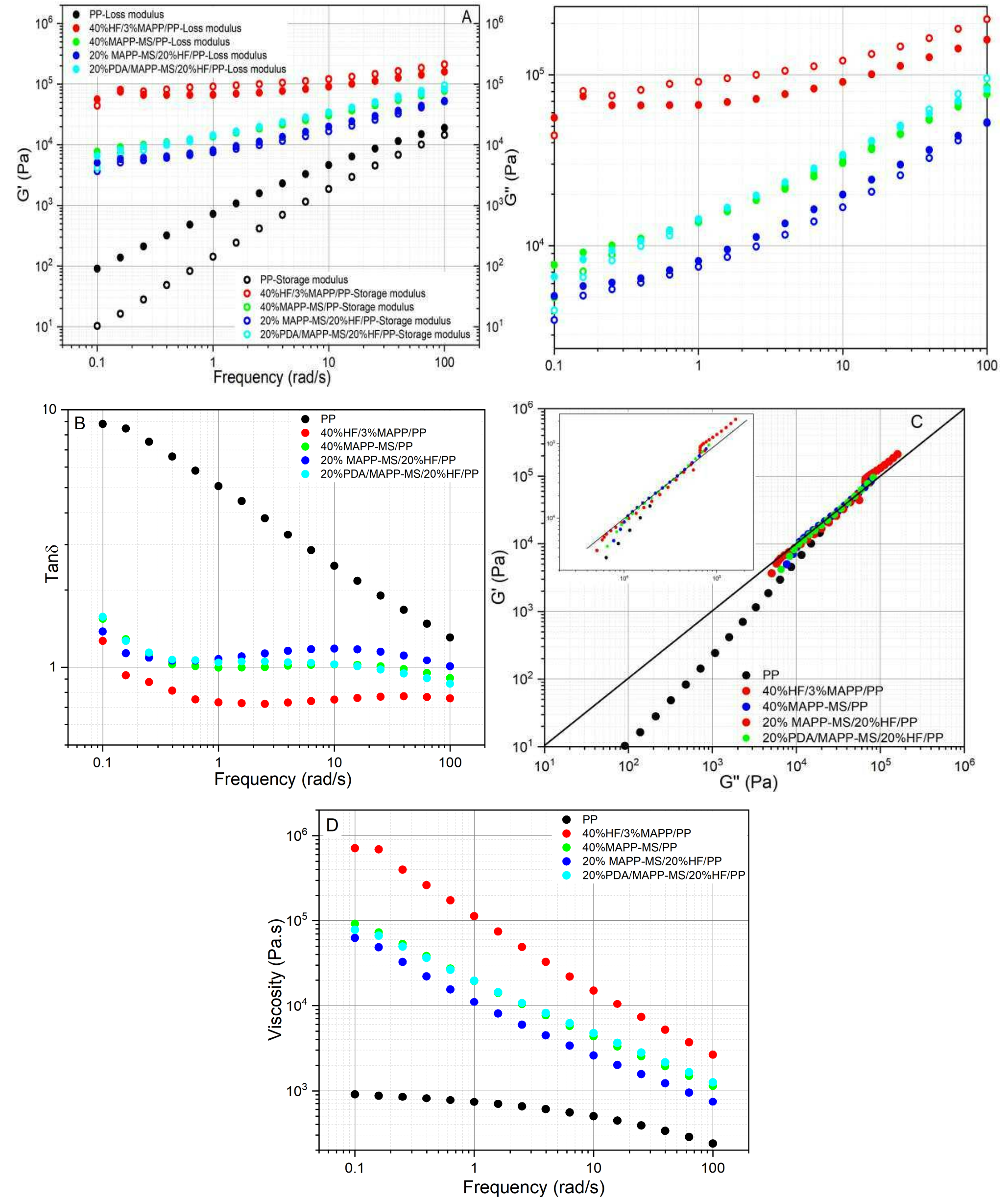

Figure 6- 19: Rheological properties of PP and its composites. (a) Storage moduli and loss moduli, (b) damping factor, (d) shear viscosity as a function of angular frequency, and (c) Han plots for PP, 40% HF/3%MAPP/PP, 40%MAPP-MS/PP, 20% MAPP-MS/20%HF/PP, and 20%PDA/MAPP-MS/20%HF/PP composites.

of mussel shell to harakeke fibre, significantly enhance the dimensional stability of PP composites under repeated mechanical stress.

6.3.8 The influence of hybrid fillers on the melt rheology behaviour of PP composites

The rheological properties of composites in the melt state provide crucial information for product processing and offer insights into the microstructure of the composite melt [37].

The melt rheology behaviour of PP composites with 40% different fillers was studied at 190°C. These fillers included 40% harakeke fibre (HF) with 3% MAPP, 40% MAPP-modified mussel shell (MAPP-MS), 20% MAPP-MS with 20% HF, and 20% PDA/MAPP-MS with 20% HF. Figure 6-19 A, B, and D illustrate the frequency dependency of storage modulus (G'), loss modulus (G"), damping factor (tan δ), and viscosity.

Figure 6-19A presents the storage modulus and loss modulus curves as functions of angular frequency. All PP composites (40% HF/3% MAPP/PP, 40% MAPP-MS/PP, 20% MAPP-MS/20%HF/PP, and 20% PDA/MAPP-MS/20% HF/PP) exhibit higher storage and loss moduli than neat PP across the entire shear frequency range. Throughout the frequency range, 40% HF/3%MAPP/PP shows the highest storage and loss moduli. The modulus curves of 40% MAPP-MS/PP and 20% PDA/MAPP-MS/20%HF/PP nearly overlap, followed by 20% MAPP-MS/20% HF/PP with slightly lower moduli. The storage and loss moduli of neat PP increase sharply with frequency, particularly in the lower frequency range. Conversely, 40% HF/3%MAPP/PP exhibits a clear plateau in the low-frequency region. This phenomenon is attributed to the high content of harakeke fibres forming a network structure in the melt, which inhibits the movement of PP molecular chains. Can *et al.* reported that when different concentrations of multi-walled carbon nanotubes (MWCNTs) were added to poly(ethylene oxide)/poly(methyl methacrylate) (PEO/PMMA 60/40) blends, a plateau was observed in the storage modulus curve of the composite with 4 wt.% MWCNTs at low frequencies. They explained that these fillers serve as entangled attractants, forming a network-like structure that significantly reduces the mobility of polymer chains [38]. Fen *et al.* also reported that increasing the content of hexagonal boron nitride (BN) in high-density polyethylene (HDPE) composites with MWCNT fillers leads to a significant increase in storage modulus in the low-frequency region, with a trend towards plateau formation. They attributed this phenomenon to a higher filler content and the synergistic effects of hybrid fillers. The formed network structure inhibits the movement of HDPE molecular chains, resulting in a shift in viscoelastic behaviour from liquid-like to solid-like in the low-frequency region [37]. As a result, the dependence of storage modulus on shear frequency becomes relatively weak. For the other three composites—40% MAPP-MS/PP, 20% MAPP-MS/20%HF/PP, and 20% PDA/MAPP-MS/20%HF/PP—both G' and G'' increase gradually with increasing frequency. As the frequency approaches 100 rad/s, G' and G'' of all four composites show a converging trend towards those of neat PP, suggesting that the predominant viscoelastic behaviour is governed by the matrix and less influenced by fillers at high frequencies.

At low frequencies, neat PP demonstrates liquid-like viscoelastic behaviour, with G'' much higher than G'. This behaviour becomes less pronounced with the addition of 20% MAPP-MS and 20% HF to PP, where G'' is only slightly higher than G'. The storage modulus and loss modulus curves of 40% MAPP-MS/PP and 20% PDA/MAPP-MS/20% HF/PP nearly overlap (G'' ≈ G'). For 40% HF/3% MAPP/PP, G' is higher than G'', demonstrating a shift in viscoelastic behaviour towards solid-like material [37].

The damping factor (tan δ = G''/G') is widely recognised as an indicator of a material's viscous and elastic characteristics. When tan δ = ∞, the material exhibits perfect viscous fluid behaviour, whereas tan δ = 0 represents a purely elastic solid. Figure 6-19B presents the damping factor curves for neat PP and four PP composites. As previously discussed in Chapter 5.9, the damping behaviour of neat PP is characterised by liquid-like melt properties. The tan δ values for 40% MAPP-MS/PP, 20% MAPP-MS/20%HF/PP, and 20% PDA/MAPP-MS/20%HF/PP rapidly approach 1 at low frequencies (<0.5 rad/s). Notably, the damping curve for 40% HF/3%MAPP/PP remains predominantly below tan δ = 1. These observations suggest that the tan δ of the four composites exhibits reduced frequency dependence, indicating a tendency towards solid-like behaviour.

Figure 6-19C presents Han plots for neat PP and PP composites. These plots provide a straightforward comparison of the elastic and viscous behaviours of the materials. The diagonal line represents G' = G'', with points below this line indicating G'' > G'. As observed in the storage and loss modulus curves, higher moduli are typically obtained at higher frequencies. In contrast to neat PP, which exhibits predominantly viscous behaviour (G'' > G') across the entire frequency range, all composites show dominant elastic character (G' > G'') in the high modulus (or high frequency) region, particularly 40% HF/3%MAPP/PP. The enhanced elastic character of 40% HF/3%MAPP/PP may be attributed to the physical network formed by the addition of 40% harakeke fibres, resulting in a highly elastic behaviour compared to other fillers.

Figure 6-19D illustrates the impact of various filler types and combinations on shear viscosity as a function of angular frequency. Neat PP exhibits constant viscosity at low frequencies, which is followed by typical shear-thinning behaviour as frequency increases. This behaviour demonstrates a clear transition from Newtonian to non-Newtonian characteristics. In contrast, the incorporation of various fillers into PP results in increased shear viscosity for all composites. This increase is primarily due to restricted polymer chain mobility caused by the presence of fillers. Consequently, composites with higher complex viscosity exhibit improved resistance to shear forces and reduced die swell during processing. However, for PP composites containing 40% fillers, it is difficult to define a critical shear rate due to the absence of a Newtonian plateau in their shear viscosity curves. In conclusion, all four composites exhibit predominantly shear-thinning behaviour in the melt state, reinforcing their suitability for processing applications.

6.4 Conclusion

This chapter comprehensively investigated the effects of incorporating harakeke fibres and modified mussel shell fillers- fibre alone and especially in hybrid form with mussel shell- on the structural, thermal, mechanical, morphological, and rheological properties of polypropylene (PP) composites. The findings demonstrated that both fillers, particularly when combined in optimised ratios, substantially enhanced the performance of PP composites across multiple property domains.

The characterisation of harakeke fibres confirmed that alkaline digestion combined with fibrillation significantly improved their suitability as reinforcing agents. The treatment reduced fibre diameter, increased surface roughness, and enhanced thermal stability and crystallinity—thereby improving fibre－matrix interaction and nucleating ability within the PP matrix. These enhancements directly contributed to improved crystallisation behaviour, thermal resistance, and mechanical properties of the resulting composites.

Incorporating hybrid fillers led to a clear synergistic effect. The 1:3 ratio of mussel shell to harakeke fibre consistently yielded the best results in terms of mechanical strength, stiffness, and dimensional stability. This ratio was particularly effective in enhancing the tensile and flexural properties as well as increasing the crystallinity of PP, which was further evidenced by higher β-PP content and improved dynamic mechanical behaviour.

While the addition of rigid fillers reduced the elongation at break, the overall mechanical and thermal properties were significantly improved.

Dynamic mechanical analysis showed that hybrid filler systems increased storage and loss moduli across the full temperature range, with reduced damping peaks indicating enhanced interfacial adhesion and reduced energy dissipation. Creep-recovery testing further demonstrated lower creep strain accumulation and superior long-term shape stability in hybrid composites, especially those with high harakeke content. Rheological tests supported these results, showing enhanced melt stiffness and solid-like behaviour in high-fibre composites.

It is worth noting, however, that the improvement in mechanical properties attributed to enhanced interfacial adhesion from PDA/MAPP co-modification, compared to MAPP modification alone, was not observed in the hybrid filler PP composites. This may be explained by the inherent complexity of the hybrid system, where both filler–matrix and filler–fibre interactions contribute simultaneously to the overall composite behaviour. As a result, the distinct advantages offered by surface modification became less dominant in influencing mechanical outcomes.

This study demonstrates that hybridising biogenic fillers (mussel shell and harakeke fibre) offers a promising and sustainable strategy for developing high-performance thermoplastic composites.Through careful control of filler type, ratio, and surface treatment, it is possible to achieve a favourable balance of stiffness, toughness, thermal resistance, and long-term dimensional stability while contributing to the valorisation of biowaste and advancing circular material solutions.

6.5 References

1. Szeluga, U., Kumanek, B., & Trzebicka, B. (2015). Synergy in hybrid polymer/nanocarbon composites. A review. *Composites Part A: Applied Science and Manufacturing*, *73*, 204-231.
2. Xu, H., Li, Y., Han, X., *et al.* (2021). Carbon black enhanced wood-plastic composites for high-performance electromagnetic interference shielding. *Materials Letters*, *285*, 129077.
3. Hemath, M., Mavinkere Rangappa, S., Kushvaha, V., *et al.* (2020). A comprehensive review on mechanical, electromagnetic radiation shielding, and thermal conductivity of fibers/inorganic fillers reinforced hybrid polymer composites. *Polymer Composites*, *41*(10), 3940-3965.

4. Oladele, I. O., Ibrahim, I. O., Akinwekomi, A. D., *et al.* (2019). Effect of mercerization on the mechanical and thermal response of hybrid bagasse fiber/CaCO3 reinforced polypropylene composites. *Polymer Testing*, *76*, 192-198.
5. Gwon, J. G., Lee, S. Y., Chun, S. J., *et al.* (2011). Physical and mechanical properties of wood–plastic composites hybridized with inorganic fillers. *Journal of Composite Materials*, *46*(3), 301-309.
6. Xanthos, M. E. (2010). Functional fillers for plastics. (M. Xanthos, Ed. Second ed.). WILEY-VCH Verlag GmbH & Co. KGaA, Weinheim.
7. Lowe, B. J., Carr, D. J., McCallum, R. E., *et al.* (2010). Understanding the variability of vegetable fibres: a case study of harakeke (Phormium tenax). *Textile Research Journal*, *80*(20), 2158-2166.
8. Le, T. M., & Pickering, K. L. (2015). The potential of harakeke fibre as reinforcement in polymer matrix composites including modelling of long harakeke fibre composite strength. *Composites. Part A, Applied science and manufacturing*, *76*, 44-53.
9. Yang, S.-Y., Lin, W.-N., Huang, Y.-L., *et al.* (2011). Synergetic effects of graphene platelets and carbon nanotubes on the mechanical and thermal properties of epoxy composites. *Carbon*, *49*(3), 793-803.
10. Suresh, A., Bhargavi, P., & Kiran Kumar, M. (2021). Simulation and mechanical characterization on kevlar epoxy reinforced composite with silicon carbide filler. *Materials Today: Proceedings*, *38*, 2988-2995.
11. Duchemin, B., & Staiger, M. P. (2009). Treatment of Harakeke fiber for biocomposites. *Journal of Applied Polymer Science*, *112*(5), 2710-2715.
12. Beg, M. D. H., Pickering, K. L., & Gauss, C. (2023). The effects of alkaline digestion, bleaching and ultrasonication treatment of fibre on 3D printed harakeke fibre reinforced polylactic acid composites. *Composites Part A: Applied Science and Manufacturing*, *166*, 107384.
13. Dayo, A. Q., Zegaoui, A., Nizamani, A. A., *et al.* (2018). The influence of different chemical treatments on the hemp fiber/polybenzoxazine based green composites: Mechanical, thermal and water absorption properties. *Materials Chemistry and Physics*, *217*, 270-277.
14. Pickering, K. L., Beckermann, G. W., Alam, S. N., *et al.* (2007). Optimising industrial hemp fibre for composites. *Composites. Part A, Applied science and manufacturing*, *38*(2), 461-468.
15. Díez, D., Urueña, A., Piñero, R., *et al.* (2020). Determination of Hemicellulose, Cellulose, and Lignin Content in Different Types of Biomasses by Thermogravimetric Analysis and Pseudocomponent Kinetic Model (TGA-PKM Method). *Processes*, *8*(9), 1048.
16. Akindoyo, J. O., Pickering, K., Beg, M. D., *et al.* (2023). Combined digestion and bleaching of New Zealand flax /harakeke fibre and its effects on the mechanical, thermal, and dynamic mechanical properties of poly(lactic) acid matrix composites. *Composites. Part A, Applied science and manufacturing*, *164*, 107326.
17. Oliveira, M. A., Pickering, K. L., Sunny, T., *et al.* (2021). Treatment of hemp fibres for use in rotational moulding. *Journal of Polymer Research*, *28*(2), 1-9.
18. Davachi, S. M., Heidari, B. S., Sahraeian, R., *et al.* (2019). The effect of nanoperlite and its silane treatment on the crystallinity, rheological, optical, and surface properties of polypropylene/nanoperlite nanocomposite films. *Composites Part B: Engineering*, *175*, 107088.
19. Bhuiyan, M. K. H., Rahman, M. M., Mina, M. F., *et al.* (2013). Crystalline morphology and properties of multi-walled carbon nanotube filled isotactic

polypropylene nanocomposites: Influence of filler size and loading. *Composites. Part A, Applied science and manufacturing*, *52*, 70-79.

20. Mi, Y., Chen, X., & Guo, Q. (1997). Bamboo fiber-reinforced polypropylene composites: Crystallization and interfacial morphology. *Journal of Applied Polymer Science*, *64*(7), 1267-1273.
21. Zheng, W., Lu, X., Ling Toh, C., *et al.* (2004). Effects of clay on polymorphism of polypropylene in polypropylene/clay nanocomposites. *Journal of polymer science. Part B, Polymer physics*, *42*(10), 1810-1816.
22. Jones, A. T., Aizlewood, J. M., & Beckett, D. R. (1964). Crystalline forms of isotactic polypropylene. *Die Makromolekulare Chemie*, *75*(1), 134-158.
23. Gohn, A. M., Rhoades, A. M., Okonski, D., *et al.* (2018). Effect of Melt-Memory on the Crystal Polymorphism in Molded Isotactic Polypropylene. *Macromolecular materials and engineering*, *303*(8), n/a.
24. Yuan, Q., Jiang, W., & An, L. (2004). Study of β–α recrystallization of the polypropylene. *Colloid and Polymer Science*, *282*, 1236-1241.
25. Labour, T., Gauthier, C., Séguéla, R., *et al.* (2001). Influence of the β crystalline phase on the mechanical properties of unfilled and CaCO3-filled polypropylene. I. Structural and mechanical characterisation. *Polymer*, *42*(16), 7127-7135.
26. Oksman, K., Mathew, A. P., Långström, R., *et al.* (2009). The influence of fibre microstructure on fibre breakage and mechanical properties of natural fibre reinforced polypropylene. *Composites Science and Technology*, *69*(11), 1847-1853.
27. Aruan Efendy, M. G., & Pickering, K. L. (2014). Comparison of harakeke with hemp fibre as a potential reinforcement in composites. *Composites. Part A, Applied science and manufacturing*, *67*, 259-267.
28. Fu, S.-Y., Xu, G., & Mai, Y.-W. (2002). On the elastic modulus of hybrid particle/short-fiber/polymer composites. *Composites. Part B, Engineering*, *33*(4), 291-299.
29. Taib, M. N. A. M., & Julkapli, N. M. (2019). Dimensional stability of natural fiber-based and hybrid composites. In *Mechanical and Physical Testing of Biocomposites, Fibre-Reinforced Composites and Hybrid Composites* (pp. 61-79). Elsevier.
30. Awais, H., Nawab, Y., Amjad, A., *et al.* (2020). Environmental benign natural fibre reinforced thermoplastic composites: A review. *Composites Part C: Open Access*, 100082.
31. Kutchko, B. G., & Kim, A. G. (2006). Fly ash characterization by SEM–EDS. *Fuel*, *85*(17), 2537-2544.
32. Etaati, A., Pather, S., Fang, Z., *et al.* (2014). The study of fibre/matrix bond strength in short hemp polypropylene composites from dynamic mechanical analysis. *Composites. Part B, Engineering*, *62*, 19-28.
33. Senturk, O., Senturk, A. E., & Palabiyik, M. (2018). Evaluation of hybrid effect on the thermomechanical and mechanical properties of calcite/SGF/PP hybrid composites. *Composites. Part B, Engineering*, *140*, 68-77.
34. Menard, K. P., & Menard, N. R. (2020). Dynamic mechanical analysis. CRC press.
35. Izwan, S. M., Sapuan, S. M., Zuhri, M. Y. M., *et al.* (2021). Thermal stability and dynamic mechanical analysis of benzoylation treated sugar palm/kenaf fiber reinforced polypropylene hybrid composites. *Polymers*, *13*(17), 2961.
36. Starkova, O., Aniskevich, K., Sevcenko, J., *et al.* (2021). Relationship between the residual and total strain from creep-recovery tests of polypropylene/multiwall carbon nanotube composites. *Journal of Applied Polymer Science*, *138*(10), n/a.

37. Feng, M., Pan, Y., Zhang, M.*, et al.* (2021). Largely improved thermal conductivity of HDPE composites by building a 3D hybrid fillers network. *Composites Science and Technology*, *206*, 108666.
38. Zhang, C., Liu, X., Liu, H.*, et al.* (2019). Multi-walled carbon nanotube in a miscible PEO/PMMA blend: Thermal and rheological behavior. *Polymer Testing*, *75*, 367-372.

Chapter 7

Effect of mussel shell fillers on the weathering resistance of polypropylene composites

7.1 Introduction

Previous chapters have explored the influence of various mussel shell fillers on the thermal and mechanical properties of polypropylene (PP) composites. This chapter extends that investigation by evaluating their potential to improve the long-term durability of PP under ultraviolet (UV) exposure.

Polyolefins, including PP, are major contributors to microplastic pollution [1; 2]. PP is particularly vulnerable to UV-induced oxidative degradation, which results in chain scission, embrittlement, and eventual fragmentation into microplastics [3]. This susceptibility limits the use of PP in outdoor applications and contributes significantly to environmental plastic waste.

To mitigate these effects, commercial polymer formulations commonly incorporate UV stabilisers to preserve mechanical, thermal, and aesthetic properties over prolonged exposure periods [4]. Conventional UV stabilisers fall into three categories: UV absorbers, which convert UV energy into harmless heat; quenchers, which deactivate excited chromophores via electron transfer [5]; and radical scavengers, notably hindered amine light stabilisers (HALS). HALS are highly effective in polyolefins, inhibiting photo-degradation by scavenging radicals rather than absorbing UV directly [6].

Although synthetic stabilisers are effective, recent research has increasingly explored natural alternatives due to their low toxicity and multifunctional properties. Melanins, for example, are biomacromolecular pigments with broadband absorption, radical scavenging, and metal-chelating capabilities that collectively inhibit oxidative chain scission [7; 8]. These features make melanin a promising stabiliser, as demonstrated by Phua *et al.* [8], who reported that incorporating 0.5 wt.% melanin nanoparticles reduced thermal degradation in both PP and polymethyl methacrylate (PMMA).

Polydopamine (PDA), a synthetic analogue of melanin, exhibits comparable UV-protective mechanisms [7]. Accordingly, this study explores its potential synergistic effect with mussel shell fillers on the weathering resistance of polypropylene.

Although mussel shell fillers have been shown to enhance the thermal and mechanical performance of PP in previous chapters, their combined effect with PDA in improving UV stability has not been comprehensively investigated. To address this, the current work examines the performance of maleic anhydride-grafted polypropylene (MAPP)-modified mussel shell fillers and PDA/MAPP co-modified counterparts, each incorporated at a concentration of 5 wt.%. Neat PP was also studied as a reference for comparative analysis. Accelerated weathering tests were carried out under laboratory conditions using a combination of UV radiation, elevated temperatures, moisture condensation, and water spray to simulate natural ageing. These intensified conditions enabled a rapid assessment of material durability and supported predictions of long-term performance within a shortened experimental period.

Changes in surface morphology, chemical structure, crystallinity, and mechanical properties were evaluated for neat PP, 5% MAPP-MS/PP, and 5% PDA/MAPP-MS/PP composites, both before and after ageing. Finally, a photooxidative degradation mechanism is proposed to account for the observed behaviours.

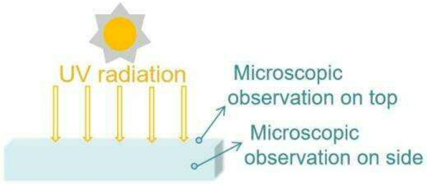

Figure 7- 1: Schematic illustration of beam Specimen observation using optical microscopy.

7.2 Effect of accelerated weathering on the surface morphology of materials

Ultraviolet (UV) exposure induces chain scission and cross-linking in polypropylene (PP), resulting in structural degradation at the surface. This process manifests as noticeable morphological changes, including crack formation, discolouration, and fragmentation.

To investigate these effects, surface morphology was comparatively examined at two specific locations on the specimens using an Olympus BX53 optical microscope: the top surface, which was directly exposed to UV radiation, and the side surface. This dual-perspective analysis allowed for detailed observation of UV-induced crack initiation and propagation patterns.

For clarity, a schematic illustrating the examined positions and the corresponding degradation features is presented in Figure 7-1.

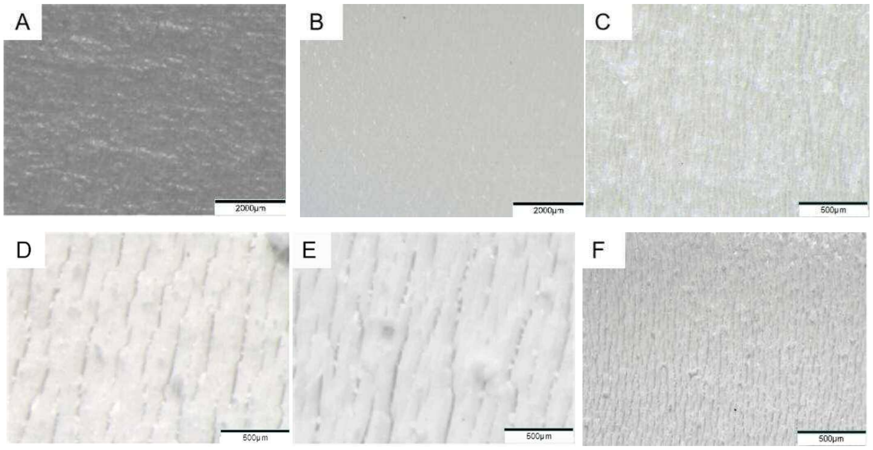

Figure 7- 3:Optical microscopic images of neat PP (top observation) after (A) 0h, (B) 120h, (C)240h, (D) 480h, (E) 740h, (F)1000h UV exposure.

7.2.1 Surface morphological changes of PP

Optical microscopy images of polypropylene (PP) beam specimens before and after UV exposure are **shown** in Figure 7-2 (top view) and Figure 7-3 (side view). Progressive surface degradation is evident. The unaged specimen (Figure 7-2A) displays a smooth, glossy surface. After 120 hours of UV exposure (Figure 7-2B), the surface appears roughened and loses its gloss. By 240 hours (Figure 7-2C), small parallel cracks begin to emerge. With further exposure—up to 480 hours and beyond (Figure 7-2D–F)—the cracks become denser and deeper, accompanied by visible fragmentation and powdery

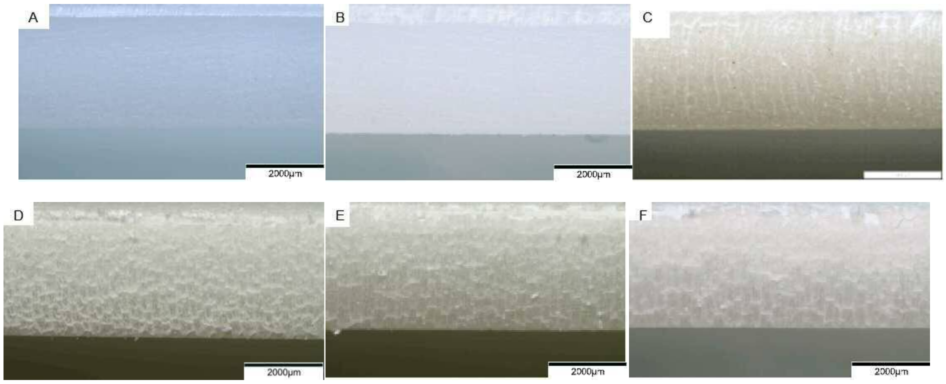

Figure 7- 5: Optical microscopic images of neat PP (side observation) after (A) 0h, (B) 120h, (C) 240 h, (D) 480h, (E) 740h, (F) 1000h UV exposure.

$$\text{Step 1}: \text{Polypropylene (P - H)} + h\nu \rightarrow P\cdot$$

$$\text{Step 2}: P\cdot + O_2 \rightarrow PO_2\cdot$$

$$\text{Step 3}: PO_2\cdot + PH \rightarrow POOH + P\cdot$$

$$\text{Step 4}: POOH + h\nu \rightarrow PO\cdot + \cdot OH$$

$$\text{Step 5}: PO\cdot + h\nu \rightarrow PO_{\text{carbonyls}}$$

$$\text{Step 6}: \begin{pmatrix} P\cdot + P\cdot \\ P\cdot + PO_2\cdot \\ PO_2\cdot + PO_2\cdot \end{pmatrix} \rightarrow \text{Termination}$$

Figure 7- 7: Scheme of photo-oxidative degradation of polypropylene **[10; 43]**.

material accumulating between the cracks. Simultaneously, a yellowish discolouration develops on the surface.

The side-view images (Figure 7-3A–F) reveal a depth-wise progression of crack formation. Cracks initiate at the UV-exposed surface and propagate progressively towards the base of the specimen, in agreement with previous studies [9; 10]. Both crack density and thickness increase with exposure duration: after 240 hours (Figure 7-3C), hairline cracks emerge near the surface; by 480 hours (Figure 7-3D), these cracks branch and interconnect. After prolonged exposure of 740 to 1000 hours (Figure 7-3E–F), extensive crack networks reach the bottom of the specimens.

These morphological changes are attributed to polypropylene (PP)'s photo-oxidative degradation mechanism. As shown in Figure 7-4, UV irradiation induces the formation of multiple free radicals in PP (Steps 1, 4, and 5). Oxygen plays a critical role in generating peroxy (POO•) radicals during Step 2 [10], which drive the propagation phase

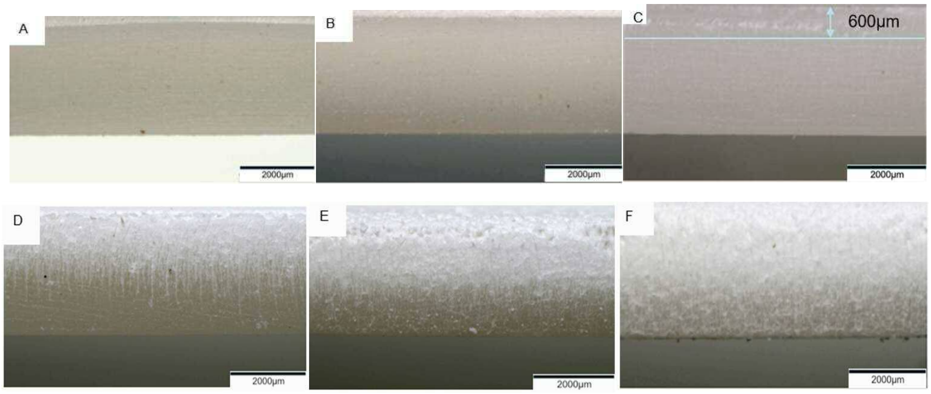

Figure 7- 9: Optical microscopic images of 5%MAPP-MS/PP (side) after (A) 0 h, (B) 120 h, (C) 240 h, (D) 480 h, (E) 740 h, (F) 1000 h UV exposure.

of degradation. Consequently, photo-oxidative degradation primarily initiates at the surface, where oxygen concentration is highest.

Once initiated, the degradation process can proceed via thermo-oxidative reactions even in the absence of further UV exposure; however, the rate diminishes as oxygen is depleted [11]. Free radical reactions result in both chain scission and cross-linking within the polymer, which in turn lead to macroscopic property changes such as embrittlement, surface cracking, and discolouration. Crack formation facilitates further oxygen penetration, accelerating the degradation process and promoting the inward propagation of cracks. As a result, a depth-wise degradation profile becomes evident within the material.

The non-uniform parallel crack patterns observed in the top-view images arise from the heterogeneous structure of PP, which comprises both crystalline and amorphous regions, as well as processing-induced anisotropy. Previous studies have reported that compression-moulded PP specimens typically exhibit random surface crack patterns upon ageing. In contrast, injection-moulded PP specimens- such as those examined in this study—develop cracks oriented perpendicular to the melt flow direction [12; 13], This difference is attributed to molecular chain alignment introduced during the injection moulding process [14].

7.2.2 Surface morphological changes of 5%MAPP-MS/PP composite

As established in Chapter 5, modification of mussel shell fillers with maleic anhydride-grafted polypropylene (MAPP) improved filler–matrix compatibility at a 5% loading. Xuting *et al.,* demonstrated that MAPP-modified polypropylene wax (PM)exhibited superior short-term UV protection compared to unmodified PP wax (PPW), due to reduced photo-oxidative degradation resulting from cross-linked structures [15]. This section examines the influence of 5% MAPP-MS on UV resistance in as-prepared PP composites (5%MAPP-MS/PP), with direct evidence from surface morphological analysis.

Figure 7-5 presents optical microscopy images before and after accelerated weathering. Only side views are shown, as they better illustrate crack development compared to unfilled PP under identical aging conditions.

Figure 7-5 demonstrates that while neat polypropylene (PP) developed cracks after 240 hours of aging, 5%MAPP-MS/PP composites showed no visible cracking until 480 hours. However, the composite's top layer exhibited progressive lightening and thickening between 120 and 240 hours (approximately 600 μm) under reflected microscopy (Figure 7-5B–C), suggesting surface fragmentation and discolouration without structural failure. By 480 h, dense surface cracks and propagating hairline cracks emerge and cover approximately 3/4 of beam height (Figure 7-5D), intensifying by 740 h (Figure 7-5E) and culminating in transverse network coverage after 1000 h (Figure 7-5F).

This delayed photo-oxidative degradation progression can be attributed to the physical shielding effects of mussel shell fillers in PP matrix. These filler particles, with interfacial adhesion improved by MAPP modification, inhibit the degradation of polypropylene by restricting oxygen diffusion and blocking ultraviolet (UV) penetration. Both factors are critical in the photo-oxidative degradation of the polypropylene matrix. Furthermore, incorporating 5%MAPP-MS shifts PP's crystalline structure from dominant α-phase to mixed α/β-phase with minor β-crystal enhancement (Chapter 5). According to Obadal *et al.*, such β-phase formation is associated with finer crack networks due to smaller spherulite sizes [16], which is consistent with the observed morphological differences between neat PP and the 5% MAPP-MS/PP composite under weathering.

Collectively, these morphological findings indicate that the incorporation of 5% MAPP-MS effectively enhances the weathering resistance of polypropylene.

7.2.3 Surface morphological changes of 5%PDA/MAPP-MS/PP composite

Chapter 5 established that introducing polydopamine (PDA) and maleic anhydride-grafted polypropylene (MAPP) co-modified mussel shell (MS) fillers into polypropylene (PP) composites enhances mechanical properties. This improvement stems from a strengthened filler-matrix interface, which enhances stress transfer efficiency and reduces interfacial void formation. The PDA/MAPP co-modified mussel shell fillers also shift PP crystalline structure to a mixed α/β-phase. Building on these findings, this section presents the influence of PDA/MAPP-MS fillers on PP's weathering resistance through surface morphological changes, particularly under combined UV radiation and oxidative conditions. The polydopamine coating imparts a black colour to the filled PP, allowing for easy visual distinction between the degraded (whitened) layer and intact beam sections.

Figure 7-6 presents the side-view optical microscopy images of PP composite containing 5% PDA/MAPP-MS before and after accelerated weathering. Compared with the 5% MAPP-MS/PP composite (Figure 7-5), the incorporation of PDA/MAPP co-modified mussel shell fillers confers superior weathering resistance.

As with the 5% MAPP-MS/PP composite, no visible surface cracks were observed in the 5% PDA/MAPP-MS/PP composite after 240 hours of ageing, as shown in the reflected light images. However, the degraded surface layer measured only 280 μm in thickness—approximately half of the 600 μm observed in the MAPP-only system under identical conditions. After 480 hours, cracks began to appear, although they were confined to the upper 20% of the specimen. By 740 hours, over half the beam thickness remained intact, as indicated by the persistence of the black surface colour and the absence of further cracking. Even after 1000 hours, the lower half of the specimen retained its original appearance, despite dense surface cracking in the uppermost layer.

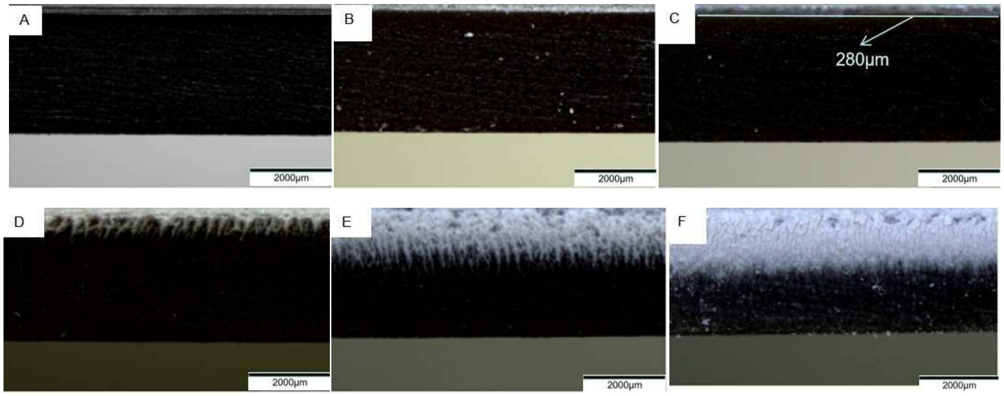

Figure 7- 11: Optical microscopic images of 5%PDA/MAPP-MS/PP (side) after (A) 0h, (B) 120h, (C) 240h, (D) 480h, (E) 740h, (F) 1000h UV exposure.

The enhanced weathering resistance of the 5% PDA/MAPP-MS/PP composite is the result of synergistic effects between the MAPP modified mussel shell fillers and polydopamine. In addition to the physical shielding provided by mussel shell fillers—which restrict oxygen diffusion and UV penetration—the PDA/MAPP co-modification also provides better filler-matrix bonding and promotes β-phase formation in the PP matrix. More significantly, the marked improvement in weathering resistance compared with the 5% MAPP-MS/PP composite is attributed to the free-radical scavenging capability of polydopamine. Previous studies have identified three primary mechanisms by which PDA mitigates degradation: (1) dissipation of radiation energy to prevent free-radical formation; (2) quenching of reactive species through electron transfer [5], and (3) activating endogenous defence systems in vivo [17]. This combination of physical shielding action, crystalline phase modification, and chemical protection effectively mitigates degradation under accelerated weathering conditions.

Surface morphological changes provide direct visual evidence that weathering resistance follows the order: 5% PDA/MAPP-MS/PP > 5% MAPP-MS/PP > neat PP. The degree of deterioration in PP and its composites increases with weathering time and depends on specimen depth. To elucidate how weathering influences the microstructure and macroscopic properties of these polymer materials, as well as the effects of 5% mussel shell fillers modified by different treatments, the following sections examine the crystalline structure, mechanical properties, and chemical composition of these polymers before and after various weathering durations.

As the photodegradation of PP and its composites occurs in a depth-dependent manner, it is important to consider the sampling depth of each characterisation technique.

XRD characterisation employed Cu-Kα radiation (energy ≈ 8.04 keV). Given the density and X-ray absorption characteristics of the PP matrix, the radiation penetrates approximately 2 mm, making XRD results representative of the crystalline composition in the material's outer layer. This is consistent with prior studies on polymeric systems [18].

For differential scanning calorimetry (DSC) and Fourier transform infrared spectroscopy (FTIR), a 0.5 mm surface layer was collected from each sample for analysis. This approach ensures that thermal and chemical changes induced by UV exposure are specifically assessed within the most affected surface region.

In contrast, mechanical characterisation—including tensile testing, three-point bending, and dynamic mechanical analysis—was performed on the entire specimen. Therefore, the measured mechanical properties reflect the integrated effect of heterogeneous degradation throughout the full sample thickness.

7.3 Effect of accelerated weathering on the chemical composites of materials - FTIR analysis

In this study, polypropylene (PP) and its two composites undergo weathering treatments combining UV radiation, heat, and moisture. These conditions, especially UV radiation, are extensively documented to induce alterations in chemical composition during photo-degradation [19-22]. The formation, modification, or removal of functional groups can substantially alter the chemical and physical properties of the resulting material.

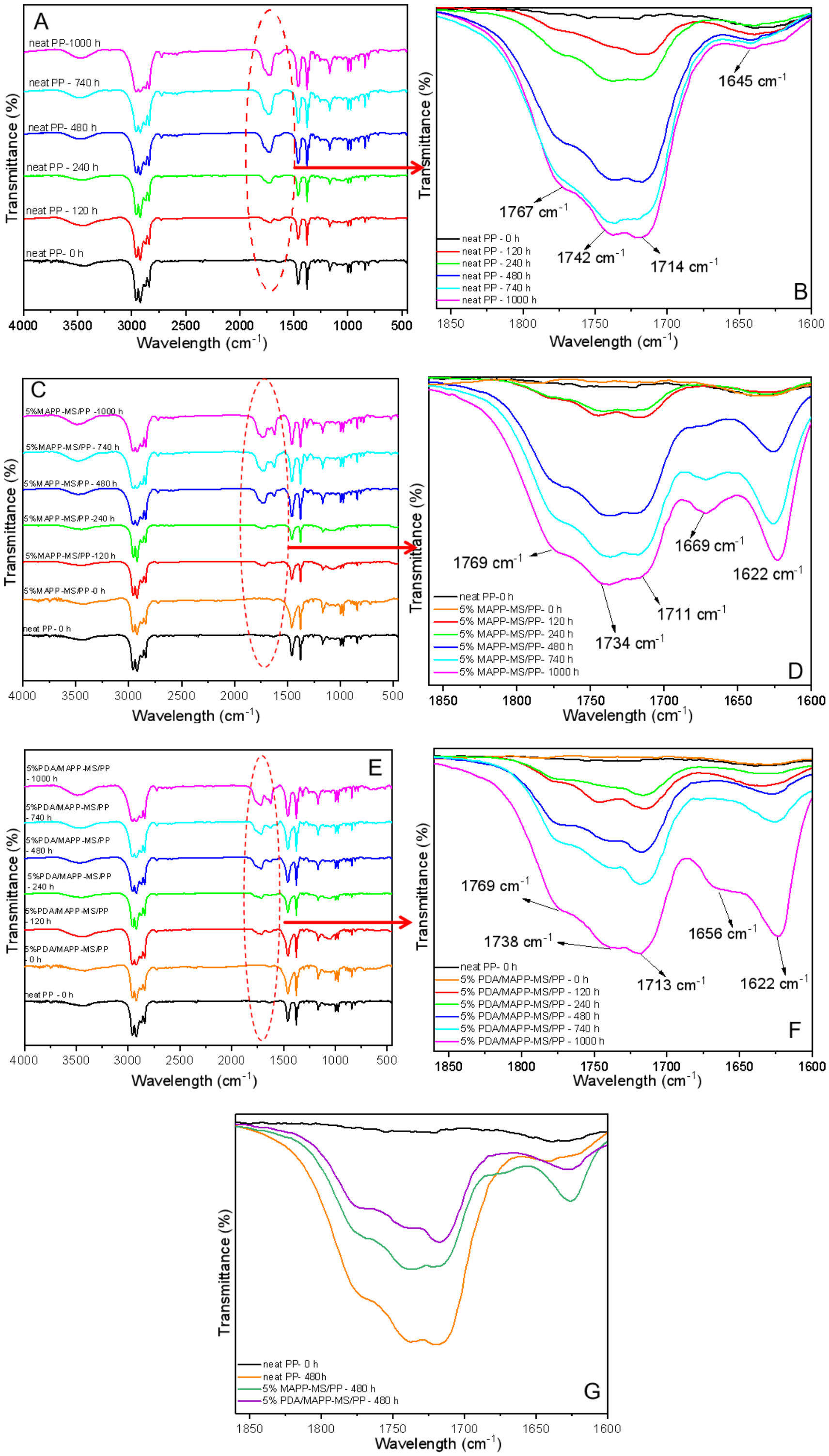

Figure 7- 13: FTIR spectra of neat PP, 5 wt% MAPP-MS/PP, and 5 wt% PDA/MAPP-MS/PP before and after weathering: full range (450 – 4000 cm^{-1}; A, C, E) and carbonyl region (1600 – 1875 cm^{-1}; B, D, F). And (G) the comparison of three polymers after 480 h weathering at carbonyl region.

Infrared (IR) spectroscopy is a widely accepted technique for studying polymer ageing.

Both transmission and attenuated total reflectance (ATR) modes are commonly used to detect chemical changes and assess the ageing status of polymers. In particular, Fourier Transform Infrared (FTIR) spectroscopy enables the monitoring of functional groups associated with the photo-oxidative degradation of polypropylene, such as carbonyl, vinyl, hydroxyl, and carboxylate groups [19; 23].

Figure 7-7 presents the FTIR spectra of neat polypropylene (PP), 5% MAPP-MS/PP, and 5% PDA/MAPP-MS/PP before and after varying weathering durations. For consistent comparison, all spectra were normalised to the highest peak at approximately 2920 cm^{-1}.

In the full-range spectra (450-4000 cm^{-1}, Figures 7-7A, 7-7C, and 7-7E), a broad absorption band appears in the region of 1600–1800 cm^{-1} following weathering, and its intensity increases with prolonged exposure. Carbonyl groups form through the oxidation of methyl groups, producing hydroperoxides that decompose to generate hydroxyl radicals. These radicals accelerate further carbonyl formation. The presence of carbonyl groups is a key indicator of PP degradation via polymer chain scission. These groups may further convert into vinyl or carboxylate structures. The broad band comprises at least three major components: carboxylic acid dimers and/or ketones (~1715 cm^{-1}), esters (~1740 cm^{-1}), and γ-lactones (~1770 cm^{-1}). Additionally, bands in the 1600–1660 cm^{-1} range confirm the formation of vinyl groups [24; 25].

For neat PP (Figure 7-7B), magnified spectra between 1600–1875 cm^{-1} reveal that carboxylic acids (peak centred at 1714 cm^{-1}) are the dominant degradation products throughout the 120–1000 h weathering period. Ester and γ-lactone peaks at 1740 cm^{-1} and 1770 cm^{-1}, respectively, become more evident after 240 hours. Similar patterns were observed for 5% MAPP-MS/PP (Figure 7-7D) and 5% PDA/MAPP-MS/PP (Figure 7-7F). However, these composites also exhibited a more pronounced shoulder in the 1622–1660 cm^{-1} range, indicating enhanced formation of vinyl groups during photo-degradation.

To compare carbonyl formation across materials, the FTIR spectra at 480 hours were selected as a midpoint of the 1000-hour exposure (Figure 7-7G). The band intensity in the 1600–1875 cm^{-1} region followed the order: neat PP >> 5% MAPP-MS/PP > 5% PDA/MAPP-MS/PP, confirming delayed degradation in the composites, especially in the presence of PDA.

A deconvolution procedure was applied to the FTIR spectra after 1000 hours of weathering to identify specific functional groups in the carbonyl and vinyl region (1600–

1875 cm⁻¹). As shown by the dashed lines in Figure 7-8 A to C, four major peaks were identified across all samples: γ-lactone (~1770 cm⁻¹), ester (~1740 cm⁻¹), carboxylic acid and ketone overlap (~1720 cm⁻¹), and vinyl groups (1600–1660 cm⁻¹) [26].

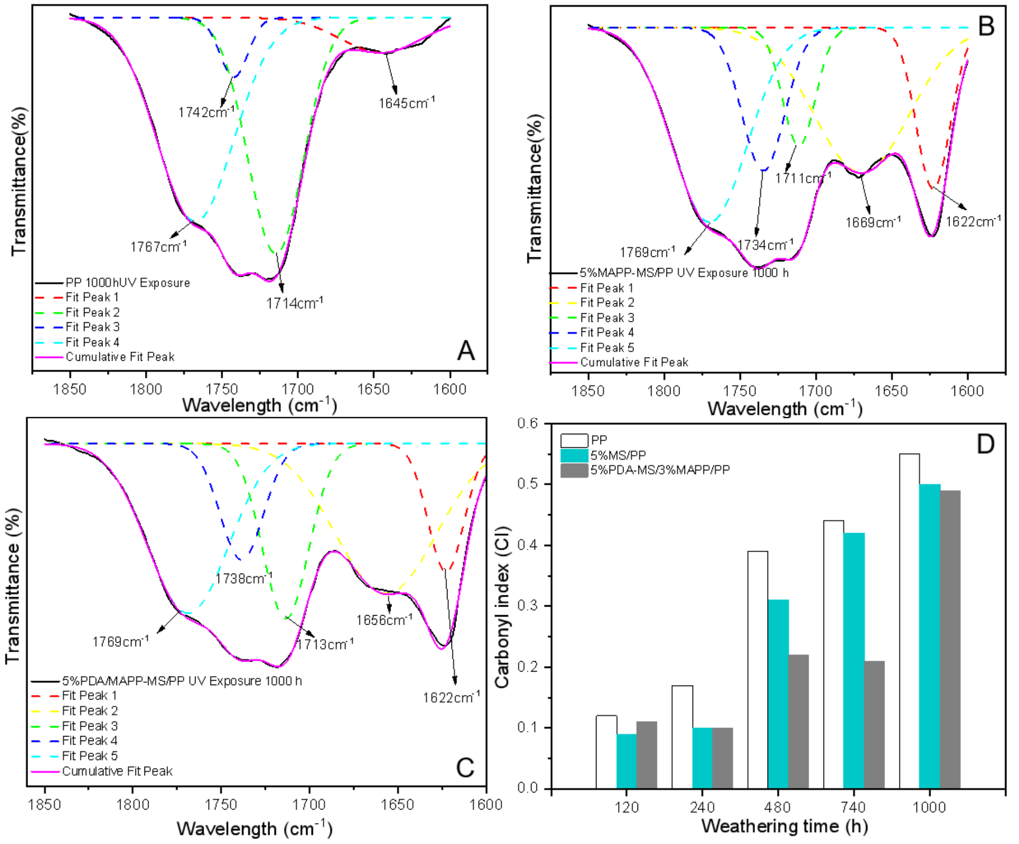

Figure 7- 15: Deconvolution of FTIR spectra of (A) neat PP, (B) 5% MAPP-MS/PP, (C) 5% PDA/MAPP-MS/PP after 1000h weathering treatment. (D) Carbonyl indices of three polymers after different weathering durations.

In neat PP, deconvolution revealed that the primary oxidation products after 1000 hours were carboxylic acids, ketones, and γ-lactones. A low-intensity shoulder around 1645 cm⁻¹ suggested only a small quantity of vinyl groups. In contrast, the composites containing 5% MAPP-MS or PDA/MAPP-MS exhibited similar oxidation products but with comparable intensities between vinyl and carbonyl bands. This indicates a greater extent of vinyl formation in the filled composites, confirming findings from previous studies [27].

To further assess the degradation rate and progression, a semi-quantitative evaluation using the carbonyl index (CI) was performed. CI analysis is a widely accepted method for estimating polymer ageing [19; 20; 25; 28].It involves calculating the ratio between the intensity or area of the carbonyl peak—which increases during degradation—and that of a reference peak, typically a stable C–H stretching band from methyl or methylene groups [23].

Due to the range of oxidation products formed and their variation across materials, the area method was selected. This method integrates the entire carbonyl and vinyl region (1575–1875 cm^{-1}) and compares it to the area of a reference region (2750–3050 cm^{-1}). The results are presented in Figure 7-8D.

The CI evolution offers insight into both the rate and extent of photo-degradation. For neat PP, CI values increased steadily from 0.12 at 120 hours to 0.17 at 240 hours, followed by a sharp rise to 0.39 at 480 hours. The values continued to climb, reaching 0.44 at 740 hours and 0.55 at 1000 hours. This trend indicates progressive and accelerating degradation over time.

In the 5% MAPP-MS/PP composite, the CI remained constant at 0.10 between 120 and 240 hours, suggesting little early-stage degradation. However, a marked increase was observed thereafter: 0.30 at 480 hours, 0.42 at 740 hours, and 0.50 at 1000 hours. These results show that MAPP-modified mussel shell fillers delay degradation onset but do not completely suppress long-term degradation.

In contrast, the 5% PDA/MAPP-MS/PP composite showed the slowest increase in CI. The value rose slightly from 0.09 to 0.10 between 120 and 240 hours and remained relatively low at 0.22 and 0.21 at 480 and 740 hours, respectively. A significant increase to 0.49 occurred only after 1000 hours. These results suggest that PDA co-modification further delays both the onset and progression of photo-oxidative degradation.

In summary, the development of CI values confirms that neat PP is most susceptible to photo-degradation, followed by the 5% MAPP-MS/PP composite, while the 5% PDA/MAPP-MS/PP composite demonstrates the greatest resistance. These findings highlight the beneficial effects of mussel shell fillers- particularly when co-modified with PDA- in enhancing the photostability of polypropylene under accelerated weathering.

7.4 Effect of accelerated weathering on the crystal structure of materials - XRD analysis

Weathering can alter the ordering characteristics of polymers, particularly crystalline composition and crystallinity, which can be evaluated using X-ray diffraction (XRD) patterns. To facilitate comparison, XRD curves were normalised to the intensity of the strongest α (040) peak. Figure 7-7 presents the XRD patterns of neat PP, 5% MAPP-MS/PP, and 5% PDA/MAPP-MS/PP after varying weathering durations.

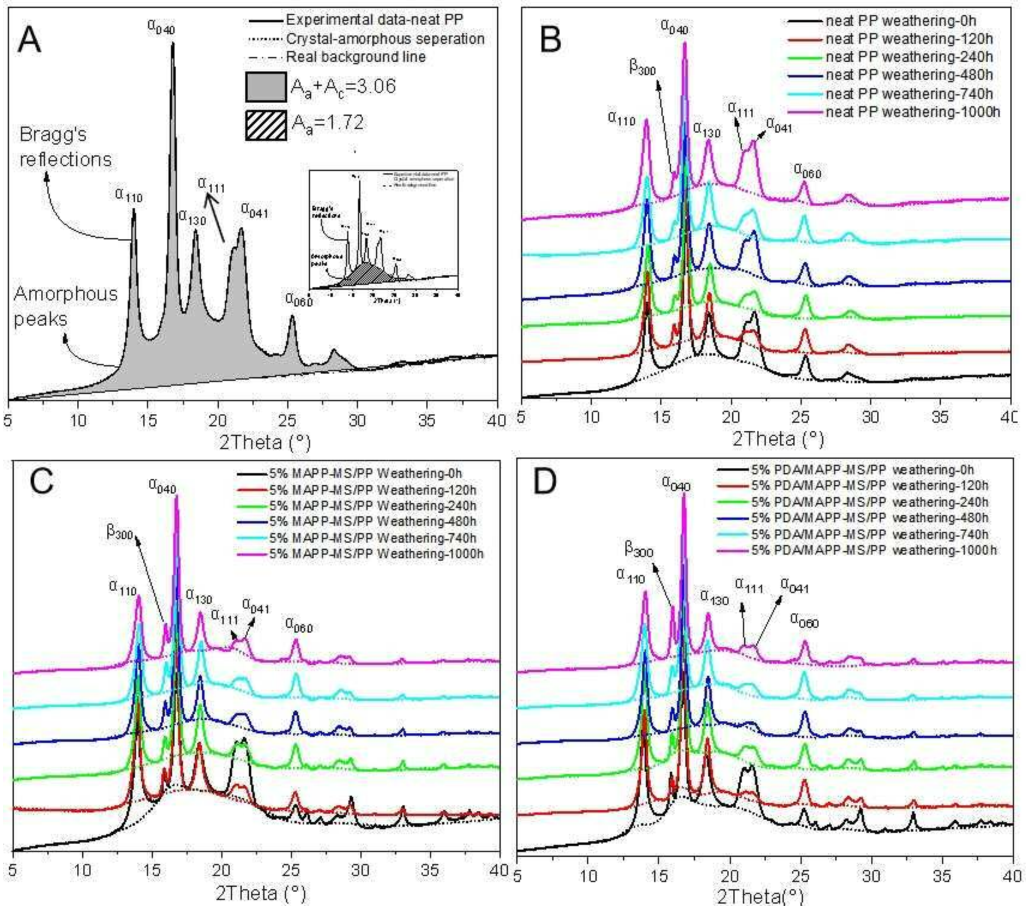

Figure 7- 17: (A) Standard XRD pattern of neat PP with different phase illustration; XRD patterns of (B) neat PP, (C) 5% MAPP-MS/PP, and (D) 5% PDA/MAPP-MS/PP after different weathering durations.

Polypropylene is a semi-crystalline polymer consisting of crystalline and amorphous phases, which can be distinguished using XRD analysis. As shown in Figure 7-9A, the XRD curve of unaged PP clearly differentiates crystalline peaks from the amorphous halo and real background line. The sum of Bragg reflection areas represents the crystalline phase portion (Ac), while the area between the amorphous halo and baseline corresponds to the amorphous phase portion (A_a). The relative crystallinity (χ_c) is calculated using Equation 7-1, as defined by Hermans and Weidinger [29] .

$$\chi_c=A_c/(A_c+A_a) \qquad \text{Eq. 7-1}$$

The amorphous area (A_a) and total area (A_c+A_a) were integrated using OriginPro 2019

Table 7- 1: Peak intensity and crystallinity of samples before and after weathering (XRD results).

		α					β	χ_c
Crystal plane		110	**040**	130	111	041	300	%
PP	0h	46.6	**100**	29.7	28.3	43.7	0.0	43.8
	120h	47.9	**100**	27.9	6.0	8.0	11.3	50.0
	240h	43.6	**100**	24.0	11.0	11.5	7.2	50.3
	480h	56.2	**100**	29.1	18.6	28.2	12.0	50.6
	740h	43.4	**100**	28.8	11.9	12.5	13.0	50.3
	1000h	52.9	**100**	30.8	27.8	36.7	14.7	50.5
5% MAPP-MS/PP	0h	79.2	**100**	38.0	40.8	50.0	19.8	38.2
	120h	64.6	**100**	31.1	10.6	11.7	17.3	48.4
	240h	55.1	**100**	31.8	11.8	12.6	14.4	48.7
	480h	52.5	**100**	29.5	9.5	10.8	16.7	51.4
	740h	44.2	**100**	28.4	6.4	10.0	16.8	50.5
	1000h	39.6	**100**	24.4	9.0	12.9	19.4	49.3
5% PDA/MAPP-MS/PP	0h	71.6	**100**	35.6	27.5	33.7	24.7	41.5
	120h	56.7	**100**	34.8	4.4	5.5	12.9	49.5
	240h	59.6	**100**	33.8	9.5	11.4	16.3	51.9
	480h	48.3	**100**	30.3	3.6	5.2	13.1	54.7
	740h	44.5	**100**	29.0	4.4	6.3	16.5	56.4
	1000h	41.7	**100**	23.5	5.9	9.2	30.0	57.8

software. For instance, as illustrated in Figure 7-7A, neat PP before weathering exhibits A_a=1.72 and a total area (A_c+A_a) of 3.06, yielding a relative crystallinity (χ_c) of:

$$\chi_c= 100\%\times (3.06-1.72)/3.06= 43.8\%$$

Relative peak intensities, normalised to the α (040) reflection (Peak intensity $I_{\alpha\,(040)}$=100%), were analysed using HighScore Plus. The resulting data are summarised in Table 7-1.

As previously discussed in Section 7.2, the photodegradation of PP and its composites exhibits a depth-dependent profile. Therefore, it is important to consider the depth of photodegradation assessed by each characterisation method, considering the underlying mechanism of each technique.

Figure 7-9 B to D shows that for all samples, five characteristic α-crystalline diffraction peaks remain present after weathering, located at 2θ = 13.9° (110), 16.7° (040), 18.4° (130), 21.1° (111), 21.9° (041), and 25.3° (060) [30; 31]. These results confirm that the α-phase remains dominant after ageing. Additionally, the two PP composites display a mixed α/β crystalline phase, evidenced by a low-intensity peak at 2θ = 15.9°, attributed to β (300). Interestingly, neat PP also begins to exhibit this β (300) peak after 120 hours of weathering, with its relative intensity increasing to 7.2–14.7 %, suggesting that β-phase formation is induced during degradation.

Table 7-1 shows that β (300) peak intensities are higher in 5% MAPP-MS/PP across all durations (14.4–19.8 %), and even more prominent in 5% PDA/MAPP-MS/PP (12.9–30.0 %), highlighting the β-phase-promoting role of these fillers.

A notable feature in the weathered samples is the flattening of the amorphous halo in their XRD curves. Before exposure, all samples displayed a distinct amorphous halo, indicating a high amorphous content. As shown in Table 7-1, neat PP and the composites all experienced a sharp increase in crystallinity after 120 hours of weathering, a trend also observed in earlier studies [32; 33].

Table 7-1 demonstrates that photodegradation leads to increased crystallinity in PP and its composites, as well as alterations in crystalline composition. This phenomenon is attributed to "Chemi-crystallisation," a process also reported in previous studies on photodegraded polymers [32; 34; 35]. In photodegraded PP and its composites, Chemi-crystallisation occurs primarily through chain scission, which releases molecular segments that can reorganise into crystalline structures. This effect is most pronounced in the amorphous regions, resulting in a net increase in crystallinity.

However, with prolonged degradation, the accumulation of “chemical defects”, such as carbonyl groups, disrupts chain regularity and limits further crystallisation, particularly in neat PP and the 5% MAPP-MS/PP composite. In contrast, the 5% PDA/MAPP-MS/PP composite continues to exhibit slightly increased crystallinity due to the least change in chain regularity, attributed to the free-radical scavenging capability of polydopamine. Nevertheless, due to the complex nature of photodegradation, the relative intensities of different crystal planes vary irregularly with weathering duration, as shown in Table 7-1.

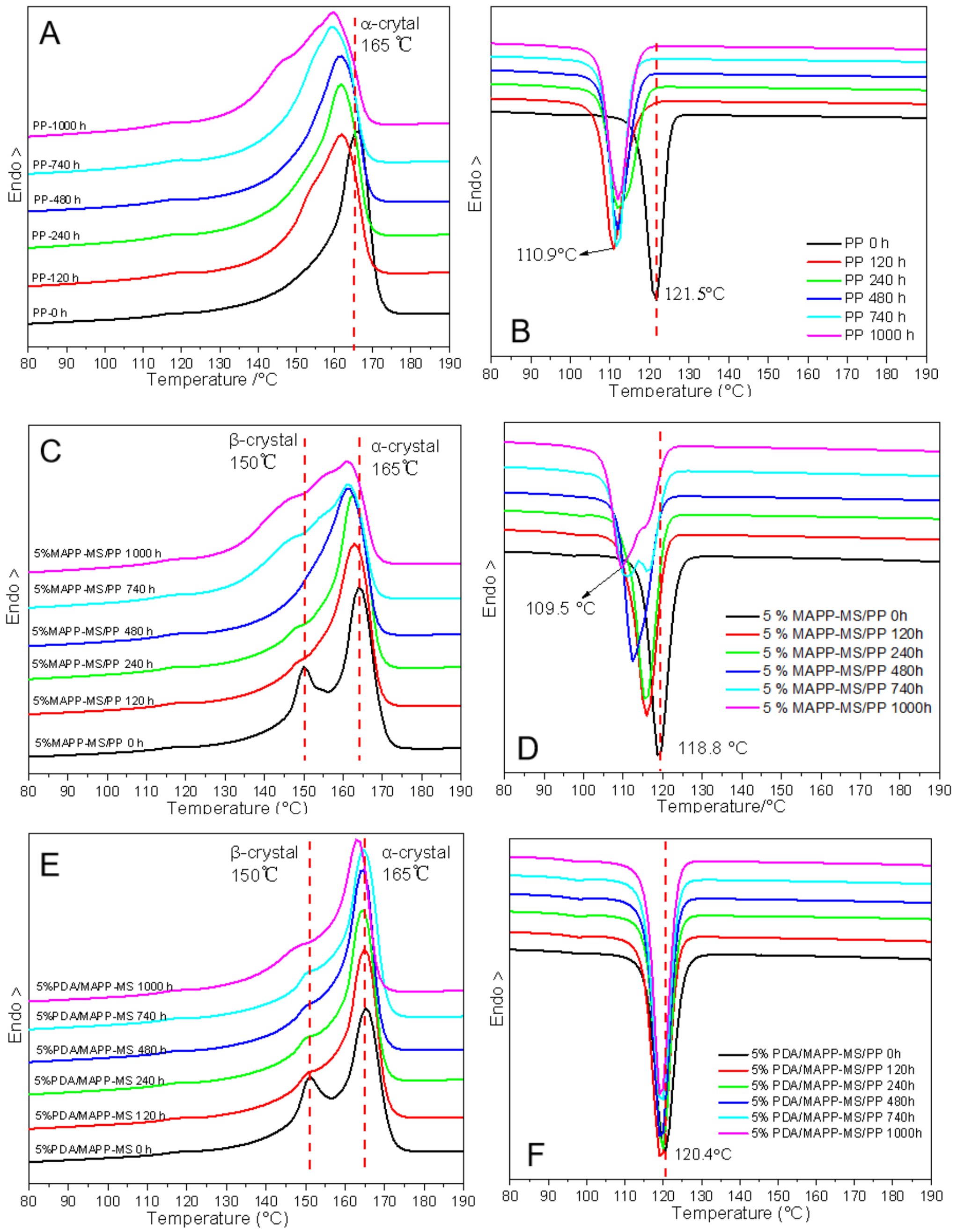

Figure 7- 19: DSC thermograms: (A) melting curves and (B) cooling curved of neat PP after different weathering durations; (C) melting curves and (D) cooling curved of 5% MAPP-MS/PP after different weathering durations;(E) melting curves and (F) cooling curved of 5% PDA/MAPP-MS/PP after different weathering durations.

7.5 Effect of accelerated weathering on the thermal properties of materials - DSC analysis

Photodegradation induced changes in crystal compositions in PP and its composites can also be identified by Differential scanning calorimetry (DSC). Figure 7-10 presents the melting and cooling curves of neat PP, 5% MAPP-MS/PP, and 5% PDA/MAPP-MS/PP. Their parameters of melting and cooling behaviour were listed in Table 7-2. The melting curves and parameters are also extracted from the second non-isothermal melting stage, where the effect of heat history was elucidate through the first heating stage.

7.5.1 Melting behaviour

From the DSC melting curves, a broadening of the melting peak and a shift to lower temperatures were observed, particularly with increasing weathering duration. For neat PP (Figure 7-10A), noticeable broadening occurred after only 120 hours of weathering. The initially sharp α-crystal melting peak at 165.0 °C declined to 161.9 °C, representing a 3.1 °C reduction. With prolonged exposure, the melting peak continued to broaden, reaching 159.6 °C after 1,000 hours- a total reduction of 4.4 °C relative to untreated PP.

In the case of 5% MAPP-MS/PP (Figure 7- 10 C), the broadening of the melting peak was less pronounced. After 120 hours of weathering, the peak temperature decreased by only 1.3°C relative to its original value of 164.2 °C. However, with prolonged weathering, the melting peak temperature further decreased to 161.0 °C after 1,000 hours, representing a 3.2 °C reduction. Notably, the melting peak after 740 hours was broadly widened, comparable to that of neat PP after 1,000 hours of weathering. The distinct β-crystal melting peak at 150 °C also disappeared after 120 hours of treatment.

For 5% PDA/MAPP-MS/PP (Figure 7- 10 E), the broadening of the melting peak remained relatively insignificant. The main peak at 165.0 °C retained its sharpness even after 1,000 hours of weathering. The peak temperature after 120 hours remained unchanged, and after 1,000 hours, it decreased marginally to 163.1 °C, representing a reduction of only 1.9 °C.

This general trend of broadened melting peaks and downward temperature shifts across all three polymers reflects the disruption of the crystalline phase and reduced thermal stability due to photodegradation within the PP matrix. Chain scission, increased imperfections in the crystalline phase, and secondary recrystallisation (Chemi-crystallisation) resulting from photo-oxidative degradation are the primary contributing factors, as reported in previous studies [36; 37]. XRD patterns revealed the emergence of a new β-PP crystalline phase in neat PP after 120 hours of weathering, with a melting peak at 150 °C. The overlap of this β-crystal peak with the primary α-peak, along with imperfect crystals from Chemi-crystallisation, accounts for the broadening. In PP composites containing 5% MAPP-MS or PDA/MAPP-MS, the presence of β-phase was confirmed both before and after weathering by XRD. Therefore, the disappearance of the β-crystal peak in their DSC melting curves is likely due to convolution rather than complete elimination.

Since changes in melting behaviour are directly correlated with photodegradation-induced alterations in crystalline composition, smaller deviations in melting peak temperature and shape indicate enhanced weathering stabilisation. The improved weathering resistance of 5% MAPP-MS/PP compared to neat PP can be attributed to stronger interfacial adhesion between the MAPP-modified mussel shell fillers and the PP matrix. This enhanced bonding restricts the rearrangement of polymer chains following degradation, resulting in fewer imperfect crystals and reduced disruption of the original crystalline structure.

Table 7- 3: Melting and cooling behaviour of PP and its composites after weathering.

Samples	**Melting behaviour**				**Cooling behaviour**	
	α crystal phase		**β crystal phase**			
	$T_{\alpha\text{-peak}}$ (°C)	ΔH_m^{α} (J/g)	$T_{\beta\text{-peak}}$ (°C)	ΔH_m^{β} (J/g)	T_c (°C)	ΔH_c (J/g)
PP UV exposure 0 h	165.0	83.8			121.5	-86.7
PP UV exposure 120 h	161.9	77.6			110.9	-86.2
PP UV exposure 240 h	161.6	78.9			112.0	-83.4
PP UV exposure 480 h	161.5	77.7			111.9	-85.9
PP UV exposure 740 h	159.3	77.0			111.9	-85.4
PP UV exposure 1000 h	159.6	78.5			112.2	-85.0
5 % MAPP-MS/PP UV exposure 0 h	164.2	73.5	150.1	6.3	118.8	-79.7
5 % MAPP-MS/PP UV exposure 120 h	162.9	77.3			116.0	-81.1
5 % MAPP-MS/PP UV exposure 240 h	162.5	76.3			115.8	-81.8
5 % MAPP-MS/PP UV exposure 480 h	161.3	75.8			112.5	-81.4
5 % MAPP-MS/PP UV exposure 740 h	161.4	77.6			116.3	-82.6
5 % MAPP-MS/PP UV exposure 1000 h	161.0	85.4			109.5	-88.7
5% PDA/MAPP-MS/PP UV exposure 0 h	165.0	73.6	151.0	6.5	120.4	-80.8
5% PDA/MAPP-MS/PP UV exposure 120 h	165.0	80.7			119.4	-82.5
5% PDA/MAPP-MS/PP UV exposure 240 h	164.4	78.8			119.8	-80.4
5% PDA/MAPP-MS/PP UV exposure 480 h	164.5	79.4			119.4	-84.5
5% PDA/MAPP-MS/PP UV exposure 740 h	164.7	77.9			119.6	-82.9
5% PDA/MAPP-MS/PP UV exposure 1000 h	163.1	76.5			119.4	-81.5

Among the three polymers, 5% PDA/MAPP-MS/PP exhibits the most minimal variation in melting behaviour, indicating the greatest enhancement in weathering resistance for PP when modified with 5% PDA/MAPP co-modified mussel shell fillers. This improvement may be attributed to two key factors: Restricted polymer mobility due to further enhanced filler-matrix adhesion with PDA/MAPP co-modification, as discussed in the previous section. Stabilising effects from the modified fillers, which suppress Chemi-crystallisation. This stabilisation likely arises from polydopamine's free radical scavenging capability, terminating polymer radicals and inhibiting the propagation of photooxidation-induced degradation.

7.5.2 Cooling behaviour

Changes in crystalline composition induced by photodegradation are also reflected in the cooling behaviour of three polymers, as shown in Figure 7-10 B, 7-10 D, and 7-10 F. For neat polypropylene (PP), the crystallisation peak temperature (T_c) decreased from 121.5 °C (pre-weathered) to 110.9 °C after 120 h of weathering, representing a reduction of approximately 10 °C. With prolonged weathering, Tc remained low (around 112.0 °C), indicating reduced crystallisability of photo-oxidised polypropylene chains. This decline results from the accumulation of carbonyl and other oxidative degradation products, which reduce the stereoregularity of polymer chains. As a result, greater supercooling is required to initiate crystallisation.

In contrast, the 5% MAPP-MS/PP composite exhibited a smaller reduction in Tc after weathering. Following 120 hours of exposure, Tc decreased from 118.8 °C to 116.0 °C, suggesting delayed degradation. However, extended weathering (up to 1000 hours) led to a further reduction to 109.5 °C, approaching the same 10 °C decline observed in neat PP.

The 5% PDA/MAPP-MS/PP composite demonstrated the greatest thermal stability. After 120 hours of ageing, Tc declined only slightly, from 120.4 °C to 119.4 °C. Remarkably, Tc remained constant even after 1000 hours of weathering. This stability is attributed to the preservation of stereoregularity in the polymer chains, due to polydopamine's radical-scavenging capability, which inhibits the formation of carbonyl and other degradation-related groups.

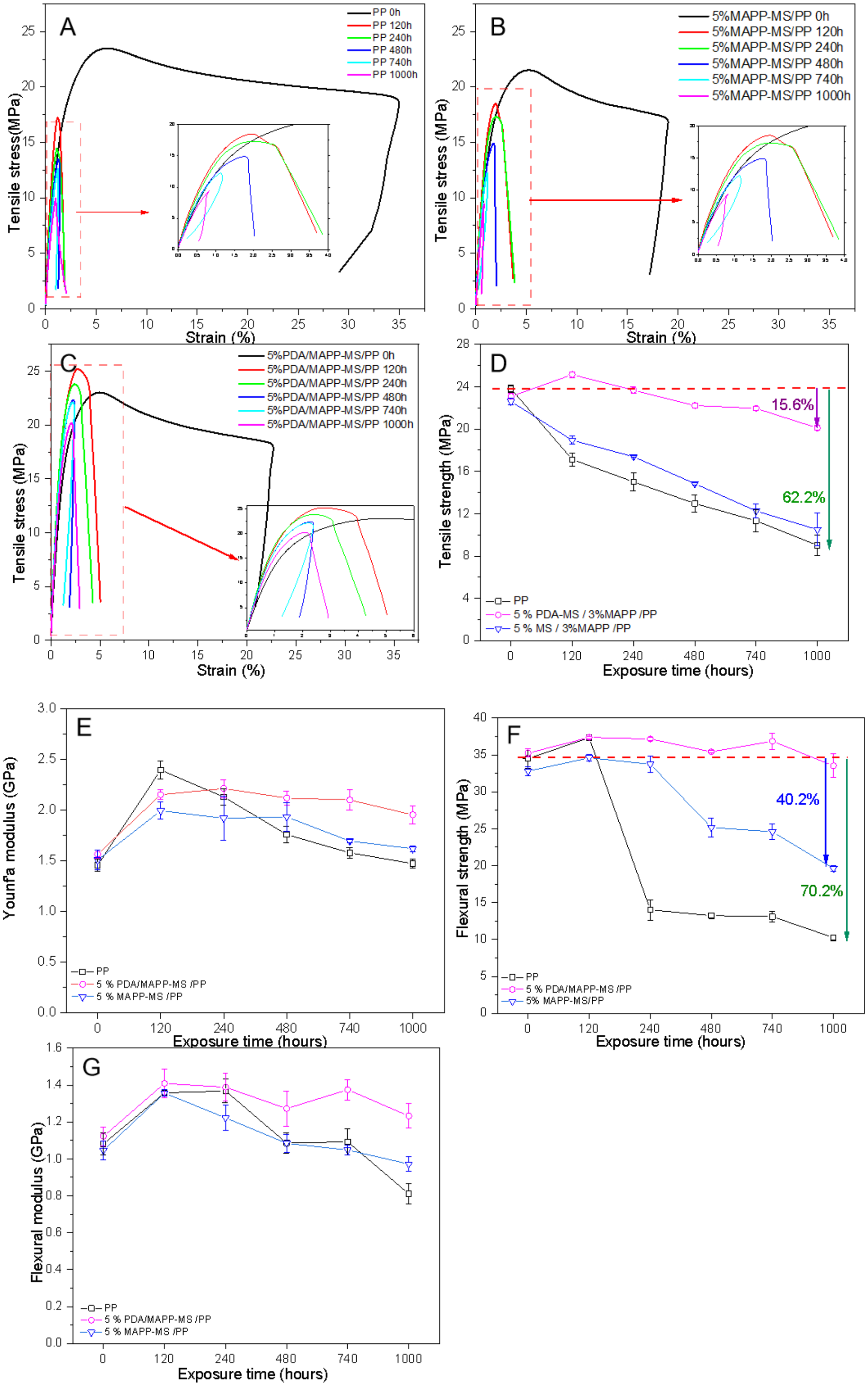

Figure 7- 21: Tensile stress-strain curves of (A) neat PP, (B) 5% MAPP-MS/PP, and (C) 5% PDA/MAPP-MS/PP. (D) Tensile strength, (E) Young’s modulus, (F) Flexural strength, and (G) Flexural modulus changes of three polymers with weathering times.

7.6 Effect of accelerated weathering on the mechanical properties of materials

The heterogeneous degradation pattern of polypropylene (PP) and its composites, which typically involves the formation of a brittle surface layer and a preserved ductile core, directly compromises mechanical integrity. This section examined how weathering-induced structural evolution affects three key mechanical properties: tensile, flexural, and temperature-dependent behaviour (via dynamic mechanical analysis).

The stress-strain curves of neat PP, 5% MAPP-MS/PP, and 5% PDA/MAPP-MS/PP are presented in Figure 7-11 (A-C), while the changes in tensile strength of these three polymers with weathering duration are plotted in Figure 7-11 (D).

As shown in the tensile stress-strain curves, neat PP, 5% MAPP-MS/PP, and 5% PDA/MAPP-MS/PP composites all exhibit reduced plastic deformation, with elongation at break decreasing to less than 5% compared to their unweathered counterparts. Additionally, ductile polymer characteristics - such as necking (yield) and cold drawing (plastic deformation) -disappeared in weathered samples.

A loss of ductility and increased brittleness were evident after 120 hours of accelerated weathering and continued to worsen with extended exposure. These changes are consistent with photodegradation-induced effects, including surface defects (e.g., cracks) and Chemi-crystallisation, both of which reduce the deformation resistance of the materials. Similar reductions in tensile strength, elongation at break, and viscosity have also been reported in other studies on aged PP [10].

Figure 7-11 (D) shows that both neat PP and 5% MAPP-MS/PP exhibit a similar degradation trend: a sharp decline in tensile strength occurs after 120 hours of weathering, followed by a continued decrease with prolonged exposure. In contrast, the tensile strength of 5% PDA/MAPP-MS/PP slightly increased after 120 hours, rising to 25.05 MPa compared to the unaged value of 23.08 MPa. After 1,000 hours of weathering, neat PP exhibited a 62.2% reduction in tensile strength, while 5% MAPP-MS/PP showed a similar loss of approximately 62%. However, the 5% PDA/MAPP-MS/PP composite demonstrated significantly greater retention of tensile strength, with only a 15.6% reduction. These results highlight the superior weathering resistance provided by the PDA/MAPP co-modified mussel shell fillers.

Figure 7–11E presents the changes in Young's modulus of the three polymers as a function of weathering duration. Prior to weathering, the Young's modulus values were 1.46 GPa for neat PP, 1.51 GPa for 5% MAPP-MS/PP, and 1.56 GPa for 5% PDA/MAPP-MS/PP. After 120 hours of weathering, all three materials exhibited a significant increase in stiffness, with Young's modulus rising to 2.40 GPa, 1.99 GPa, and 2.15 GPa, respectively.

However, with prolonged exposure, the modulus values began to decline. After 1000 hours of weathering, the modulus values were 1.47 GPa for neat PP, 1.62 GPa for 5% MAPP-MS/PP, and 1.95 GPa for 5% PDA/MAPP-MS/PP.The change in Young's modulus with weathering duration can be attributed to the combined effects of two competing factors: increased crystallinity and molecular weight reduction due to photodegradation. The net modulus value at any given time depends on which factor predominates.It is well established that Young's modulus increases with the degree of crystallinity [38]. As revealed by XRD analysis, crystallinity increased in all three materials after 120 hours of weathering, which corresponds to the initial rise in modulus. However, with further weathering, chain scission becomes more dominant. The resulting reduction in molecular weight eventually outweighs the effect of increased crystallinity, leading to a stabilisation or slight decline in modulus over time.

A similar non-uniform trend in elastic modulus with weathering duration was also observed by Navarro et al., who reported that the mechanical behaviour of degraded PP does not follow a linear progression with exposure time, supporting the pattern observed in this study [39].

As shown in Figure 7–11E, neat polypropylene (PP) exhibited an initial 8% increase in flexural strength after 120 h of weathering, followed by a sharp 59% reduction at 240 h and a pronounced 70.2% decline after 1000 h. The 5% MAPP-MS/PP composite showed more gradual changes, with increases of 6% at 120 h and 3% at 240 h, remaining stable until 740 h before decreasing by 40.2% at 1000 h. In contrast, the 5% PDA/MAPP-MS/PP composite demonstrated superior retention, with strength gains of 6% (120 h) and 5% (240 h), and only a 5% reduction after prolonged exposure.

The flexural modulus results in Figure 7–11F exhibit similar trends. Neat PP showed initial improvements of 25.6% (120 h) and 26.6% (240 h), followed by a return to baseline and a 25.0% decrease after 1000 h. The 5% MAPP-MS/PP composite maintained more sustained increases: 29.7% (120 h), 16.9% (240 h), and 3.9% (480 h), remaining stable

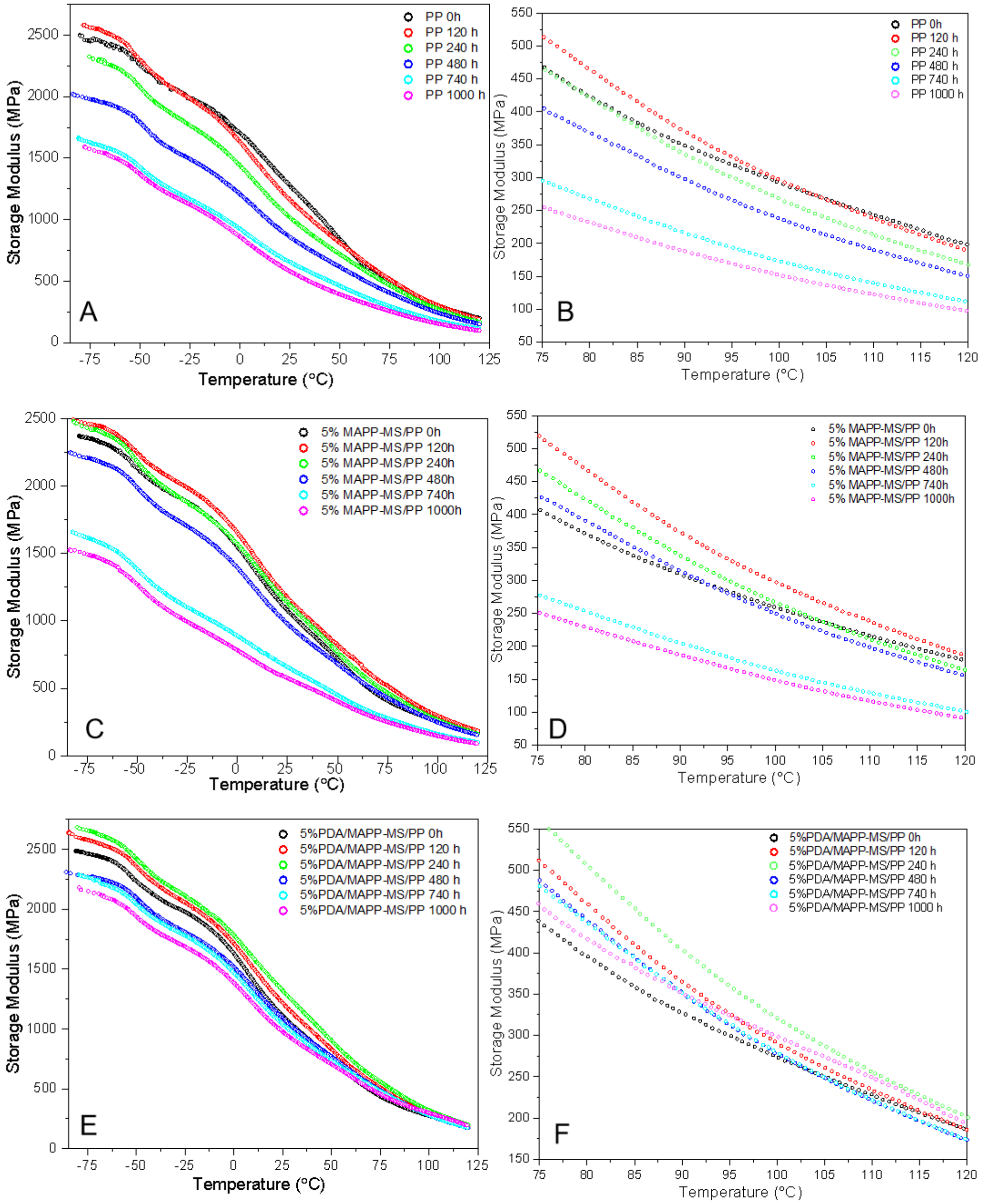

Figure 7- 23:DMA curves as a function of temperature, (A) storage modulus and (B) enlargement of neat PP before and after weathering, (C) storage modulus and (D) enlargement of 5% MAPP-MS/PP before and after weathering, (E) storage modulus and (F) enlargement of 5% PDA/MAPP-MS/PP before and after weathering.

until 740 h before a 7% drop at 1000 h. Notably, the 5% PDA/MAPP-MS/PP composite consistently outperformed the others, with modulus increases of 25.5% (120 h), 23.7% (240 h), 13.4% (480 h), 22.5% (740 h), and 9.8% (1000 h).

These trends result from competing mechanisms during weathering exposure. Initial improvements (≤240 h) are attributed to Chemi-crystallisation, where chain scission promotes molecular rearrangement and increased crystallinity. With continued weathering, photo-oxidative degradation dominates, characterised by chain scission, molecular weight reduction, and defect formation- effects that outweigh the benefits of crystallinity, especially in neat PP. The delayed decline in 5% MAPP-MS/PP and the strong retention observed in 5% PDA/MAPP-MS/PP reflect the protective mechanisms discussed previously, including filler-induced shielding and polydopamine's radical scavenging function, which collectively mitigate structural deterioration.

The temperature dependence of the dynamic mechanical properties of neat PP, 5% MAPP-MS/PP, and 5% PDA/MAPP-MS/PP before and after weathering is illustrated in Figures 7–12, 7–13, and 7–14. Dynamic mechanical analysis (DMA) is an effective method for studying phase transitions, relaxation behaviour, and stiffness characteristics in polymers. It evaluates key parameters such as storage modulus (E′), loss modulus (E″), and damping factor (tan δ). The storage modulus reflects the elastic behaviour of polymers, representing resistance to deformation under stress, and is closely related to Young's modulus [23].

The storage modulus reflects the elastic behaviour of polymers, representing resistance to deformation under stress, and is closely related to Young's modulus. Figure 7–12 shows a general decline in storage modulus with increasing temperature for all three materials, both before and after weathering. This trend is primarily due to increased polymer chain mobility and a reduction in intermolecular forces at elevated temperatures, leading to decreased elasticity and reduced resistance to deformation [40].

As discussed in previous chapters, PP and its composites exhibit three distinct regions over the temperature range of –70 to 120 °C: the highly packed glassy region (< –20 °C), the glass transition region (–20 °C to 25 °C), and the rubbery region (>25 °C). Since chain mobility increases with temperature, the influence of photodegradation on viscoelasticity varies across these regions. To better understand this, storage modulus values at –50 °C and 120 °C were selected for comparison and are summarised in Table 7–3.

Photodegradation involves competing mechanisms: chain scission reduces molecular weight and increases molecular mobility, while cross-linking and increased crystallinity from Chemi-crystallisation restrict this mobility. This complexity governs the evolution of viscoelastic properties during weathering and is reflected in the DMA results.

As illustrated in Figure 7-12A and Table 7-3, at –50 °C (glassy region), neat polypropylene (PP) exhibits an 18% increase in storage modulus after 120 hours of weathering. This initial enhancement is attributed to increased crystallinity and the formation of a new β-phase, both induced by Chemi-crystallisation. After 240 hours, the storage modulus shows a smaller rise (6.96%) relative to untreated PP, followed by a progressive decline with continued weathering. Ultimately, prolonged exposure results in a 29.71% reduction in storage modulus after 1000 hours.

In Figure 7-12C, similar but less pronounced increases in storage modulus for 5% MAPP-MS/PP are detected at 120 and 240 hours of weathering (5.23% and 2.59%, respectively). This is because crystallinity increases after weathering, but the composite already possesses an α/β mixed crystalline structure before treatment. As weathering continues to 480–1000 hours, storage modulus decreases, reaching a 40.50% reduction after 1000 hours.

Figure 7-12E demonstrates comparable increases in storage modulus for 5% PDA/MAPP-MS/PP at 120 and 240 hours, as this composite also features a mixed crystalline composition and experiences a slight crystallinity increase due to Chemi-crystallisation. With prolonged weathering, the storage modulus of 5% PDA/MAPP-MS/PP decreases by less than 10% after 480 and 740 hours, and only 13.14% after 1000 hours.

At 120 °C (rubbery region), where molecular mobility is much higher, the influence of weathering displays a pattern similar to that observed in the glassy region for all three materials. This highlights the consistent competition between chain scission and Chemi-crystallisation across the temperature spectrum.

From Figure 7-12B, neat PP initially shows a slightly higher storage modulus after 120 hours of weathering, attributable to increased crystallinity from Chemi-crystallisation. However, with further exposure, the storage modulus curves for PP after 240 and 480 hours fall below those of the untreated material, and a significant reduction is observed after 740 and 1000 hours. This progressive decline reflects the dominance of chain scission over crystallinity enhancement as weathering continues.

Figure 7-12D illustrates that the storage modulus curves for 5% MAPP-MS/PP after 740 and 1000 hours are markedly reduced compared to the untreated composite. Notably, samples weathered for 120–480 hours maintain higher storage modulus values in the rubbery region, indicating improved weathering resistance during this period. Nevertheless, prolonged weathering ultimately leads to substantial property loss.

In contrast, Figure 7-12F demonstrates that the storage modulus curve for 5% PDA/MAPP-MS after 1000 hours remains above that of the untreated composite, signifying excellent retention of elastic properties. This result underscores the superior weathering resistance of 5% PDA/MAPP-MS/PP, as it effectively balances the competing mechanisms of chain scission and Chemi-crystallisation.

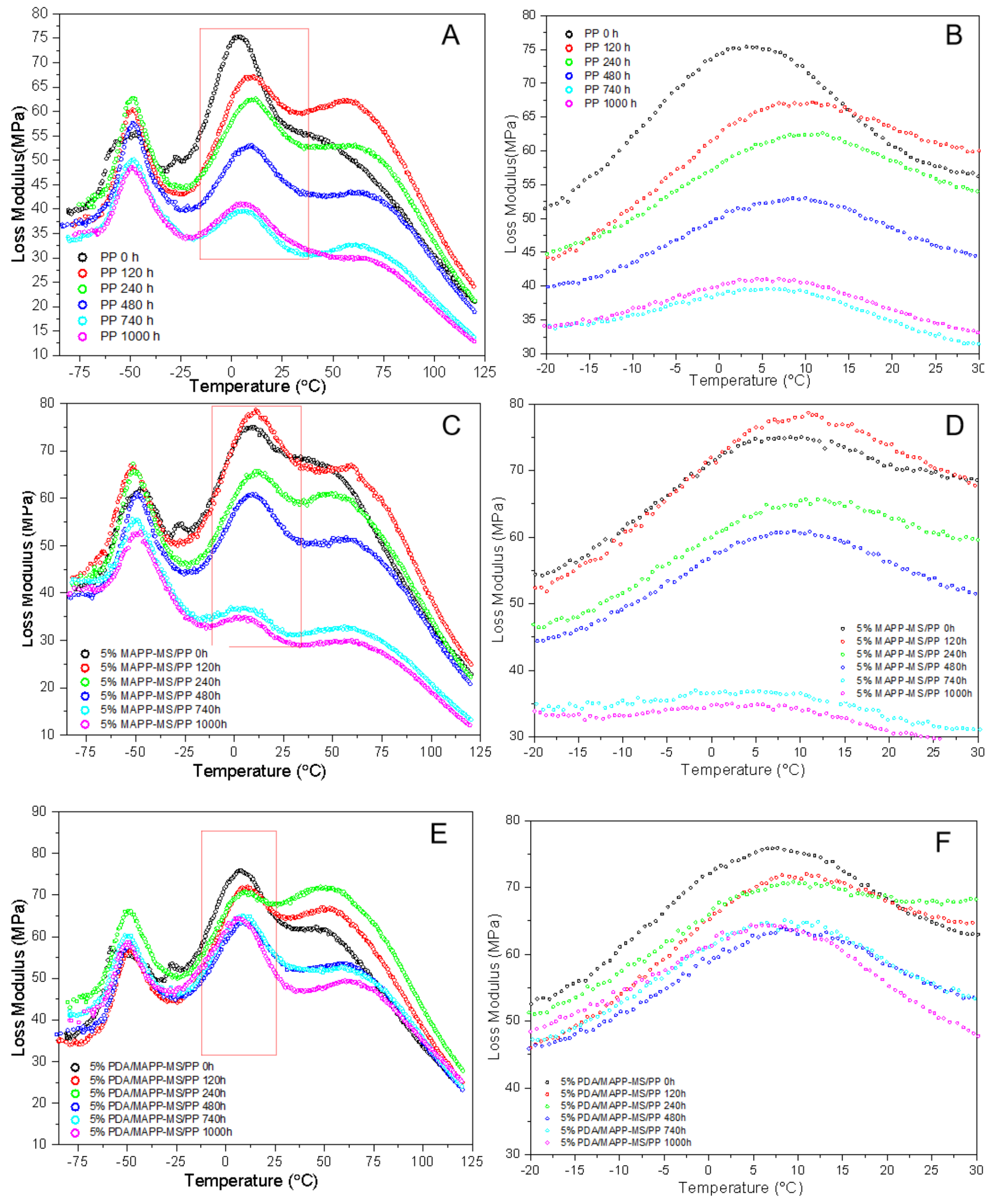

Figure 7- 25: DMA curves as a function of temperature, (A) loss modulus and (B) enlargement of neat PP before and after weathering, (C) loss modulus and (D) enlargement of 5% MAPP-MS/PP before and after weathering, (E)loss modulus and (F) enlargement of 5% PDA/MAPP-MS/PP before and after weathering.

Supporting these observations, Table 7-3 quantifies the changes: storage modulus values for neat PP decrease by 15.81% after 240 hours, and by 43.54% and 51.13% after 740 and 1000 hours, respectively. Similarly, 5% MAPP-MS/PP experiences significant reductions of 43.21% and 48.30% after 740 and 1000 hours. In contrast, the storage modulus of 5% PDA/MAPP-MS/PP varies only within a narrow range of –5% to 5% throughout the entire weathering period (120–1000 hours), confirming its exceptional stability and resistance to photodegradation.

Figure 7-13 (A–F) presents the loss modulus as a function of temperature for polypropylene (PP) and its composites at various weathering durations. The loss modulus corresponds to viscous behaviour and quantifies energy dissipation; a lower loss modulus indicates reduced energy dissipation under stress, typically resulting from material weakening due to chain scission and molecular weight loss during degradation.

In the glassy–rubbery transition region, the glass transition temperatures (Table 7-3) for PP and its two composites show only minor changes after weathering. However, the loss modulus for all three materials decreases in the transition region as weathering progresses, reflecting altered viscoelastic properties.

For neat PP, the loss modulus decreased continuously with prolonged weathering, showing a reduction of 11.20% after 120 hours, 16.94% after 240 hours, and 29.82% after 480 hours. A substantial decline was observed at extended durations, with a 47.53% decrease after 740 hours and a 45.48% decrease after 1000 hours.

For 5% MAPP-MS/PP, loss modulus increases by 4.49% (120 hours), 13.23% (240 hours), and 18.83% (480 hours), but decreases by about half after 740 hours (51.06%) and 1000 hours (53.85%). The least decrease in loss modulus is observed for 5% PDA/MAPP-MS/PP, with a maximum decrease of 16.73% after 1000 hours, supporting previous findings that PDA and MAPP co-modified mussel shell fillers improve the weathering resistance of PP.

Figure 7-14 presents the damping factor as a function of temperature after different weathering durations. The least change in damping factor curves over the entire temperature range is observed for 5% PDA/MAPP-MS/PP, further confirming that this composite has the best weathering resistance compared to neat PP and 5% MAPP-MS/PP.

These dynamic mechanical results clearly demonstrate that the 5% PDA/MAPP-MS/PP composite possesses the most improved weathering resistance among the three polymers examined. This is supported by its consistently minimal reductions in storage and loss modulus across both the glassy and rubbery regions, as well as the least variation in damping factor curves over the full temperature range.

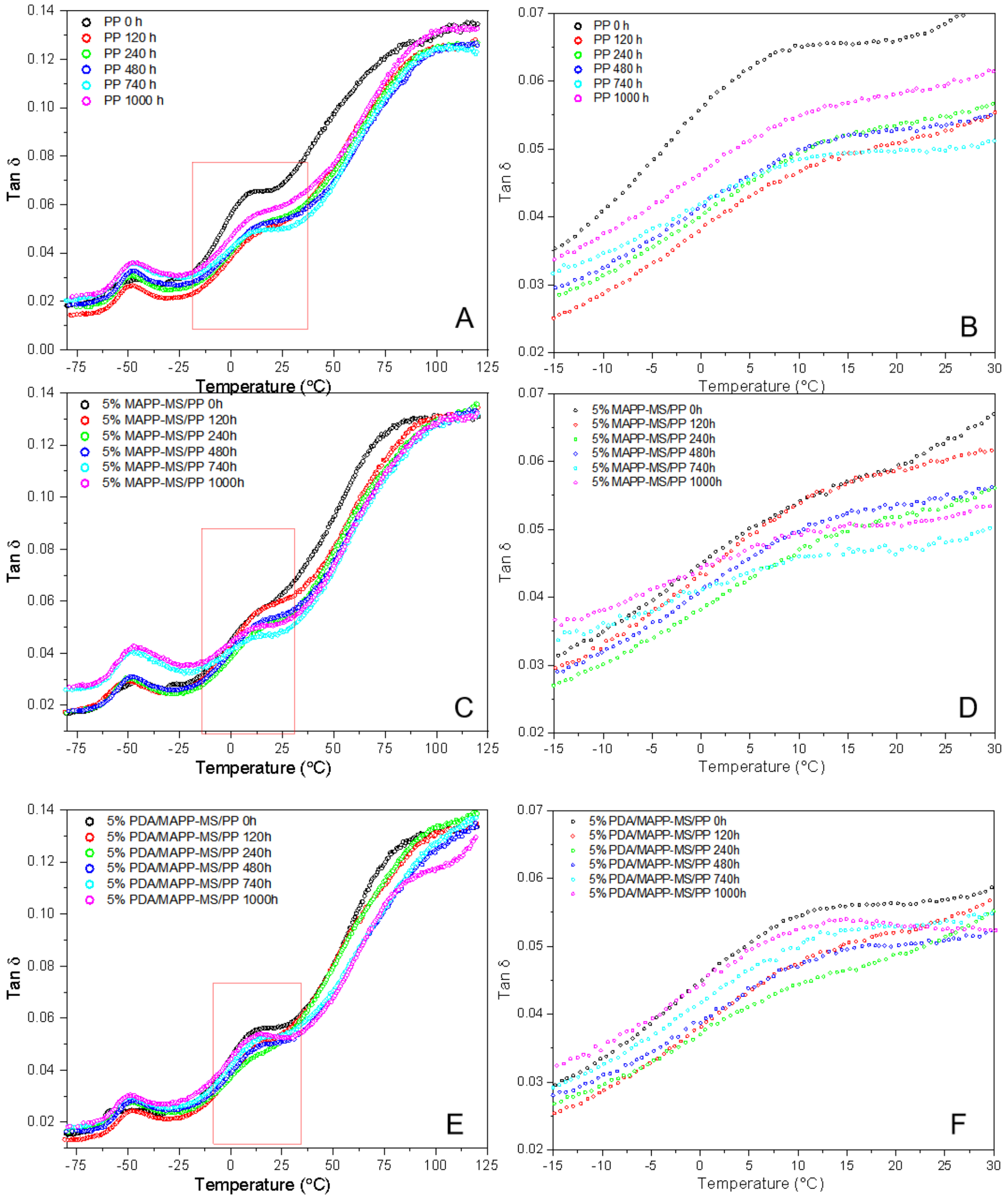

Figure 7- 27: DMA curves as a function of temperature, (A) damping factor and (B) enlargement of neat PP before and after weathering, (C) damping factor and (D) enlargement of 5% MAPP-MS/PP before and after weathering, (E) damping factor and (F) enlargement of 5% PDA/MAPP-MS/PP before and after weathering.

7.7 Mechanism of UV resistance improvement

The macroscopic properties of polymers are inherently governed by their microstructure. Changes in physical and chemical properties reflect the underlying microstructural evolution [23]. In this study, the observed changes in the macro-properties of polypropylene (PP) materials are primarily attributed to competing photodegradation mechanisms—namely, chain scission, molecular rearrangement, and cross-linking—induced by UV radiation during weathering.

The microstructural evolution of neat PP, 5% MAPP-MS/PP, and 5% PDA/MAPP-MS/PP is illustrated in Figure 7–15.

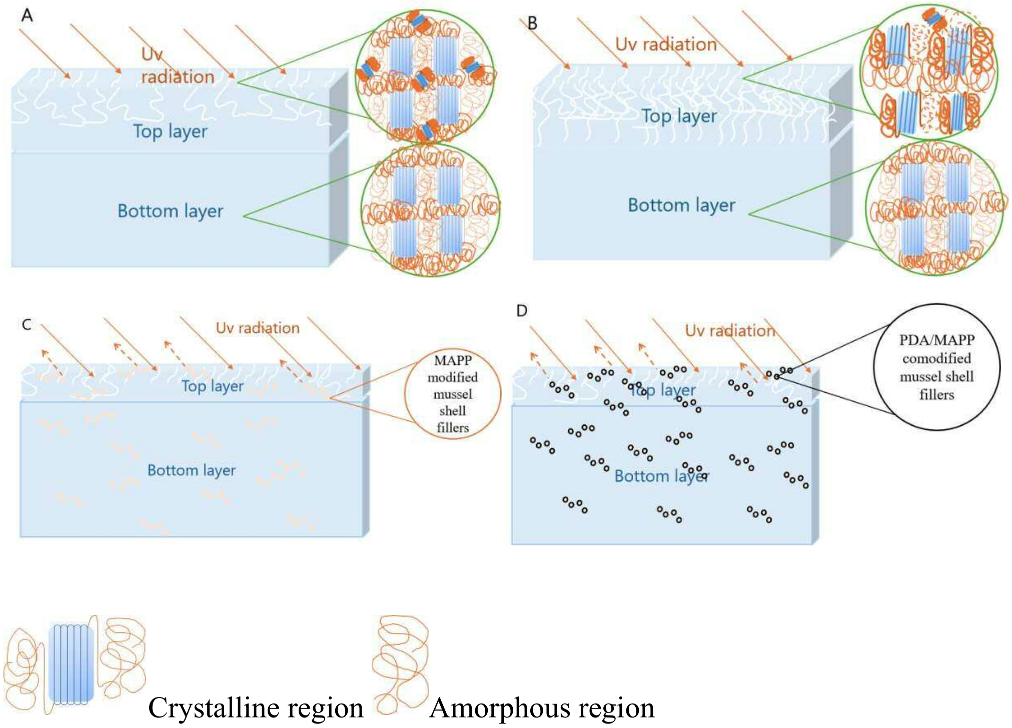

Figure 7- 29: Schematic of the microstructural evolution of neat PP during photodegradation (A) at early stage and (B) after intensive weathering treatment; (C) PP with 5% MAPP-MS fillers and (D) PP with 5% PDA/MAPP-MS fillers under weathering treatment.

As shown in Figure 7–15A, polypropylene exhibits a typical semicrystalline morphology, consisting of crystalline and amorphous phases. During the early stages of weathering, microstructural changes are localised to the surface layer directly exposed to UV radiation. Chemi-crystallisation and UV-induced cross-linking led to the formation of new, less perfect crystals and a reduction in amorphous regions, respectively. The synergistic action of these two processes results in an increase in crystallinity during short-term weathering. However, as weathering progresses, degradation penetrates deeper into the material. The thickness of the affected surface layer increases, and the crystalline regions begin to deteriorate under prolonged UV exposure. Consequently, chain scission becomes the dominant mechanism, surpassing cross-linking effects. This results in increased molecular breakage, defect formation, and the development of surface cracks, as illustrated in Figure 7–15B. These cumulative effects significantly compromise the mechanical integrity of PP. Surface crack formation stems from embrittlement caused by cross-linking and stress localisation due to Chemi-crystallisation, which together undermine structural cohesion—a mechanism similarly observed in UV-aged polyethylene [41].

The improved weathering resistance of PP containing 5% MAPP-coated mussel shell fillers is illustrated in Figure 7–15C. Although this composite still undergoes photodegradation under UV exposure, the inclusion of MAPP-MS alters the crystalline morphology of PP, resulting in a coexisting α/β crystalline structure. This mixed crystalline configuration exhibits enhanced durability against UV-induced degradation. Furthermore, mussel shell fillers provide a physical shielding effect, scattering incident UV radiation and reducing its penetration into the polymer matrix. These mechanisms contribute to the observed short-term improvements in properties such as flexural strength and storage modulus. However, with prolonged weathering, high-energy UV radiation drives chain scission to dominate, ultimately resulting in property deterioration. After 1000 hours of exposure, the mechanical properties of 5% MAPP-MS/PP approach those of neat PP, indicating limited long-term protection.

As discussed in Figure 7–7, photodegradation in PP is governed by an oxygen-controlled mechanism involving the propagation of various free radicals, which contribute to extensive chain cleavage. In this context, the 5% PDA/MAPP-MS/PP composite demonstrates the highest weathering resistance, as evidenced by minimal surface cracking and the most retained mechanical performance. This superior resistance arises from the synergistic interaction between polydopamine and MAPP-coated mussel shell fillers.

Figure 7–15D illustrates the proposed mechanism of PP with 5% PDA/MAPP-MS/PP. Photodegradation involves competing mechanisms: chain scission reduces molecular weight and increases polymer chain mobility, while Chemi-crystallisation-induced cross-linking or crystallinity restricts mobility. This complexity governs the evolution of material properties during weathering.

Polydopamine enhances UV resistance through two key mechanisms. Firstly, it prevents free radical formation by dissipating UV radiation energy. Meredith *et al.* [42] reported that eumelanin can non-radiatively dissipate over 99.9% of absorbed UV and visible radiation, based on its radiative relaxation quantum yield. Polydopamine, as a synthetic analogue of eumelanin, shares a similar chemical structure and functional groups. It exhibits a broad absorption spectrum across the UV to near-infrared region, as demonstrated in Chapter 4.

Secondly, polydopamine contributes to the termination of free radicals during photodegradation via its polycatechol structure [5]. The redox-active catechol groups enable effective scavenging of reactive radical species [17]. This dual functionality—UV energy dissipation and radical scavenging—underpins the significantly improved weathering resistance observed in the 5% PDA/MAPP-MS/PP composite.

7.8 Conclusion

This chapter investigated the effects of accelerated weathering on the thermal and mechanical properties of polypropylene (PP) and its composites with MAPP-modified and PDA/MAPP co-modified mussel shell fillers. The results revealed that photodegradation leads to significant microstructural and property changes in neat PP, including increased crystallinity, surface embrittlement, and reduced tensile, flexural, and dynamic mechanical performance over time. The incorporation of 5% MAPP-MS improved short-term resistance through enhanced filler–matrix interaction and UV shielding effects, although long-term degradation remained significant. In contrast, the 5% PDA/MAPP-MS/PP composite exhibited the highest weathering resistance, with minimal declines in melting temperature, and most maintained mechanical strength even after 1000 hours of UV exposure. This superior performance is attributed to the synergistic effects of polydopamine, which not only scavenges free radicals but also dissipates UV energy, effectively delaying photodegradation. Dynamic mechanical analysis further confirmed enhanced viscoelastic stability in PDA/MAPP-modified composites across the entire temperature range. Overall, the findings demonstrate that the co-modification of mussel shell fillers with MAPP and PDA significantly enhances the durability of PP under accelerated weathering, offering a promising strategy for extending the service life of bio-based polymer composites.

7.9 References

1. Koelmans, A. A., Redondo-Hasselerharm, P. E., Nor, N. H. M., *et al.* (2022). Risk assessment of microplastic particles. *Nature Reviews Materials*, *7*(2), 138-152.
2. Weinstein, J. E., Crocker, B. K., & Gray, A. D. (2016). From macroplastic to microplastic: Degradation of high-density polyethylene, polypropylene, and polystyrene in a salt marsh habitat. *Environmental toxicology and chemistry*, *35*(7), 1632-1640.
3. Law, K. L., & Narayan, R. (2022). Reducing environmental plastic pollution by designing polymer materials for managed end-of-life. *Nature Reviews Materials*, *7*(2), 104-116.
4. Brostow, W., Lu, X., Gencel, O., *et al.* (2020). Effects of UV Stabilizers on Polypropylene Outdoors. *Materials*, *13*(7).
5. Xiong, S., Wang, Y., Yu, J., *et al.* (2014). Polydopamine particles for next-generation multifunctional biocomposites. *Journal of materials chemistry A*, *2*(20), 7578-7587.
6. Hussain, I., & Redhwi, H. H. (2002). Development of polypropylene-based ultraviolet-stabilized formulations for harsh environments. *Journal of materials engineering and performance*, *11*, 317-321.
7. El-Naggar, N. E.-A., & Saber, W. I. (2022). Natural melanin: current trends, and future approaches, with especial reference to microbial source. *Polymers*, *14*(7), 1339.
8. Phua, S. L., Yang, L., Toh, C. L., *et al.* (2013). Simultaneous enhancements of UV resistance and mechanical properties of polypropylene by incorporation of dopamine-modified clay. *ACS applied materials & interfaces*, *5*(4), 1302-1309.
9. White, J. R., & Shyichuk, A. V. (2007). Macromolecular scission and crosslinking rate changes during polyolefin photo-oxidation. *Polymer Degradation and Stability*, *92*(7), 1161-1168.
10. Yakimets, I., Lai, D., & Guigon, M. (2004). Effect of photo-oxidation cracks on behaviour of thick polypropylene samples. *Polymer Degradation and Stability*, *86*(1), 59-67.
11. Andrady, A. L. (2011). Microplastics in the marine environment. *Marine Pollution Bulletin*, *62*(8), 1596-1605.
12. Paukszta, D., & Bednarek, W. H. (2018). In situ optical microscope studies at isotactic polypropylene crystallization induced by shear forces – A review. *Polymer Testing*, *72*, 238-243.
13. Deng, L.-F., Yin, J., Zhang, J., *et al.* (2024). In-situ synchrotron X-ray investigating crystallization of isotactic polypropylene with β-nucleating agent during injection molding. *Polymer*, *310*, 127469.
14. An, Y., Kajiwara, T., Padermshoke, A., *et al.* (2024). Photooxidative degradation and fragmentation behaviors of oriented isotactic polypropylene. *Polymer Journal*, *56*(4), 379-389.
15. Wang, X., & Song, K. (2024). Improvement of UV resistance and mechanism in polypropylene wax on wood surface through maleic anhydride and β-nucleating agent modification. *Polymer Degradation and Stability*, *226*, 110842.
16. Obadal, M., Čermák, R., Raab, M., *et al.* (2005). Structure evolution of α- and β-polypropylenes upon UV irradiation: A multiscale comparison. *Polymer Degradation and Stability*, *88*(3), 532-539.
17. Hu, J., Yang, L., Yang, P., *et al.* (2020). Polydopamine free radical scavengers. *Biomaterials Science*, *8*(18), 4940-4950.

18. Mendoza, R., Régnier, G., Seiler, W., *et al.* (2003). Spatial distribution of molecular orientation in injection molded iPP: influence of processing conditions. *Polymer*, *44*(11), 3363-3373.
19. Anshari, R., Tsuboi, M., Sato, H., *et al.* (2025). Raman and ATR-FTIR unmask crystallinity changes and carboxylate group and vinyl group accumulation in natural weathering polypropylene microplastics. *Scientific Reports*, *15*(1), 2518.
20. Celina, M. C., Linde, E., & Martinez, E. (2021). Carbonyl identification and quantification uncertainties for oxidative polymer degradation. *Polymer Degradation and Stability*, *188*, 109550.
21. Mylläri, V., Ruoko, T. P., & Syrjälä, S. (2015). A comparison of rheology and FTIR in the study of polypropylene and polystyrene photodegradation. *Journal of Applied Polymer Science*, *132*(28).
22. François-Heude, A., Richaud, E., Desnoux, E., *et al.* (2014). Influence of temperature, UV-light wavelength and intensity on polypropylene photothermal oxidation. *Polymer Degradation and Stability*, *100*, 10-20.
23. Tian, R., Li, K., Lin, Y., *et al.* (2023). Characterization Techniques of Polymer Aging: From Beginning to End. *Chemical Reviews*, *123*(6), 3007-3088.
24. Delprat, P., Duteurtre, X., & Gardette, J.-L. (1995). Photooxidation of unstabilized and HALS-stabilized polyphasic ethylene-propylene polymers. *Polymer Degradation and Stability*, *50*(1), 1-12.
25. S. Gomes, R., Fernandes, A. N., & Waldman, W. R. (2024). How to Measure Polymer Degradation? An Analysis of Authors' Choices When Calculating the Carbonyl Index. *Environmental science & technology*, *58*(17), 7609-7616.
26. Pilař, J., Michálková, D., Šeděnková, I., *et al.* (2011). NOR and nitroxide-based HAS in accelerated photooxidation of carbon-chain polymers; Comparison with secondary HAS: An ESRI and ATR FTIR study. *Polymer Degradation and Stability*, *96*(5), 847-862.
27. Lv, Y., Huang, Y., Yang, J., *et al.* (2015). Outdoor and accelerated laboratory weathering of polypropylene: A comparison and correlation study. *Polymer Degradation and Stability*, *112*, 145-159.
28. Rouillon, C., Bussiere, P. O., Desnoux, E., *et al.* (2016). Is carbonyl index a quantitative probe to monitor polypropylene photodegradation? *Polymer Degradation and Stability*, *128*, 200-208.
29. Machado, G., Denardin, E. L. G., Kinast, E. J., *et al.* (2005). Crystalline properties and morphological changes in plastically deformed isotatic polypropylene evaluated by X-ray diffraction and transmission electron microscopy. *European Polymer Journal*, *41*(1), 129-138.
30. Davachi, S. M., Heidari, B. S., Sahraeian, R., *et al.* (2019). The effect of nanoperlite and its silane treatment on the crystallinity, rheological, optical, and surface properties of polypropylene/nanoperlite nanocomposite films. *Composites Part B: Engineering*, *175*, 107088.
31. Bhuiyan, M. K. H., Rahman, M. M., Mina, M. F., *et al.* (2013). Crystalline morphology and properties of multi-walled carbon nanotube filled isotactic polypropylene nanocomposites: Influence of filler size and loading. *Composites. Part A, Applied science and manufacturing*, *52*, 70-79.
32. Rabello, M. S., & White, J. R. (1997). Crystallization and melting behaviour of photodegraded polypropylene — I. Chemi-crystallization. *Polymer*, *38*(26), 6379-6387.
33. Kotek, J., Kelnar, I., Baldrian, J., *et al.* (2004). Structural transformations of isotactic polypropylene induced by heating and UV light. *European Polymer Journal*, *40*(12), 2731-2738.

34. Craig, I. H., White, J. R., & Kin, P. C. (2005). Crystallization and chemi-crystallization of recycled photo-degraded polypropylene. *Polymer*, *46*(2), 505-512.
35. Wu, H., Zhao, Y., Dong, X.*, et al.* (2021). Probing into the microstructural evolution of isotactic polypropylene during photo-oxidation degradation. *Polymer Degradation and Stability*, *183*, 109434.
36. Gulmine, J. V., Janissek, P. R., Heise, H. M.*, et al.* (2003). Degradation profile of polyethylene after artificial accelerated weathering. *Polymer Degradation and Stability*, *79*(3), 385-397.
37. Výchopňová, J., Čermák, R., Obadal, M.*, et al.* (2007). The role of specific nucleation in polypropylene photodegradation. *Polymer Degradation and Stability*, *92*(10), 1763-1768.
38. Machado, G., Denardin, E., Kinast, E.*, et al.* (2005). Crystalline properties and morphological changes in plastically deformed isotatic polypropylene evaluated by X-ray diffraction and transmission electron microscopy. *European Polymer Journal*, *41*(1), 129-138.
39. Navarro, R. F., d'Almeida, J. R. M., & Rabello, M. S. (2007). Elastic properties of degraded polypropylene. *JOURNAL OF MATERIALS SCIENCE*, *42*(6), 2167-2174.
40. Seshweni, M. H. E., Makhatha, M. E., Botlhoko, O. J.*, et al.* (2023). Evaluation of Mechanical and Thermal Properties of Polypropylene-Based Nanocomposites Reinforced with Silica Nanofillers via Melt Processing Followed by Injection Molding. *Journal of Composites Science*, *7*(12), 520.
41. Rodriguez, A. K., Mansoor, B., Ayoub, G.*, et al.* (2020). Effect of UV-aging on the mechanical and fracture behavior of low density polyethylene. *Polymer Degradation and Stability*, *180*, 109185.
42. Meredith, P., & Riesz, J. (2004). Radiative Relaxation Quantum Yields for Synthetic Eumelanin. *Photochemistry and Photobiology*, *79*(2), 211-216.
43. Rätzsch, M., Arnold, M., Borsig, E.*, et al.* (2002). Radical reactions on polypropylene in the solid state. *Progress in Polymer Science*, *27*(7), 1195-1282.

Chapter 8

Conclusion

This thesis has comprehensively investigated the development and characterisation of polypropylene (PP) composites reinforced with biogenic filler-mussel shell (MS) fillers and harakeke fibres, with an emphasis on improving mechanical, thermal, and weathering resistance properties through surface modification strategies. The research addressed the critical challenges associated with filler–matrix compatibility and UV-induced degradation in PP, proposing a hybrid reinforcement system using polydopamine (PDA) and maleic anhydride-grafted polypropylene (MAPP) as effective surface modifiers.

8.1 Mussel Shell Filler Characterisation and Modification

The initial phase of the study focused on characterising the physicochemical properties of mussel shell fillers and confirming the successful polymerisation of dopamine into polydopamine. Solid-state Nuclear Magnetic Resonance (SS-NMR) and Fourier transform infrared (FTIR) analyses confirmed the formation of PDA with characteristic indole structures and quinone functional groups, while 3.2.14 Ultraviolet - visible (UV- vis) spectroscopy demonstrated its potential as a UV absorber.

The crystalline structure of mussel shell fillers, identified through X-ray diffraction (XRD) and SS-NMR, showed a predominance of aragonite and calcite phases. PDA surface modification did not alter the crystalline phases but improved thermal stability and introduced nitrogen-containing functional groups, as confirmed by Thermogravimetric analysis (TGA) and X-ray photoelectron spectroscopy (XPS). Pristine mussel shell and mussel shell after two main surface treatments, MAPP modification and PDA/MAPP co-modification, were investigated for surface properties. Contact angle measurements were used to calculate surface energy with the Fowkes and Owens–Wendt models. The results showed that PDA coating increased the polar component of the mussel shell surface energy. This change made the fillers more hydrophilic. As a result, their dispersion in the non-polar PP matrix was limited. MAPP modification, particularly when used in conjunction with PDA, effectively reduced the surface energy and minimised filler agglomeration. The combined PDA/MAPP treatment exhibited the lowest work of adhesion difference (ΔWa), indicating enhanced compatibility with non-polar PP.

8.2 Effect of Mussel Shell Fillers on Composite Properties

The incorporation of mussel shell fillers into PP demonstrated that performance is highly dependent on surface modification and loading level. TGA revealed that different mussel shell fillers, particularly those modified with PDA/MAPP, enhanced both the onset and maximum degradation temperatures of PP, indicating thermal reinforcement. Differential scanning calorimetry (DSC) and XRD confirmed that these fillers acted as nucleating agents, promoting both α- and β-crystalline forms of PP and increasing crystallinity. A notable 12.72% increase in crystallinity was achieved with 40 % PDA/MAPP-MS loading. Mechanical performance also reflected the influence of surface modification. Composites containing untreated fillers exhibited a continuous decline in tensile and flexural strength with increasing loading, with a 15% reduction at 40% MS/PP, attributed to weak interfacial adhesion. By contrast, MAPP-modified fillers mitigated these losses, with tensile and flexural strength showing modest gains at 30–40% loadings due to improved dispersion and bonding. PDA/MAPP-MS fillers consistently outperformed both untreated and MAPP-only systems, owing to favourable interfacial bonding achieved through dual modification. At 40% loading, PDA/MAPP-MS/PP composites displayed the highest mechanical properties: tensile strength increased by 6.2% compared with neat PP and by 2.6% relative to 40% MAPP-MS/PP. Flexural strength improved by 15.1% and 4.0%, respectively, while Young's modulus increased by 66.1% compared with neat PP and by 8.2% over 40% MAPP-MS/PP. The flexural modulus reached a maximum of 1.65 GPa at 40% PDA/MAPP-MS, representing gains of 53.1% and 8.8% relative to neat PP and 40% MAPP-MS/PP, respectively.

Morphological observations supported these results. SEM images of fracture surfaces provided direct evidence of improved filler–matrix bonding, with fewer interfacial voids and polymer fibrils adhering strongly to filler surfaces in MAPP-MS and PDA/MAPP-MS systems.

Dynamic mechanical analysis (DMA) further confirmed these enhancements. All mussel shell fillers increased the storage modulus of PP composites across the temperature range, indicating higher stiffness. PDA/MAPP-MS fillers induced the most pronounced improvement in the rubbery region, reflecting stronger interfacial adhesion. Loss modulus and damping behaviour revealed agglomeration effects at higher filler loadings (40%). Polymer chain mobility was most effectively restricted at low loading (5%) in MAPP-MS systems. By contrast, the lower loss modulus and lowest damping factor observed in PP with 30% PDA/MAPP-MS indicated superior interfacial adhesion at higher loadings.

Creep resistance was also improved by the incorporation of mussel shell fillers. PDA/MAPP-MS composites showed the greatest resistance, particularly under low temperatures and stress, due to restricted chain mobility arising from strong filler–matrix adhesion. Melt rheology investigations confirmed these effects: both MAPP-MS and PDA/MAPP-MS fillers induced a transition from melt-like to solid-like behaviour, especially at low frequencies, indicating altered viscoelastic responses caused by restricted polymer chain dynamics.

Taken together, SEM observations and mechanical test results support the proposed mechanism that MAPP and PDA/MAPP modifications enhance filler–matrix bonding. This improved interaction explains the superior thermal, mechanical, and rheological performance of PP composites reinforced with surface-modified mussel shell fillers.

8.3 Effect of hybridisation mussel shell filler with Harakeke Fibre on composite properties

The study was extended to hybrid systems incorporating alkali- and fibrillation-treated harakeke fibres. Alkaline treatment increased fibre crystallinity (up to 76.45%) and thermal stability ($T_5\%$ = 303°C), while also producing a rougher surface morphology, making the fibres more effective as PP reinforcements. When combined with surface-modified mussel shell fillers, these hybrid systems showed clear synergistic enhancements in both thermal and mechanical behaviour.

Thermal analysis confirmed that PP composites reinforced with harakeke fibres or hybrid combinations exhibited higher maximum decomposition temperatures than neat PP (458°C), indicating improved thermal stability. Hybrid composites displayed better thermal stability than fibre-only systems, with a higher proportion of modified mussel shell fillers delaying the onset of thermal decomposition. However, the $T_5\%$ values of PP/harakeke composites were generally lower than neat PP, reflecting the earlier degradation of cellulose.

XRD results revealed that harakeke fibres or hybrid combinations, like mussel shell fillers alone, promoted the coexistence of α- and β-crystalline forms in PP. The optimal synergistic effect was observed in hybrid composites containing 10% modified mussel shell fillers and 30% harakeke fibres, which achieved the highest β-crystal contents (17.32% for MAPP-MS and 16.71% for PDA/MAPP-MS). This ability to tailor the α/β crystal balance is significant, as α-crystals enhance stiffness and tensile strength, while β-crystals contribute to toughness and elongation at break, yielding PP composites with balanced mechanical properties.

Mechanical testing confirmed these advantages. Tensile strength and modulus increased markedly with fibre content. For example, 40% HF/3% MAPP/PP improved tensile strength by 91.6% and Young's modulus by 101% compared with neat PP. Hybrid systems also enhanced tensile properties: 10% MAPP-MS/30% HF/PP and 10% PDA/MAPP-MS/30% HF/PP increased tensile strength by about 48% relative to neat PP. Overall, hybrid fillers produced superior tensile and flexural properties compared with single mussel shell systems, regardless of surface treatment, at equivalent 40% loading levels. These synergistic effects are attributed to improved dispersion and stronger interfacial adhesion when both harakeke fibres and mussel shell fillers are incorporated.

Morphological characterisation supported these findings. SEM and BSE imaging showed strong fibre–matrix adhesion, minimal voids, and uniform dispersion of mussel shell fillers. EDS mapping further confirmed the complementary distribution of organic (harakeke) and inorganic (MS) phases within the PP matrix.

These structural features translated into improved dynamic mechanical behaviour, creep resistance, and rheological performance. DMA results demonstrated that the optimised 1:3 ratio of mussel shell fillers to harakeke fibres (MAPP-MS or PDA/MAPP-MS) provided the best reinforcing efficiency, owing to improved filler–matrix adhesion and dispersion. Hybrid composites with 10% PDA/MAPP-MS and 30% HF were particularly effective, showing reduced creep strain accumulation under cyclic loading and enhanced dimensional stability. Melt rheology analyses revealed that hybrid fillers improved the resistance of PP to shear forces, owing to the more network-like structures. These suggest reduced die swell during processing, improving processability in addition to end-use performance.

8.4 Weathering Resistance Enhancement

The final phase of this thesis evaluated the UV durability of PP composites under accelerated weathering. Neat PP showed severe photo-oxidative degradation, characterised by surface cracking, a marked increase in carbonyl index, reduced crystallinity, and a substantial loss in tensile strength (62% after 1000 hours). By comparison, 5% MAPP-MS/PP delayed visible cracking until 480 hours, while 5% PDA/MAPP-MS/PP exhibited superior resistance, with minimal crack formation and good retention of surface appearance even after 1000 hours.

UV irradiation initiates chain scission in PP, with the formation of carbonyl groups serving as a key indicator of degradation. FTIR analysis of the carbonyl index (CI) confirmed that neat PP was the most vulnerable to photodegradation, followed by 5% MAPP-MS/PP. In contrast, 5% PDA/MAPP-MS/PP demonstrated the greatest resistance, significantly delaying both the onset and progression of oxidation.

XRD analysis revealed that photodegradation increased crystallinity in PP and its composites through Chemi-crystallisation, a process driven by chain scission. However, the 5% PDA/MAPP-MS/PP composite maintained better chain regularity and developed controlled crystallinity due to the free-radical scavenging ability of polydopamine.

DSC results further highlighted these differences. Neat PP and 5% MAPP-MS/PP exhibited broadening and downward shifts in melting peaks with extended weathering, indicating crystalline phase disruption and reduced thermal stability. In contrast, the 5% PDA/MAPP-MS/PP composite showed only minor changes in melting behaviour, confirming its enhanced weathering resistance. Similarly, crystallisation peak temperature (Tc) decreased markedly for neat PP, less so for MAPP-MS/PP, and remained most stable in PDA/MAPP-MS/PP, reflecting superior preservation of polymer chain stereoregularity.

Mechanical testing showed that all materials became more brittle after weathering, with reduced plastic deformation and tensile strength. Neat PP and 5% MAPP-MS/PP both suffered major strength losses, around 62% after 1000 hours. By contrast, the 5% PDA/MAPP-MS/PP composite retained much of its strength, with only a 15.6% reduction after 1000 hours. Dynamic mechanical analysis (DMA) supported these findings, confirming the superior viscoelastic stability and resistance to UV-induced degradation of PDA/MAPP-modified composites across the full temperature range.

8.5 Overall Contributions and Implications

This thesis demonstrates that mussel shell fillers, when properly surface-modified, are effective bio-based reinforcements for thermoplastics. Polydopamine contributes multifunctional benefits—thermal stability, UV absorption, and radical scavenging—making it a valuable modifier in weatherable polymer composites. Hybrid reinforcement with harakeke fibre and mussel shell fillers enables a tailored balance of stiffness, toughness, thermal resistance, and dimensional stability. The PDA/MAPP co-modification strategy represents a practical, sustainable, and scalable method for enhancing the performance of PP composites across multiple application areas. These results contribute to the growing body of knowledge in bio-based polymer composites and present a viable pathway for reducing reliance on synthetic additives while improving environmental resilience and functional performance.

8.6 Future Work and Outlook

This study has advanced the understanding and performance enhancement of polypropylene (PP) composites reinforced with mussel shell fillers and harakeke fibres. However, several research directions remain to further exploit the potential of these sustainable materials.

8.6.1 Broadening the Filler Source

The present work focused on mussel shells as the sole mollusc-derived filler. Given their similar chemical composition, other abundant aquaculture wastes in New Zealand—such as oyster, scallop, cockle, and clam shells—could be processed either individually or in combination. Co-processing these shells may offer a practical route for large-scale valorisation, improve supply chain flexibility, and support commercialisation by enabling continuous, scalable production.

Advanced Characterisation of Dispersion and Interfaces

Future studies should employ three-dimensional, non-destructive techniques such as X-ray micro-computed tomography (micro-CT) to assess filler dispersion, filler – fibre interactions, and interfacial bonding quality. This approach would enable detailed visualisation of voids, agglomeration, filler orientation, and interfacial gaps, providing deeper insight into the microstructural mechanisms influencing mechanical performance and failure. Comparative imaging of composites containing untreated, MAPP-modified, and PDA/MAPP co-modified fillers—both with and without harakeke fibres—would help establish structure – property relationships more precisely.

8.6.2 Influence of Higher Filler Loadings on Weathering Resistance

Weathering studies in this work focused on low filler loadings (5 wt.%). Investigating higher levels (10 – 40 wt.%) could reveal how filler concentration influences UV resistance, degradation kinetics, and long-term mechanical stability. Such findings would be critical for defining optimum loading thresholds for outdoor applications.

8.6.3 Real-World Weathering Validation

While accelerated weathering tests provide valuable screening data, real-world field trials are essential to verify long-term durability. Testing under varying climatic conditions-UV intensity, humidity, temperature fluctuations, and airborne pollutants-would offer a more comprehensive understanding of material stability, including microplastic generation and property retention.

8.6.4 Upscaling and Industrial Integration

To bridge laboratory research and commercial deployment, scaling up filler processing and composite manufacturing using industry-compatible methods should be prioritised. This includes optimising grinding, surface modification, and drying processes; ensuring batch-to-batch consistency; and evaluating cost-effectiveness. Partnerships with industry stakeholders could accelerate the translation of these sustainable composites into automotive, construction, and packaging markets.

Addressing these research avenues will not only deepen scientific understanding but also facilitate the industrial adoption of biogenic fillers in high-performance PP composites. Such efforts will contribute to a circular materials economy, reducing reliance on fossil-derived polymers and promoting sustainable, value-added utilisation of aquaculture and plant-based wastes.